OBSERVATIONS ON THE SODIUM AIRGLOW

P.A. Greet, B.Sc.(Hons)

A thesis for the degree of Doctor of Philosophy

THE MAWSON INSTITUTE FOR ANTARCTIC RESEARCH

UNIVERSITY OF ADELAIDE

October 1988

This thesis contains no material which has been accepted for the award of any other degree or diploma in any University, and, to the best of the author's knowledge and belief, it contains no material previously published or written by another person, except when due reference is made in the text. I consent to this thesis being made available for photocopying and loan by the librarian of the University of Adelaide upon acceptance of the degree.

(P.A. Greet)

Abstract

Observations on the sodium airglow using a Fabry-Perot spectrometer (FPS) at Mt. Torrens (35° S, 139° E) are described. Modifications to the instrument and assessment of two new etalons are described. Three years of observations of the sodium twilight emission using the high-resolution FPS have been made to obtain wind and temperature estimates from the 90 km altitude region. Attempted observations of the sodium dayglow emission with the dual FPS are discussed.

Analysis of the sodium emission line is complicated by its hyperfine structure. A hollow-cathode sodium lamp has been used to obtain the FPS instrument function, to define the hyperfine structure in the analysis, and to give a rest wavelength for wind determinations. Care must be exercised in analysis as contamination by both Rayleigh scattered sunlight and the photochemical excitation of the emission affect results obtained. The twilight- and day- glow are excited dominantly by resonant scattering of sunlight.

A summer mean temperature of 150 K and a winter mean temperature of 199 K have been determined from 2 years of data. A systematic difference between dusk and dawn temperatures of up to 37 K in March and April is ascribed to the diurnal tide. The FPS measurements of the dawn − dusk temperature difference are in reasonable agreement with those calculated using a recent theoretical model together with measurements of the amplitude and phase of the diurnal tide from the nearby Buckland Park, spaced-antenna, partial-reflection (SAPR) radar.

Comparisons of the FPS and SAPR radar horizontal wind measurements are presented. There is excellent agreement in some cases and, in general, agreement between the two methods is good when the wind field is uniform spatially. Short-term variability, some of which may be ascribed to gravity waves, is seen in both the temperature and wind measurements.

The project has shown that high-resolution Fabry-Perot spectrometer observations of the sodium airglow provide a useful means of studying the dynamics of the 85–90 km region.

Acknowledgements

The author would like to acknowledge the supervision of this project by Dr. F. Jacka who enthusiastically contributed guidance and ideas at every opportunity. Other staff of the Mawson Institute also provided support for the project, D. Creighton with electronics, and F. Fone with mechanical construction and modifications. Fellow students of the Mawson Institute, especially Norm Jones, Paul Wardill, and Gina Price shared knowledge and experiences from which we all benefited.

The collaboration of Dr. R. Vincent and other members of the Atmospheric Physics group in the Physics Department is acknowledged. The group provided the Buckland Park radar data and were always willing to consider and discuss results obtained.

I would like to thank Niel McKenzie for suggesting improvements to the first draft of this thesis.

Finally I would like to thank Tony Morland, my father and mother, sisters and brother for providing moral support and stability, and who acepted my necessary absences.

Contents

Chapter 1

INTRODUCTION

The λ 589.0/ 589.6 nm doublet is emitted by sodium distributed in a thin layer in the atmosphere and excited by resonant scattering of sunlight, and by a photochemical mechanism. The emission was first observed by Slipher (1929) and more extensive studies of it both at twilight and at night were made by Bernard (1938). Recent studies of the sodium layer have been made using lidars. These have shown that atmospheric sodium is confined in the region centered at a height of 85–90 km in the upper mesosphere. The layer height is quite stable, varying only slightly with season.

Fabry-Perot spectrometers have been used for observations of the thermospheric oxygen emissions, allowing determination of winds and temperatures of the emission regions (Jacka 1984). The aim of this project was to investigate whether the Fabry-Perot spectrometer developed by the Mawson Institute, described in chapter 3 and located at Mt. Torrens, near Adelaide, could be used for observations of the sodium emission to study the dynamics of the mesosphere.

Successful observations of this emission have now been achieved and they allow determinations of winds and temperatures in the 85–90 km region. This region is important for study of the coupling between the neutral atmosphere and ionosphere and the saturation and dissipation of gravity waves produced in the troposphere. Coupling between and energy transport from one region to another have been a focus of interest in atmospheric physics in recent years. The

troposphere is a rich source of gravity waves which propagate into and deposit their energy and momentum in the mesosphere. This has a major impact on the mean flow in that region. The diurnal and semidiurnal tides also have large amplitudes in the mesopause region and strongly affect the temperature and wind variations.

The middle atmosphere, the region from 10 km to the homopause near 110 km, is difficult to study as, especially at the higher altitudes, few methods of measuring fundamental parameters such as temperature and density are available. Where applicable, ground-based observations using optical and radio techniques provide a relatively inexpensive means of obtaining such information with reasonable temporal coverage. The existence of the sodium layer permits detailed optical observations of the mesopause region, different techniques providing different information. These optical techniques, and other measurements on the same region, and their contributions to atmospheric physics are reviewed in chapter 2.

Temperature measurements of the mesopause region have been obtained using rockets (Philbrick *et al.* 1985), and more recently using lidars. Density variations measured using Rayleigh backscatter lidars can be used to determine temperatures up to about 75–80 km (Hauchecorne *et al.* 1987b; Chanin *et al.* 1987; Shibata *et al.* 1986). Fricke and von Zahn (1985), von Zahn *et al.* (1987a), and von Zahn and Neubar (1987) have used a technique pioneered by Gibson *et al.* (1979) to obtain temperature estimates by measuring the hyperfine structure of the emission from the sodium layer using resonant backscatter from tunable, narrow-bandwidth lasers. Temperature measurements are also obtained from incoherent backscatter radars (Wand 1983a,b; Fukuyama *et al.* 1987; Lathuillere *et al.* 1983). Such studies have shown the temperature structure to be complex with contributions from tides and gravity waves. Breaking gravity waves produce superadiabatic lapse rates and large amplitude waves can reverse the mean temperature trend in the mesopause region. Only a few laboratories in the world are capable of measurements of temperatures in this region using any of the techniques mentioned above. Temperatures obtained from Fabry-Perot spectrometer observations of the sodium emission

may thus make a valuable contribution. Temperature measurements obtained by this study are presented in chapter 6 and the required analysis in chapter 5.

Extensive observations of the mesospheric winds have been obtained using spaced antenna partial reflection radars (Vincent 1984b). The radars measure the velocity of drift of irregularities in ionization which are assumed to move with the neutral wind. One such radar is located at Buckland Park, 50 km west-north-west of Mt. Torrens. The Buckland Park radar is capable of measuring horizontal winds in the height range 60–100 km. Studies of gravity waves (Vincent 1984a; Vincent and Fritts 1987), tides (Vincent *et al.* 1987), and gravity wave momentum fluxes (Reid and Vincent 1987; Fritts and Vincent 1987) have been made. The radar can be used to sample the same height range as the Fabry-Perot Spectrometer and comparisons of horizontal winds from both experiments are made in chapter 7. A comparison of the results from the two wind measurement techniques allows both the verification of the methods and more detailed study of atmospheric phenomena.

Chapter 2

THE MIDDLE ATMOSPHERE

This chapter places the project in context by reviewing current developments in atmospheric physics. It has three inter-related sections and they are devoted to: the sodium layer, middle atmosphere temperature structure, and middle atmosphere dynamics.

2.1 SODIUM LAYER

2.1.1 Vertical distribution of sodium

The λ 589.0/589.6 nm doublet of sodium was first recognized in nightglow spectra by Slipher (1929). The existence of a thin layer of neutral sodium atoms was inferred from measurements of twilight intensity of the emission (Bernard 1938). Neutral sodium atoms are excited resonantly by sunlight. As the sun sets and the Earth's shadow passes over the layer, emission intensity rapidly decreases. During the day, in order to detect it, the emission must be isolated from the background of Rayleigh scattered sunlight. Rayleigh scattering occurs mainly from the lower, more dense, regions of the atmosphere so at twilight, when the sun has set at 30 km but is still illuminating the sodium layer at 90 km, the sodium emission is visible with minimal background contamination. Photometer measurements of the change in emission intensity through twilight were used to obtain the height and general shape of the layer and to calculate sodium abundance (number of sodium atoms per unit column of atmosphere). Bullock and Hunten (1961) found a

seasonal variation in the height of the maximum density of the layer (layer peak) and in the mean abundance. A maximum abundance of 4.7×10^9 atoms cm^{-2} occurred in winter and a minimum of 1.0×10^9 atoms cm^{-2} occurred in summer. The height of the layer peak also varied from 88 km in spring to 85.2 km in autumn. These observations were made at Saskatoon, Canada (52° N). Observations from New Zealand (44° S) indicated similar variations; a maximum abundance of 15×10^9 atoms cm^{-2} in winter and a minimum of 2.5×10^9 atoms cm^{-2} in summer (Hunten *et al.* 1964).

Lidar observations have been made at several locations most of which are listed in table 2.1 . Variations in the measured characteristics occur from one location to another but all are in general agreement and relate well to other types of measurements. The sodium layer also varies considerably at a single location over quite short time scales. This will be discussed further later. Values quoted in this section are usually means of many measurements over an extended period, short term variations being averaged out.

Lidar (light induced detection and ranging) systems use a laser to illuminate the sky. The λ 589 nm sodium emission is induced by resonant excitation. By appropriately timing transmission of the laser pulses and recording of the returned signal, variations of sodium density with height can be determined. Lidars with a height resolution of about 1 km and obtaining density height profiles every 15 minutes have shown the sodium layer to be structurally complex. The layer often has two peaks in density separated by 6 or 7 km. (Blamont *et al.* 1972). These peaks propagate through the layer which suggests they are manifestations of wave motions. Because of subsidiary peaks, height information is more sensibly given in terms of centroid height rather than the height of maximum density. Average centroid heights and mean abundances are also given, where available, in table 2.1. Figure 2.1 shows the variations in density profiles through a typical night. Structural variations in the sodium layer will be discussed further in section 2.3. The better height resolution obtainable with lidars has shown that in winter the increase in sodium abundance is due to increases in sodium concentration on the bottomside of the layer.

Table 1: Summary of sodium layer lidar studies. (S=summer, W=winter, A=autumn)

location	reference	type duration	temperature (K)	abundance $\times 10^{13}(m^{-2})$	peak height centroid (c) (km)	layer width FWHM (km)	other comments
Winkfield, England (0.7°W, 51.4°N)	Gibson and Sandford, 1971	night-time 12mths		S[1] ~ 3 W ~ 9	S 87.5 W 91		seasonal variations abundance enhancements
	Gibson and Sandford, 1972	daytime 7 days					first daytime measurement day/night abundance ratio
	Thomas et al., 1977	steerable night-time					horizontal variations
	Gibson et al., 1979	hyperfine 2 nights	220 K and 170 K				first temp. measurement using hyperfine structure
Menlo Park, Cal., USA (37°N, 122°W)	Hake et al., 1972	night-time 2 days			90	~ 10	abundance enhancements
Haute Provence, France (44°N, 5°W)	Blamont et al., 1972	night-time 8 months	171–215 K	A 8	W 93 S 87		seasonal variation absorption cell temp.
	Megie and Blamont, 1977	night-time 3 years			87–92.5		seasonal variation stratificationlayer model
	Granier and Megie, 1982	day+night 2 years		W 6.9	87–94		day/night abundance ratio twilight variability
Sao Jose dos Campos, Brazil (23°S, 46°W)	Simonich et al., 1979	night-time 5 years		4.4	94	22.8	seasonal and nocturnal var. 85 km subsidiary peak
	Clemesha et al., 1982	day+night 10 days		5.9	91		tidal variations vertical winds
	Batista et al., 1985	day+night 20 days					tidal variations
	Kirchhoff et al., 1986	twilight 31 days					twilight varaiations
Illinois, USA (40°N, 88°W)	Richter et al., 1981	night-time 12 months			90		gravity waves
	Gardner et al., 1986b	night-time 6 years		2–10	c 92	10.0	seasonal variations nocturnal variations
	Gardner and Voelz, 1987	night-time 6 years					gravity waves
	Kwon et al., 1987	day+night 4 days		16.6	c 90.9	12.2	tidal variations vertical winds
	Beatty et al., 1988	CEDAR					sporadic layers
+AFGL, Bedford, Mass., USA (42°N, 71°W)	Gardner et al., 1986a	night-time 3 days		7.1	c 90.1	11.0	horizontal variations 4 sites studied, dynamics
Mauna Kea, Hawii (20°N, 155°W)	Kwon et al., 1988	night-time 5days					sporadic layers
Svalbard (78°N, 16°W)	Gardner et al., 1988	day+night 2 months		A 4.8 S 0.6	A c 93.5 S c 91	A 7.6 S 9.0	summer polar depletion
Andoya, Norway (69°N, 16°W)	Fricke and von Zahn, 1985	hyperfine night-time	195 at peak				instrument description analysis techniques
	von Zahn and Neuber, 1987	hyperfine 4 months	profiles 82–108 km				Winter profile, lapse rates mesopause 100km 194 K
	von Zahn et al., 1987a	night-time					sporadic layers
	von Zahn and Hansen, 1988	day+night					sporadic layers
	von Zahn et al., 1988	day+night 10 days		W 5.8 S 0.6	W 89.2 S 93	W 9.8 S 6	summer polar depletion
	Neuber et al., 1988	hyperfine 2 winters	monthly mean profiles				mesopause 100±2 km temperature variations
Syowa, Antarctica (Japan) (69°S, 40°E)	Nomura et al., 1987	night-time 7 months			90	13	seasonal and nocturnal var. auroral effects
Heyss Island, USSR (80°N, 50°E)	Megie et al., 1978b	night-time 3 months	219 K, 202 K, and 220 K	W 6 (4–7.5)	87	10–20	absorption cell temperatures

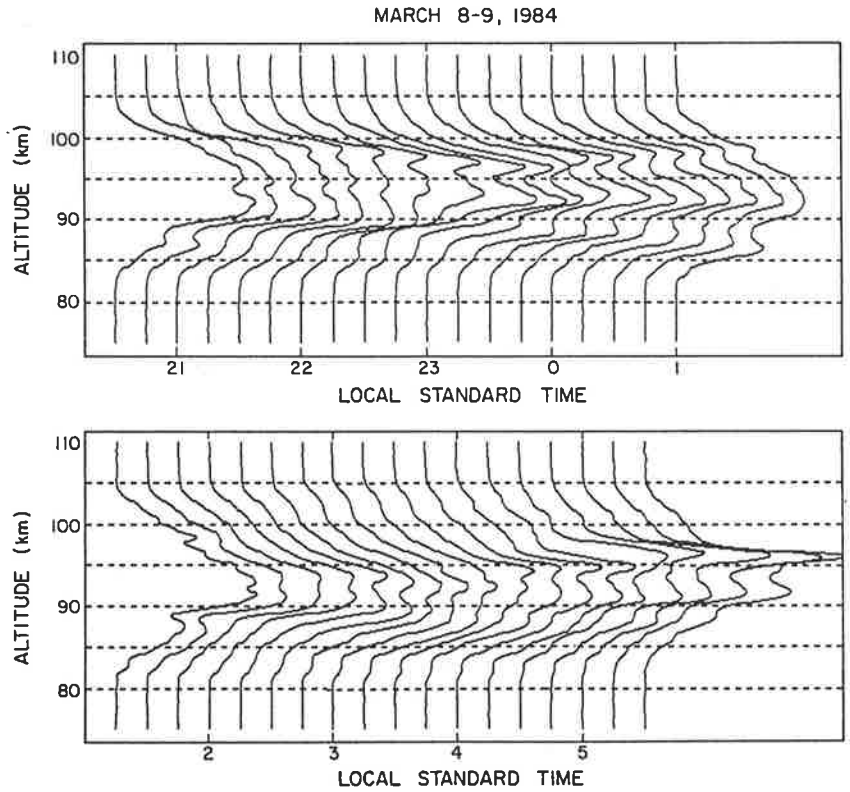

Figure 2.1: Sodium density profiles from Urbana, Illinois. The profiles are normalized so that each has the same abundance, filtered to remove high frequency variations, and plotted at 15 min intervals. (from Gardner *et al.* 1986b).

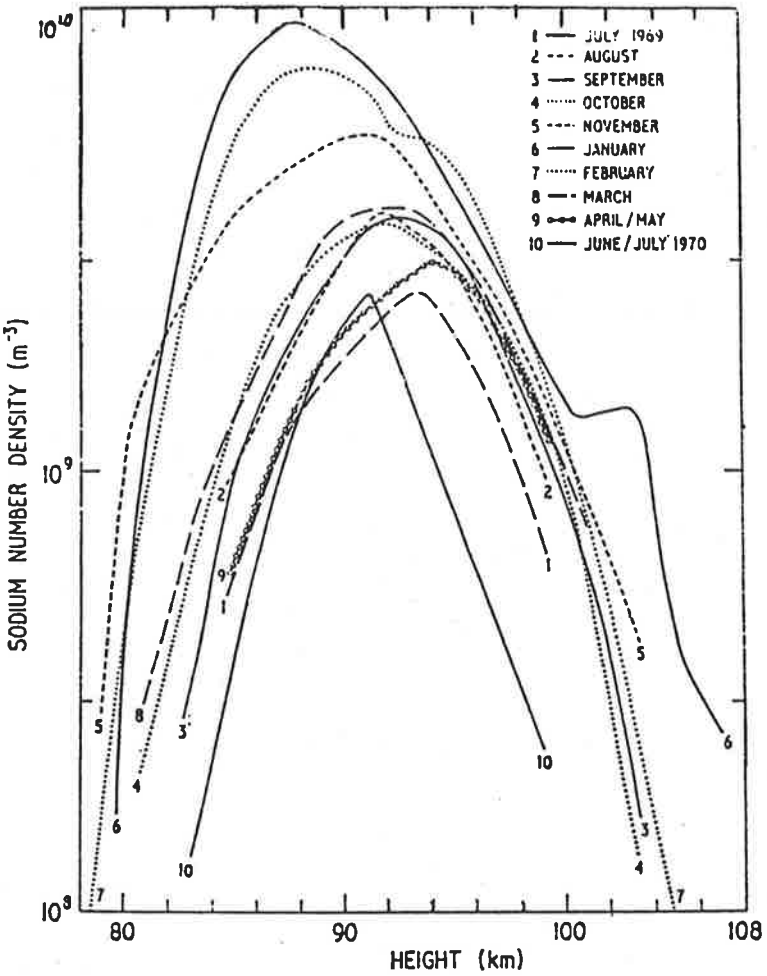

Figure 2.2: Monthly mean height distribution of sodium from lidar measurements at Winkfield, 51.4° N, 0.7° W. (from Gibson and Sandford 1971).

The height of peak concentration also decreases in Winter. This is illustrated in figure 2.2 which shows monthly mean density profiles of sodium measured by Gibson and Sandford (1971).

2.1.2 Horizontal structure in the sodium layer

Photometer records show large intermittent enhancements in the λ 589 nm doublet emission intensity suggesting increases in sodium abundance (Kirchhoff and Takahashi 1984; Bullock and Hunten 1961). Lidar observations of enhancements have shown that increases in abundance occur on the topside of the layer (Clemesha *et al.* 1978, 1980; Gibson and Sandford 1971; Megie and Blamont 1977) and this supports the hypothesis that some at least of the atmospheric sodium originates from meteors. Meteors contain about 0.6% sodium (Kirchhoff and Takahashi 1984) and would deposit most material above 90 km. Local enhancements in the sodium

concentration are carried horizontally by winds and are transient at any one point. Clemesha *et al.* (1980) inferred wind velocities of approximately 200 ms^{-1} from spaced measurements of an enhancement 10 times the normal density at the peak of the layer.

Two types of meteors enter the Earth's atmosphere. Sporadic meteors have no preferred direction or time of entry. The other type is associated with a cometry orbit and entry of these meteors occurs only when the Earth crosses the orbit. Thus showers of meteors occur at well-known times throughout the year and come from particular directions in the sky (the radiant of the shower). Tinsley and Vallance-Jones (1962) noted that the variation in sodium abundance was six months out of phase with the variation in the meteor influx. Recent measurements of the meteor influx (Olsson-Steel and Elford 1987) have shown that a large number of hitherto unaccounted sporadic meteors occur in the height-range 100–140 km. If the sporadic meteors account for a large part of the atmospheric sodium then the contribution from meteor showers would be less significant. Gardner *et al.* (1986b) suggests that the seasonal variation in sodium abundance is primarily a consequence of the temperature dependence of the major loss mechanisms and not due to variations in the source flux.

Sodium is one of three alkali metals present in the Earth's atmosphere. Lithium and potassium have also been studied although the intensity of their emissions is considerably less than that of sodium. It is likely that all three elements have the same source. It was at one time proposed that sublimation of sodium from aerosols was the main source for the sodium layer (eg. Megie *et al.* 1978b), the sodium, originating from the sea, being transported vertically to the required height. Sublimation of sodium from aerosols would depend on solar heating hence a significant diurnal variation in the sodium abundance would be expected. However, the sodium layer does not show the expected diurnal variation and the ratio of alkali metal concentrations (ie. [Na]/[K] and [Na]/[Li]) are not in agreement with those found in sea-water (Jegou *et al.* 1985a).

It seems unlikely that volcanic activity could be the principal source of sodium atoms because

most volcanic dust does not reach the mesosphere; hence vertical transport from tropospheric and stratospheric levels would be required. Some volcanic eruptions do deposit material at mesospheric heights; the eruptions of Mt. Agung in 1963 and Mt. St. Helens in 1981 are two recent examples. An increase in sodium abundance during the 1964 summer was reported by Burnett (1965). Such volcanic eruptions do not occur frequently enough to maintain the sodium layer nor would they explain the patchiness apparent in all observations. Ablation of sodium from meteors is the most likely source of the atmospheric sodium layer.

Some reports have suggested that sodium emission line enhancements occur in the auroral zone in association with aurorae (Hunten 1955; von Zahn *et al.* 1987b) but they are not a principal feature of the aurora. Rees *et al.* (1975) found no correlation between sodium emission intensity and auroral activity at College, Alaska. They also questioned the validity of previous claims of sodium emission enhancements being associated with auroral activity by pointing out how easily the twilight enhancement could be misinterpreted as auroral enhancements. Nomura et al. (1987) reported a decrease in sodium abundance during auroral activity. Their measurements were made using a lidar at Swoya station, Antarctica (69° S, 40° E). Whether the sodium layer is affected by auroral activity is not yet clear and requires further observations.

Donahue *et al.* (1972), using sodium dayglow observations from the satellite OGO-6, found their results contaminated by scattering of sunlight from ice crystals in noctilucent clouds. Noctilucent clouds form at the summer polar mesopause where temperatures are very low.

Recent observations in the northern polar summer have found large depletions in sodium abundance. Mean summer densities of 0.6×10^9 cm^{-2}, approximately $\frac{1}{10}^{th}$ winter densities, have been reported from 69° N and 78° N (von Zahn *et al.* 1988; Gardner *et al.* 1988). At mid-latitudes the winter/summer density ratio is about 5. The extreme summer mesopause temperatures are likely to be a contributing factor as sodium loss mechanisms are highly temperature dependent (Swider 1985). Von Zahn (op cit.) also noted that the layer is somewhat higher in summer, the peak height being near 93 km, and frequently a very sharp cutoff occurs

on the bottomside near 90 km.

Several recent reports have described sudden enhancements in the sodium layer (von Zahn *et al.* 1987b, 1988; von Zahn and Hansen 1988; Kwon *et al.* 1988). Very narrow, well defined layers form in 10 – 15 min. These layers, of ~1 km full-width at half-maximum (FWHM) persist for up to several hours. They usually appear near 95 km and have been observed to descend with time. Densities of $\sim 3 \times 10^4$ cm^{-3} are typical at the sporadic layer peak. These densities are 12 – 24 times normal at the height of the sporadic layer. Beatty *et al.* (1988) reported very dense short-lived layers at lower altitudes (87 km). These layers were 140 m FWHM and lasted only for a few minutes.

Several mechanisms have been suggested to explain the formation of these layers. Von Zahn and Hansen (1988) have correlated the formation of sporadic sodium layers with the formation of sporadic E layers. They suggested that the two layers may be formed by a common process. Two processes were suggested: release of sodium from dust particles by auroral excitation, and a two-step process whereby Na^+ ions are formed and then converted to neutral Na atoms. They favoured the first process and ruled out any possibility of direct ablation of meteors because the geometry and extent of the layers is incompatible with a meteor shower. Kwon *et al.* (1988) and Beatty *et al.* (1988) suggest possible links with the diurnal tide. Although sporadic E layers occurred simultaneously with some layers seen by Kwon *et al.*, they were not present in all cases.

Further study of these layers and further development of possible mechanisms to explain their formation is required. The layers may be produced by different mechanisms. The layers seen in auroral regions by von Zahn and Hansen (1988) may have a different source than those at lower latitudes (Kwon *et al.* 1988; Beatty *et al.* 1988). Some link with sporadic E layers has been found but the actual relationship with sporadic E layers is still unclear.

2.1.3 Sodium ions

A layer of sodium ions also exists; Zbinden et al. (1975) found the peak of the ion layer was around 95 km and the maximum density was about one tenth that of the sodium neutral layer. Olsson-Steel and Elford (1987) found the peak in the height distribution of radar-meteor echoes at between 100-108 km. Sodium atoms or ions would be deposited at these heights depending on the exact mechanisms of meteor ablation. Lidar observations show enhancements in the sodium layer to occur between 95 and 105 km. Two possible mechanisms have been suggested for the production of enhancements in the sodium layer by meteors; either direct ablation of meteors i.e. ablation producing sodium atoms or ablation of meteors at higher levels producing sodium ions. Vertical transport of ions into convergence zones by interaction of the neutral wind with the magnetic field could occur in a similar manner to that suggested by Chimonas and Axford (1968) for sporadic-E. Where an eastward wind blows, interaction with the magnetic field produces a force, $\mathbf{F} = q\mathbf{V} \times \mathbf{B}$, resulting in an upward positive ion motion. For a westward wind a downward ion motion is produced. A convergence zone is produced where upward meet downward travelling ions in a region of wind shear. The diurnal and semidiurnal tides produce reversals in the horizontal winds with height in the region of the sodium layer which could cause the formation of regions of sodium ion enhancement. Downward vertical drift of these ion enhancements and their subsequent neutralization may explain some enhancements in the upper regions of the neutral sodium layer.

Avery and Tetembaum (1983) compared neutral wind velocities, derived from meteor-trail radar echoes, with sodium density perturbations derived from lidar observations. They concluded that the transport of Na^+ could not account for density fluctuations in the sodium layer. Kirchhoff and Batista (1983) extended the model of Chimonas and Axford (loc. cit.) to include, with transport of ions by $q\mathbf{V} \times \mathbf{B}$, the vertical drift of ions induced by the electric field. The results obtained showed that ion convergence layers form during the day and have a downward drift of about 1 km in 2 h. During the night no convergence zones form and ions are swept

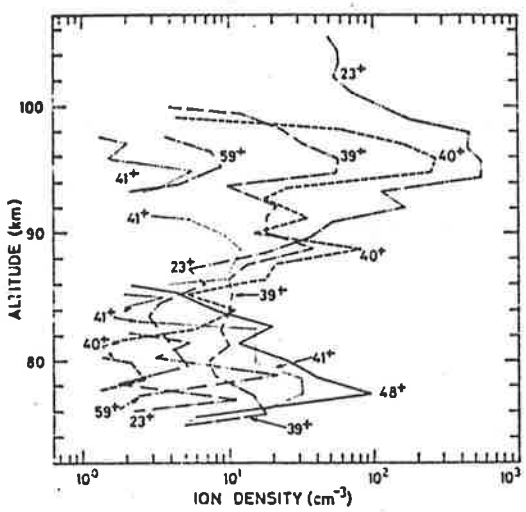

Figure 2.3: Rocket mass spectrometer profiles of ions in the mesosphere. 23^+ indicates Na^+ 40^+, 41^+, and 59^+ in the lower region (below 85 km) are presumably NaO^+, $NaOH^+$, Na^+H_2O, and $Na^+(H_2O)_2$. (from Zbinden *et al.* 1975)

down through the region.

Other ions may also be important on the bottom-side of the sodium layer as a sink for neutral sodium. Zbinden et al. (loc. cit.) also measured the presence of ions assumed to be NaO^+, $NaOH^+$, Na^+H_2O, and $Na^+(H_2O)_2$. Figure 2.3 shows their results. The importance of these ions in the sodium layer chemistry will be discussed further in the next section.

2.1.4 Models of the sodium layer

Kirchhoff (1986) has reviewed the sodium layer chemistry. Modelling of the sodium layer is based on the chemistry but is hampered by a lack of knowledge of reaction rates and densities and height distributions of sodium compounds and ions. Sodium layer models must be able to reproduce the general shape of the layer, the abundance of sodium, and the intensity of the emissions. Once this has been achieved, temporal variations and other dynamics can be included.

The two most important reactions in producing sodium nightglow are

$$Na + O_3 \rightarrow NaO + O_2 \tag{2.1}$$

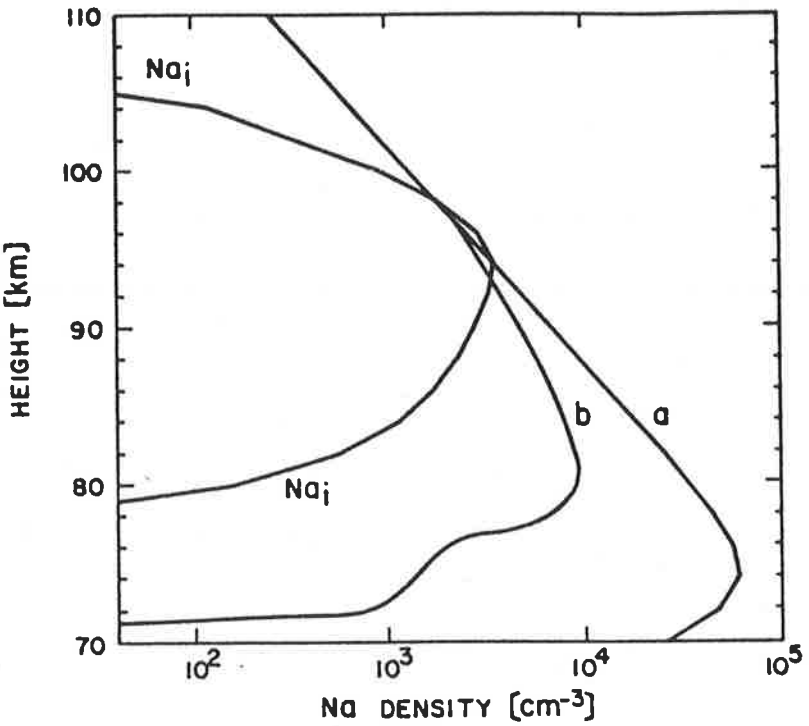

Figure 2.4: Sodium density profiles. Na_i is an average of measurements, 'a' is a model profile without a sink, and 'b' from a model which includes a sodium sink at 91 km. (from Kirchhoff *et al.* 1981)

$$NaO + O \rightarrow Na^* + O_2, \qquad Na^* \rightarrow Na + h\nu_{589.3} \tag{2.2}$$

This process is known as the Chapman mechanism for the production of the D lines. These two reactions formed the basis of early models but are not sufficient because the layer predicted by such a simple model is far too wide. Figure 2.4 (Kirchhoff *et al.* 1981) compares the sodium layer from such a model, another model layer which includes a sink on the lower side of the layer, and an average empirical layer. Production of sodium atoms by meteor ablation is assumed and a somewhat arbitrary source function is used. Two mechanisms have been proposed for a sink. Both involve the irretrievable loss of neutral sodium to sodium compounds.

Richter and Sechrist (1979a, b) proposed cluster ions as a sink for sodium; the sodium ion becomes attached to water molecules. Na^+CO_2, Na^+N_2, and Na^+O_2, also form but $Na^+(H_2O)_n$ is the only cluster ion sufficiently stable to provide a loss mechanism. Jegou *et al.* (1985a, b) developed this model further by considering wind transport and temperature variations; experimental wind and temperature profiles were used. Seasonal variations in abundance and

peak altitude of the three alkali metals Na, Li, and K were calculated. Reasonable agreement was obtained with experimental lidar values from France at 44° N (Megie and Blamont 1977). At latitudes where both wind and sodium abundance measurements were available comparisons were made between theoretical predictions and experimental values of sodium abundance and peak heights. Again reasonable agreement was obtained.

The cluster ion loss mechanism is highly temperature dependent. In winter the mesospheric temperature is warmer than in summer, the clustering efficiency is lower, and hence the sodium density increases. Such a temperature dependence of a loss mechanism could at least partly explain the seasonal variation in sodium abundance.

Granier *et al.* (1985) used the same model to examine diurnal variations but had less success. Kirchhoff (1986) points out that they did not compare theoretical and experimental profiles and below 85 km the sodium density should decrease, not increase as the model predicts.

The second mechanism involves the loss of sodium by reactions producing NaOH and NaO_2. Such a mechanism was first proposed by Liu and Reid (1979) who noted that NaOH should be dominant below the sodium layer because it is chemically the most stable species. The photochemical model was further developed by Sze *et al.* (1982), Swider (1985, 1986a, b), Kirchhoff *et al.* (1979, 1981a, b, 1983a, b), and Kirchhoff (1983). A complex system of reactions is involved; Kirchhoff (1983) uses 19 reactions, the most important being (Swider, 1986a)

$$Na + O_3 \rightarrow NaO + O_2 \tag{2.3}$$

$$Na + O_2 + M \rightarrow NaO_2 + M \tag{2.4}$$

$$NaO + O \rightarrow Na^* + O_2$$

$$NaO + H_2O \rightarrow NaOH + OH \tag{2.5}$$

$$NaO + O_3 \rightarrow NaO_2 + O_2$$

$$NaO_2 + O \rightarrow NaO + O_2 \tag{2.6}$$

$$NaO_2 + OH \rightarrow NaOH + O_2 \tag{2.7}$$

$$NaOH + H \rightarrow Na + H_2O \tag{2.8}$$

where M stands for any other molecule. Also during the day photolysis of NaOH and NaO_2 cycle sodium back into the system.

$$NaOH + h\nu \rightarrow Na + OH \tag{2.9}$$

$$NaO_2 + h\nu \rightarrow Na + O_2 \tag{2.10}$$

Thus during the day the major loss mechanism in this model is the loss of sodium to sodium compounds at the bottom of the layer. Photolysis of NaOH recycles sodium back into the system. At night however the concentration of NaOH increases and reactions (2.5) and (2.7) provide a sink for sodium in the lower part of the layer.

Swider (1985) showed that the rate of the three body loss reaction (2.4) is temperature dependent,

$$L_3 = 0.21 k_{2.4} \frac{[M]^2}{T} \tag{2.11}$$

since $[O_2] = 0.21$ [M] where [M] is the total atmospheric density. Model calculations showed that at high latitudes (60° N) the loss rate was approximately 4 times larger in summer than in winter at heights of 80–85 km. At 90 km the increase was less. Also at low latitudes, where the temperature variations are less extreme, the loss rate was less variable and had two peaks, approximately centred on the equinoxes.

Kirchhoff and Clemesha (1983b) and Kirchhoff (1983) used a photochemical model to study diurnal variations in density. They obtained reasonable agreement with experimental measurements. These photochemical models use a source function of neutral sodium at a somewhat arbitrary height in the atmosphere. Kirchhoff and Clemesha (1983b) assume direct ablation of meteors as the source of neutral sodium. A Gaussian source function centred at 94 km with a height integrated strength of 7×10^3 cm^2s^{-1} was used. This value was based on estimates of the meteor flux (Kirchhoff *et al.* 1981a). No attempt was made to include ionic reactions in the model. Kirchhoff and Clemesha (1983a) used the model to simulate a meteor influx by

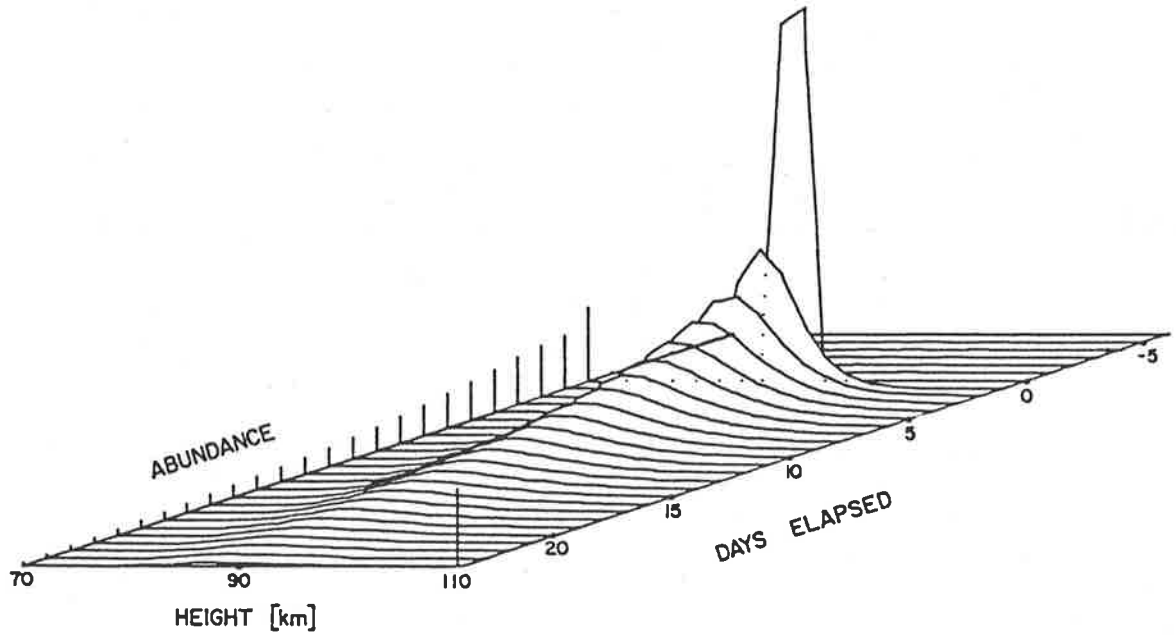

Figure 2.5: A model of an influx of sodium from Kirchhoff and Clemesha (1983a) The excess sodium density profiles are shown at daily intervals. The excess abundance, vertical bars, is also indicated. The bar in the right hand corner represents an abundance of 2×10^9 cm^{-2}

increasing the source function for a short period. Figure 2.5 shows the variation with time of the distribution of excess sodium in the layer. The time required for the influx to decrease to 1/e of its initial value varied with height, being 8.1 days at 96 km, 12.6 days at 90 km, and 17.5 days at 80 km. The dissipation of the cloud was assumed to be only by eddy diffusion and sodium was lost at the bottom of the layer through the photochemical sink. Although this is a highly simplified model it does provide a reasonable explanation of some observed enhancements. Fresh enhancements are fairly narrow layers which, in a few days, disperse forming a more broadly enhanced layer.

Jegou *et al.* (1985a, b) have shown the importance of including dynamics in a model of the sodium layer. This is supported by diurnal observations with lidars which have shown the influence of tidal motions on the sodium layer (Kwon *et al.* 1987; Gardner *et al.* 1986b; Batista *et al.* 1985). The influence of tides and other winds needs to be included in future photochemical models.

Thomas *et al.* (1983) present a model based on the photochemical reactions described above and also allowing for cluster ion reactions. They were able to model the layer height, the gradient of the height distribution above the peak, and diurnal variation within the layer. The sensitivity of the model to various input parameters was also noted. Ion processes were found to have a significant effect on the gradient of sodium density on the topside of the layer. Swider (1986a) also noted the importance of ions on the topside of the layer. He suggested that increased photoionization of sodium on the topside during the larger number of hours of daylight in summer could explain the loss of sodium observed there in summer.

Photochemical layer models were initially based on the Chapman mechanism for production of the D line emissions. Swider (1986b) has shown that these two processes, (2.1) and (2.2), have little effect on the total sodium density which is mainly controlled by reaction (2.4). This reaction has little effect on the intensity of the line emissions because the OI density is not sufficiently high to allow production of NaO via reactions (2.3) and (2.6) to compare with the rate of production via (2.1). The controlling factor in the production of the D line emissions is the ozone density. The intensity of the nighttime emission is at a peak near the equinoxes when the ozone density peak occurs and not in winter when the sodium density peaks. Clemesha *et al.* (1978) report simultaneous observations of λ 589.3 nm nightglow, from a photometer, and lidar observations of the sodium density. Data from 19 nights were obtained. The variations in airglow intensity did not correlate with the density variations at the peak of the sodium layer. Sodium density profiles were used to estimate the emission intensity assuming Gaussian layers at different heights of varying width. Clemesha *et al.* found that a layer centred on 88 km with a width of 10 km gave, on average, the best correlation with the airglow intensity. The average sodium density profile for a single night peaks at about 92 km. Although the nighttime emission does not originate from a layer coincident with the neutral sodium layer the daytime and twilight emission would as production is by resonant excitation of neutral sodium.

In conclusion, observations have shown the sodium layer to be a narrow, well-defined layer

centred near 90 km. Considerable variability is seen in the layer abundance and vertical distribution of atoms in the layer, reflecting both temporal and spatial variations. Photochemical models are successful in reproducing some of the variations observed. The layer produces the sodium λ 589.0/589.6 nm doublet photochemically via the Chapman mechanism and by resonant excitation during daylight hours. Observation of this emission using a high-resolution Fabry-Perot spectrometer was the aim of the present project. Line profiles obtained using such a spectrometer are used to estimate wind and temperature of the emission region. The middle atmosphere temperature structure and dynamics are reviewed in the following sections.

2.2 MIDDLE ATMOSPHERE TEMPERATURE STRUCTURE

Figure 2.6 illustrates the atmospheric temperature profile. The sodium layer, centred at 88-90 km, is situated just below the mesopause. The thermosphere is heated by absorption, mainly by O and N_2, of EUV and X-ray radiation from the sun. A warmer region in the lower atmosphere at about 50 km, in the stratosphere/mesosphere, is produced by absorption of insolation by ozone. The region of minimum temperature between the mesosphere and thermosphere is known as the mesopause. In this region and below energy deposition and transfer via wind, wave, and tidal motions is important and significantly modifies the temperature structure. Balloon-borne experiments allow measurements up to about 30 kilometers. The thermosphere is fairly stable and temperature measurements using optical and satellite techniques are available. Few data have been available from the mesopause/mesosphere region.

Battaner and Sanchez-Saavedra (1984) give a brief outline of optical methods for temperature determination and they are from: molecular band emission, Fabry-Perot emission line profiles, and lidar measurements. Other methods usually involve rocket or satellite measurements and derivation of temperature from density or absorption measurements.

Intensities of three or more lines of the OH band emission, from 85 km, or the O_2 ($^1\Sigma_g^+$) band emission from 92 km, can be used to determine rotational temperatures. The ratio of the

intensity of the lines is dependent on temperature. Rotational temperatures are representative of the atmospheric temperature only if the excited state is in thermal equilibrium with the rest of the atmosphere. Takahashi *et al.* (1986) used a tilting filter photometer at visual wavelengths for observations of both the OH (9,4) band at λ 775 nm and the O_2 ($^1\Sigma_g^+$) at λ 865 nm. Simultaneous measurements of these two bands and the OI λ 558 nm emission were made. Temperatures determined from the two emissions varied in a similar way although significant differences on some nights were noted. The average O_2 temperature was 195 K.

Figure 2.7 shows a compilation of emission heights for OH, O_2, Na, and OI λ 558 nm. The OI and O_2 profiles were obtained from ETON 1 measurements (Greer *et al.* 1986), the sodium profiles from Megie and Blamont (1977), and the parameters for the OH layer deduced from a number of observations (von Zahn *et al.* 1987a; Baker *et al.* 1985; Greer *et al.* 1986). These studies show the OH layer to be quite variable. Temperature measurements derived from these emissions are representative of a slab of atmosphere approximately as thick as the half-width of the layer. Myabro (1984, 1986) reports OH temperature measurements from polar latitudes, 78° N, using 1 m and $\frac{1}{2}$ m Ebert-Fastie spectrometers. Spectrometers provide better wavelength resolution over a longer wavelength range than photometers. Baker et al. (1985) also reported OH temperatures obtained during the 1980 Energy Budget Campaign. In these reports OH temperature variations with time scales of hours and days can be seen. Myabro (1986) noted that variations on a day to week time scale were reflections of large scale changes of circulation and temperature in the lower mesosphere and stratosphere. Short-term variations are most likely to be linked to atmospheric wave activity.

Blamont et al. (1972) incorporated a sodium absorption cell into a lidar system to determine the temperature of the sodium layer but the method was unable to achieve very good height or time resolution and the measurement uncertainty was $\pm$ 25 K.

Gibson et al. (1979) pioneered a technique for obtaining mesopause temperatures by using a lidar to measure hyperfine structure of the sodium line: they obtained a temperature of 222

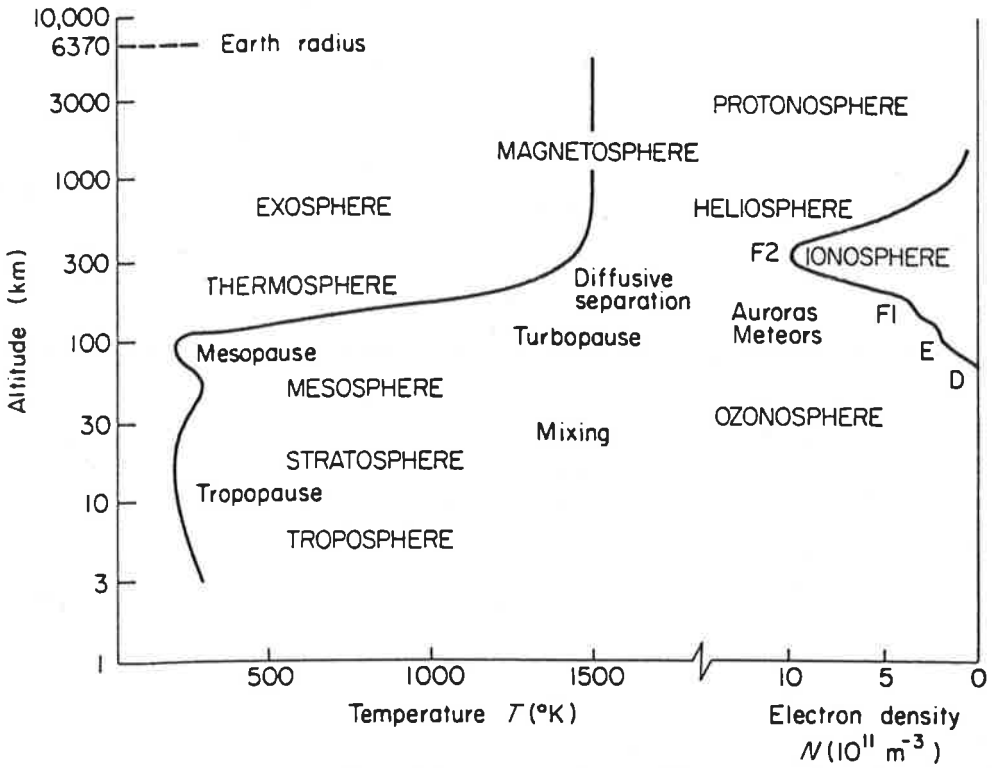

Figure 2.6: Temperature profile of the atmosphere. The conventional names for the various regions are given. (from Rishbeth and Garriot, 1969)

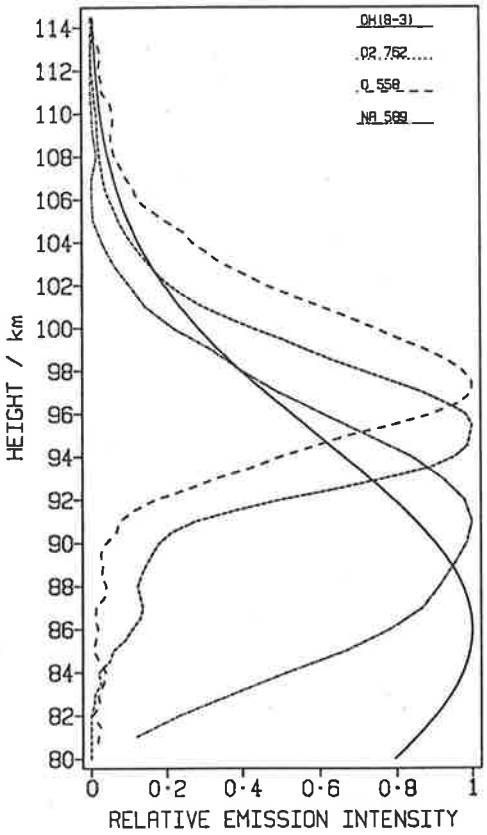

Figure 2.7: Mesospheric emission height profiles.The OI and O_2 profiles were obtained from ETON 1 measurements (Greer *et al.* 1986), the sodium profiles from Megie and Blamont (1977), and the OH profile is Gaussian centred on 86 km of 12.5 km halfwidth.

± 16 K. The sodium emission has six hyperfine components. These blend into two groups of three components, separated by 0.22 pm for the D2 line and two groups of two components, separated by 0.22 pm for the D1 line. By measuring the emission line-width and allowing for line structure the temperature can be determined. Two hyperfine groups are distinguishable at mesopause temperatures. The method has been used by Fricke and von Zahn (1985) and von Zahn and Neuber (1987). Their laser has a line width of about 0.12 pm. They can obtain a height resolution of 1 km for temperature measurements and 200 m for density measurements. Uncertainties in the measured temperatures vary from 2 K near the layer peak to 10–15 K near the extremities. This larger error is due to poor signal and variability in the density near extremes of the layer. Figure 2.8, from von Zahn and Neuber (1987), shows points of the emission line and the best fit temperature profile for these points. The laser wavelength is tunable within ± 0.02 pm and the backscattered intensity at particular wavelengths is recorded. Figure 2.9, from von Zahn and Neuber (1987), shows an atmospheric temperature profile obtained from five minutes integration time. This ground-based method provides a reliable way of obtaining temperature profiles of the mesopause region and for studying short-term variations.

Von Zahn *et al.* (1987a) compared simultaneous lidar atmospheric temperature profiles with rotational temperatures determined from OH spectra. From these measurements the OH layer peak was determined to be at 86±4 km and the mesopause just above 100 km. Wave activity in the temperature measurements was noted.

Rayleigh backscatter lidars have also been used to determine temperatures. Chanin *et al.* (1985, 1987) present temperature profiles from 35–75 km determined from density profiles. Although these profiles do not reach the mesopause region the method may be improved in future to enable it to do so. It has also been proposed (Jacka and Argall 1987) to use a lidar system to measure temperatures from line profiles of Rayleigh backscatter by incorporating a high-resolution Fabry-Perot spectrometer into the receiving optics. Such a method would remove some of the assumptions in the determination of temperatures from density profiles and

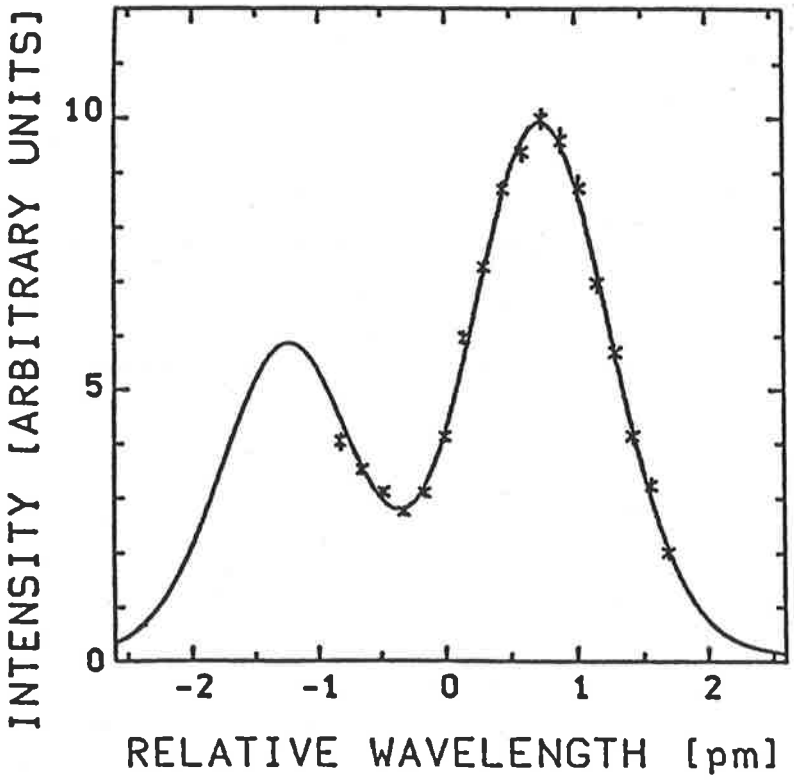

Figure 2.8: Sodium emission intensity measurements, (x), and a least squares fit to these points giving a sodium emission line profile with a temperature of 179 K (from von Zahn and Neuber 1987).

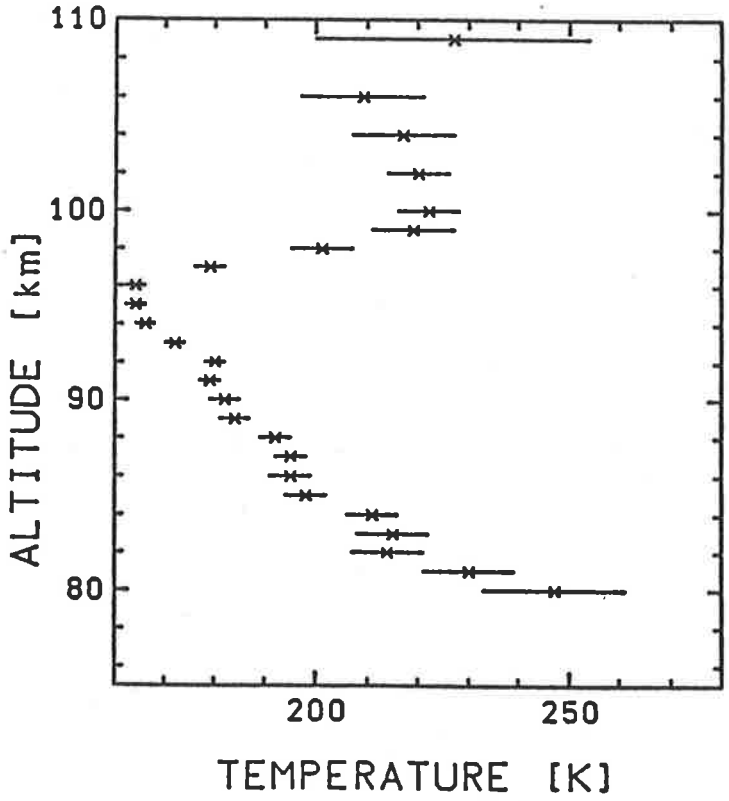

Figure 2.9: Atmospheric temperature profile, for 80–110 km, obtained from lidar measurements (from von Zahn and Neubar 1987).

may permit sampling over a larger height range.

High-resolution Fabry-Perot spectrometers have been used to determine thermospheric temperatures using the oxygen λ 630 nm emission and, less extensively, the λ 558 nm emission. Temperatures are determined from the width of the line profile by use of the equation

$$\delta\lambda = \sqrt{2(ln2)}\sqrt{(\frac{2kT}{M})}\frac{\lambda}{c}, \tag{2.12}$$

where $\delta\lambda$ is the line-width at half-maximum, λ is the central wavelength, and T the temperature of the emitting species of atomic weight M. This method has also been used to determine temperatures from the sodium emission at twilight (Sipler and Biondi 1975, 1978; Hernandez 1975). Sipler and Biondi (1978) described seasonal variations in sodium layer temperature from measurements made at Laurel Ridge Airglow Observatory, Pennsylvania (40°N, 79°W). Their measurements varied from 160 K in summer to 220 K in early winter. It is not possible to accurately determine temperatures from the night-time sodium emission as profiles are chemically broadened; emission occurs when the sodium atom is not in thermal equilibrium with the surrounding atmosphere. Sipler and Biondi (1978) estimated an energy of 46±4 meV in excess of thermal energy.

Temperature can be determined from density measurements given the hydrostatic equation

$$dP = -\rho g dz, \tag{2.13}$$

and the ideal gas law

$$P = \frac{\rho RT}{M}. \tag{2.14}$$

These two equations give

$$-\frac{M}{R}g\rho dz = d(\rho T). \tag{2.15}$$

When integrated this gives

$$T_2 = T_1\frac{\rho_1}{\rho_2} - \frac{M}{R}g\int_{z_1}^{z_2}\frac{\rho}{\rho_2}dz. \tag{2.16}$$

If an initial temperature T_1, for a given height z_1 and density ρ_1 is determined from model

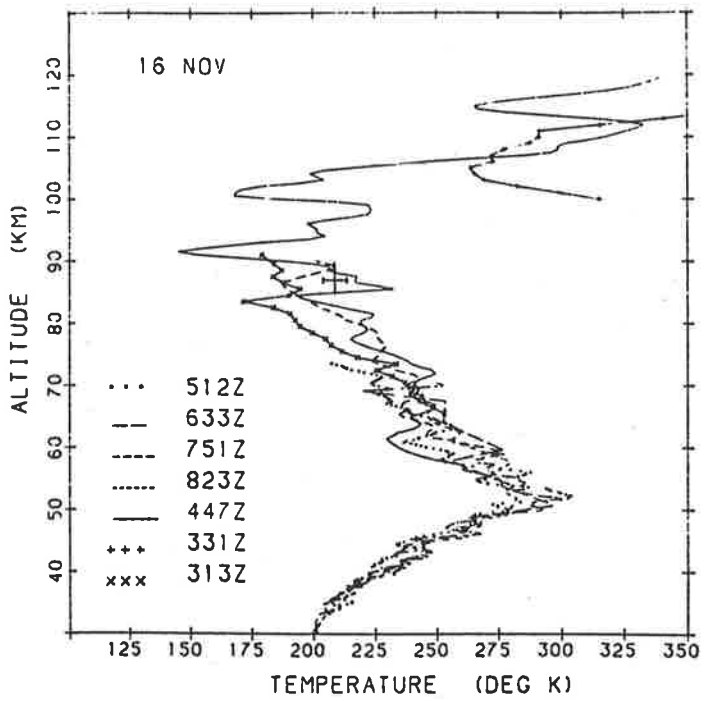

Figure 2.10: Temperature profiles from rocket salvos at Esrange, Sweden. The single cross at 87 km denotes the temperature determined from OH measurements. (from Philbrick *et al.* 1985).

calculations or by some other means then T_2 can be determined. About 10 km from z_1 the result is insensitive to the initial value assumed for T_1 (Philbrick *et al.* 1985).

Philbrick *et al.* (1985) reported temperature measurements from 30 to 150 km using a variety of rocket based methods. Ground-based OH rotational temperatures were also compared with measurements obtained. Agreement between all methods was satisfactory. Figure 2.10 is an example of the results obtained and shows the wave activity typical of that seen in most profiles.

Mesopause temperatures show an annual variation. The winter mesopause is warm, and the summer mesopause is cold. The stratosphere is warm in summer and cold in winter. At high latitudes towards the end of winter the stratosphere can rapidly change from cold winter conditions to summer conditions. Such changes have been described as 'sudden stratospheric warmings'. Sudden stratospheric warmings have been closely linked to planetary waves. The MAP/WINE (Middle Atmosphere Program / Winter In Northern Europe) project (reviewed by

von Zahn 1987) produced extensive and co-ordinated observations of winds and temperatures in the stratosphere and mesosphere in northern Europe. Petzoldt *et al.* (1987) showed that a major stratospheric warming depended on breakdown of the subtropical mesospheric jet. Wave energy from the stratosphere propagates up into the mesosphere and there energy propagation depends on the wind field. The subtropical mesospheric jet focuses wave energy into the tropics. If this jet breaks down and wave conditions are such that energy is propagated into the polar regions, then a sudden stratospheric warming occurs. Hauchecorne *et al.* (1987a) and Offerman *et al.* (1987) found wave components in the WINE temperature data. Waves of 144, 54, 27.4, 13.3, and 9.6 days were reported from temperatures in the 20–90 km region.

Hauchecorne *et al.* (1987b) measured temperature inversions in the mesosphere which can be explained by energy deposition by breaking gravity waves. These data were obtained with a Rayleigh lidar at Haute Provence Observatory (44°N, 6°E). In another study using an extension of the same data set, Chanin *et al.* (1987) found long-term variations due to changes in solar UV flux and planetary wave activity. The latter is possibly affected by changes in solar activity as well.

From temperature measurements at different locations, and using information on heating of the atmosphere, models of global atmospheric temperatures have been developed (Forbes 1985; Barnett and Corney 1985; CIRA 1972; Groves 1985; Hedin 1983, 1987). Temperature models have been based, especially for the 85–120 km height range, on limited data sets constructed mainly from rocket measurements. Such models do not therefore reproduce hemispheric or longitudinal differences very well. With the establishment of Rayleigh lidars and hyperfine structure sodium lidars further study will increase understanding of temperature variations in the mesosphere and mesopause regions. Temperatures derived from observations of the sodium layer using a Fabry-Perot spectrometer are presented in chapter 6.

2.3 MIDDLE ATMOSPHERE DYNAMICS

Motion in the Earth's atmosphere can be decomposed into several components. Prevailing winds are produced by mean or global temperature variations. Deviations from mean conditions are produced by short term fluctuations including tides and waves. Waves propagate both horizontally and vertically and transport energy and momentum from one region to another. Tides are large scale waves with periods of a fraction of a day. The major tides are the lunar gravitational tide and the solar thermal tide. Tides and waves break and dissipate in the atmosphere thus depositing their energy in regions away from the energy source. Turbulence is produced when waves and tidal motions break into smaller and smaller scale motions. Other factors which must be considered include ion drag and electric and magnetic field effects at ionospheric heights and the Coriolis force which has a significant effect below the mesopause.

Motion of the atmosphere may be described by the Navier-Stokes equation

$$\frac{d\mathbf{U}}{dt} = -2\boldsymbol{\Omega} \times \mathbf{U} + \mathbf{g} - \frac{1}{\rho}\nabla p - \nabla\Psi + \frac{\mu}{\rho}\nabla^2\mathbf{U} - \nu_{ni}(\mathbf{U} - \mathbf{U_{ni}}) \tag{2.17}$$

where $\mathbf{U}$ is the neutral air velocity, $\frac{d\mathbf{U}}{dt} = \frac{\partial \mathbf{U}}{\partial t} + (\mathbf{U}.\nabla)\mathbf{U}$ is the acceleration following the motion of the air. The Coriolis acceleration is given by $-2\boldsymbol{\Omega} \times \mathbf{U}$, $\boldsymbol{\Omega}$ being the angular velocity of the Earth. $\mathbf{g}$ is the acceleration due to gravity (including $\boldsymbol{\Omega} \times \boldsymbol{\Omega} \times \mathbf{r}$ the centripetal acceleration, $\mathbf{r}$ being the geocentric radius). ρ is the density and p pressure. $\frac{1}{\rho}\nabla p$ is the pressure gradient force and $\frac{\mu}{\rho}\nabla^2\mathbf{U}$ the viscous force per unit mass. Ψ is the scalar gravitational potential and $\nabla\Psi$ the tidal force per unit mass. $\nu_{ni}(\mathbf{U} - \mathbf{U_{ni}})$ is the ion drag which represents the transfer of momentum from ions to neutral particles.

In the mesosphere and lower thermosphere at mid-latitudes ion drag is negligible. To estimate prevailing winds further simplification of the Navier-Stokes equation is made by assuming that viscosity is not important, there are no tidal effects, motion is constrained to the horizontal plane, and steady state holds i.e. $\frac{d}{dt} = 0$. The equation then becomes

$$2\boldsymbol{\Omega} \times \mathbf{U} = \frac{1}{\rho}\nabla p. \tag{2.18}$$

This is known as the geostrophic approximation; the pressure gradient force just balances the Coriolis force, resulting in winds flowing parallel to isobars (clockwise in the northern hemisphere and anticlockwise in the southern hemisphere around a high pressure cell). Labitzke *et al.* (1987) compared geostrophic winds calculated from radiance measurements from SAMS (Stratospheric and Mesospheric Sounder) measurements on the Nimbus 7 satellite with mean winds from radar measurements at Saskatoon. The radar measurements had tidal contributions removed. Good agreement was only obtained for limited times of the year without planetary wave activity and when gravity wave activity was minimal. Such a comparison is useful if only to highlight the effect of wave activity on the mean flow (i.e. the geostrophic approximation is not good).

In the remainder of this section, gravity waves and tides will be treated in more detail. Special emphasis will be given to their importance at mesospheric heights. It should also be borne in mind that although the term dynamics is used to refer to motions in the atmosphere, the motions are either a reflection of, or produce, changes in other atmospheric phenomena. Tidal and wave effects can be seen as variations in temperature or density as well as wind variations.

2.3.1 Gravity Waves

Gravity (or buoyancy) waves are waves which propagate both horizontally and vertically in a stratified fluid. The atmosphere provides such an environment and in the past few years the importance of gravity waves in the momentum budget, especially at mesospheric heights, has been recognized. Fritts (1984) or Geller (1983) review effects of gravity waves on the middle atmosphere. That topic will be discussed in the next section. The importance of gravity waves in the atmosphere was first suggested by C. O. Hines (1960). He pioneered the use of internal gravity waves to explain atmospheric phenomena with particular reference to meteor trail observations, travelling ionospheric disturbances (TIDs), and other small scale atmospheric motions. This section will briefly introduce concepts required to understand some aspects of

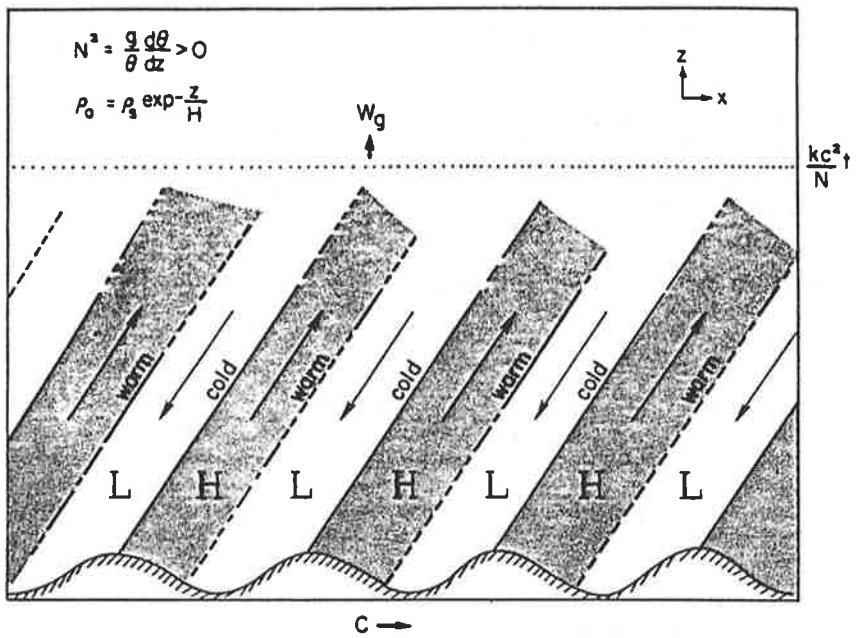

Figure 2.11: Schematic diagram of a forced, upward propagating, gravity-wave of phase speed c. The corrugated boundary layer exerts a positive stress on the fluid in the x-direction. (from Dunkerton 1981)

gravity waves.

Gravity waves are a three dimensional phenomenon but visualization of the wave is easier if they are assumed to be two dimensional; the horizontal axis aligned parallel to the direction of propagation of the wave. A corrugated sheet moving with constant velocity, c, in the horizontal direction will excite internal gravity waves in the fluid above. Figure 2.11 , after Dunkerton (1981), shows the phase fronts generated by such a wave. Phase fronts tilt forward and appear to move down but energy propagates upwards. Displacement of a particle is greatest at crests and troughs of a wave; the velocity at those points is smallest. Pressure variations are in phase with velocity variations, regions of high pressure occurring on the rising edge of the wave. Density variations are largest where displacement is greatest. Since the fluid is approximately adiabatic, rising motion causes a decrease in temperature and falling motion an increase. Temperature variations are 180° out of phase with displacement and density. Temperature maximizes at the wave trough and minimizes at the wave peak.

Figure 2.11 does not express variation in wave amplitude with height. However, in the

atmosphere density, ρ_0, varies as $e^{-z/H}$, where H is the scale height. If the wave does not dissipate, the energy, E, remains constant.

$$E = KE + PE = \frac{1}{2}\rho_0({u'_o}^2 + {w'_o}^2) + \frac{1}{2}g\rho'\zeta \tag{2.19}$$

where u', w', are the horizontal and vertical perturbation velocities u'_o and w'_o their amplitudes, ρ' the increase in density above ρ_0, and ζ the displacement of a parcel of fluid by the wave. Since total energy remains constant, amplitude must increase exponentially with height. In practice waves may saturate at certain heights where the phase speed of the wave reaches that of the mean flow of the background wind, so that energy is lost from the wave.

Gravity waves are derived mathematically by considering oscillating solutions to the Navier-Stokes, conservation of energy, and mass continuity equations. A detailed mathematical treatment can be found in Gossard and Hooke (1975) and more simplified treatments in most other atmospheric physics texts. Solutions to the equations of the form $u'_0 e^{i(kx+mz-\omega t)}$ are assumed where u'_0 is say the perturbation velocity amplitude, k is horizontal wavenumber, m vertical wavenumber, and $\omega = kc$ is intrinsic frequency (the frequency of the wave with respect to the mean flow). When these solutions are substituted into the equations with relevant simplifying assumptions, a dispersion relation is obtained viz.

$$m^2 = \frac{k^2(N^2 - \omega^2)}{\omega^2 - f^2}, \tag{2.20}$$

or

$$\omega^2 = \frac{k^2N^2 + m^2f^2}{k^2 + m^2}. \tag{2.21}$$

Here $f = 2\Omega \sin\theta'$ is the Coriolis parameter, and θ' latitude. N is called the Viasala-Brunt frequency and is characteristic of the fluid. N^2 can be expressed in terms of potential temperature θ, or specific entropy, s. If c_p is the specific heat at constant pressure, c_v the specific heat at constant volume, $\gamma = \frac{c_p}{c_v}$, and c_s the speed of sound $({c_s}^2 = \gamma\frac{p_0}{\rho_0})$ then

$$N^2 = \frac{g}{\theta}\frac{d\theta}{dz} = -g(\frac{1}{\rho}\frac{\partial\rho}{\partial z} + \frac{g}{c_s^2}) = \frac{g}{c_p}\frac{ds}{dz}. \tag{2.22}$$

Alternatively,

$$N^2 = -g(\frac{g}{c_s^2(1-\gamma)} - \frac{2}{c_s^2}\frac{\partial c_s^2}{\partial z}). \tag{2.23}$$

A parcel of fluid displaced vertically in a stably stratified environment, in the absence of friction, will oscillate at the Viasala-Brunt frequency.

The Viasala-Brunt frequency also defines an upper limit on gravity wave frequencies; $\omega < N$. As $\omega \rightarrow N$, i.e. at high frequencies, gravity waves propagate nearly horizontally. The dispersion relation also gives a lower frequency limit for gravity waves. For m^2 to be positive, both $N^2 > \omega^2$ and $\omega^2 > f^2$ are required; $f < \omega < N$. If m^2 is negative, m is imaginary and the wave decays exponentially with height only propagating horizontally. $f = 2\Omega \sin\theta'$ is the inertial period at which a fluid will oscillate if the acceleration terms and the Coriolis terms are in balance. For 35° S, the latitude of the observations presented here, the inertial period is approximately 21 h. At 90 km altitude the Viasala-Brunt period is approximately 5 min.

Most importantly wave motions result in the transfer of energy and momentum in the atmosphere. Hines (1960) and Gossard and Hooke (1975) developed equations for energy and energy dissipation of a gravity wave. Energy propagates in the direction of the group velocity. For phase velocities propagating downwards, energy propagates upwards and vice versa. The vertical components of the phase and group velocities are usually in opposite directions and the horizontal components are usually in the same direction. Waves can reach a criticl level where the phase speed of the wave equals that of the mean flow; reflection or absorption then occurs. When the wave amplitude can no longer grow exponentially with height and saturation occurs the waves lose energy to the mean flow. The next section discusses in more detail the effects of wave activity on the mean flow.

2.3.2 Gravity-wave mean-wind interaction

Geller (1983) summarized problems produced by attempts to model the middle atmosphere without including gravity wave saturation and dissipation. Figure 2.12, from Geller (ibid.),

compares the observed zonal winds and temperatures with those obtained from a model assuming radiative equilibrium and the geostrophic approximation. Any differences between the two pictures must be produced by dynamic transport of energy in the atmosphere. The model does not feature the temperature minimum at the tropical tropopause, the temperature maximum in the winter polar mesopause, and minimum at the summer polar mesopause. Although the temperature maximum at the stratopause is found the winter minimum is too low. This feature is produced by the absorption of solar radiation by ozone. Geostrophic winds derived from the temperature distribution are far from the observed winds especially in the mesosphere. The winter eastward jet and summer westward jet are too high and not closed.

Radiative models can be improved by adding a Rayleigh drag term; this is a mathematical contrivance to produce better results. In the model it acts to counter zonal accelerations and produces qualitative agreement between predicted and observed winds and temperatures.

Lindzen (1981) first proposed a way of incorporating gravity wave and tidal breakdown into atmospheric models. Gravity waves cannot propagate with a phase speed exceeding the mean wind. Wave energy is deposited in the region between where the wave starts saturating, z_s, and the critical level, z_c, beyond which the wave cannot propagate. This is shown schematically in figure 2.13 (Fritts 1984). Upward flux of zonal momentum and induced variations in mean wind are also shown. The troposphere is a major source of gravity waves, waves being generated by topographic features, frontal weather systems, thunderstorms, and various instabilities in the wind field. Waves generated in the troposphere and propagating vertically are filtered by the mean wind in the stratosphere and mesosphere. Waves reaching the mesosphere thus have a preferred direction of travel, determined by the wind field at lower levels, and act, on saturating or breaking, to accelerate, and can reverse, the mean wind. On saturation, waves bring the mean wind toward the phase speed of the wave. This is shown in figure 2.14 (Lindzen 1981) where zonal winds from rocket profiles are compared with the calculated geostrophic wind. The level at which gravity waves start breaking is indicated by an arrow. Above these heights there

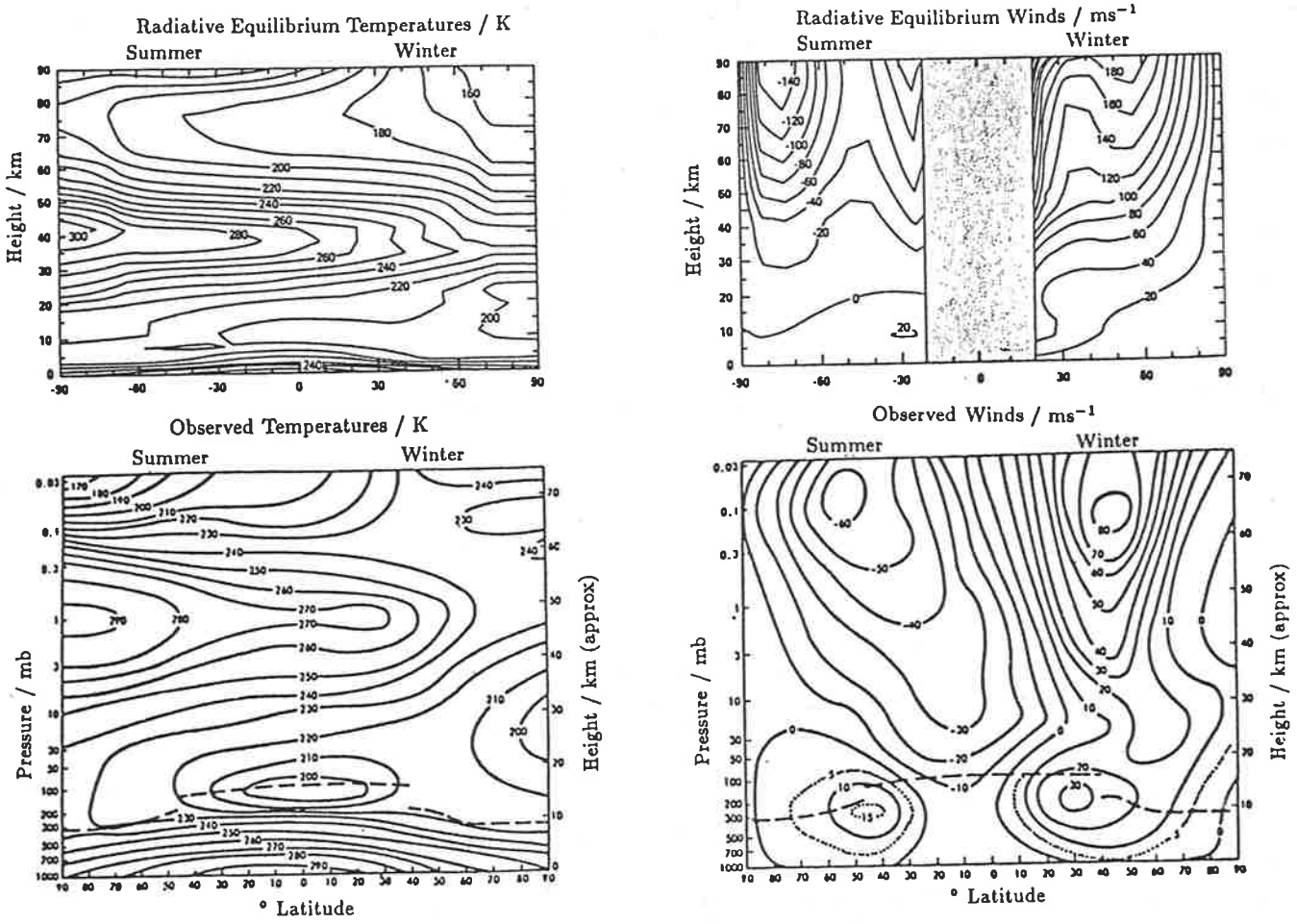

Figure 2.12: Comparison of observed temperatures (K) and zonal winds (ms^{-1} E) (bottom) and those from a radiative equilibrium model (top). In the plots of measurements the dotted line indicates the tropopause level. (from Geller 1983)

is a marked deviation of the winds from geostrophy.

Inclusion of gravity wave breaking in the atmospheric momentum budget has been developed further by Holton (1982,1983), Miyahara (1985), and Schoeberl (1985). Agreement between observed wind profiles and models incorporating gravity wave saturation is better than for Rayleigh drag models. This is largely because gravity waves can actually reverse the mean wind whereas Rayleigh drag acts proportionally to the mean wind amplitude and cannot actually reverse wind direction. Models require specification of the gravity wave spectrum. Few long-term gravity wave studies have been made so global variations in the gravity wave field can only be coarsely described. However even quite simplistic gravity wave parameterization can provide improved agreement in atmospheric models (Holton 1983; Garcia and Solomon 1985). As more observations of gravity waves become available, improvement in model descriptions of temperature and wind fields can be expected.

A cold summer mesopause and warm winter mesopause are the result of gravity wave motions. In radiative equilibrium the meridional pressure gradient between the cold winter pole and the hot summer pole is balanced by the Coriolis force to produce an east-west zonal flow. Thus in radiative equilibrium there are no meridional winds: the wind field is limited to a zonal flow. In practice saturation of gravity waves and their interaction with the background wind at mesospheric heights causes a drag which is balanced by the Coriolis force associated with a meridional component of the wind thus generated.

In an adiabatic atmosphere rising air cools and sinking air warms the surroundings. Thus warm air rising above the summer polar stratosphere cools the mesosphere. The meridional component of the flow carries it to the winter pole where, now cooler than its surroundings, it sinks thus warming the winter polar mesosphere.

Energy transfer from wave motion to the mean flow has been linked with generation of turbulent layers in the atmosphere. Fritts and Rastogi (1985) have reviewed the theory and observations of convective and dynamic instabilities produced by gravity wave motions in the

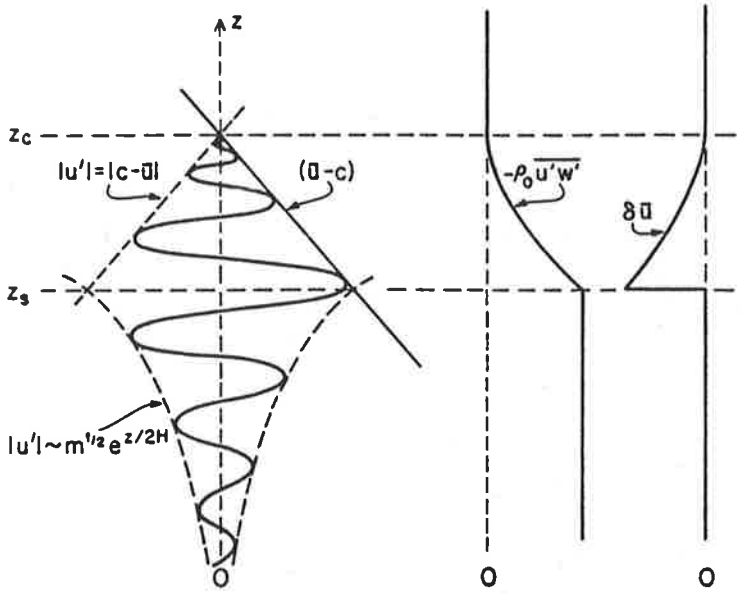

Figure 2.13: Schematic diagram, from Fritts (1984), of growth with height and saturation of a gravity wave. Wave damping produces both a divergence of vertical flux of horizontal momentum and an acceleration of the mean flow toward the phase speed of the wave. 'z_c' denotes the critical level and 'z_s' the level at which saturation occurs.

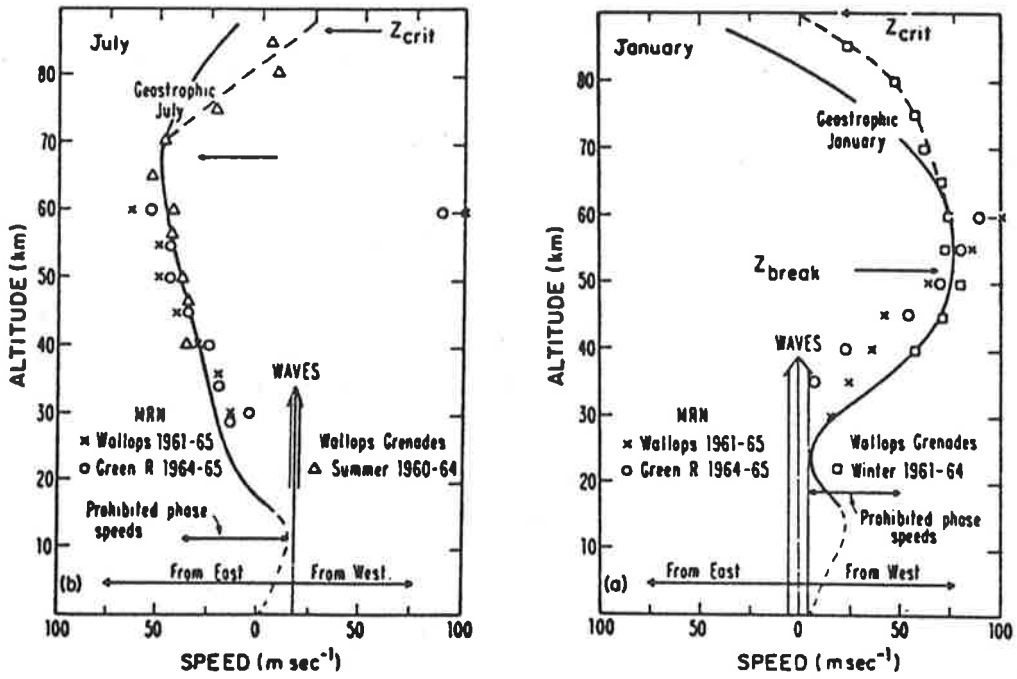

Figure 2.14: Schematic diagram, (from Lindzen 1981), showing measured and modelled geostophic wind profiles, for summer and winter at Wallops Island. Gravity wave saturation and critical levels are shown by arrows. The double headed arrow indicates phase speeds of waves which will not propagate from the troposphere to the mesosphere.

middle and upper atmosphere. They suggest three mechanisms for gravity wave dissipation: Kelvin-Helmholtz instabilities, convective or Rayleigh-Taylor instabilities, and non-linear interaction of wave motions producing energy transfer from large-scale to small-scale motions. Kelvin-Helmholtz instabilities occur when a wave encounters a narrow interface in which velocity and density gradients are large. The wave encompasses the whole layer producing billows, turns in upon itself, and breaks, creating considerable turbulence in the center of each wave period. Patterns known as billows, cats-eyes, and braids can be seen in cloud formations and in laboratory simulations of Kelvin-Helmholtz instabilities. Few cases of such structures have been seen in mesospheric observations. However most measurement techniques do not have the spatial and temporal resolution required to distinguish them. Structures indicative of Kelvin-Helmholtz instabilities have been observed in noctilucent cloud formations which form in the summer polar mesopause region (Witt 1962).

Superadiabatic lapse rates have been observed in atmospheric temperature profiles where reasonable vertical resolution can be obtained (Hauchecorne *et al.* 1987b; von Zahn and Neuber 1987; Philbrick *et al.* 1985). In such regions the atmosphere is unstable and turbulence acts to restore stability. Super-adiabatic lapse rates are produced in regions of enhanced gravity wave amplitude and can be produced by superposition of gravity waves or reflection of waves from density discontinuities (see Fritts and Rastogi op. cit. for references to theoretical and laboratory studies). Large wave amplitudes carry heavier fluid over lighter fluid thus reversing the normal stratification and producing unstable conditions. Many observations of narrow bands of intense turbulence in the atmosphere have been made; such layers are produced by convective instabilities.

High frequency gravity waves are more likely to dissipate in convective instabilities and Kelvin-Helmholtz instabilities are associated more often with low frequency gravity waves.

In summary gravity waves carry energy from one region of the atmosphere to another. When waves saturate or dissipate the wave energy and momentum deposited affect the mean

flow. Such effects occur on such a large scale that mean global wind and temperature fields are significantly affected, especially at mesospheric heights.

2.3.3 Gravity wave observations

Observed gravity waves fall into two main categories; quasi-monochromatic variations due to a single wave and those in which (after tidal and mean components have been removed) the variations are due to a broad spectrum of wave periods. Airglow observations are usually confined to hours of darkness and hence do not extend over 24 hour periods; airglow intensity or rotational temperature may be determined. Since tidal and mean trends in these parameters cannot be determined identification of gravity waves is limited to isolation of monochromatic components in the data.

Some airglow emissions are produced in thin layers and interaction of gravity waves with such layers has been studied and modelled by Garcia and Solomon (1985), Shelton *et al.* (1980), Gardner and Shelton (1985), and Hines and Tarasick (1987). The interaction is quite complex as airglow brightness depends on several parameters including density, temperature, and emission reaction rates which may also be temperature dependent. Gravity waves can affect all these parameters. Most work has concentrated on the oxygen λ 558 nm emission as production mechanisms are known and reliable estimates of the required variables exist. Gardner and Shelton (op. cit.) simulated the density response of the sodium layer to gravity waves. Sodium lidars observe density fluctuations in the sodium layer with a height resolution of about 1 km. Monochromatic gravity wave events have been observed at most lidar facilities. Gardner and Voeltz (1987) reported 171 gravity wave events over 34 nights. These observations were used to determine amplitude, vertical and horizontal wavelengths, kinetic energy, and vertical phase velocity. The waves they observed were influenced by dissipation rather than saturation. Gravity wave amplitudes at sodium layer heights are often large and sodium density gradients tend to enhance wave perturbations. Gardner and Voeltz (1985) discuss gravity wave saturation effects

on wave motions in the sodium layer.

Fruend and Jacka (1979) and Jacob and Jacka (1985) used a spaced-field photometer observing variations in λ 558 nm oxygen emission to determine horizontal phase speeds of gravity waves. Gravity waves seen were related to tropospheric fronts. Similar observations using a scanning photometer were reported by Meek and Manson (1983).

Other monochromatic gravity wave variations have been observed simultaneously in two or more emission features. The oxygen λ 558 nm emission from 97 km, the sodium λ 589 nm photochemical emission from 85 km, the OH emission from 86 km, and the O_2 emission from 94 km provide a means of obtaining limited height resolution in gravity-wave observations. Thus the direction of vertical phase propagation can be determined. Also OH and O_2 observations can be used to determine rotational temperature so temperature variations at different heights can be considered.

Taylor *et al.* (1987) used an imaging TV system to record a gravity wave in the λ 558 nm, sodium, and OH emissions. A wavelength of 6.5 km, phase velocity of 5 ms^{-1}, and phase propagation angle of 75° from vertical were determined from the data. Myabro *et al.* (1987) compared sodium emission intensities and OH rotational temperatures and emission intensities. Considerable fine structure with periods of 5–15 min was attributed to high-frequency gravity waves. Longer-period waves ($1\frac{1}{2}$–2 hours) were also seen. It was suggested that high-frequency waves were generated by low-frequency waves at altitudes above 80 km. Variations in OH temperatures of up to 60 K were reported. Different variations in OH temperature and emission intensity were ascribed to breaking gravity waves. Takahashi *et al.* (1986) reported initial results of simultaneous measurements of OH and O_2 rotational temperatures and intensities, and O1 λ 558 nm emission intensity. Variations in the O_2 temperature of up to 50 K were obtained. Although the OH and O_2 temperatures were generally correlated, at some times there were significant differences indicating considerable temperature gradients in the mesosphere. These four emissions were used to study gravity wave activity in the mesosphere (Takahashi *et al.*

1985).

A more comprehensive review of variations in airglow emissions is provided by Forsyth and Wraight (1987).

Some extensive studies of gravity waves from partial reflection radar observations have been made at Buckland Park, near Adelaide (Vincent 1984a; Vincent and Fritts 1987). These studies are of particular interest as the Buckland Park radar is located 50 km from Mt. Torrens where the observations presented in this thesis were made. Radar wind velocities are obtained throughout the day so that the tidal amplitudes and phases can be determined. The mean wind is calculated by averaging over 7 days. These components can be subtracted leaving other wave motions. The radar samples wind from 60–100 km with a height resolution of a few kilometers. Results of the radar observations will be summarized with emphasis on the later work (Vincent and Fritts op. cit.).

A seasonal variation in wave amplitudes is observed with a maximum occurring in winter and another, less marked, in summer. These seasonal variations are linked to variations in the mean flow, maximum wave activity occurring with strongest mean winds. Gravity wave components in the zonal direction were noted as being smaller than meridional components. A decrease in energy density with height indicating saturation or dissipation was observed. Waves tend to be propagating in the north-south direction with summertime waves having an easterly component as well. Vincent (1984) found that 65% of the total gravity wave energy was propagating upwards.

A technique for measuring mesospheric gravity wave momentum fluxes has been developed (Vincent and Reid 1983; Reid and Vincent 1987). The Buckland Park radar was used to look in two directions and the vertical flux of zonal (or meridional) gravity wave momentum, $\rho\overline{u'w'}$ ($\rho\overline{v'w'}$), can be shown to be proportional to the difference of the variances of the Doppler velocities measured in each beam. Thus interaction of gravity waves with the mean flow and tide can be determined. All studies of gravity waves in the mesosphere note variability in gravity

wave flux and attribute it to variations in gravity wave sources or changes in propagation conditions for waves (Vincent and Reid op. cit; Reid and Vincent op. cit.; Fritts and Vincent 1987). Reid and Vincent compare the Coriolis torque associated with the meridional mean wind with acceleration produced by the gravity wave momentum flux. Balance between these two components is only obtained in the absence of large (6–8 day) planetary wave-like oscillations.

Fritts and Vincent obtained better time resolution than other studies and were able to measure waves with periods down to 8 min. They found that waves with periods less than 1 hour accounted for about 70% of the inferred zonal drag on the mean wind. Such high frequency waves would have wavelengths < 100 km, and steep propagation paths combined with high vertical group velocities would produce rapid local forcing in the mesosphere. Fritts and Vincent also noted interaction of the diurnal tide with gravity wave motions. A diurnal modulation of gravity wave flux can be linked to changes in wind shear produced by the diurnal tide. Changes in gravity wave flux also alter apparent amplitude and phase of the tide.

2.3.4 Tides

A detailed account of tidal theory is given by Chapman and Lindzen (1970), Forbes (1981,1982a, b, 1984), and Forbes and Garret (1979). Emphasis here will be on the generation of tides and their manifestations in the mesosphere; observations will be limited to those from the sodium layer.

Solar diurnal and semidiurnal thermal tides are the most important in the atmosphere. These tides are driven by absorption of solar radiation by ozone and water vapour in the atmosphere. Ozone forms a layer centred around 50 km and water vapour is confined to a layer centred about 8 km. Tides are forced from these regions and propagate, as waves, into other regions of the atmosphere. Water vapour and ozone concentrations vary spatially and temporally and the ability of models to accurately describe observed tidal variations depends, in part, upon an accurate description of the forcing functions. Forbes and Garret (1978) discuss

excitation mechanisms. Groves (1982a, b) has improved the description of tidal excitation by including a cloud layer.

A thermospheric tide is also generated by absorption of UV and EUV in the thermosphere. Propagating modes excited in the middle atmosphere can also contribute to the thermospheric tide but only if the vertical wavelength is such as to allow propagation to thermospheric heights. Thus the semidiurnal tide from the middle atmosphere contributes more to the thermospheric tide than the diurnal tide. Excitation of thermospheric tides is treated in more detail by Forbes and Hagan (1982) and Forbes (1982a, b).

The lunar semidiurnal tide with a period of 12.4 hours has also been studied. The excitation of this tide, by gravitational forcing, is well known and hence the theoretical calculations of the tidal forcing and the resulting motions can be confidently calculated. The effects of this tide are however an order of magnitude less than the solar thermal tide and little more will be said here about it.

Tides are normally described in terms of Hough functions and equivalent depths. The Hough functions form a complete and orthogonal set and are used as eigenfunctions in the eigenvalue/eigenfunction solution to the set of equations describing forced atmospheric motions. The eigenvalues define equivalent depths and fix vertical structure of the tide and the Hough functions define horizontal structure. Hough functions are usually denoted $\Theta_{n,m}$ where m and n are integral, $m > 0$, and there are $\mid n \mid -m$ nodes between the north and south poles in the function. Figure 2.15 from Forbes (1982a, b), gives important Hough modes for the diurnal and semidiurnal tides. With each Hough mode there is associated a wavenumber, k_{mn}. Negative values of n indicate evanescent tides (waves) which do not propagate vertically out of their region of excitation. Tides with positive n indicate tidal (wave) amplitudes which increase exponentially with height until dissipation or saturation occurs. Two types of solutions to tidal equations are found; they are propagating modes which travel westwards with the apparent velocity of the subsolar point and stationary or trapped modes. Propagating modes dominate

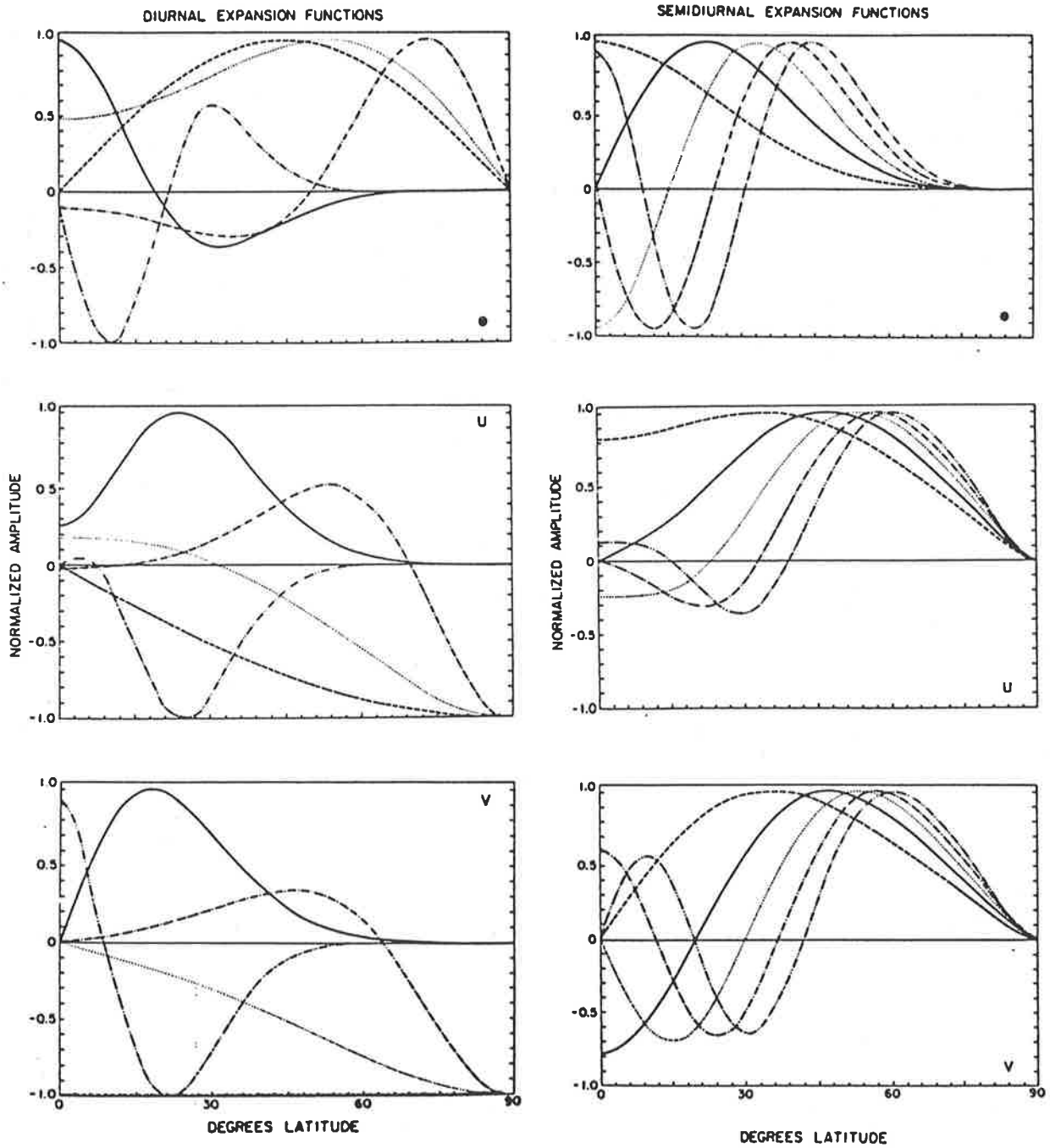

Figure 2.15: Hough functions for the solar diurnal and semidiurnal tides (from Forbes 1982a, b). For the diurnal components the modes are represented by (1,1) solid line, (1,-1) dashed line, (1,-2) dotted line, (1,2) dash double dotted line; for the semidiurnal components, (2,2) dashed line, (2,3) solid line, (2,4) dotted line, (2,5) dot dashed line, (2,6) dash double dotted line. Below the Hough modes are northerly velocity, u, and westerly velocity, v, expansion functions. All functions are normalized to maximize at unity. Normalization factors are given in the reference.

at low latitudes and trapped modes are more important at high latitudes.

Important tidal variations of temperature and density in the middle atmosphere occur in addition to the zonal, u, meridional, v, and vertical, w, winds. The diurnal tide can be expressed in terms of the (1,1), (1,-1), (1,-2), (1,-4), and (1,2) Hough modes shown in figure 2.15 (Forbes 1982a). Velocity and temperature variations are given at 6° latitude increments from the surface to 400 km in Forbes and Gillette (1982). The Hough modes for the semidiurnal tide are (2,2), (2,3), (2,4), (2,5), and (2,6); also shown in figure 2.15. The terdiurnal tide, with a period of 8 hours, and other components with periods of an integral fraction of 24 hours are also seen at times. These components are not as persistent or large in amplitude as the semidiurnal and diurnal tides.

There are two basic forms of tidal motions, a summer structure and a winter structure. During equinoxes, over a period of about two weeks, tides change rapidly from one form to the other. Other short term variations in amplitude and phase, see Forbes (1984) for examples, have not been adequately explained. It is highly likely that they result from interactions of tidal motions with gravity waves and the mean wind as suggested in Fritts and Vincent (1987).

Figure 2.16 (Chapman and Lindzen 1970) shows distribution, in latitude, of variations in temperature and wind components, u, v, and w. Both amplitude and phase relationships are shown. In the mesosphere at Adelaide, 35° S, the mean wind and gravity wave contribution to the wind field are of the same order as the tidal contribution. At low latitudes the diurnal tide is larger and tends to dominate the wind field; for experimental results see, for example, Vincent and Ball (1981). Thus when analysing measurements from the mesosphere, tidal effects can account for substantial variations in the results obtained.

2.3.5 Observed tidal variations in the sodium layer.

Tides in the middle atmosphere have been studied most extensively using radar observations of winds: both partial reflection and meteor radars have been used. This section will review tidal

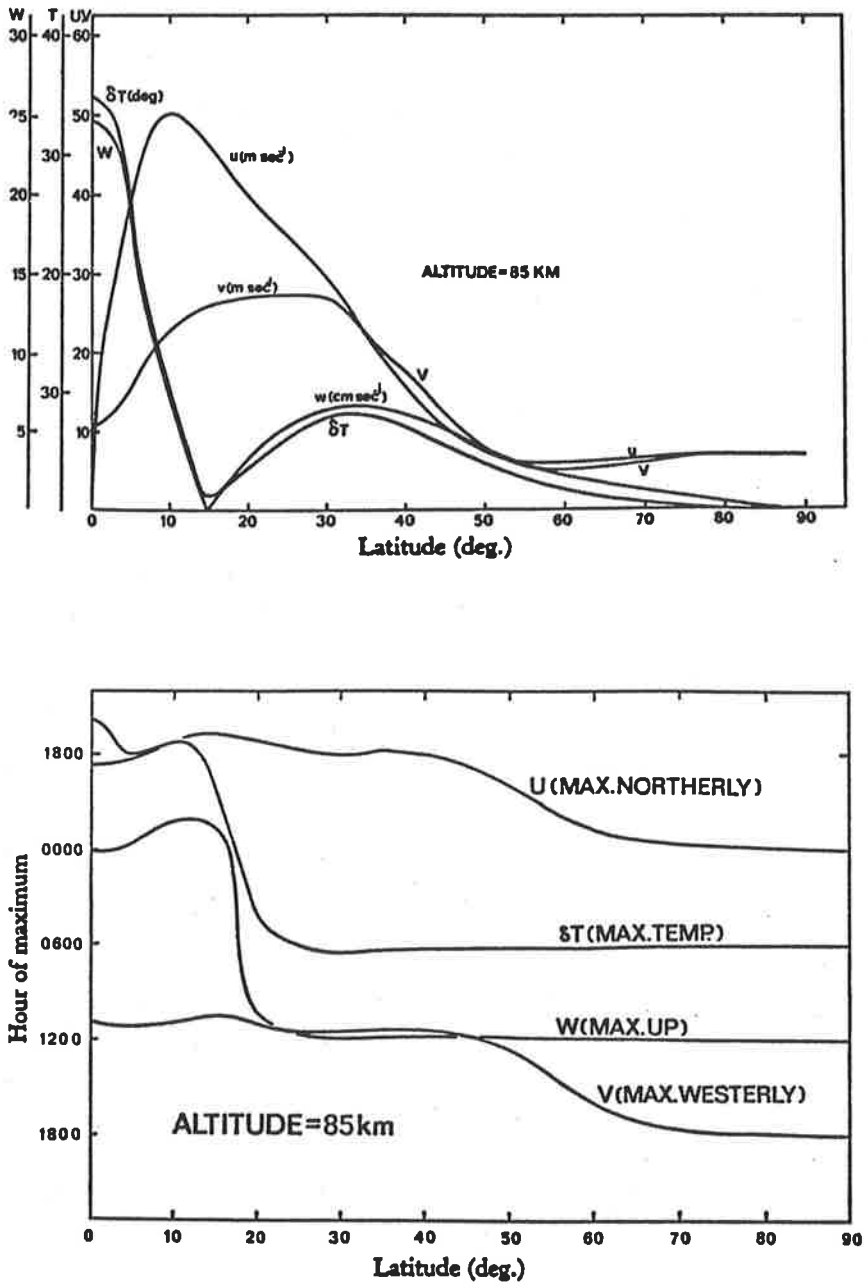

Figure 2.16: Latitude distribution of the amplitude (top) and phase (bottom) of the solar diurnal tide components at 85 km. (from Chapman and Lindzen 1970)

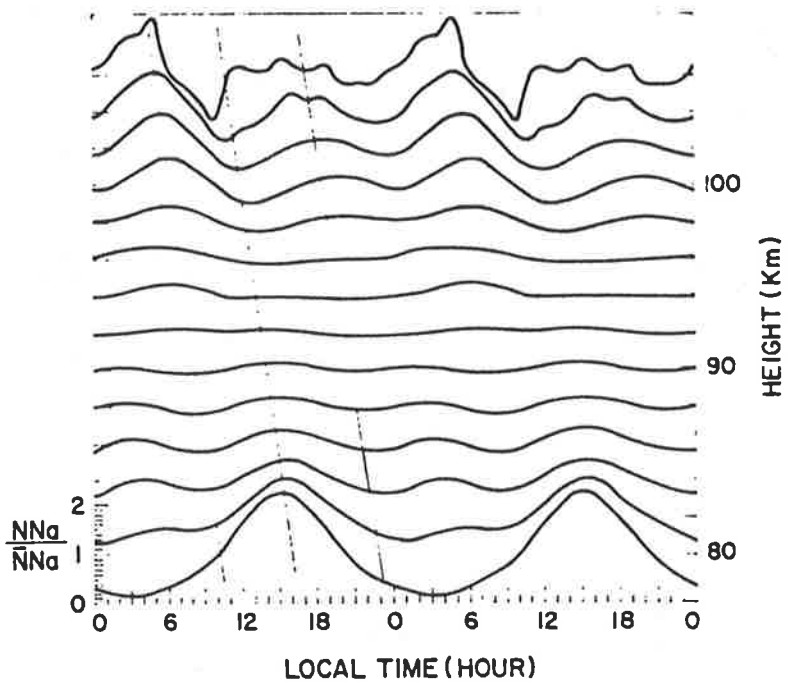

Figure 2.17: Normalized sodium density variations over 24 hours. The apparent phase propagation of the semidiurnal tide is suggested by tilted lines. (from Batista *et al.* 1985)

variations in observations of the sodium layer.

Diurnal and semidiurnal tides affect the sodium layer. Although data sequences of six or more hours in length allow observation of the semidiurnal tide, sequences of at least 24 hours are required to separate effects of both the diurnal and semidiurnal tides. 24 hour lidar observations of the sodium layer have been reported since 1972 (Gibson and Sandford, 1972). However neither Gibson and Sandford nor Granier and Megie (1982) noted tidal variations in their data. Batista *et al.* (1985) and Kwon *et al.* (1987) have observed large tidal variations in sodium density particularly near the top and bottom of the layer. Figure 2.17, from Batista *et al.*, shows normalized sodium density variations. A semidiurnal variation is apparent with a phase reversal near the peak of the layer. This was explained by consideration of interaction of the layer with the tide.

Production and loss mechanisms for sodium have a long time constant; individual sodium atoms remaining, on average, several days in the layer. Perturbations of a wave with period T can be allowed for without considering production and loss terms if T << several days.

By considering variations in density of a minor constituent, n, and variations of the major constituent, N, Batista *et al.* derived the following equation for density variations of a wave given by $\exp(i2\pi t/T)$;

$$\frac{\Delta n}{n_o} = \frac{\Delta N}{N_o} + \frac{iT}{2\pi}\left(\frac{1}{n_o}\frac{dn_o}{dz} - \frac{1}{N_o}\frac{dN_o}{dz}\right)W \tag{2.24}$$

where W is the vertical velocity due to the wave. By considering typical values of quantities involved it was shown that the second term in this equation dominated in determination of $\frac{\Delta n}{n_o}$. Also the equation shows that the second term will lead W by $\frac{\pi}{2}$ above and lag by $\frac{\pi}{2}$ below the layer peak as the density perturbations of the minor constituent decrease above the layer peak. It can be seen in figure 2.17 that the transition region of this phase change for tidal oscillations is between 92 and 98 km thus indicating that $\frac{\Delta N}{N_o}$ has a smaller effect than the second term. The equation above was then used to interpret behaviour of both the diurnal and semidiurnal oscillations in various parts of the sodium layer. The following approximation can be made far from the sodium layer peak:

$$\frac{\Delta n}{n_o} \cong \frac{iT}{2\pi}\left(\frac{1}{n_o}\frac{dn_o}{dz} - \frac{1}{N_o}\frac{dN_o}{dz}\right)W.$$

Batista *et al.* used this equation to estimate vertical velocity. Values of 5–20 ms^{-1} were obtained; these are in reasonable agreement with model predictions. By separating the diurnal and semidiurnal components a semidiurnal vertical wavelength of about 50 km was obtained. The diurnal vertical wavelength was much larger than the layer width and could not be calculated.

Analysis by Kwon *et al.* (1987) gave a vertical wavelength of 56 km for the semidiurnal tide for observations at another site. Both groups compared their measurements, where possible with models. Reasonable agreement was obtained between results and Forbes' (1982a, b) tidal model.

Takahashi *et al.* (1984) compared variations in O1 λ 558 nm, Na D, and OH emission and rotational temperature. A marked semidiurnal variation in the oxygen emission was found; and, although present in the Na D emission, the semidiurnal variation was not as marked. Data lengths of 5-10 hours were used to obtain monthly means in the analysis. Changes due to

photochemical processes at the emission height, 85 km, may partially mask variations due to the semidiurnal tide which is quite obvious in density variations.

Other observations of tidal variations in the mesosphere include studies of the oxygen λ 558 nm emission. Attempts to model these variations have been reasonably successful (Petitdidier and Titelbaum 1977; Akmaev and Shved 1980; Yee and Abreu 1987). Myabro (1984) noted tidal variations in the OH emission. Forbes (1981, 1982c) has investigated tidal variations in temperature and ion concentrations in the D and E regions of the ionosphere. On the basis of these studies it is expected that tidal variations will be present in both wind and temperature measurements obtained from observations of the sodium emission using a Fabry-Perot spectrometer.

Chapter 3

THE FABRY-PEROT SPECTROMETER

3.1 THEORY OF THE FABRY-PEROT ETALON

3.1.1 Ideal etalons.

Light multiply reflected by two plane, parallel surfaces distance h apart will form interference fringes. Fringes are formed both in the reflected beam — dark fringes on a bright background, and in the transmitted beam — bright fringes on a dark background. As illustrated in figure 3.1 the fringes can be imaged at P and P′ using lenses L and L′. When the angle θ is very small the fringes formed are known as Fabry-Perot fringes, and the instrument as a Fabry-Perot interferometer. The pair of glass plates forming the parallel surfaces are known as a Fabry-Perot etalon.

The theory of ideal etalons is treated in most optics texts, for example Born and Wolf, (1970) or Jenkins and White, (1976). Hernandez (1986) deals with Fabry-Perot interferometers presenting a complete treatment of Fabry-Perot theory. The presentation here will follow the basic outline presented by Jacka (1984).

For two surfaces h apart, separated by a medium with refractive index n, and for light of

wavelength λ, incident at angle θ, the phase difference between two reflected or transmitted beams in a Fabry-Perot etalon is given by

$$\delta = \frac{4\pi}{\lambda} nh\cos\theta + 2\phi. \tag{3.1}$$

where ϕ is the phase change on reflection at each plate surface. The maximum intensity of the interference pattern occurs when the order of interference, m, is integral: where m is given by

$$m = \frac{\delta}{2\pi} = \frac{2nh\cos\theta}{\lambda} + \frac{\phi}{\pi}. \tag{3.2}$$

In general $m = m_o + e$ where m_o is integral and e is a fractional part of an order.

The intensity of light reflected from and transmitted through an etalon can be calculated by considering the reflected and transmitted amplitude of the beam at each intersection with a surface. The resulting equations are known as Airy's formulae;

$$I^{(r)} = \frac{(2-2\cos\delta)\mathcal{R}}{1+\mathcal{R}^2-2\mathcal{R}\cos\delta} I^{(i)} = \frac{4\mathcal{R}\sin^2(\delta/2)}{(1-\mathcal{R}^2)+4\mathcal{R}\sin^2(\delta/2)} I^{(i)} \tag{3.3}$$

$$I^{(t)} = \frac{\mathcal{T}^2}{1+\mathcal{R}^2-2\mathcal{R}\cos\delta} I^{(i)} = \frac{\mathcal{T}^2}{(1-\mathcal{R}^2)+4\mathcal{R}\sin^2(\delta/2)} I^{(i)} \tag{3.4}$$

$I^{(i)}$, $I^{(r)}$, and $I^{(t)}$, are the intensity of the incident, reflected, and transmitted beams respectively. $\mathcal{R}$, and $\mathcal{T}$ are the reflectance and transmittance of the plate. Given the reflection co-efficient, r, and the reflectance defined by

$$r = \frac{\text{reflected amplitude}}{\text{incident amplitude}} \quad \text{and} \quad \mathcal{R} = \frac{\text{reflected intensity}}{\text{incident intensity}} \tag{3.5}$$

then $\mathcal{R} = r^2$. Similarly for the transmission co-efficient and transmittance. Using

$$F = \frac{4\mathcal{R}}{(1-\mathcal{R})^2} \quad \text{and} \quad \tau_A = \frac{\mathcal{T}^2}{(1-\mathcal{R})^2} \tag{3.6}$$

the Airy function for the transmitted intensity becomes

$$A'(m) = \frac{\tau_A}{1+F\sin^2(\pi m)}. \tag{3.7}$$

Figure 3.2 illustrates fringes of order m and m+1 (for m integral) for varying reflectivity. A compromise between fringe contrast and transmission is always made when choosing an etalon

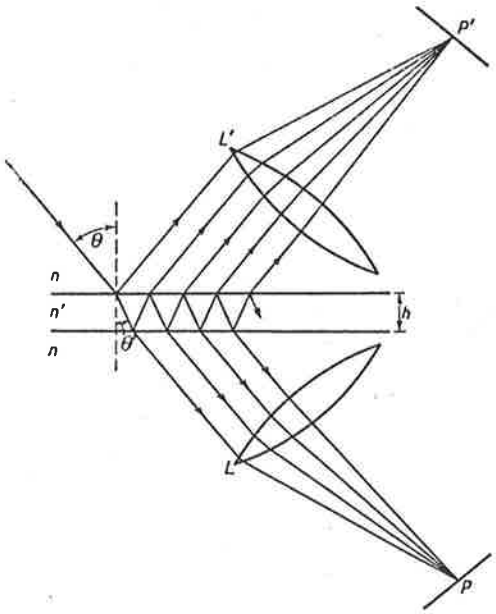

Figure 3.1: Reflection of a plane wave in a plane parallel plate. The lenses L and L′ form the fringe images at the points P and P′.

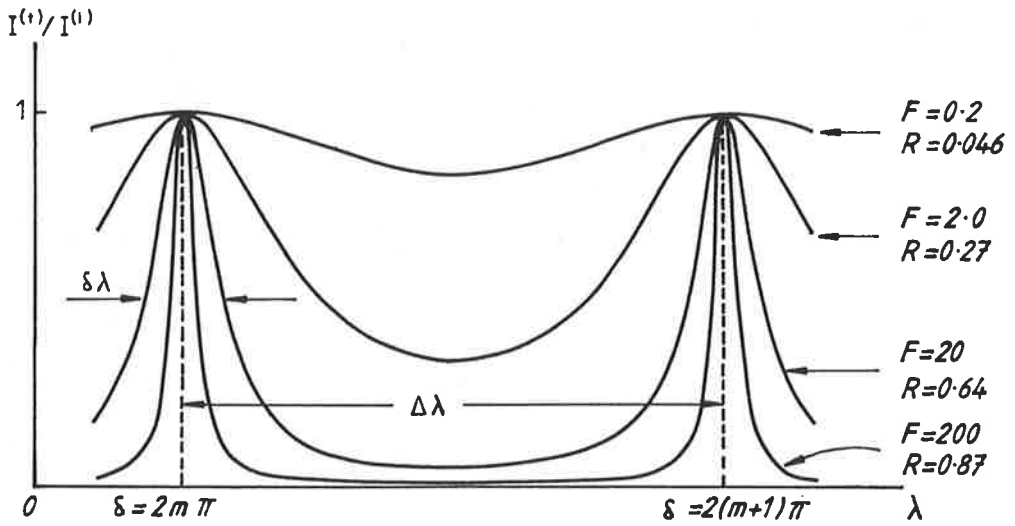

Figure 3.2: The ratio of transmitted to incident intensity as a function of phase difference for varying etalon reflectivity. m is an integer. The full width of the fringes, $\delta\lambda$ at half maximum for R = 0.64 and free spectral range, $\Delta\lambda$, are shown.

design. High contrast or very fine fringes produce low transmission of the incident light. If high transmission is obtained then contrast of the fringes is poor. This is usually expressed in terms of finesse, $\mathcal{F}$, of the etalon. Finesse is defined as the ratio of separation between two fringes, $\Delta\lambda$, to the full width at half maximum of a fringe, $\delta\lambda$;

$$\mathcal{F} = \frac{\Delta\lambda}{\delta\lambda}. \tag{3.8}$$

The quantities $\delta\lambda$ and $\Delta\lambda$ are indicated in figure 3.2. The separation between two fringes, $\Delta\lambda$, is known as the free spectral range of the etalon and is given by

$$\Delta\lambda = \frac{\lambda}{m} = \frac{\lambda^2}{2t}, \tag{3.9}$$

where t is the effective spacing of the etalon given by

$$m = \frac{2t}{\lambda} \quad \rightarrow \quad t = nh\cos\theta + \frac{\lambda\phi}{2\pi}. \tag{3.10}$$

For an ideal etalon the instrument finesse is defined by the reflectivity of the etalon plates:

$$N_A = \frac{\Delta\lambda}{\delta_A(\lambda)} = \frac{\pi\sqrt{\mathcal{F}}}{2} = \frac{\pi\sqrt{\mathcal{R}}}{(1-\mathcal{R})}, \tag{3.11}$$

where $\delta_A\lambda$ is the width of the Airy function.

The concepts presented so far have assumed a perfectly flat etalon and a finite field of view. In practice this cannot be achieved.

3.1.2 Non-ideal etalons

A brief review of non-ideal Fabry-Perot theory will be given: it is based on those by Jacka (1984) and Wilksch (1985). Hernandez (1986) provides a more extensive review.

Two parallel surfaces are required in a Fabry-Perot etalon. Defects in the plate surfaces, non-uniformities in the coatings, and imperfections in the plate mountings, parallelism control, and scanning mechanisms all contribute to departures of the etalon from the nominal spacing. Such departures are described by the defect function, $D'(\bar{t}-t)$ and defined by

$$D'(\bar{t}-t)dt = \frac{dS}{S} \tag{3.12}$$

where $\bar{t}$ is the mean effective plate separation. The defect function is the fraction of the plates over which the effective plate spacing lies in the range t to $t + dt$. In terms of wavelength the defect function is expressed as

$$D(\bar{\lambda} - \lambda) = D'(\bar{t} - t)\frac{m_o}{2}, \tag{3.13}$$

where m_o is a reference order such that $m_o\bar{\lambda} = 2\bar{t}$. This function has width $\delta_D\lambda$, so the defect finesse is given by

$$N_D = \frac{\Delta\lambda}{\delta_D(\lambda)} = \frac{\lambda}{2\delta_D(t)}, \tag{3.14}$$

since $\delta_D(\lambda) = (2/m_o)\delta_D(t)$. Thus $1/N_D$ is the width of the defect function $D'(\bar{t} - t)$ in units of $\lambda/2$.

Considering the etalon to be composed of sections of mean spacing $\bar{t}$ such that $\bar{\lambda}$ is transmitted at order m_0, the etalon transmission of the range of wavelengths $d\lambda$ at $\bar{\lambda}$ is given by

$$dE = A(\lambda)D(\bar{\lambda} - \lambda)d\lambda, \tag{3.15}$$

where $A(\lambda)$ is the Airy function described in the previous section. The total transmission for a finite range of wavelengths is

$$E = \int A(\lambda)D(\bar{\lambda} - \lambda)d\lambda. \tag{3.16}$$

This is the convolution of A and D denoted by

$$E(\lambda) = A(\lambda) * D(\lambda) \quad or \quad E = A * D. \tag{3.17}$$

Convolution is commutative, associative and distributive — Bracewell (1978) gives definitions of these properties.

The etalon finesse is defined by

$$N_E = \frac{\Delta\lambda}{\delta_E(\lambda)}, \tag{3.18}$$

where (see Jacka 1984 for proof)

$$\delta_E^2(\lambda) \simeq \delta_A^2(\lambda) + \delta_D^2(\lambda), \tag{3.19}$$

and

$$\frac{1}{N_E^2} \simeq \frac{1}{N_A^2} + \frac{1}{N_D^2}. \tag{3.20}$$

Thus the etalon finesse describes the quality of the etalon.

When a Fabry-Perot etalon is used in a spectrometer some form of wavelength scanning is required. From equation 3.10 it is clear that the wavelength can be scanned by varying t. This can be achieved either by varying the physical spacing, h, of the etalon by applying a voltage to piezoelectric ceramic supports, or by varying the index of refraction, n, of the gas between the plates by changing the pressure (see references in Jacka 1984) or by imaging the fringe pattern on a two dimensional array of detectors the etalon can be effectively spatially scanned by varying θ (Hays *et al.* 1981; Killeen *et al.* 1983).

Incorporating the etalon into a spectrometer also requires a finite field of view. Jacka (1984) assumes the etalon subtends a solid angle $\Delta\omega = \omega_2 - \omega_1$ at the field stop and defines the aperture function $F(\lambda_1 - \lambda)$ by

$$-F(\lambda_1 - \lambda)d\lambda = \frac{d\omega}{\omega}. \tag{3.21}$$

Thus the aperture function is the fraction of the total solid angle $\Delta\omega$ within which the wavelength of maximum transmission lies in the interval λ to $\lambda + d\lambda$. This can also be expressed as

$$-F(\lambda_1 - \lambda) = \frac{2\pi}{\lambda_o \Delta\omega}, \tag{3.22}$$

where λ_o is the wavelength transmitted at $\theta = 0$. The aperture finesse is defined as

$$N_F = \frac{\Delta\lambda}{\delta_F(\lambda)}. \tag{3.23}$$

Convolving the aperture and etalon functions gives the instrument function;

$$I(\lambda) = E(\lambda) * F(\lambda). \tag{3.24}$$

The instrument finesse is determined by

$$\frac{1}{N_I^2} \simeq \frac{1}{N_E^2} + \frac{1}{N_F^2} \simeq \frac{1}{N_D^2} + \frac{1}{N_A^2} + \frac{1}{N_F^2}. \tag{3.25}$$

Thus the instrument response to an infinitely narrow spectral line (a Dirac delta function) is given by equation 3.24.

The width of an emission line is determined by the temperature of the emitting species. The Doppler line-width at half-intensity is given by

$$\delta\lambda = 2\sqrt{ln2}\sqrt{\frac{2kT}{M}}\frac{\lambda}{c}, \tag{3.26}$$

where k is Boltzman's constant, M the atomic weight, and c the speed of light of wavelength λ. A transmission profile recorded by a spectrometer is the convolution of the instrument profile and the emission line profile. The source function is given by $B(\lambda)$,

$$B(\lambda)d\lambda = \frac{dL}{L}, \tag{3.27}$$

where L is the total radiance and dL the radiance of the source in the region of the spectrum from λ to $\lambda + d\lambda$. The recorded profile $Y(\lambda)$ is thus given by

$$Y(\lambda) = B(\lambda) * I(\lambda). \tag{3.28}$$

Using the properties of commutation and association of convolution, and equations 3.24 and 3.17, this becomes

$$Y(\lambda) = A(\lambda) * D(\lambda) * F(\lambda) * B(\lambda). \tag{3.29}$$

The width at half-maximum of the recorded function, $\delta_Y(\lambda)$, is finally obtained as

$$\delta_Y^2(\lambda) \simeq \delta_I^2(\lambda) + \delta_B^2(\lambda) \simeq \delta_A^2(\lambda) + \delta_D^2(\lambda) + \delta_F^2(\lambda) + \delta_B^2(\lambda). \tag{3.30}$$

The width of the recorded function can be measured, so if the instrument function at the appropriate wavelength is known then the width of the source function can be calculated. Hence by equation 3.26 the temperature of the emitting species can be calculated.

In practice a narrow bandpass filter is usually required to isolate a single line from the source spectrum. When viewing the night sky a 5 nm filter is usually adequate to isolate the required emission line although when the spectrum is cluttered with lines a narrower filter may be required.

3.2 MT. TORRENS HIGH-RESOLUTION SPECTROMETER

3.2.1 Optical configuration

The high-resolution Fabry-Perot spectrometer at Mt. Torrens was developed for night-time airglow studies (Jacka *et al.* 1980; Wilksch 1975). For this project several modifications to the system were made to improve performance and to implement changes developed for a similar instrument installed at Mawson, Antarctica (Jacka 1984). Figure 3.3 shows the optical layout of the Mt. Torrens spectrometer. All parts labelled in figure 3.3 are listed in table 3.1. For night-time and twilight observations the mirror labelled LR11 is removed and the field stop, lens, and periscope are positioned above the main cabinet. The periscope extends through the roof. Observations through 360° in azimuth and 90° in zenith angle are obtained by rotation of the periscope.

The objective lens HR2 focuses light on the field stop HR4. This stop defines the field of view of the spectrometer and various diameter stops are available to optimize spectrometer operation at different wavelengths. The field stop can also be illuminated by a calibration light source which is introduced via an optical fibre and removable diffusing screen, HR3. A camera release cable is used to operate the diffusing screen. HR5 is a 970 mm focal length, high quality, collimating lens; it consists of a singlet and cemented doublet and has been designed to correct spherical aberration.

The etalon is mounted below the collimating lens. New etalons were obtained for both the high-resolution and the low-resolution instruments because an improvement in etalon finesse was desired. The new high-resolution plates are homosil, 150 mm in diameter and have 45° facets for parallelism control on the lower plate. Finesse measurements for the new etalon are presented in sections 3.2.4 and 3.3.4 of this chapter. Parallelism control is automated using the method developed by Ramsay (1962). An external light source is introduced via fibers and lenses and traverses the etalon gap twice, by reflection in the facets in the bottom plate, before being detected by a PIN diode. The PIN diode is most sensitive to wavelengths from 700–

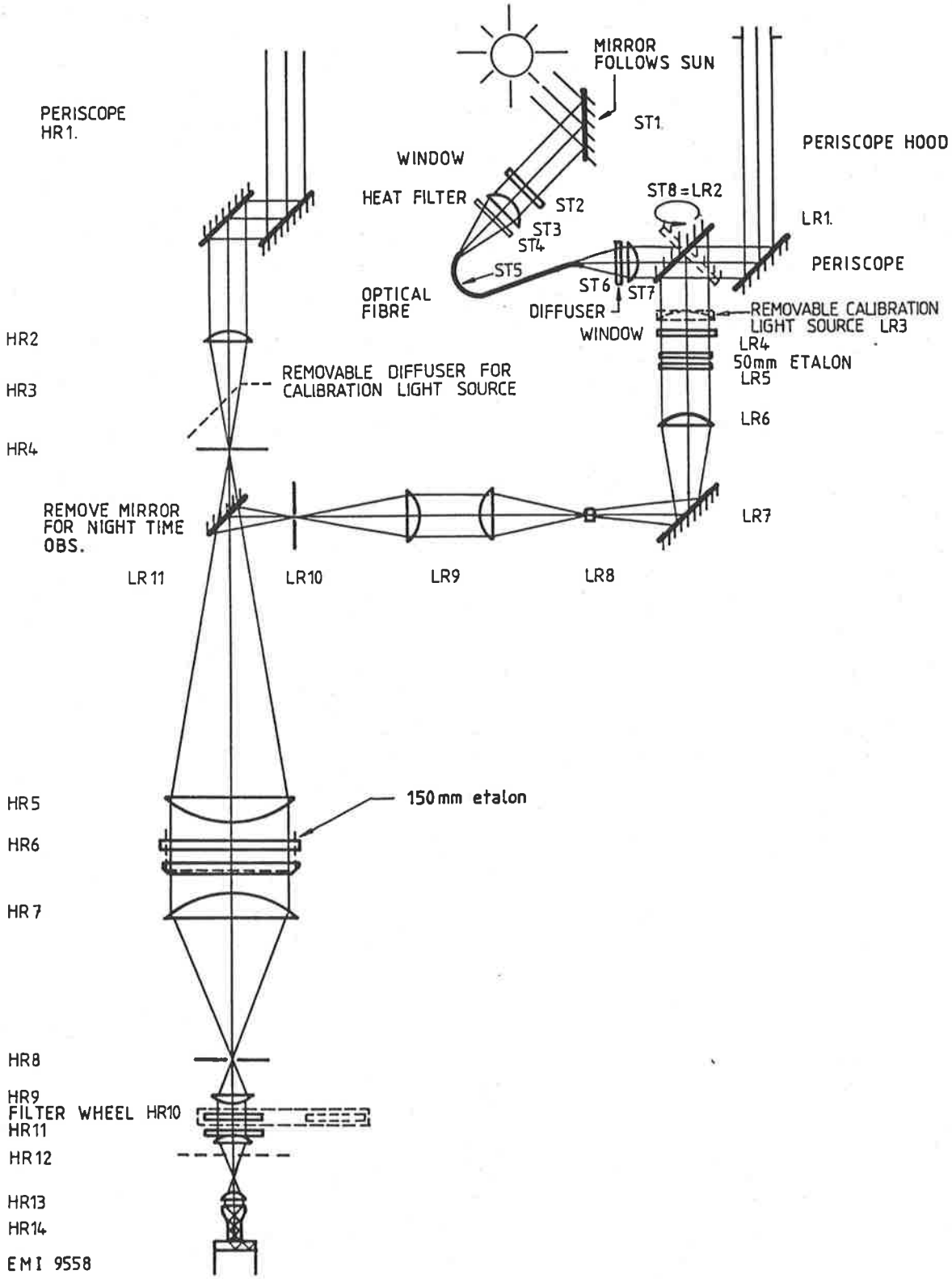

Figure 3.3: Optical layout of the Mt. Torrens Spectrometer. For night-time and twilight observations the mirror labelled LR11 is removed and the components above installed. The components are identified by their labels in table 3.1. (Not to scale.)

High resolution optical components	
HR1	periscope for selecting zenith angle of observations
HR2	objective lens, f=160 mm
HR3	removable diffuser for calibration light source
HR4	field stop
HR5	collimating lens, Cooke triplet with f=970 mm.
HR6	high resolution 150 mm etalon with infra-red parallelism control mechanism
HR7	aspherized collecting lens, f=267 mm
HR8	aperture to minimize off-axis scattering into photomultiplier
HR9	CR13 moulded aspheric collimating lens, f=64 mm
HR10	filterwheel with choice of six narrow-bandpass filters also fixed infra-red blocking filter
HR11	CR13 moulded aspheric collecting lens, f=64 mm
HR12	electric shutter
HR13	collimating lens, f=23 mm
HR14	perspex cone to maximize total internal reflections in photocathode
HR15	photomultiplier, EMI9558 Cooled to −30°C

Low resolution optical components for dual etalon system	
LR1	front surfaced mirror, with 500 mm hood to minimize scattering into field of view, can be rotated in azimuth and zenith
LR2	front surfaced mirror, rotates to allow choice of either sun or sky observations
LR3	removable diffuser for calibration light source
LR4	glass window for temperature control
LR5	low resolution, 50 mm, etalon
LR6	objective lens, f=300 mm
LR7	front surfaced mirror
LR8	field lens,f=63 mm
LR9	2× f=137 mm lenses to optically couple into high resolution system
LR10	field stop for dual etalon system
LR11	front surfaced mirror

Solar telescope components	
ST1	front surfaced mirror which tracks sun
ST2	perspex window
ST3	CR13 aspheric collecting lens, f=64 mm
ST4	heat filter
ST5	optical fibre
ST6	diffusing screen
ST7	CR13 aspheric collimating lens
ST8	=LR2 rotated about a vertical axis

Table 3.1: This table identifies the components in the Mt. Torrens spectrometer by the labels given in figure 3.3.

900 nm and several filters are incorporated so that only light in the range 740–780 nm enters the etalon chamber. This allows observations of the λ 734 nm OH emission, if wanted, without significant contamination by scattered light from the parallelism control system. Above this range the photomultiplier response is poor and observations are impossible. The external light source replaces small incandescent bulbs which were previously mounted above the top etalon plate.

The spectrometer output optics were significantly modified for this project. The objective was to incorporate a filter wheel to facilitate rapid filter changes with minimal disturbance of the instrument. Previously a filter had been incorporated above HR2. A new Peltier cell cooler for the photomultiplier replaced the original coolant system.

The filter wheel contains five, 50 mm diameter, narrow bandpass filters and an empty filter holder for transmission of prefiltered calibration sources. A 0.5 nm filter is required for night-time observations and a 0.3 nm filter for daytime observations of the sodium emission. Use of such filters requires the incident light to be collimated. To achieve this a moulded CR13 aspheric lens, HR9, is used. The 150 mm collecting lens, HR7, directly below the etalon had to be aspherized to achieve the required degree of collimation without loss of light. This was achieved by shaping the flat surface of the lens. A ray-tracing program was used to calculate the amount of glass to be removed from the lens. Figure 3.4 shows a schematic representation of the final lens shape and the associated table gives the amount to be removed at 5 mm steps across the lens. J. Cole, of Quentron Optics, did the required shaping and smoothly graded the surface between the specified points. The final lens shape produced a focus of less than 1 mm diameter at 267.5$\pm$0.5 mm from the flat surface.

The aperture HR8 and fixed infra-red blocking filter below the filter wheel are incorporated to remove any light scattered from the parallelism control beams into the field of view of the photomultiplier.

HR10 is also a moulded CR13 aspheric lens, used in conjunction with HR13 to produce a

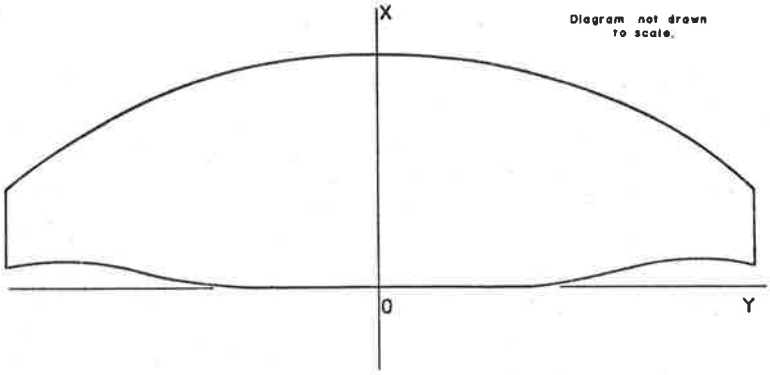

Figure 3.4: A schematic representation of the aspheric lens shape.

Table 3.4: The amount of glass removed from the lens at distance Y from the centre.

Y	0.0	5.0	10.0	15.0	20.0	25.0	30.0	35.0	40.0
ΔX	0.0000	0.0028	0.0111	0.0247	0.0425	0.0645	0.0892	0.1152	0.1415
Y	45.0	50.0	55.0	60.0	65.0	70.0	75.0	77.5	80.0
ΔX	0.1666	0.1883	0.2052	0.2152	0.2163	0.2065	0.1837	0.1668	0.1458

narrow collimated beam for the perspex cone HR14. The perspex cone was designed to introduce light into the photocathode at greater than the critical angle so that multiple internal reflections occurring inside the front window and photocathode effectively increase the quantum efficiency of the photomultiplier. The perspex cone, similar in principle to those of Hircshfeld (1968), has an extended end which passes through the narrow bore of a solenoid used for magnetic defocusing. The end of the perspex cone is optically contacted to the photocathode using oil. Figure 3.5 shows dimensions of the cone and insulated delrin holder which is mounted in front of the Peltier cell cooler. Attached to the Peltier cell cooler an electric shutter, HR12, allows the photomultiplier to be isolated when not in use.

Assessment of optical components and alignment of lenses was checked on the optical bench before required optical coatings were applied. Antireflection coatings on optical components make a significant contribution to the reduction of transmission losses. The application of coatings to the optical components is discussed further in Appendix A.

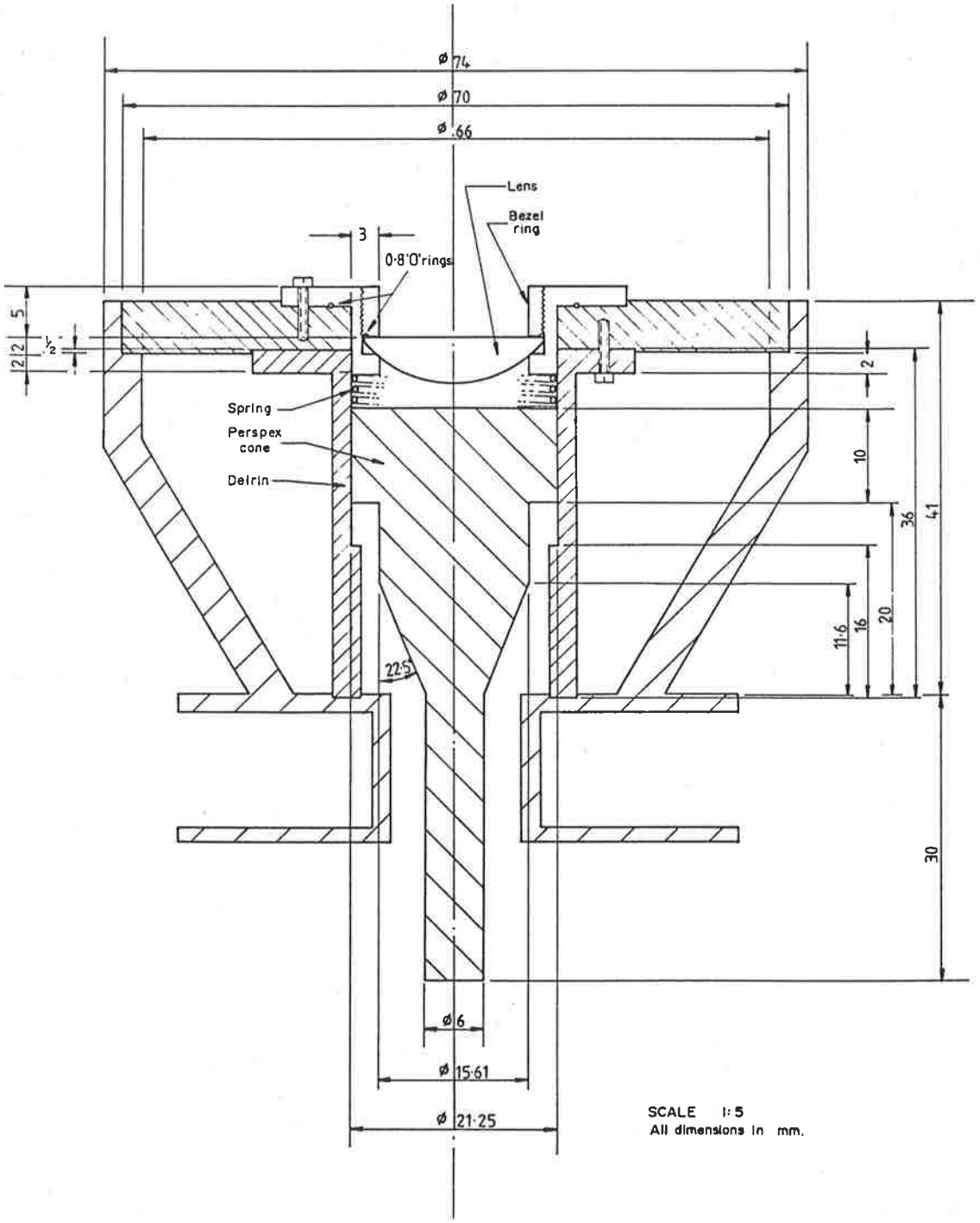

Figure 3.5: Dimensions of the perspex cone used to introduce light at greater than the critical angle so that multiple internal reflections occur within the front window and photocathode of the photomultiplier. The mounting of the cone and lens HR14 in the delrin holder, which fits into the front of the Peltier cell cooler, are shown.

3.2.2 Operation of high-resolution spectrometer

Operation of the Mt. Torrens high-resolution spectrometer involves etalon maintenance, data acquisition, and light collection. As mentioned in the previous section the viewing direction is determined by the periscope. Alterations are made manually and about 30 seconds are required to change viewing direction. The whole instrument is encased within a light tight shell and mounted on springs in an insulated cabinet. The building housing the instrument has been designed so that minimal room light can be scattered into the field of view.

The etalon plates must be kept parallel. Near infra-red beams traverse the plates in two orthogonal directions as described in the previous section. These beams form white light superposition fringes. The intensity of the fringes is measured by a PIN diode. The top plate is mounted on three points mechanically coupled to three piezoelectric ceramic tubes. Application of a voltage across the wall of the ceramic tube produces a small change in length. A voltage with a frequency of approximately 1.3 kHz is applied to the ceramic tubes to wobble the top plate by a few nanometers. This alters the seperation traversed on either side of the plates. A maximum in intensity of the fringe pattern seen at the PIN diode occurs when the separation on either side is equal. The signal from the diode is used to control correction voltages applied to ceramic supports for the lower plate. When the plates are within half a fringe of parallelism a servo control mechanism keeps the plates parallel. At the beginning of an observing session parallelism is obtained by manually altering the voltages on the lower plate. No further manual adjustments are usually required.

If the spectrometer has had a major disturbance (such as that required to open the filter box or change the plate separation by several millimetres) physical adjustments of the top etalon may be required to obtain parallelism. This was achieved with a special tool which alters the fine and coarse screw threads which attach to the ceramic mounts. Care was taken when making such alterations that the etalon remained perpendicular to the optical axis. This can be checked by autocollimation at the field stop. If the etalon was not perpendicular to the optical axis the

instrument profile became asymmetrical. Details of the plate mountings and other parts of the spectrometer not altered for this project can are described by Jacka *et al.* (1980) and Wilksch (1975).

The voltages applied to the lower plate (0–600V) are used to correct parallelism errors, set the separation of the plates to a fraction of an order, and to scan the plate separation. The movement of the ceramic mounts allows up to five orders to be scanned. The system is most stable when operating over one order at the centre of the voltage range.

Large changes in separation are made by altering the lower plate's position. Three columns support the meehanite ring in which the lower plate is mounted. These columns have fine threads and a motor and gear at the bottom of the etalon chamber are used for coarse adjustments. The gear can be turned manually for smaller adjustments. The threads are very precisely cut so that even after several millimeters movement the plates are usually very close to parallel.

A capacitive displacement transducer is attached to the lower plate mount. An invar rod, resting on the movable stainless steel discs in the capacitive bridge is clamped to the meehanite ring in which the upper plate is mounted. This system is capable of measuring changes in plate separation as small as 0.1 nm. Scanning the required distance is achieved by applying a stepped, saw-tooth waveform. During routine observations only a fraction of an order is scanned but adjustments are available to scan up to five orders. The separation is servo-controlled, the correction being applied to the lower plate.

Changes in temperature and air pressure also affect the refractive index of the air gap between the etalon plates. The instrument is therefore temperature controlled. Thermostats are used to control heaters in the etalon chamber, collimating lens and cabinet ducts. Fans circulate air in the cabinet through ducts. The temperature is maintained at 30° C with fluctuations of 0.5° C. The hut containing the instrument is air-conditioned and room temperature is maintained at 24° C. A pressure transducer senses changes in barometric pressure and adds a correction to the separation control voltage. Changes in air pressure of 0.6 mb or greater are

sufficient to affect the instrument operation if no correction is applied. The whole instrument is mounted on springs to mechanically isolate it from vibrations in the building.

Small changes in the separation of the plates still occur on a timescale of hours, probably due to the long-term temperature changes. Such drift is monitored by observing a calibration source, either the λ 546 nm from a Hg 198 lamp or one of the D-lines of a hollow cathode sodium lamp.

An EMI 9558 photomultiplier is used to detect the signal. The photomultiplier is cooled to about -20°C using a Peltier cell cooler. This significantly reduces the photomultiplier dark count. During night-time observations signal levels are very low; the signal to noise ratio is usually less than 1. In such circumstances it is beneficial to use the magnetic defocusing coil which reduces noise levels. The amount of signal reduction is less and improves the signal to noise ratio. During twilight and daytime observations signal levels are very high and the major source of noise is produced in amplification and counting of the signal so that no benefit is derived from magnetic defocusing applied to the photomultiplier.

The signal from the photomultiplier is amplified before being sent to the multichannel analyser. The amplifier can either be used in a photon counting digital mode or, for daytime observations, in analogue mode. The contents of the analyser can be recorded when the acumulated profile has sufficient counts. For the purpose of the following discussion the term profile will be used to describe the record of pulse counts per channel. Data are usually recorded in 128 channels, the analyser stepping in synchronism with scan voltage. 256 or 512 channels can also be used if a larger scan range is required for calibration purposes. Scanning the instrument over two orders allows the number of channels corresponding to the free spectral range, for a given wavelength and order, to be calculated. If the order of operation is known then the wavelength step per channel can be estimated using equation 3.9. One channel corresponds to approximately 0.12 pm for typical values of order and free spectral range used for sodium observations. The dwell-time per channel can be varied; typically, for twilight observations,

40 ms was used.

At the outset of the project data were recorded on cassette tape. Data are now recorded, along with housekeeping information such as start and stop time, filter in use, direction of viewing, etc., on magnetic disc using a personal computer. The data are transferred to the University of Adelaide's main computer system for analysis.

A chart recorder can be used to monitor signal levels. This is most useful to see changes in background conditions. When observing conditions are marginal, due to cloud or fog, a chart record can be used to isolate contaminated profiles.

3.2.3 Optimization for sodium observations

The optimum configuration of the Fabry-Perot spectrometer is that which gives highest transmission with instrument bandwidth comparable with the source line width. To determine the required instrument parameters for sodium observations the following criteria were used (after Jacka (1984)):

$$\delta_I(\lambda) = \delta_B(\lambda), \tag{3.31}$$

$$\delta_F(\lambda) = \delta_A(\lambda), \tag{3.32}$$

$$\delta_A(\lambda) = \delta_D(\lambda), \tag{3.33}$$

$$\text{and } \delta_D(\lambda) \text{ is as small as possible.} \tag{3.34}$$

$\delta_D(\lambda)$ is set by the quality of the etalon and parallelism control mechanism. $\delta_A(\lambda)$ is determined by coatings applied to the etalon. Although design of the reflective coatings can be changed replacement is expensive. The width of the aperture function $\delta_F(\lambda)$ is given by

$$\delta_F(\lambda) = \frac{1}{2}\lambda\theta_2 = \frac{\lambda D^2}{8f^2} \tag{3.35}$$

where f is focal length of the collimating lens and D is diameter of the field stop. This is used, given values of N_D and N_A, to determine the field stop diameter. By considering equation 3.32

and equation 3.9, the separation, t, of the plates is given by

$$t = \frac{4f^2\lambda}{D^2 N_E}. \tag{3.36}$$

This gives a guide for determining the plate separation. The D1 and D2 lines of the sodium emission are separated by 0.6 nm so that even with a 0.3 nm bandpass filter for, say, the D2 line, some small transmission of the D1 line will occur. The exact order was chosen so that this parasitic transmission did not contaminate the required line profile. The D1 order, n, was chosen so that the D2 order was given by $n + m + 1/2$, for n and m integral. This limits the separation to values given by

$$t = 1.45 \times 10^{-4} \times n \tag{3.37}$$

for n integral and odd.

An initial estimate of etalon finesse of 20 gave values of D=4.0 mm and t=6.98 mm. Later measurements showed that the etalon finesse was less than 20. The values of D and t given above were still used because the measured etalon finesse did not vary sufficiently to justify modifications.

The etalon was set to the approximate separation using a micrometer incorporated into the etalon chamber. Small adjustments were then made so that equation 3.37 was satisfied. This was checked by scanning the two D-lines using a calibration lamp. The order could then be measured, as described by Jacka (1984), using the sodium D-lines and a neon line, λ588.189 nm. Thus the operating order for sodium measurements at λ589.592 nm was 23150. At times the separation was changed for observations of the λ630 nm atomic oxygen emission and also for finesse measurements. Using the above procedure to reset the order for sodium observations ensured that the order was always within $\pm$100 of 23150.

3.2.4 Instrument assessment

The old etalon had an etalon finesse of 16.5 at λ630 nm. The new etalon was specified to have $N_D = N_A = 50$. Unfortunately these criteria were not met. The etalon did initially have

$N_D \approx 42$. When gluing support lugs to the plates some stress was introduced and localized defects occurred for about 2 cm around the lugs. This was minimized, but not completely removed, when the lugs were removed and reglued with a mixture of epoxy resin, and silica microspheres. The lugs should be glued to the plates before the final matching (polishing). The matching of the etalon was downgraded when the hard antireflection coatings were removed from the back surface (Greet 1986 (see Appendix A)). The final defect finesse, as measured in the flatness testing instrument, was $N_D = 38 \pm 2$.

The methods for measurement of etalon characteristics were described by Jacka (1984). Defect finesse is determined from measurements of the reflective finesse and etalon finesse. Design values of reflectance and phase change on reflection were supplied by the coating manufacturer (R. Schaeffer, pers. comm.) Reflectance as a function of wavelength is shown in figure 3.6. Reflectance before and after application of soft AR-coatings on the back surfaces is also shown. The difference between the top and bottom plates is also shown. Profiles at the centre and edge were made to check uniformity. No variation was measurable for the bottom plate but the top plate varied by about 1% in the wavelength regions 610–720 nm and 460–490 nm.

A comparison of the theoretical and measured values is given in table 3.2. The measured values were determined: (1) using the reflectance as given by the final spectrometer measurements, (2) assuming that 1% is lost by reflection at the back surface (the soft AR coatings decrease the loss by reflection from 4% to approximately 1%), and (3) using the technique described by Jacka (1984). All measurements are made over only a fraction of the plate area and there are variations of about 1% in the uniformity of the coatings both between the top and bottom plate and across a plate. Considering this reasonable agreement is obtained between the measured values but only if allowance for reflection at the back surface is made. Figure 3.6 and table 3.2 show that the design criteria were not met but in view of the lower than expected defect finesse the lower values of N_A are desirable.

The average of several measurements of etalon finesse is shown in table 3.3. Using these

Table 3.2: Reflective finesse measurements for the 150 mm etalon. The design specifications are given and in line (1) the finesse was calculated from spectrometer reflectance measurements; in line (2) the calculations allowed for the 1% reflection loss at the back surface; in line (3) the measurements were made in the Fabry-Perot spectrometer.

N_A	730 nm	633 nm	590 nm	558 nm	546 nm
design	40	49	49	40	33
(1)	32 ± 1	26 ± 1	33 ± 1	30 ± 1	26 ± 1
(2)	28 ± 1	24 ± 1	30 ± 1	27 ± 1	24 ± 1
(3)		24 ± 2	29 ± 4		20 ± 2

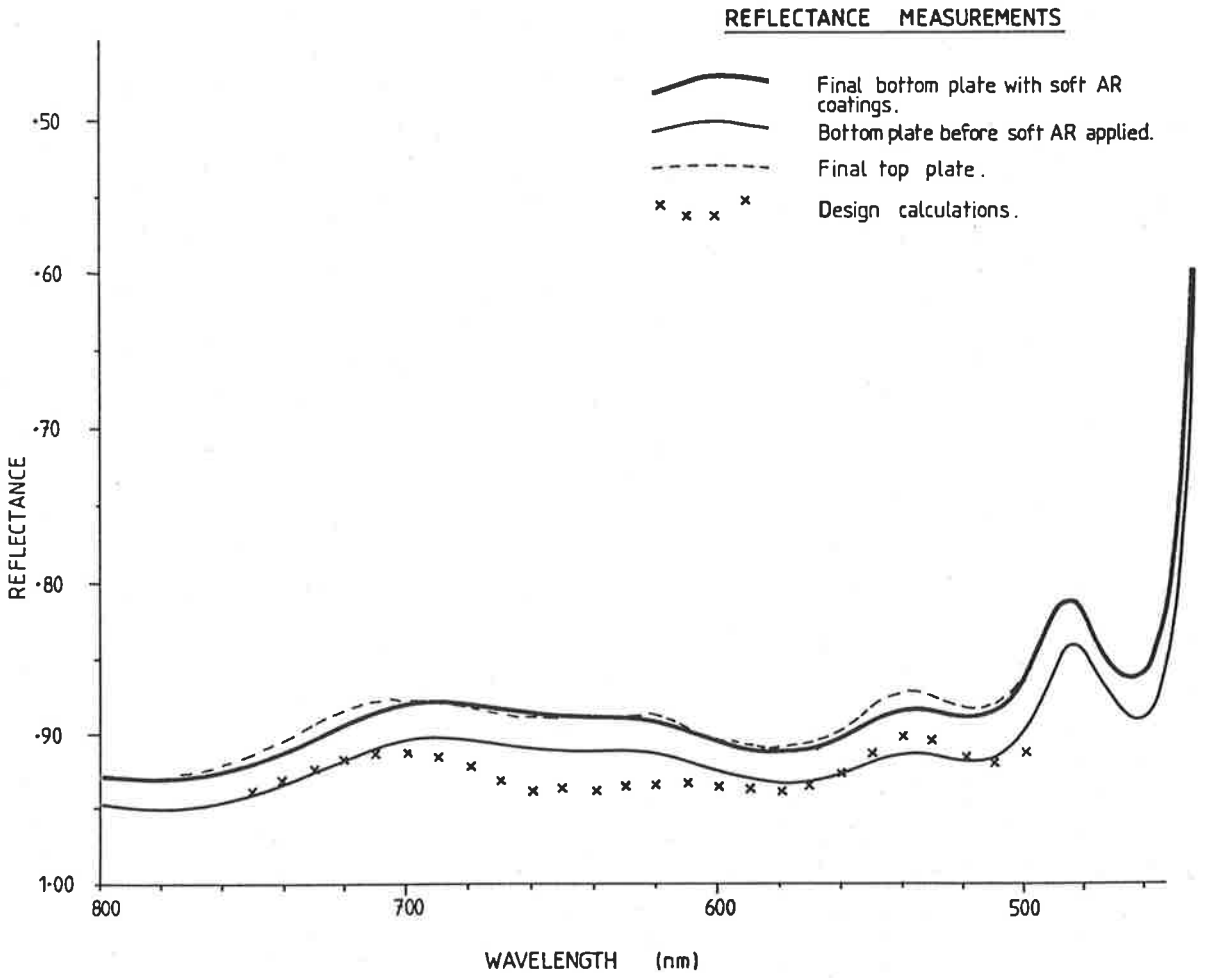

Figure 3.6: Reflectance measurements of the 150 mm etalon. The crosses are the design values. The other lines are measurements made in a spectrometer. The heavy line is for the bottom plate in final form with soft AR coatings, the dashed line for the top plate. The light line is for the bottom plate before the application of the soft AR coatings.

Table 3.3: Etalon and Defect finesse measurements for the 150 mm etalon. N_E and N_D (1) were determined from averages of several measurements using the method described by Jacka (1984). N_D (2) was calculated from flatness testing at λ 633 nm.

wavelength	632.8 nm	589.6 nm	589.0 nm	546.1 nm
N_E	15.9 ± 1.4	15.9 ± 1.4	15.9 ± 0.5	12.1 ± 0.6
N_D (1)	22 ± 4	21 ± 3	19 ± 2	15 ± 2
N_D (2)	38 ± 2	35 ± 2	35 ± 2	33 ± 2

and values of N_A given in table 3.2, N_D has been determined (N_D (1) in table 3.3). The defect finesse obtained by this method is considerably less than that obtained using the flatness testing instrument with a λ 630 nm HeNe laser (N_D (2) in table 3.3). Values at other wavelengths have been calculated from this measurement. The difference between the two methods is in the means of maintaining parallelism control. In the flatness testing instrument, parallelism is maintained by observing the fringe pattern and manually adjusting the piezoelectric ceramic supports for the bottom plate. In the FPS, as mentioned previously, parallelism control is automated using two small areas on either side of the etalon. It is possible, when one of these area has a localized defect, that the servo-control mechanism will hold the plates slightly away from the ideal position. It is also possible that the method of obtaining flatness measurements by selecting random points on fringes across the plates does not adequately sample the whole plate.

The instrument function at any wavelength, λ_x, is its response to a delta function at that wavelength. This can be determined from a calibration lamp profile at a known temperature and the reflective finesse at both the lamp wavelength, λ_l, and the required wavelength, λ_x. If the source function and the Airy function at the lamp wavelength, λ_l, are deconvolved from the recorded lamp profile and this function is convolved with the Airy function at the required wavelength, λ_x, the instrument function at λ_x can be determined. A hollow cathode sodium

lamp, operating at about 400K, provides a source at the operating wavelength. The sodium emission has hyperfine structure so this must be removed to obtain the instrument function. Use of the sodium lamp for analysis will be discussed in the next chapter. The sodium lamp D1 profile used for twilight analysis is shown in figure 3.7.

A measurement of instrument finesse was made using a λ 546 nm line from a ^{198}Hg lamp operating at 300 K. The calculation used values of reflective finesse given above and a lamp profile recorded at the separation and with the field stop used for sodium observations. Figure 3.8 shows the instrument function obtained. An instrument finesse of 12.0 $\pm$ 0.1 at λ 589 nm was obtained. Unfortunately this is only a slight improvement over the previous etalon.

3.3 DUAL-ETALON SPECTROMETERS FOR DAYGLOW OPERATION

Single etalon Fabry-Perot spectrometers are limited by their multiple passbands to observations of simple emission features isolated by narrow bandpass filters; one passband and one emission feature coinciding. By incorporating further etalons the FPS transmission can be reduced to a single passband. The high resolution etalon is normally operated in conjunction with a narrow bandpass filter. This allows transmission of many orders of the etalon as illustrated in figure 3.9. When a third element is incorporated (i.e. a low-resolution etalon) only the central order of the high-resolution etalon is selected, as in figure 3.10. Some small transmission of other orders occurs and these are known as ghosts or parasitic passbands.

Poly-etalon Fabry-Perot spectrometers can be used to study complex spectra such as the solar absorption spectrum or the spectrum of the day sky. The theory of poly-etalon systems has been discussed by McNutt (1965), Hernandez (1986), and Skinner *et al.* (1987). A summary of the required concepts will be given in this section and operation and instrument assessment in following sections. Reference will be made to discussions of the poly-etalon systems: PEPSIOS instruments (Mack *et al.* 1963; Burnett and Burnett 1983) , and HRDI (Skinner *et al.* 1987).

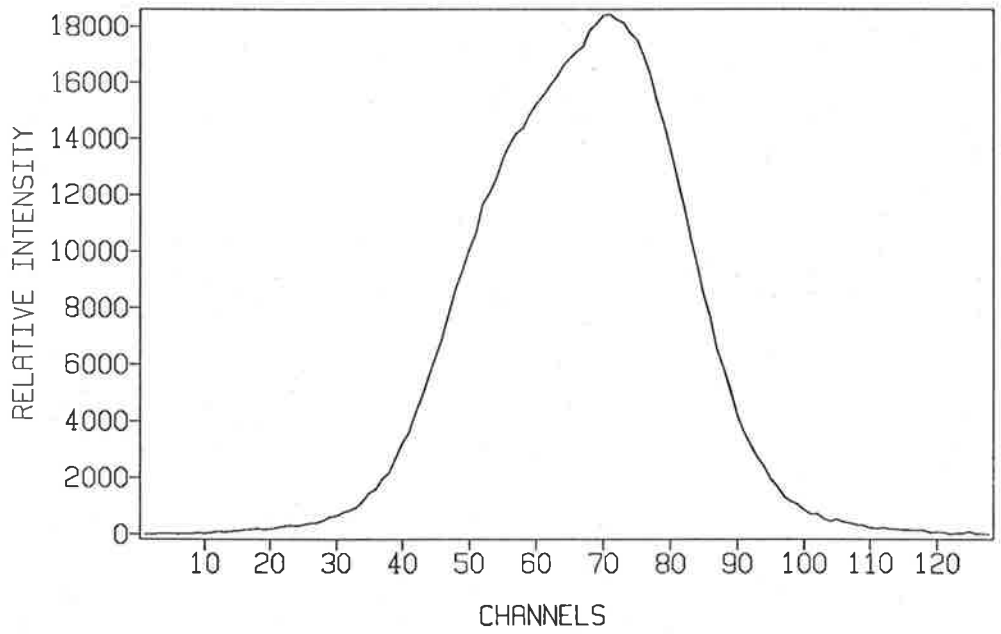

Figure 3.7: A high-resolution spectrometer profile of λ 589.6 nm D1 sodium emission from the hollow cathode lamp. An acquire time of 4.1 minutes was used. The hyperfine structure of the sodium emission produces the asymmetry of the profile.

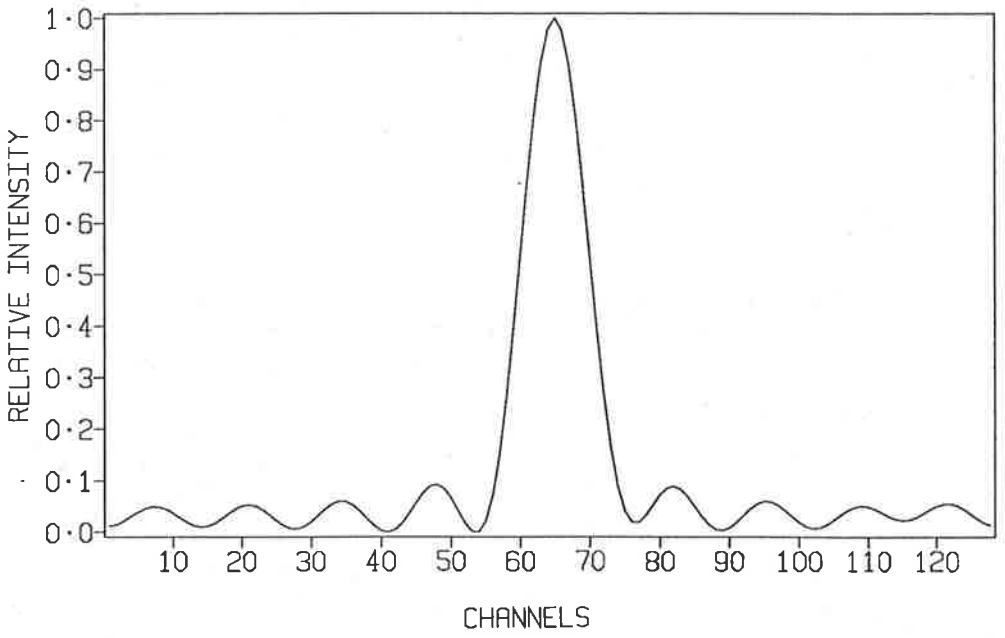

Figure 3.8: A high-resolution spectrometer instrument profile at λ 589.6 nm. The profile was determined from a ^{198}Hg lamp profile at λ 546.1 nm as described in the text. The structure away from the peak is due to the removal of noise from the spectrum by truncation of the profile in the Fourier transform domain.

(a)

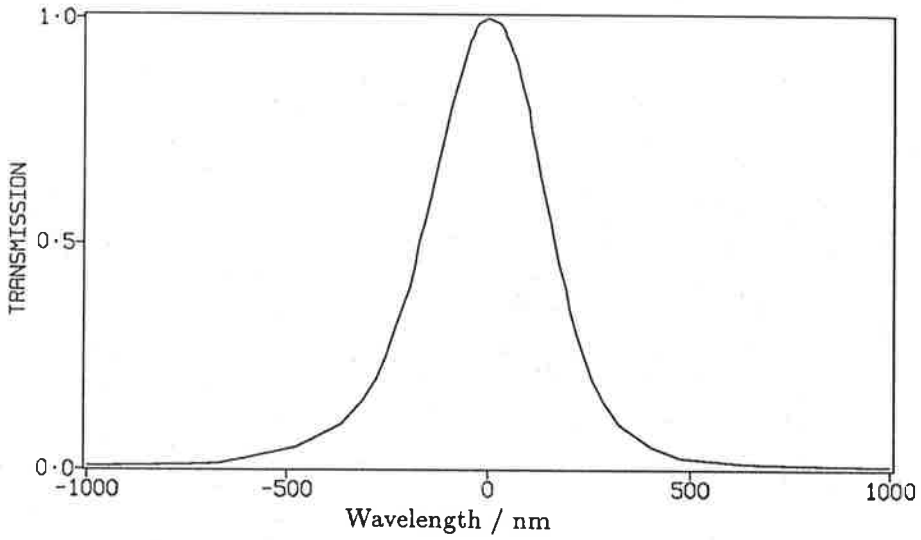

(b)

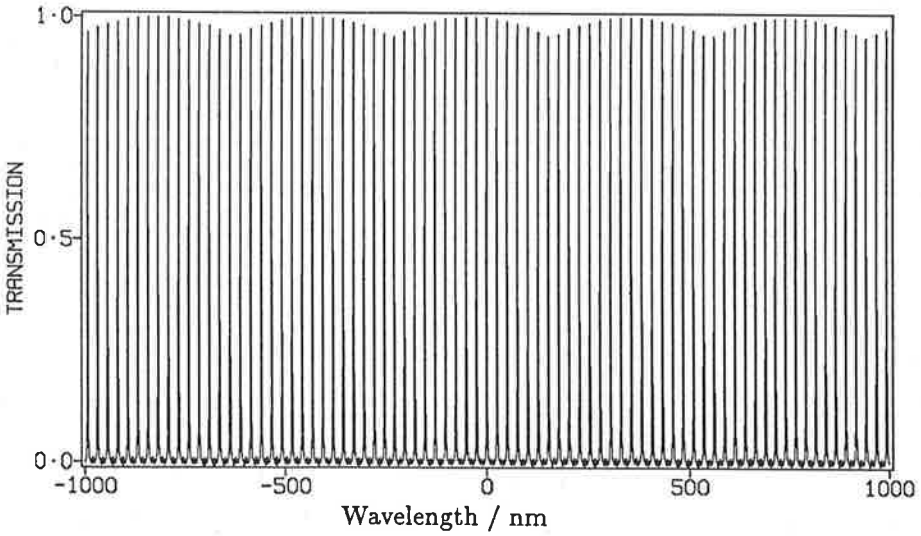

(c)

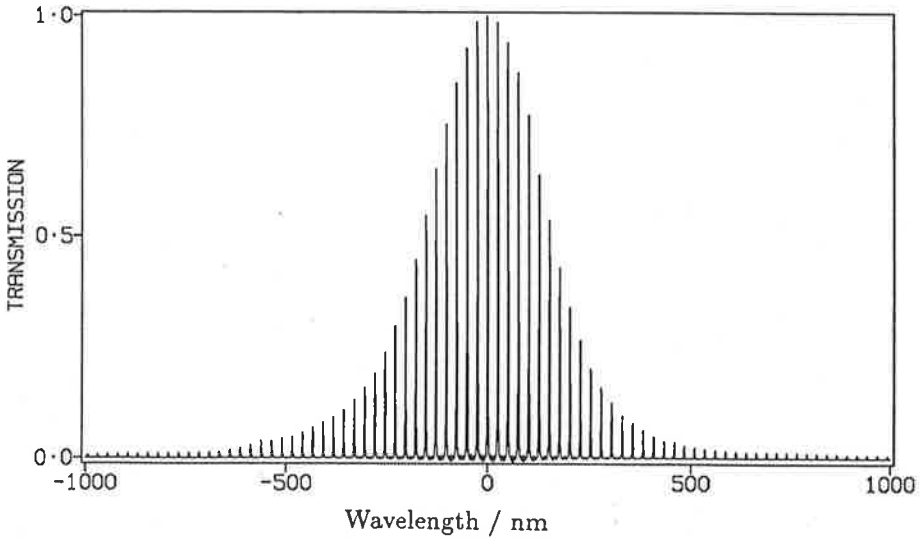

Figure 3.9: A simulation of the high-resolution spectrometer instrument profile at λ 589.6 nm is shown in (c). The profile is obtained by multipling the filter transmission profile, (a), by the high-resolution profile, (b), covering the same wavelength region of approximately two nanometres. The high-resolution profile is obtained from an empirical profile replicated over the required number of orders.

(a)

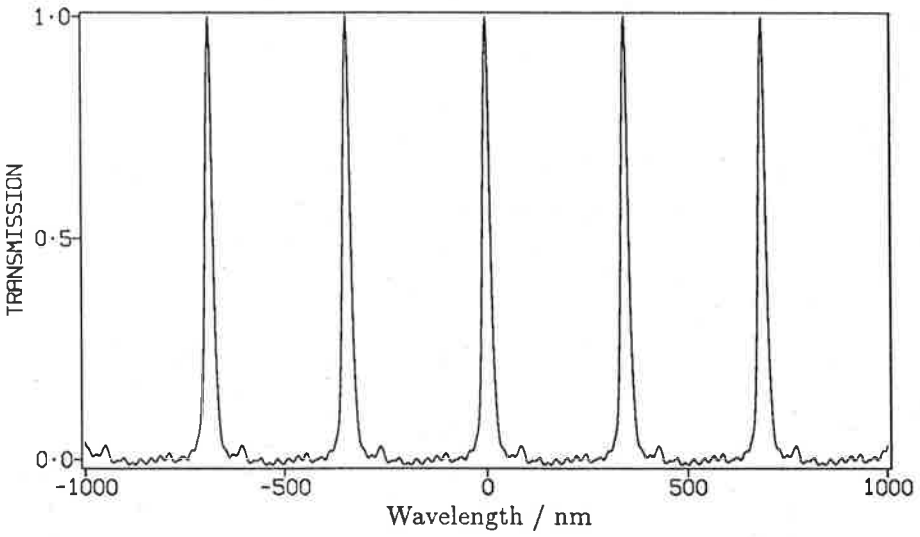

(b)

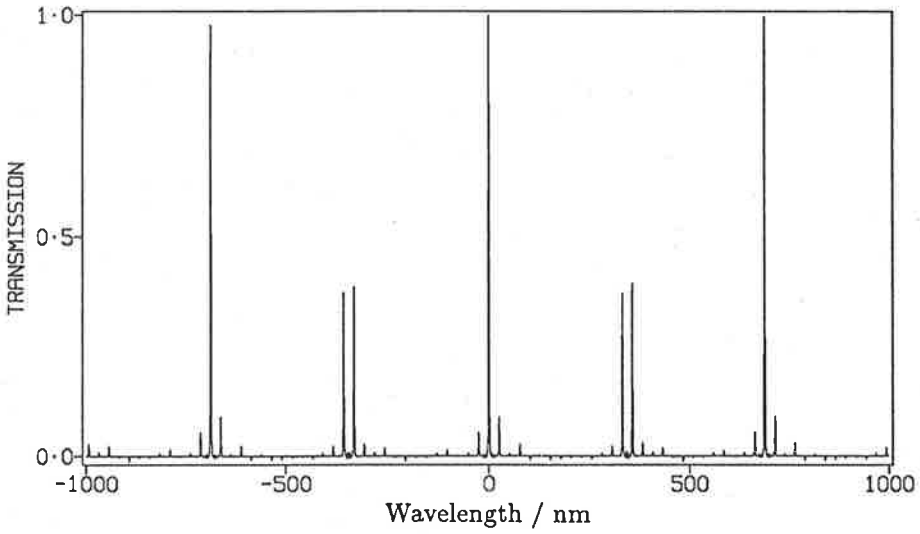

(c)

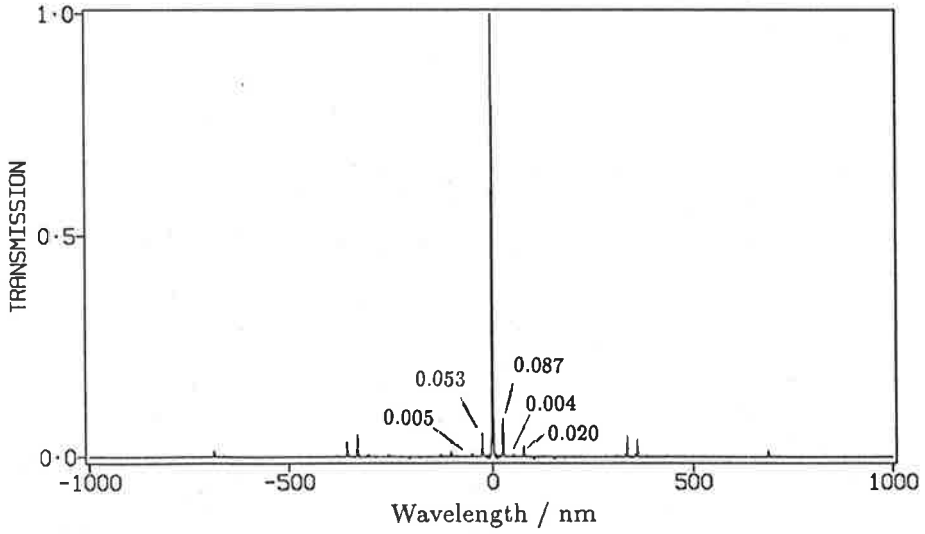

Figure 3.10: A low resolution etalon profile at λ 589.6 nm is obtained by replicating an empirical profile over the required number of orders (a). In (b) the combination of the high and low-resolution etalon profile was chosen to minimize the transmission at the second of the low-resolution passbands. When combined with the filter a simulation of the dual scanning spectrometer instrument profile is obtained, (c). The filter profile and wavelength scale are the same as that used for figure 3.9.

The Mt. Torrens instrument is simpler, incorporating only 2 etalons and a narrow bandpass filter and is similar in principle to the instrument used by Bens *et al.* (1965).

Design of a poly-etalon Fabry-Perot spectrometer involves a compromize between transmission, suppression of ghosts, resolution, and the number of etalons required. Cocks (1977) has recorded the theory and constraints used to design the Mt. Torrens dual scanning spectrometer. Three types of etalon configurations exist: (1) the etalons can be nearly identical as in TESS (Hernandez *et al.* 1981), (2) the etalon spacings can be related by large factors and are known as simple etalon systems as in the Mt. Torrens system or HRDI, and (3) the etalon spacing can be related by small differences as in the PEPSIOS and are known as vernier-compound etalon systems.

For optimum operation the etalons for a simple configuration should be coupled without loss of entendue, $S\Omega$. Thus for a high-resolution etalon of area S_1, field of view Ω_1, and resolvance R_1 and a second etalon with S_2, Ω_2, and R_2

$$\frac{S_2}{R_2} \geq \frac{S_1}{R_1} \tag{3.38}$$

The Mt. Torrens instrument is designed so that $S_1/S_2 = 3/1$. Two lenses of focal length 970 and 300 mm are used to couple the etalons. This approximately fits the criterion for coupling (Hernandez 1986)

$$\frac{f_1}{f_2} = \frac{D_1}{D_2} = \frac{\Omega_2}{\Omega_1}. \tag{3.39}$$

The etalon separations should also fit the criterion

$$\frac{t_1}{t_2} = \frac{D_1^2}{D_2^2}. \tag{3.40}$$

Reflections occur between two or more etalons in a poly-etalon system. These reflections can be removed from the system by slightly off-setting one from perpendicularity to the optical axis or by introducing some absorptance. With the large separation of etalons and lenses in the Mt. Torrens system it has been assumed that no extra reflections occur. The transmission of a perfect poly-etalon system is given by the product of the Airy functions. For an ideal system

with no absorptance

$$I(\lambda) = A_1(\lambda)A_2(\lambda)....A_n(\lambda). \tag{3.41}$$

For a two etalon system, where the ratio of spacers is given by 'a', and using the notation of section 3.1.1,

$$I(\lambda) = \left[1 - \frac{A}{1-R}\right]^4 \left\{\left\{1 + F\sin^2\frac{\delta}{2}\right\}\left\{1 + \frac{F}{2}(1 - \cos(a\delta)\right\}\right\}^{-1} \tag{3.42}$$

where A is the absorptance of the coatings (Hernandez 1986). Equation 3.42 yields plots similar to those given in figure 3.10. The transmission through all peaks other than the desired one is known as white or parasitic light and is given by

$$W = \frac{\int_{-\infty}^{+\infty} I(\lambda)d\lambda - \int_{\lambda_o - \frac{\Delta\lambda}{2}}^{\lambda_o + \frac{\Delta\lambda}{2}} I(\lambda)d\lambda}{\int_{\lambda_o - \frac{\Delta\lambda}{2}}^{\lambda_o + \frac{\Delta\lambda}{2}} I(\lambda)d\lambda} \tag{3.43}$$

For an ideal etalon W = 0. Parasitic light is also described by another ratio called filterage, which for an ideal etalon is 0.5. White light is a function of etalon spacings in the system and wavelength of operation. Minimizing white light can be used as a criterion for determining optimum separation ratios of the etalons. Skinner *et al.* (1987), compared white light ratios for various poly-etalon designs. Consideration of plate defects and a finite reflective finesse leads to broadening of the instrument profile (as for a single etalon) and hence to larger ghosts or a higher white light ratio. The maximum acceptable height of the largest ghost, signal to noise ratio, and expected reflective finesse were used to determine a separation ratio of 10 for the Mt. Torrens instrument (Cocks 1977).

The finite field of view must be considered when choosing the low-resolution etalon order. Equation 3.10 shows the order to be a function of θ. For a dual etalon in the positive lens configuration of the Mt. Torrens system movement across the common aperture causes variation in θ for the two etalons. Thus a misalignment will occur towards the edge of the aperture if etalons are tuned for bandpasses to coincide on the optical axis. This effect can be minimized by increasing the t_2/t_1 ratio by approximately 30% thus broadening the Airy function for the

low-resolution etalon. The separation ratio for the Mt. Torrens instrument was increased from 10 to 13 to allow for this (Cocks 1977).

With the basic design of the instrument fixed the system had to be optimized for observations of the sodium emission. This involved choosing the appropriate order and field stop.

3.3.1 Mt Torrens dual scanning spectrometer for dayglow observations

Figure 3.3 and table 3.1 show the optical layout of the Mt. Torrens dual scanning spectrometer. For dual etalon observations components HR1–4 are replaced by a mirror, LR11. For observations of dayglow emission, a solar profile is required to provide a measurement of background Rayleigh scattered light (see section C.2). The mirror, ST8/LR2, rotates to allow observations of either the sun, through a solar telescope, or sky. Electronic control of this mirror allows automatic scanning of the sun and sky according to a predetermined ratio; for example 18 sky scans for 6 sun scans. The mirror takes approximately 1 scan or 6.4 s to alternate. Micro-switches are used to locate the required position. The periscope and solar telescope are new components in the system. Previous solar profiles were obtained by illuminating a ground glass screen with sunlight. The new periscope has motor driven control of azimuth and zenith viewing directions. The section over the calibration light source extends above the field station roof; it is stored just below the roof and placed in position for observations when required.

The solar telescope mirror, ST1, rotates to maintain an image of the sun on the end of an optical fibre. A heat filter is used to protect the fibre. The mirror, ST1, can be manually tilted to allow for variations in solar declination. Such adjustments are required at approximately weekly intervals. The optical fibre ends near the focal point of an aspheric collimating lens, ST7. The individual fibres are glued to a small conical mount. They, along with the diffusing screen and reflective, non-luminous, white coating within the mount, ensures beam uniformity across the aperture of the etalon to within 10%. The solar telescope is permanently mounted on the field station roof.

A calibration light source, LR3, can be inserted above the low-resolution etalon to allow instrument profiles of the dual system to be recorded. The plane glass window, LR4, isolates the etalon chamber for temperature control. An old etalon was repolished and coated to improve etalon finesse. Similar coatings were used for low and high-resolution etalons. All lenses in the low-resolution section were coated with hard AR coatings. The mirrors ST1, LR1, LR2/ST8, LR7, and LR11 have protected front-surfaced silver coatings with dielectric reflecting booster layers. The solar telescope lenses were not coated because small losses in this section were tolerable.

Individual sections of the dual system can be aligned by adjusting separately the coupling optics, high-resolution etalon and lenses, and low-resolution etalon. By removing mirror LR7 and auto-collimating from the etalon, perpendicularity with the optical axis is obtained. Alignment of lenses and mirrors above LR7 can be checked by placing a point source at the focus of collecting lens LR7 and checking the image position in the periscope hood. Alignment of the complete system is checked by auto-collimation in both directions at the field stop, LR10. Small deviations from alignment can be corrected by repositioning the mirrors LR7 and LR11. When replacing LR11, locating holes are used to ensure correct positioning of the mount. Small adjustments of the mirror within the mount are used for alignment.

3.3.2 Operation of dual scanning spectrometer

The low-resolution etalon is mounted in a heavy bronze support stand designed to ensure both temperature and mechanical stability. This stand is located within a metal chamber which is mounted on springs within another metal chamber. Lenses and glass windows seal the optical path from external air movements allowing both chambers to be temperature controlled. The inner chamber mount, with springs in oil-filled dash pots, is used to damp vibrations. The outer chamber is mounted in a wooden cabinet which is packed with insulation to improve thermal stability. The coupling optics, LR8–LR10, are mounted on the top of the high-resolution

instrument cabinet. All joins in the system are covered with concertinaed black rubber to ensure the whole system is light tight but not mechanically coupled.

Low-resolution etalon parallelism is not servo-controlled. Coarse adjustment of parallelism can be achieved by differential screw threads in the etalon mount. A light source on a table is used to set the etalon approximately parallel before it is placed in the inner chamber. Once inner chamber temperature stability is obtained further fine adjustments of the screw mounts can be made through the lid. The top plate is clamped onto three piezoelectric ceramic tubes. These small ceramic tubes exhibit considerable hysteresis in their movement. The plates are scanned continuously to avoid this. A scan can be paused in any channel while etalon separation is tuned. Final parallelism adjustments must be made while the plates are scanning. Voltages on the ceramic tubes are varied to make required fine adjustments. A fringe-viewing eyepiece is introduced into the beam between LR7 and LR8 to determine if the plates are parallel. Two mirrors and a doublet allow observations of several orders so that a visual assessment of etalon parallelism can be made. When almost parallel, a final tweak of the voltages to maximize the photomultiplier signal at the peak of the passband produces the optimal operating conditions.

Operation of the dual scanning spectrometer is summarized by Cocks *et al.* (1980), and described in more detail by Cocks (1977). To operate the dual-etalon system, the two etalons must be tuned to the correct wavelength and then scanned synchronously. When observing an emission for which a laboratory source lamp is available tuning is achieved by maximizing the signal on a ratemeter when the scan is paused in the required channel. Low and high-resolution etalons should be tuned alternately until maximum transmission is obtained. This procedure should be completed as quickly as possible because hysteresis of the ceramic supports will begin to significantly affect the signal. The final tuning should be checked in a short pause in the required channel.

Cocks *et al.* (1980) describe the method for obtaining scan synchronism. Briefly it involves altering the scan amplitude of the low-resolution etalon until both tuned and detuned scan

spectra have similar shapes. Although checked at regular intervals the scan amplitude did not require significant change. When scanning in synchronism with the high-resolution etalon the low-resolution etalon only covers a small fraction of an order. The high-resolution etalon scan range can be changed by factors of 2. The low-resolution etalon has two scanning ranges — low range for operation in synchronism with the high-resolution, and high range which scans through an order or more. Scans over an order or more are used for instrument assessment. A fine gain control is used for small adjustments required to achieve scan synchronism with the high-resolution etalon.

Alternate 128 or 256 channel observations of the sun and sky can be made. Single profiles of 512 channels can be acquired with approximately 2.5 high-resolution orders of the sodium D1 line.

For dayglow observations the signal count levels are high and analogue detection was used. The photomultiplier anode current was amplified with gains for sun and sky observations set separately and altered from a control unit. Thumbwheels on the control unit were used to set the sun to sky scan ratio.

For alternate observations of the sun and sky, profiles are accumulated in two separate blocks of multichannel analyser memory. If an observing sequence commences with sky observations, accumulated in block 1 of memory, when the required number of scans is complete the acquisition pauses while mirror LR2 rotates for sun observations. The required amplifier gain and memory block are changed when the mirror locates in the new position. Acquisition commences at the beginning of the next scan and the etalons keep on scanning. The analyser steps through a scan in synchronism with the scan voltage generator. The sequence continues, returning to sky observations, when the required number of sun scans is complete.

The above procedure is automated and profiles are accumulated until an adequate signal to noise ratio is obtained. The accumulation can be interrupted at the end of a scan, or preferably, at the end of a frame (a set of sun/sky scans) to assess the accumulated profiles. As for high-

resolution observations, the profiles are recorded on the PC. The control unit counts the total number of sun and sky scans in a sequence. If mishaps occur and for any reason the acquisition and scanning get out of step an alarm sounds.

3.3.3 Optimization for sodium observations

The resolution required for daytime observations was the same as that required for twilight observations. This determines the high-resolution etalon separation and field stop. The high-resolution etalon may therefore be used for twilight observations without any gross change in separation by simply replacing the mirror LR11 with the field stop, lens, and periscope and retuning the etalon.

The low-resolution etalon separation was determined by considering the design value of high/low resolution separation ratio (13), the relative positions of the D1 and D2 passbands, and white light ratio. The filter passband corresponds to approximately two orders of the low-resolution etalon. If one peak is centred in the filter passband, some small transmission of the two peaks on either side occurs through the filter profile wings. To minimize transmission at these peaks the low-resolution order was chosen so that $n' + \frac{1}{2}$ free spectral ranges of the high-resolution etalon corresponded to 1 free spectral range of the low-resolution etalon. This ensured that the high-resolution passband peaks did not correspond with the low-resolution passband peaks in the filter profile wings. This minimized the white light ratio. So that the low-resolution D1 and D2 passbands do not overlap the separation is limited to values defined by equation 3.37. The high-resolution order and free spectral range are known so the low-resolution free spectral range is given by

$$\Delta\lambda_{lr} = (n' + \frac{1}{2})\Delta\lambda_{hr} = (n' + \frac{1}{2}) \times 25.41 \times 10^{-12} m \tag{3.44}$$

which gives

$$m_{lr} = \frac{m_{hr}}{n' + \frac{1}{2}} \tag{3.45}$$

for n' an integer.

This gives two sequences of desired values for m_{lr}. At low orders equation 3.37 need not be so strictly adhered to since the resolution is considerably less; hence the free spectral range of the low-resolution etalon is 5 or 6 times the width of the recorded profile. Values of n of 3.5 or 4.5 are adequate to ensure that the D1 and D2 passbands do not overlap.

Low-resolution order was thus set to 1715, very close to that value determined by $n' = 13$ or n=3.5. This implies that the ratio of separation of high to low-resolution etalons is 13.50.

Observation of a white spectrum through the dual etalon system, with it tuned to the wanted wavelength, allows precise tuning of the narrow bandpass filters. The filter passband can be modified by tilting the filter with respect to the optical axis. This shifts the passband to lower wavelengths but also broadens the passband; Hernandez (1986) gives more quantitative details. The filter mounts are designed to give tilts of up to 5°. The D1 filter was tuned to maximize the D1 emission. Only a small tilt was required ($< 1°$). Over a period of a year or more the filter passband has shifted slightly to lower wavelengths. Such shifts are very small and do not have a significant effect on the instrument function.

3.3.4 Instrument assessment

The low-resolution etalon finesse is difficult to measure because uniform illumination over the whole etalon is required. The illumination used has low output and bright sources are required to obtain finesse measurements even when using the whole etalon area. Reflective finesse measurements using the procedure outlined by Jacka (1984) are impossible as sources sufficiently bright to provide enough illumination over a fraction of the plate aperture are not available. Finesse measurements at λ 633 nm were obtained using a PIN diode detector placed at the focus of LR6. Measurements at the sodium wavelength were made through the high-resolution system as filters are required to isolate the required line from the lamp spectrum. By wedging the high-resolution etalon so that at least one whole order or two or more fringes occur across the high-resolution etalon, the transmission of any wavelength occurs somewhere on the etalon

Table 3.4: Etalon, defect, and reflective finesse measurements for the 50 mm etalon. The values in N_A (1) are from spectrometer measurements, the values N_D (1) are calculated from the etalon finesse measurements assuming the N_A (1) values are correct. The values in N_D (2) are from flatness tests at λ 633 nm and the values N_A (2) are calculated from the etalon finesse measurements assuming the N_D (2) values are correct.

wavelength	730 nm	633 nm	589 nm	558 nm	546 nm
N_E		19 ± 1	22 ± 1		
N_A (1)	24.1 ± 0.5	22.5 ± 1.0	29.2 ± 0.7	26.9 ± 0.6	21.5 ± 0.2
N_D (1)		35 ± 2	33 ± 2		
N_D (2)	36 ± 4	31 ± 4	29 ± 4	27 ± 4	27 ± 4
N_A (2)		24 ± 4	34 ± 4		

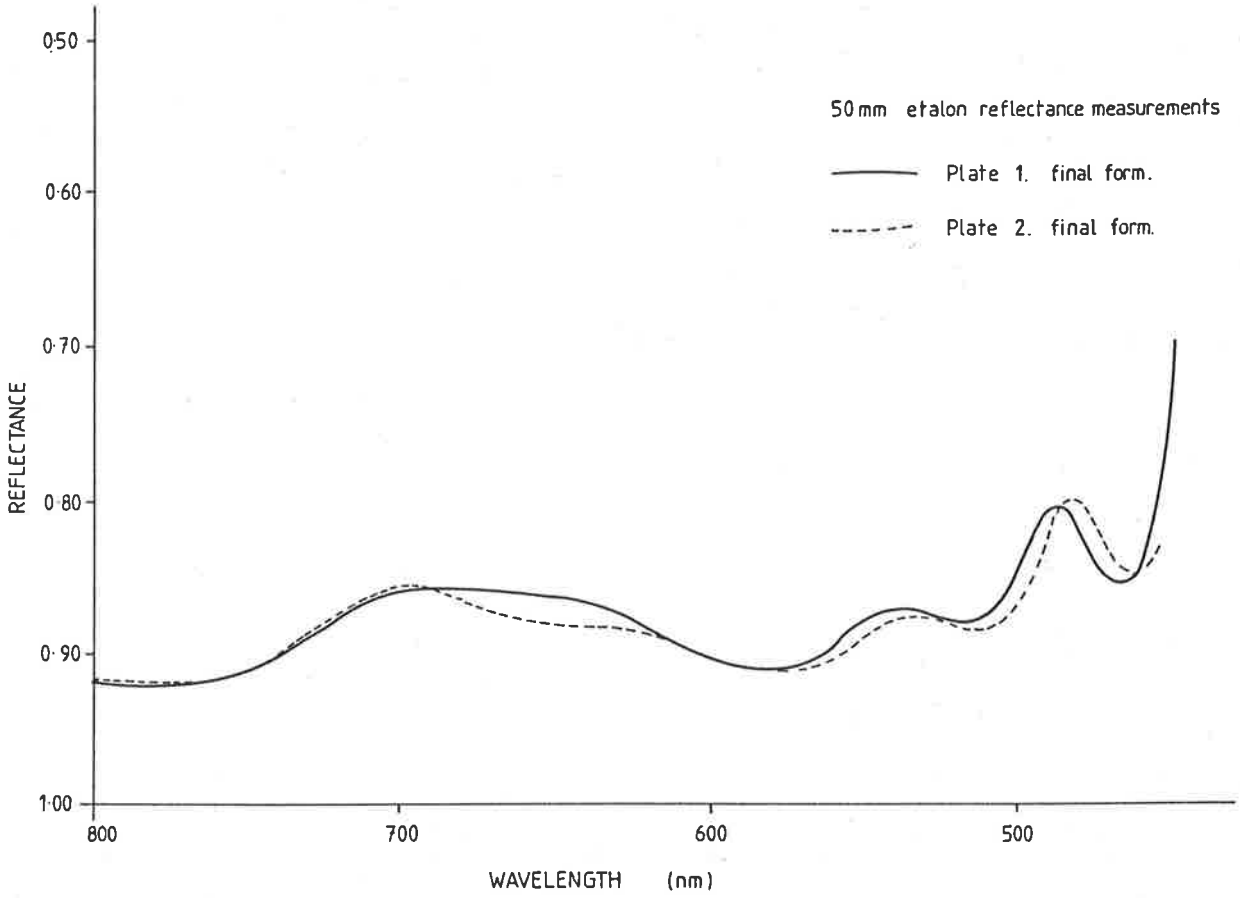

Figure 3.11: Reflectance measurements from a spectrometer for plate 1 (solid curve) and plate 2 (dashed curve) of the low-resolution etalon. The two plates are nominally identical.

transmission varied somewhat across the filter aperture. The filter profile used had a full-width half-maximum of 0.32 nm and was identical to that provided by the manufacturer. Some other measurements indicated wider passbands. The effect of wider filter bandwidths is to increase the transmission through the low-resolution passbands one order from the central passband. The widest measurement obtained, 0.44 nm, produced peaks at the second passbands of the low-resolution approximately twice as intense as those obtained for a 0.32 nm profile. Different filter profiles had a negligible effect on the ghosts in the central passband of the low-resolution etalon. To improve the filter description a white light profile was incorporated to accurately describe the peak of the filter. The white light profile is a dual etalon profile of a white light source through the filter. Incorporation of the white light profile into the filter profile had neglible effect on ghost intensity. The filter profile used is shown in figure 3.9.

High and low-resolution profiles used in the simulation were based on empirical profiles from the instrument and are shown in figures 3.9 and 3.10. An instrument profile for each etalon covering one order was obtained. The order, free spectral range, and width of each channel in picometres were obtained for both etalons from order measurements. This allowed the empirical profiles to be replicated over the required wavelength range. Background noise was removed by averaging counts away from the central passband and subtracting this average from each channel. The apparent variation in high-resolution passband heights seen in figure 3.9 is due to the array size in the simulation limiting the sampling of the high-resolution passband. Each peak should have the same transmission.

The profiles were combined to produce the dual etalon spectrometer profile seen in figure 3.10. The intensity of ghost passbands is also indicated. To verify that the simulated profile was reasonable, a 512 channel profile of the sodium lamp was made (see figure 3.12). The ghosts in the recorded profile can be seen but their intensity is considerably less than that predicted by the simulation. Several causes are possible: the simulation could be wrong; for example the low-resolution finesse could be larger than that of the profile used, the etalons may not be

scanning synchronously, or subtraction of noise from the empirical profile may not be justified. The low-resolution etalon illumination causes very low transmission of the calibration source. A single scan high signal-to-noise laser profile was recorded to check the background correction . The simulation was varied for these conditions but similar results were obtained. Ghost transmissions for the laser profile were 0.03 and 0.02 times the transmission of the central bandpass. The background counts were very low; in some channels no counts were recorded. An example is shown in figure 3.13. Other checks were made. The simulation was found to be fairly insensitive to small changes in the free spectral range of both high and low-resolution etalons. Several low-resolution profiles were used; instrument profiles from both laser and sodium profiles were tried and little variation found. Scanning of the etalons was exhaustively checked using the method described by Cocks, (1977), and the instrument appeared to be working correctly.

In conclusion, lamp profiles show the dual scanning spectrometer to be working correctly and better than predicted. An empirical measurement of the instrument transmission over the full wavelength range of the filter was impossible as both etalons cannot scan over the required distance. However the simulation at least gives a useful idea of the spectrometer passbands.

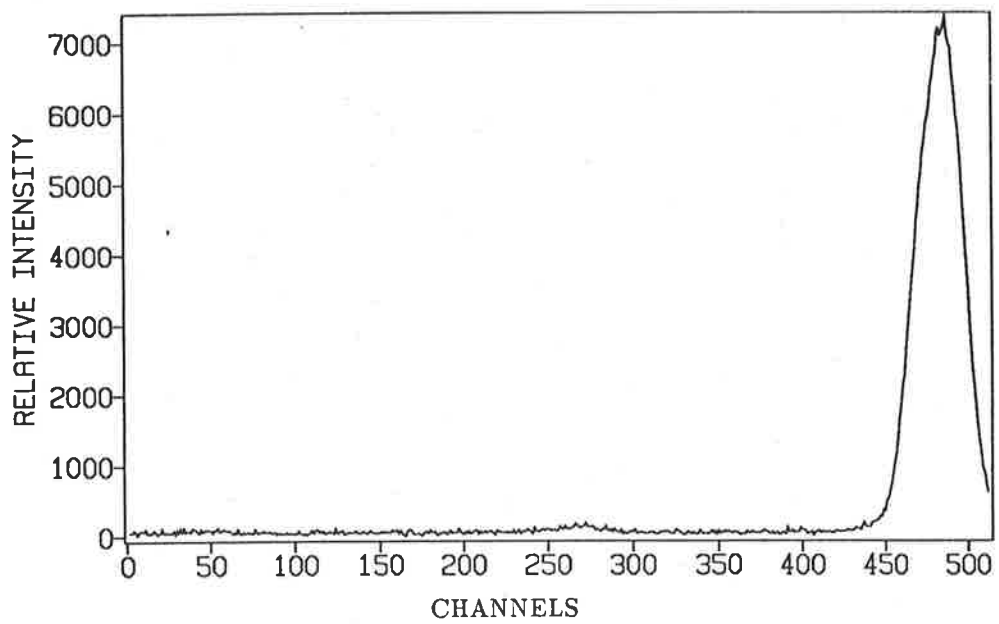

Figure 3.12: A 512 channel dual etalon sodium lamp profile. The first and second ghost peaks can be seen to the left of the main passband.

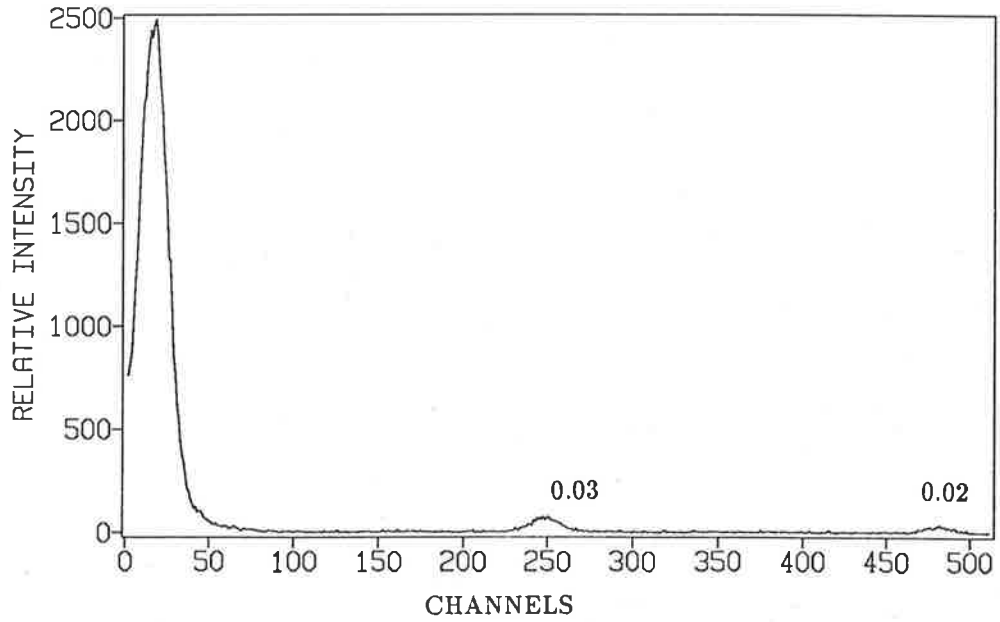

Figure 3.13: A 512 channel dual etalon profile of the HeNe λ 632.8 nm laser. Ghost intensities, relative to the central passband, are shown.

Chapter 4

SODIUM DAYGLOW

4.1 Introduction

Observations of the sodium dayglow emission, using a PEPSIOS spectrometer, have been made at Fritz Peak (40°N, 105°W) by Burnett *et al.* (1975). These measurements were made principally to determine whether diurnal variation in the sodium dayglow intensity inferred from Zeeman photometer studies was present in PEPSIOS observations. However, observations of the sodium dayglow should also allow determinations of winds and temperatures using standard Fabry-Perot analysis techniques (see chapter 5). The major difficulty is isolating the sky emission from the background of scattered sunlight. This is usually achieved by observing the sun and sky alternately and using the direct solar spectrum to estimate the Rayleigh scattered background in the sky spectrum. A suitably normalized solar spectrum, when subtracted from the sky spectrum, gives the emission feature and another contribution from the sky called the Ring effect. Figure 4.1 shows the emission feature, obtained by subtracting the sun profile from the sky profile, from PEPSIOS measurements (Burnett *et al.* 1975). The sodium dayglow emission feature is obvious in the sky spectrum.

The principles of dayglow observation and dayglow measurements of both the oxygen λ 630 nm and sodium D emissions are presented in more detail in appendix C. The remainder of this

(a)

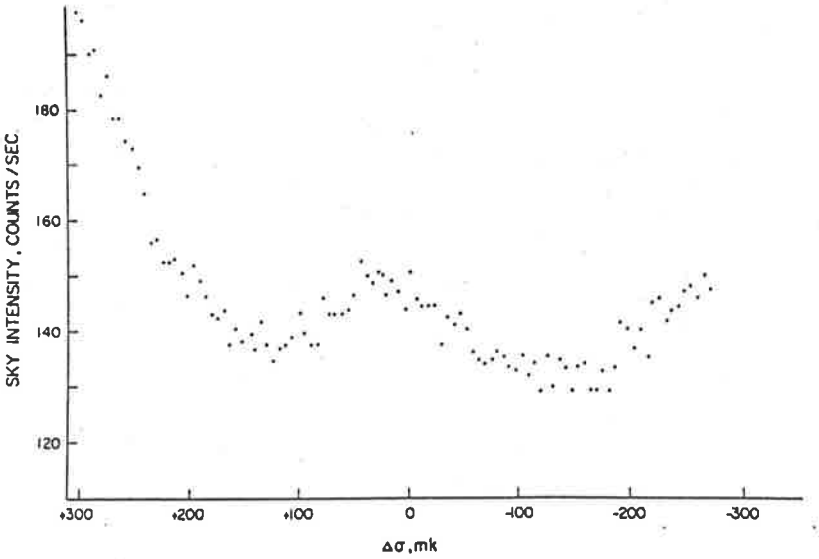

(b)

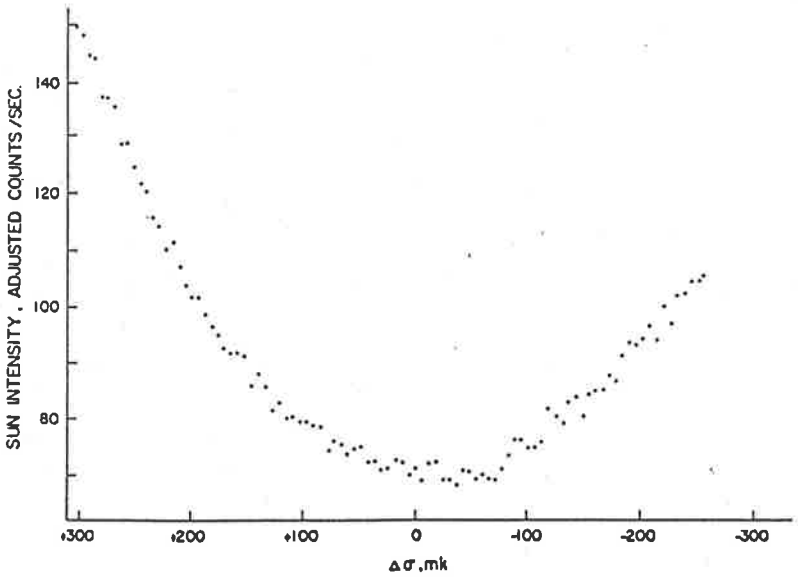

(c)

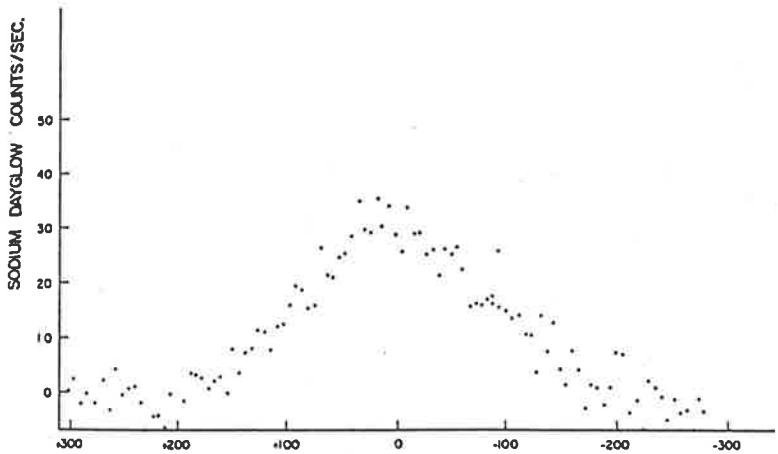

Figure 4.1: Isolation of the sodium D2 emission from the daytime sky spectrum using PEPSIOS observations (Burnett *et al.* 1975). The emission feature is clearly visible in (a), the sky spectrum. On subtraction of (b), a normalized solar spectrum, the emission feature is obtained (c).

chapter discusses attempts to observe the sodium dayglow using the dual scanning FPS at Mt. Torrens.

4.2 Mt. Torrens dayglow observations

Figure 4.2 shows a sun and sky pair of observations made with the Mt. Torrens dual scanning spectrometer. The profiles were obtained near 0230 LT on DOY 063, 1987. 256 channels, or approximately 30.7 pm, centred on the D1 line were scanned with 12 sky and 12 sun scans made alternately until 72 scans of each were obtained. About 15 minutes were spent acquiring each profile. The general shape of the spectrum is influenced by the filter profile which can be determined from the spectrum of a white light source. The white light spectrum is flat over the wavelength range of the scan. Figure 4.2 also shows a white light spectrum recorded during the observing period — the effects of the filter can be seen. No emission feature is obvious in the sky spectrum.

The D2 emission is approximately twice as intense as the D1 emission. No emission feature was visible when the instrument was configured to observe the D2 line. Most observations were made of the D1 emission as the D2 filter available had a bandpass centred too low to be useful for dayglow observations. The effect of a displaced filter passband on the instrument profile would be to increase greatly the ghost transmission at the second, off-centre, low-resolution passband in figure 3.10.

The example presented in figure 4.2 is typical of those obtained on many days. A polarizer was incorporated to improve background rejection. Pausing the scan near the beginning of a profile, away from the emission line, and setting the polarizer to minimize counts for an observing direction at 90° to the sun, should improve the sky emission/background intensity ratio but no emission feature was visible when this was done. Acquiring data over a longer time period also had no apparent effect.

Subtraction of the sun profile from the sky profile did not reveal any obvious structure

(a)

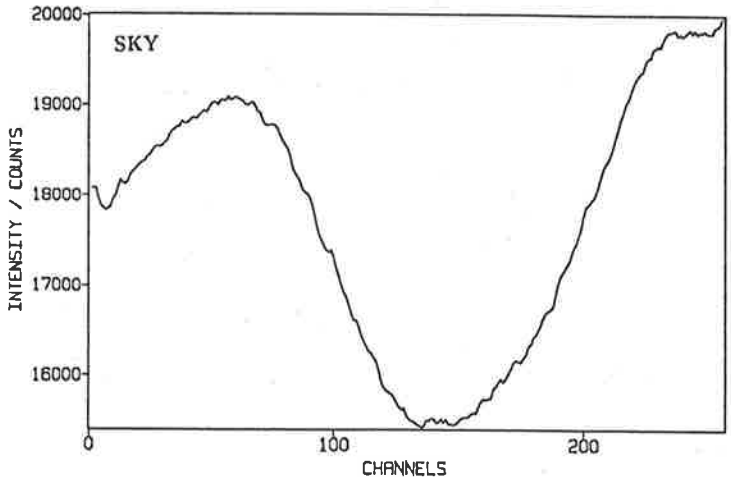

(b)

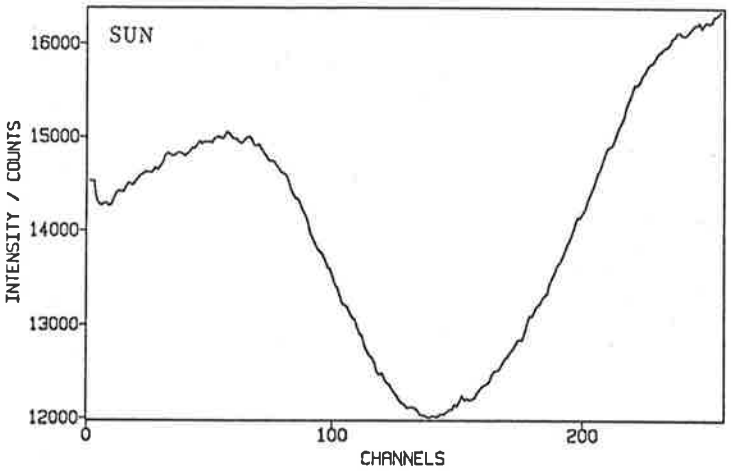

(c)

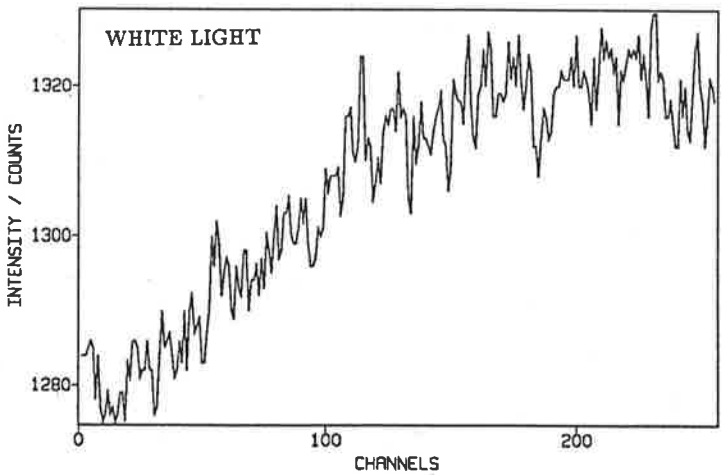

Figure 4.2: Sky (a) and sun (b) profiles obtained on DOY 063, 1987, with the Mt. Torrens dual scanning FPS. No emission feature is visible in the sky profile. The general shape of the spectrum is influenced by the filter profile illustrated by the white light spectrum (c).Both sun and sky profiles were from 72 scans of 256 channels, acquired with a dwell time of 50 ms per channel.

(a)

(b)

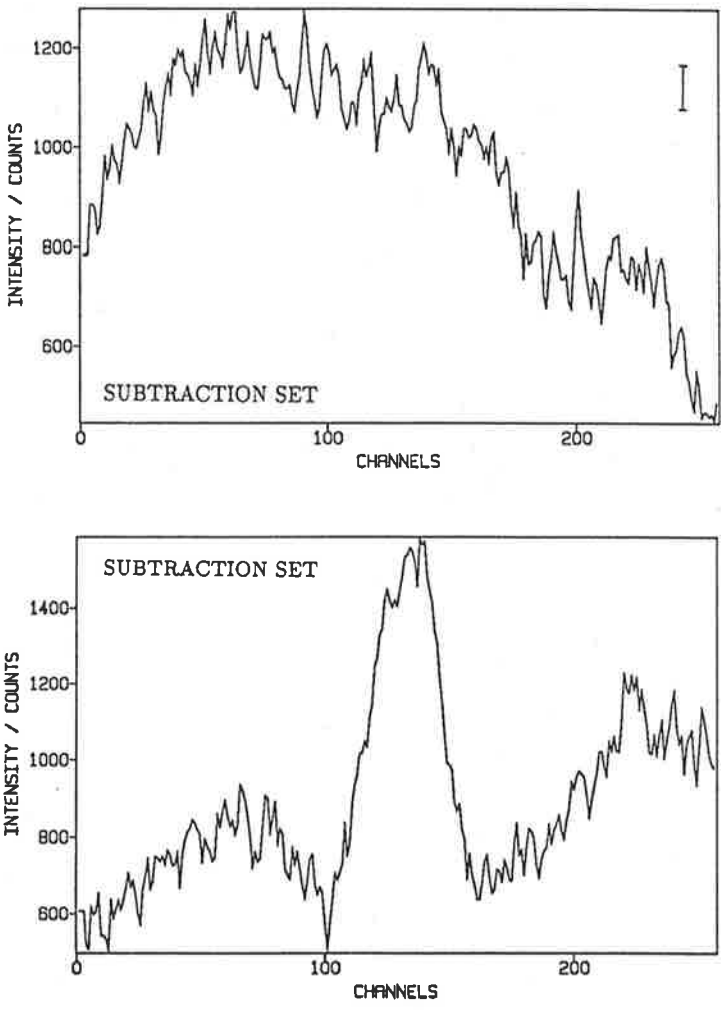

Figure 4.3: Sky – normalized sun profiles. (a) is the subtraction set from the profiles in figure 4.2 and (b) from a profile in which the hollow cathode lamp was superimposed on the sky profile using a glass beamsplitter. The small bar in the top right-hand corner of (a) indicates the expected intensity from twilight measurements.

in the subtraction set — an example is given in figure 4.3. These results were obtained by subtracting a normalized sun profile from the sky profile. In two groups of channels, away from the emission feature, a sun/sky ratio was found and the average of this ratio used to normalize the sun profile. This is a fairly crude method but does allow more detail in the spectrum to be resolved. To check that the subtraction was adequate, the scaling was varied to produce several subtraction sets — no emission feature was apparent in any of these. However, if the normalization factor is too large or too small a positive or negative contribution from the sun profile will be present.

As a check on all procedures a sodium lamp signal was superimposed on the sky signal by using a sheet of glass as a beamsplitter in front of the periscope. The lamp contribution was clearly visible in the sky spectrum and on subtraction the lamp spectrum was superimposed on the background structure. Figure 4.3 shows such a lamp profile obtained soon after those shown in figure 4.2.

The expected intensity of the dayglow emission can be estimated by using dual scanning FPS observations through twilight. The dayglow intensity is two or three times the twilight intensity for a given sodium abundance (Chamberlain 1961). The exact value depends on the Earth's albedo and the solar and observing zenith angles. The albedo of the Earth near Mt. Torrens would be low as the surrounding land use, for some distance, is mainly grazing and dryland cropping. Snow is very rare and never lies on the ground for more than a few hours. Thus the noon dayglow intensity would be approximately twice the twilight intensity— a value similar to that obtained experimentally by the PEPSIOS dayglow measurements (Burnett 1975).

A twilight profile obtained with the dual scanning system is shown in figure 4.4. The instrument was used to observe through twilight and a profile recorded every 25 scans. Three profiles similar to that shown in figure 4.4 were obtained at both dusk and dawn on DOY 063. The average peak count rate was 16 counts when the region of the scan away from the emission line was used to define the background value. Thus for a sky profile of 72 scans, assuming a

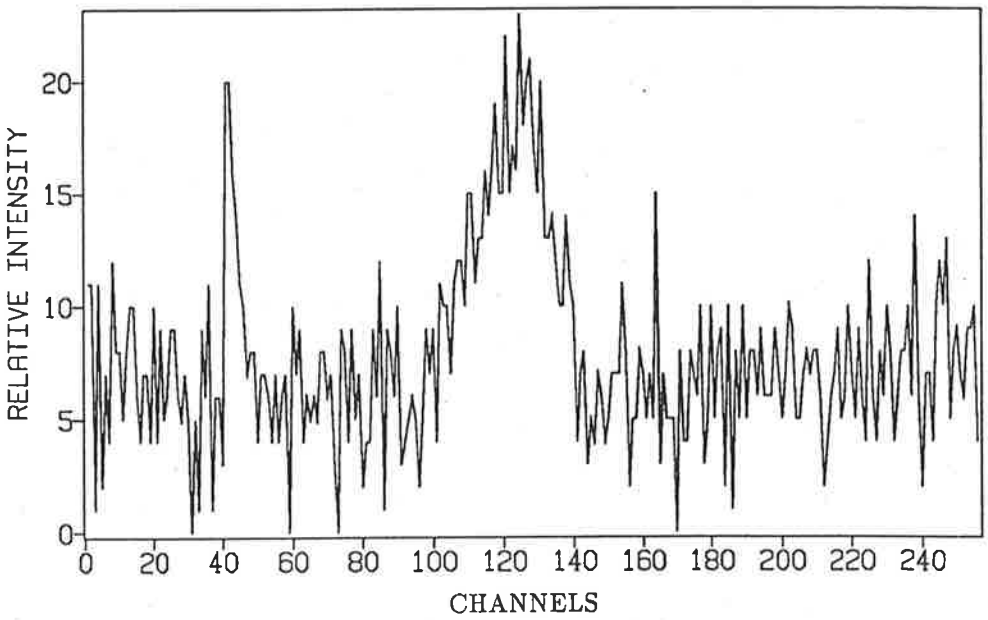

Figure 4.4: A twilight profile, from dawn on DOY 063, using the dual scanning FPS. The profile presents 25 scans of 256 channels acquired with a dwell time of 50 ms/channel.

dayglow/twilight intensity ratio of 2, a peak count of about 90 counts would be expected. This is indicated by a bar in figure 4.3. An emission feature of this size would be obscured by noise in both the sky spectrum and the subtraction set.

4.3 Conclusions

The emission feature could be isolated if an increase by a factor of 4 or more was obtained in the signal intensity. A new filter allowing observations of the D2 emission would immediately provide twice the signal intensity. Observing at 90° to the sun with a polarizer set to minimize the background transmission would allow further improvement.

Parasitic light appears to be a problem with the current instrument because a large range of signal intensity is obtained over the scan range. The PEPSIOS profiles, scanned over a range of approximately 21 pm, had background count rates, at the extremes of the profile of three times the emission intensity. The Mt. Torrens background count rates are much larger than this, indicating a considerably higher contribution by parasitic light. Decreasing parasitic light, by using a three period rather than a two period filter, would give an improvement in the

signal/background intensity ratio. A three period filter has a sharper wavelength profile with less transmission in the wings of the profile.

The sodium Fraunhofer line is very deep (96% of the continuum is absorbed) and the width is about 20 pm. Pressure broadening considerably increases the wings of the absorption profile. It is not possible to scan the whole profile with the Mt. Torrens spectrometer. The scan needs to be sufficiently wide that a region with no contribution from the emission line in the sky spectrum, or the telluric absorption line in the sun spectrum, can be used to normalize the solar profile. Normalizing the sun profile by using the slope of the edges of the profile, with an allowance for the Ring effect, would improve the subtraction procedure.

Observations of the sodium dayglow emission would allow temperatures and winds, from the sodium layer height, to be studied. With the improvements mentioned above it should be feasible to isolate the emission from the sky spectrum thus allowing studies of longer time sequences than those permitted by twilight measurements. This is important for studying waves and tides in the mesopause region.

Chapter 5

TWILIGHT SODIUM OBSERVATIONS AND ANALYSIS

5.1 Twilight observations

The λ 589.0/589.6 nm sodium emission is excited by resonant scattering of sunlight. During twilight this emission may be observed with minimal contamination by sunlight Rayleigh scattered from the lower atmosphere. The duration of twilight observations depends on latitude and time of year. At Mt. Torrens, 35° S, 139° E, twilight observations can be made for 15–20 minutes.

The high-resolution Fabry-Perot spectrometer was made operational in December, 1985. Twilight observations were then made whenever possible. More data were obtained in Summer months as the sky is more often clear then. More dusk than dawn measurements were made as the field station, in the Adelaide Hills, often becomes cloud covered after dusk.

The night-time intensity of the photochemical emission is very low; this, coupled with scattering of light from sodium street lamps in Adelaide and nearby towns, makes night-time observations useless at Mt. Torrens.

Table 5.1 lists days on which data were obtained during twilight and the type of observations

made. Cardinal point observations, at a zenith angle of 60° in the north, south, east, and west, allowed more observations in a single twilight because sunset, and the required conditions for observations, occurs in the east about 15 minutes prior to sunset in the west. Zenith observations were made to obtain a clearer understanding of twilight progression. All data except those on days 062, 072, and 083, 1986, were from observations of the D1 line. The D2 emission is more intense than the D1 emission but the only D2 filter available had a peak passband approximately 0.1 nm too low so the instrument transmission for that line was lower than for the D1 line.

Table 5.1: Twilight observations. The days on which observations were obtained are indicated by the day of year in the appropriate column.

year	month	dusk		dawn	
		zenith	cardinal	zenith	cardinal
1986	Jan	005,006,008,009, 025,026,027	022,028,029	005,006	022,027,028
	Feb	054,056,057	042,051,052	054	042
	Mar	063,072,085	062,070,082,083	062,063	079
	Apr	091	099		090
	May	128,132	133		
	Jun		153,154		153
	Jul				
	Aug				
	Sep				
	Oct				
	Nov	324,325,326,328		325,326,328,331	
		331			
	Dec	337			
1987	Jan	013,015		015	
	Feb	035,036,037,056	040,043	035,036,037,056	040,043
	Mar	069,083		069,083	
	Apr	114		114	
	May				
	Jun		158		158
	Jul		182,184,186,187, 188,189		184,186,187,188
	Aug				
	Sep		245,253,254,258, 259,260,264		253,258,259,260, 264,265
	Oct		274,275,298		275,298
	Nov		331		331
	Dec		346,347,351,355, 363		346,347,355,363

The remainder of this chapter discusses the analysis and interpretation of the twilight data. Temperature and wind results from twilight observations will be presented in chapters 6 and 7.

5.2 Analysis

The source profile for the sodium emission is not a simple Gaussian curve. The D1 line has 2 × 2 and the D2 line 2 × 3 hyperfine components. In the D1 line the two groups of hyperfine

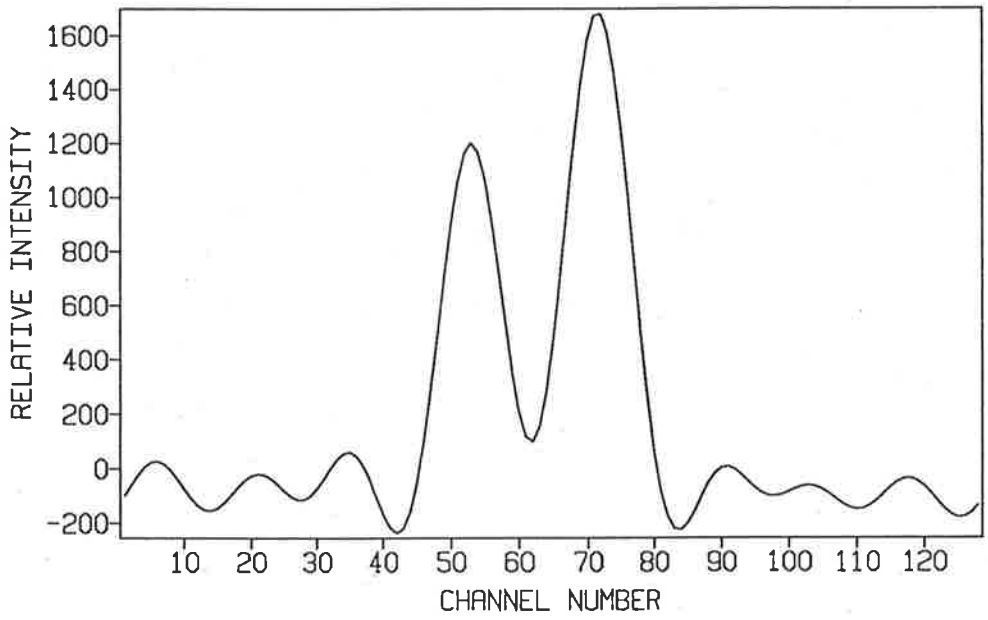

Figure 5.1: The source profile of a sodium emission profile from DOY 063. The instrument function, calculated from a mercury lamp profile, has been deconvolved from the recorded spectrum to produce a source profile. Analysis of this profile gave an estimated temperature of 178 K. The high frequency components in the curve are a result of truncation in the Fourier transform domain during deconvolution.

components are separated by about 2.1 pm and each group is 0.2 pm wide (very small compared to the Doppler width). In the D2 line the 2 groups are separated by about 2.1 pm and each group is 0.1 pm wide. Table 5.2 (Chamberlain, 1961) gives further details. If the instrument profile is deconvolved from the recorded profile the hyperfine components appear as two Gaussian curves as in figure 5.1. The positions of the peaks of the two Gaussian curves contain the wind information and the width of each Gaussian curve the temperature. To extract this information the source profile can be represented as the convolution of a Gaussian curve at the temperature of the emission and a combination of delta functions. These delta functions are the sodium profile at zero Kelvin. Figure 5.2 illustrates this description.

The analysis schemes used follow the general principles for analysis of a simple Gaussian emission line as described by Wilksch (1975). Computer programs required for this analysis were available. A least-squares fitting routine is used to fit a Gaussian curve to the source spectrum in the Fourier transform domain. Noise is removed by truncation of the noise dominated

Table 5.2: Wavelengths and wavenumbers of the two sodium D lines. The deviations of the hyperfine structure from the line centre and the relative intensities of each component are given.(Chamberlain, 1961)

	ν_0 m^{-1}	λ_0 (nm)			ν_0 m^{-1}	λ_0 (nm)	
D1	1695.6	589.59231		D2	1697.3	588.99531	
	$\Delta\nu$ m^{-1}	$\Delta\lambda$ (pm)	I		$\Delta\nu$ m^{-1}	$\Delta\lambda$ (pm)	I
D1	-2.62	0.9107	5	D2	-2.39	0.8291	1
	-1.98	0.6883	5		-2.27	0.7632	5
					-2.07	0.7181	14
	3.29	-1.1437	1		3.45	-1.1969	2
	3.93	-1.3661	5		3.52	-1.2211	5
					3.64	-1.2628	5

components of the Fourier transform. Temperature is estimated using equation 3.26. For the temperature to be interpreted as the atmospheric temperature it must be assumed that the emitting species is in thermal equilibrium with the dominant neutral species. This assumption is certainly valid for the twilight sodium emission, which is produced by resonant excitation by sunlight. The line-of-sight component of the wind velocity, v, in the height region of the emission can be determined from the Doppler shift of the line from the rest wavelength, λ_0, using

$$v = c\frac{(\lambda - \lambda_0)}{\lambda_0}. \tag{5.1}$$

It is necessary to allow for the hyperfine structure in the sodium emission profiles in determining both the temperature and velocity.

Initially two methods of analysis were examined. In the first method the sodium profile at zero Kelvin was convolved with an empirical instrument profile. This combined profile was deconvolved from the recorded profile yielding a Gaussian curve, the location and width of which estimate the wind and temperature of the emitting region.

In the second method, the instrument profile was deconvolved from the recorded profile and

five parameters were fitted to the source profile: two peak positions, two intensities, and one temperature. In a trial analysis of three twilight data sets, the average separation between the two fitted Gaussians was 2.2 ± 0.1 pm and the average ratio of the two intensities was 0.6 ± 0.1. These values are in agreement with those from Chamberlain (1961).

These two methods require knowledge of the instrument function. A ^{198}Hg λ 546.1 nm lamp profile was recorded regularly during observing sessions. The Airy functions at λ 546 nm and λ 589 nm can be calculated given a value of reflective finesse. If the Airy function at λ 546 nm and the Hg source function are deconvolved from the lamp profile then convolution with the Airy function at λ 589 nm gives the instrument function at that wavelength.

In 1987 a hollow-cathode sodium lamp was obtained. These lamps produce low temperature and pressure emission profiles with little self-absorption occurring in the emission. Since then FPS profiles of the hollow-cathode lamp emission have been recorded during observation periods. The lamp operates at a temperature of about 400 K. Another analysis procedure was developed to use information available from the lamp profile.

If a source Gaussian curve of the correct temperature is deconvolved from the lamp profile the remaining profile, the sodium $*$ instrument profile, is a convolution of the instrument profile and the sodium profile at zero Kelvin. The sodium profile at zero Kelvin contains the necessary information about the sodium hyperfine structure. A Gaussian curve, convolved with the sodium $*$ instrument profile, is fitted to the raw data following the procedure developed by Wilksch (1975). The temperature and wind information are obtained from the fitted Gaussian curve. Figure 5.2 illustrates this analysis.

Two major advantages arise from having a lamp at the wavelength of the observations. When calculating the emission temperature the instrument profile at the wavelength of the observation is required. For observations of the λ 558 nm and λ 630 nm oxygen emissions lamps are not readily available as the emissions involve forbidden transitions. This is usually overcome by using a nearby emission line and measuring the values of reflective finesse at the

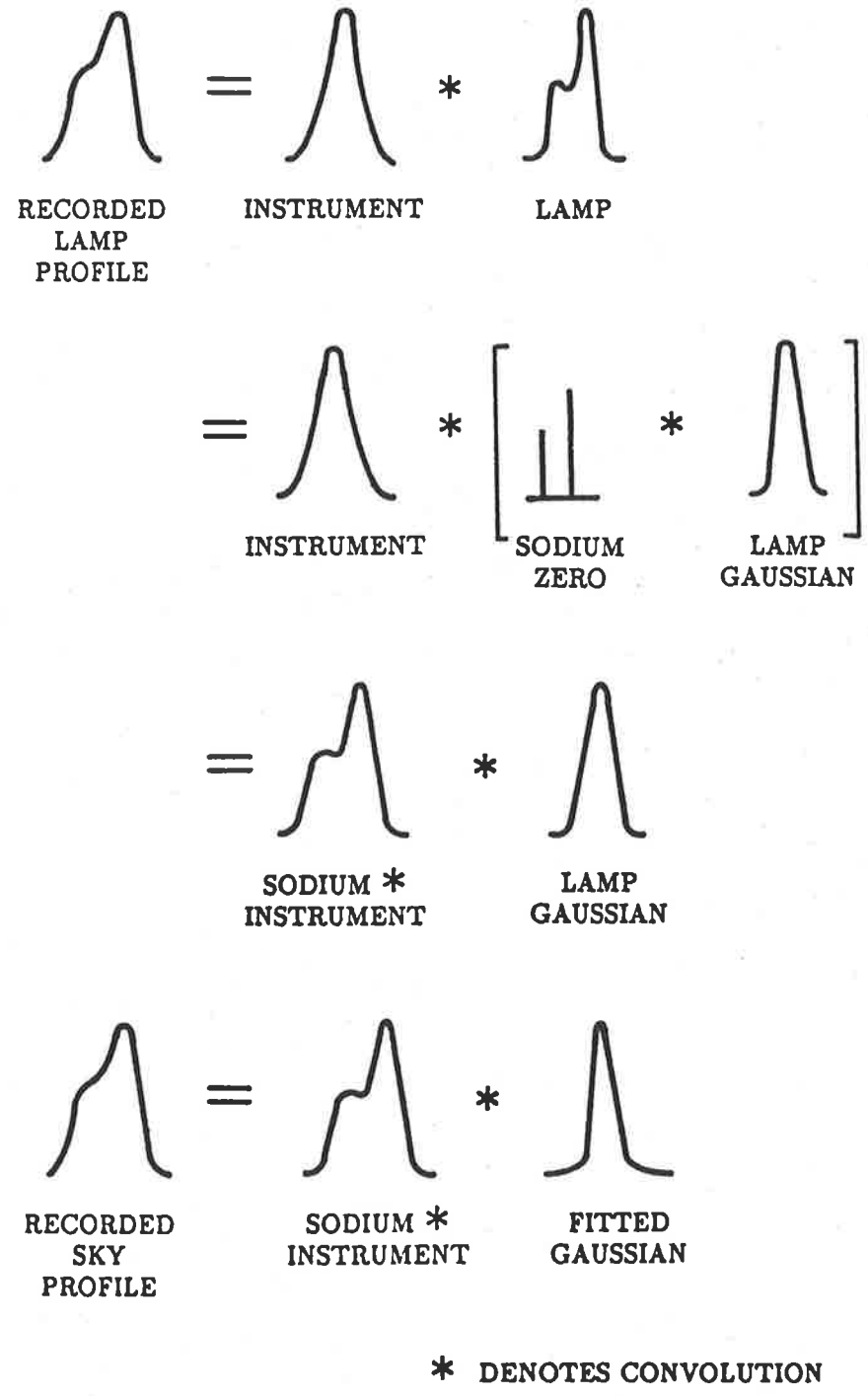

Figure 5.2: Schematic representation of the analysis procedure. The asterisk denotes convolution. The recorded lamp profile is a convolution of the instrument profile and the lamp profile. The recorded sky profile is the convolution of the instrument profile and the sky sodium profile. In both cases they may be expressed as a convolution of the sodium $*$ instrument profile (at zero kelvin) and a source profile. The parameters of the Gaussian curves contain information on temperature and velocity of the source; they are adjusted for best fit with the recorded lamp and sky profiles.

observing wavelength and at the wavelength of a calibration source as described above. The difficulty with this procedure is in obtaining accurate values of reflective finesse. By having a laboratory source of the line under observation such difficulties are removed. The second advantage arises when calculating the wind from the Doppler shift of the emission line. When no laboratory source is available the rest wavelength is usually determined from a mean of zenith measurements made throughout the observing period. This assumes that the average vertical velocity is zero. Such assumptions are not necessary when the rest wavelength can be determined from a laboratory source.

The third method, as well as having the advantages of the lamp at the operating wavelength mentioned above, also uses an empirical measurement of the hyperfine structure. This removes uncertainties in the order and channels per order measurements required in calculating the sodium profile at zero Kelvin. Also, by not deconvolving the instrument or sodium * instrument profile from the recorded profile, more stability in the analysis was obtained. The fitting was done in the Fourier transform domain and only those parts of the spectrum where the signal greatly exceeds the noise were used. The Fourier transform of the sodium profile at zero Kelvin is a very broad function. When deconvolving, division by the Fourier transform occurs. This, combined with noise truncation, can give misleading high frequency components which make fitting the required function difficult.

5.3 Simulation

All analysis routines were checked using simulated data. Lamp and instrument profiles were constructed from simulations of the component parts illustrated in figure 5.2. The relative intensities and separation of the hyperfine components, from table 5.2, were used to simulate a sodium profile at zero Kelvin. A source Gaussian curve of the required width was calculated and the profile shifted to simulate a Doppler shift. The instrument profile does not have a simple analytic description being essentially determined by the defect function which is not

necessarily symmetrical. For these simulations the instrument function was arbitrarily chosen to be a Gaussian shape and the width set to approximately the width of the source function. By convolving the Gaussian and sodium * instrument profiles and adding noise a simulation of a recorded sodium data profile was generated.

Noise was produced in digital acquisition by the variations in time of the dark current of the photomultiplier. This did not have a simple analytic form which could be easily simulated. Two techniques of noise simulation were investigated; neither gave very satisfactory results. Initially noise was generated using a Poisson noise generator. This required a background component to be added to the profile so that the counts in each channel were of the same order of magnitude and the noise contribution was similar for all channels. The second type of noise was generated using a random number generator. The problem with both techniques was that temperatures calculated were slightly larger, on average, than expected. The expected temperature was within the error limits on the temperature returned by the analysis. Running the simulations without noise gave the exact result. Although not ideal, the results obtained with the noise described above were considered adequate.

Simulation runs with various signal-to-noise ratios were completed for the initial analysis methods. As expected simulated profiles with higher signal-to-noise ratios gave smaller errors in estimated temperatures and velocities. This was not pursued further because for twilight observations the available time is the limiting factor.

In the discussion which follows references to temperature calculations will generally be made because temperature was the most sensitive parameter in the fitting routine.

The significance of the third analysis method lies in use of the lamp profile to describe both the instrument function and hyperfine structure of the sodium emission. Empirical lamp profiles are used and so effects of noise in these profiles were investigated. Two parameters were used to describe noise: the number of components in the Fourier transform of the lamp profile, and the signal-to-noise ratio. In the simulation a lamp profile was used to analyse a recorded profile.

Figure 5.3(a) shows how the estimated temperature varied (from an actual value of 200 K) for different signal-to-noise lamp profiles. Noise was generated using the internal random number generator on a VAX-VMS computer. Means of 15 simulation runs for each signal-to-noise ratio were used to calculate the values plotted. In the analysis the profile is truncated in the Fourier transform domain to where the power is less than the average high frequency noise power. Thus only a certain number of components of the Fourier transform are used in the fitting procedure. Figure 5.3(b) shows how the estimated temperature varied when a different number of components of the lamp profile were used.

From the figures it can be seen that at least 8 components and a signal-to-noise ratio of at least 100,000 are required. These two criteria are not independent. Analysis of a series of empirical lamp profiles showed that profiles of at least 2 minutes duration fulfilled these criteria.

In the lamp analysis a source profile is removed from the recorded lamp profile to give the sodium * instrument function. The source profile is calculated assuming a lamp temperature and a Gaussian emission line profile. The current used to drive the hollow-cathode lamp determines both the intensity of the emission and the temperature at which the lamp operates. To obtain sufficient counts in a reasonable time the lamp is usually run with a current of 5 mA and a profile is accumulated for two or three minutes. At this current the lamp runs at approximately 400 K. In a simulation the lamp profile was generated assuming a certain temperature, 400 K. When analysing another profile the assumed lamp temperature was varied. The effect of variation in lamp temperature on the estimated temperature of the analysed profile is shown in figure 5.4. A simulation run using noise shows the noise effects described above. Averages of 15 simulations, ignoring profiles with $\chi^2 > 5$, were obtained. A run without noise confirms that, for each degree of assumed lamp temperature departure from 400 K, the temperature inferred from the data profile changes by one degree.

Two steps were taken to minimize the effects of uncertainty in the lamp temperature. First the lamp temperature was determined as accurately as possible and second a single lamp profile

(a)

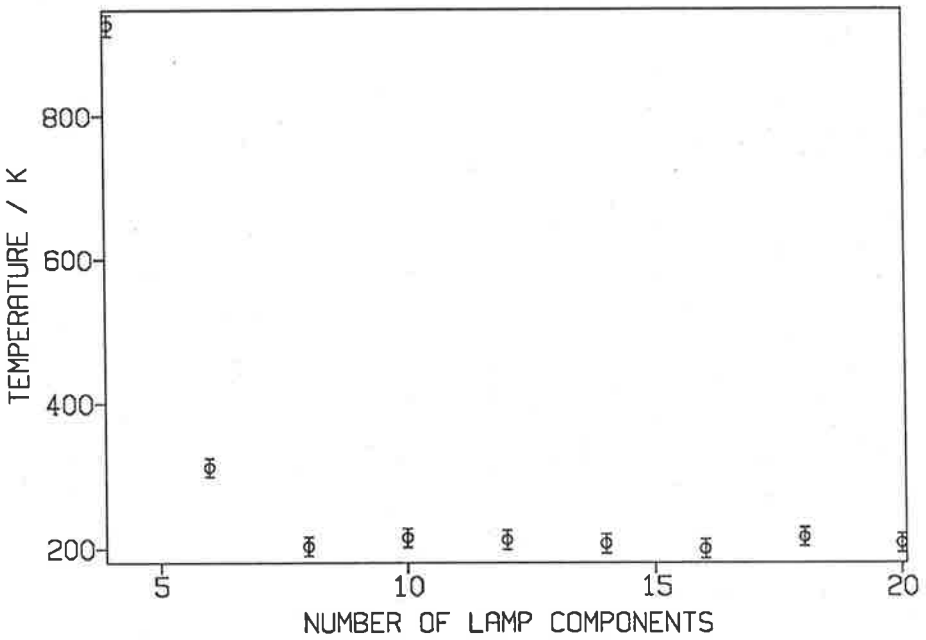

(b)

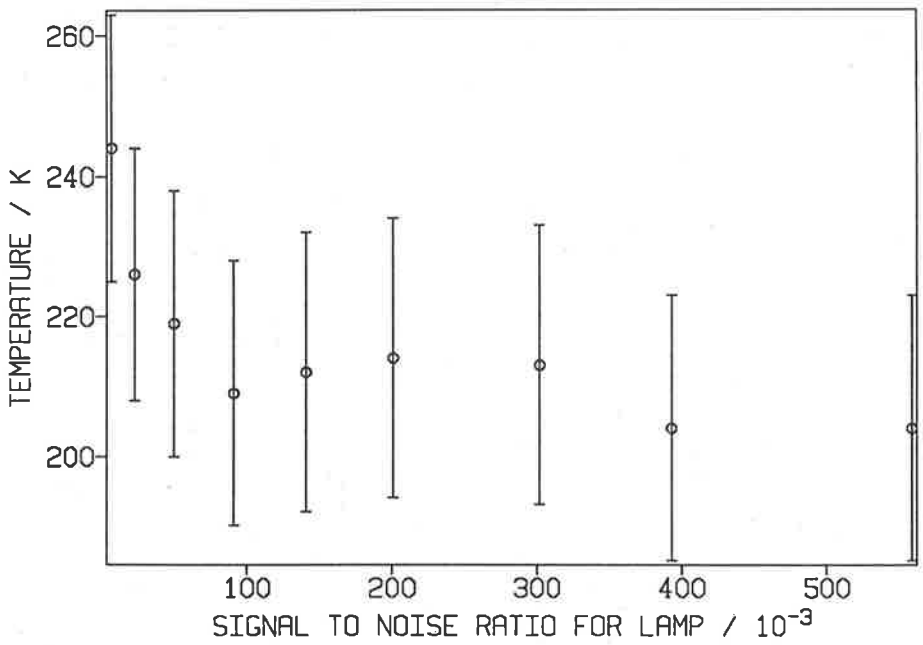

Figure 5.3: Estimated temperature of a simulated profile as determined by analysis with a simulated lamp profile. In (a) the number of components in the Fourier transform of the lamp profile was varied. In (b) the signal-to-noise ratio for the lamp profile was varied. In both cases the actual temperature of the profile was 200 K.

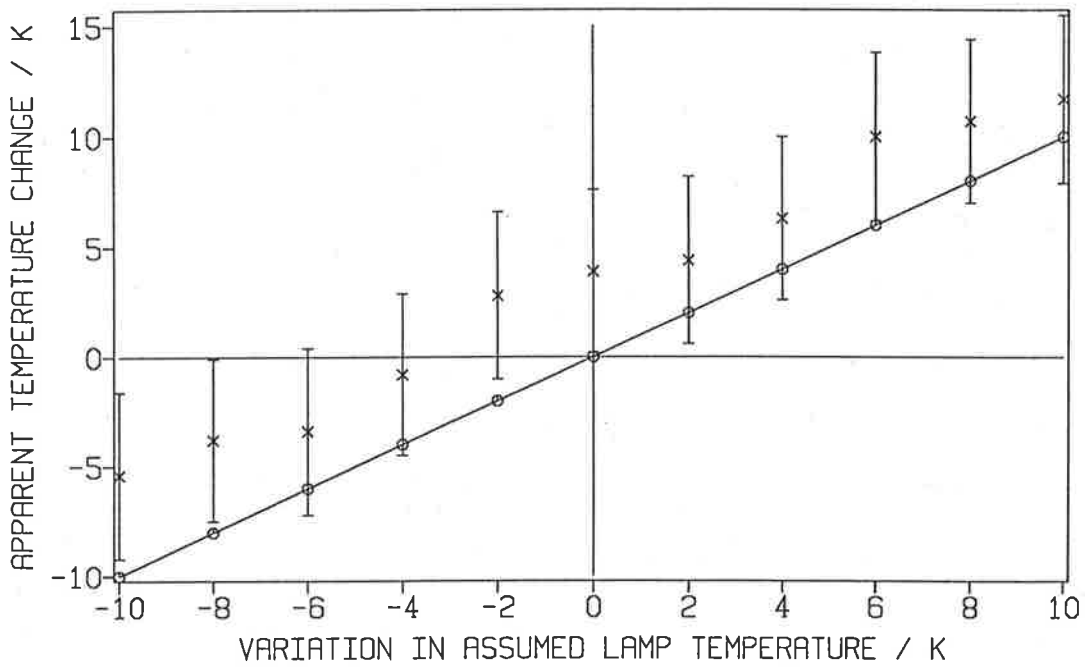

Figure 5.4: A simulated lamp profile was assumed to have a temperature different from the actual value used to generate the profile. The lamp profile was used to analyse another profile and the effect on estimated temperature is plotted above. The circles are from a noiseless run and the crosses are means from 15 runs with noise. The error bars indicate the mean of the errors from the fitting routine.

was used to analyse all D1 data. Therefore if there does exist an absolute error in the temperature estimates, variations in temperature would still be correct. The temperature of lamp profiles used for analysis can be estimated using one of the fitting routines in which an empirical instrument profile is determined from a ^{198}Hg λ 546 nm profile. Because the mercury/sodium mass ratio is large an uncertainty of 10 K in the mercury lamp temperature estimate will give about a 1 K uncertainty in the sodium lamp temperature. This allows an estimate of the sodium lamp temperature to within ± 1 K. The least-squares fit to the sodium lamp profile also involves an uncertainty so a total uncertainty of approximately 1 or 2 K can be expected depending on the signal-to-noise ratio of the profile being analysed. Using a single lamp profile to analyse all data assumes that the instrument profile and order are the same for all observations. The order could be set to within ± 100 of 23150 using the method outlined in section 3.2.2. As no major alterations likely to change the instrument function occurred during the period in which observations were made the above assumption should be valid.

5.4 Twilight analysis

Figure 5.5 shows a series of D1 zenith profiles obtained at dusk on day of year (DOY) 063, 1986. Each profile is the sum of about 50 scans in a 5 minute interval except profile 9 which was of 10 minutes duration. Dwell times of 40 ms per channel were used for 128 channel profiles so that in a single scan little variation in the background intensity occurred. The background has been subtracted to show spectral structure in the profiles. The sodium Fraunhofer absorption line can be seen in profiles 1–3. This is due to a contribution from Rayleigh scattering of the solar spectrum from the lower atmosphere. As the sun sets at increasing altitude, resonant scattering from the sodium layer at 90 km becomes the dominant feature in the spectrum (e.g. profiles 5–7). As the sun sets on the sodium layer the intensity of the emission rapidly decreases and the profile broadens as the photochemical reaction, which is exothermic, becomes the dominant source of photons. Profiles 8 and 9 in figure 5.5 show photochemical contamination.

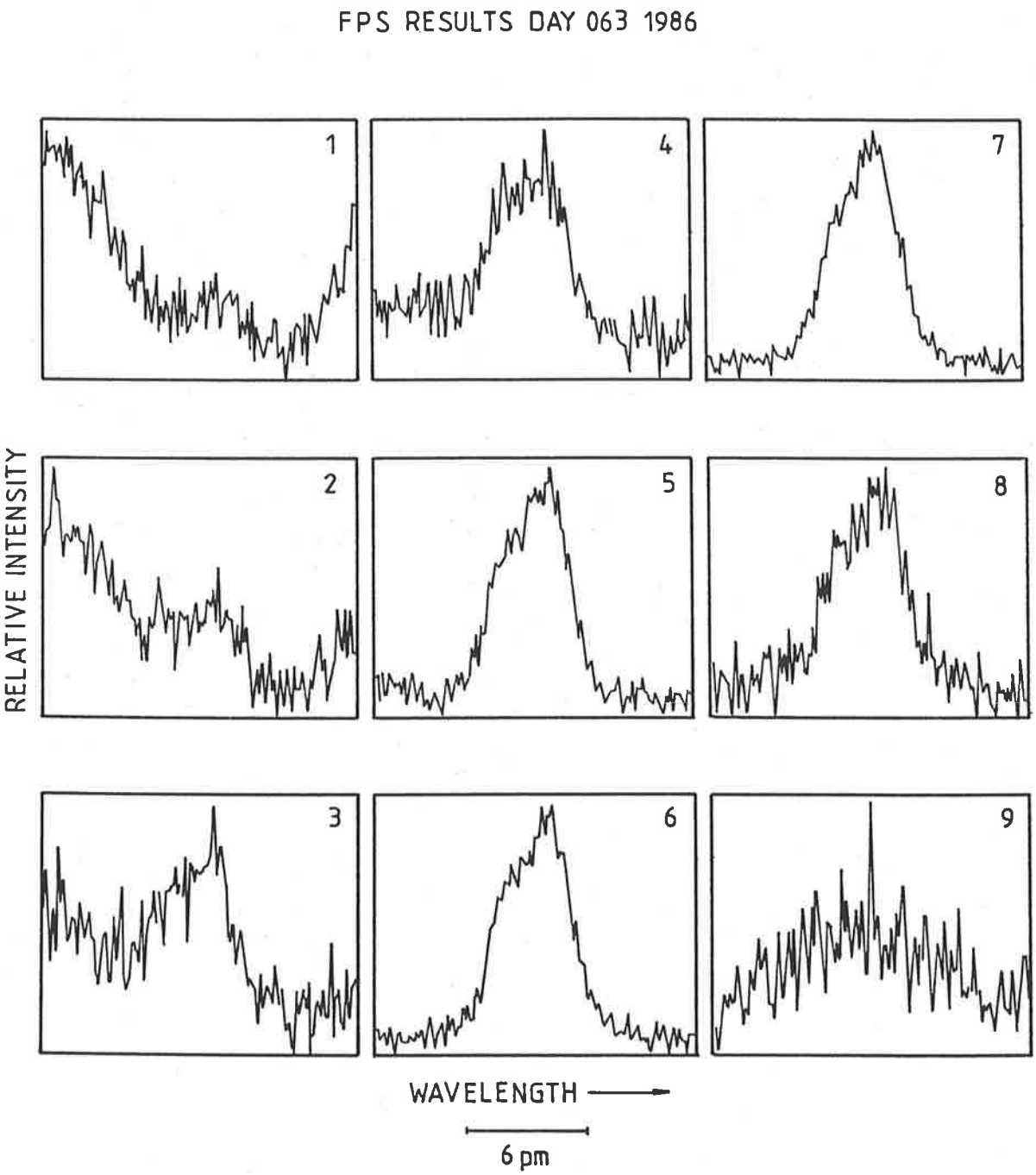

Figure 5.5: Sodium D1 line profiles from dusk on DOY 063, 1986.The background has been subtracted to illustrate the spectral features. In profiles 1–4 features of the solar spectrum can be seen. In profiles 4–8 the emission line produced by resonant scattering of sunlight is the dominant feature. In profiles 8 and 9 the line width is broader due to the exothermic photochemical excitation mechanism.

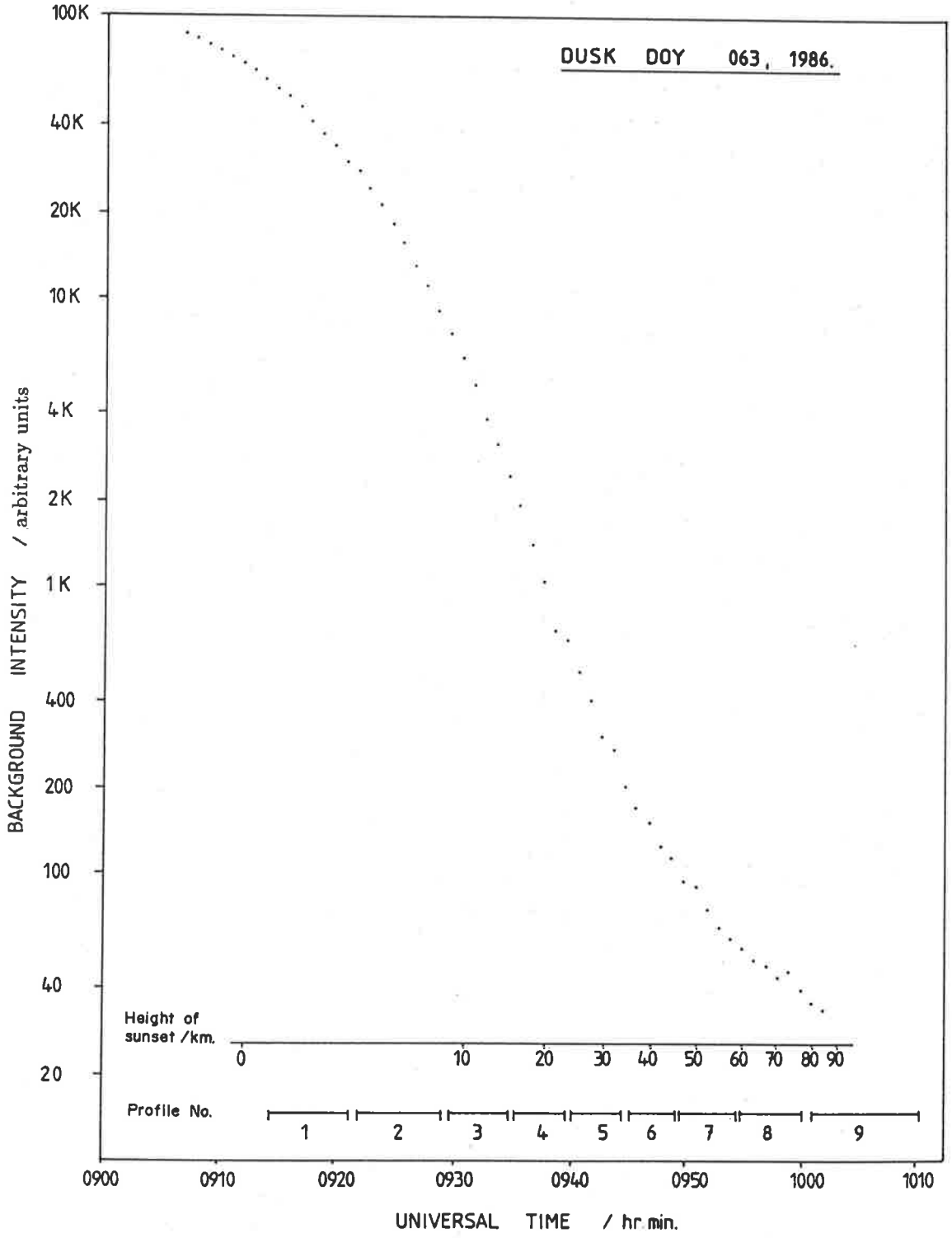

Figure 5.6: Background intensity, obtained from chart records is plotted as a function of Universal Time for dusk on DOY, 063. The height of sunset at different times is also shown. The bars at the bottom of the figure indicate the duration of recording of the profiles given in figure 5.5.

Figure 5.6 shows the variation in background intensity through twilight on DOY 063. These data were obtained from the chart recording of the photomultiplier output. The time of sunset at different altitudes, calculated using formulae from the Astronomical Almanac and from Chamberlain (1961), is indicated at the bottom of the plot. Individual FPS scans are accumulated in a multichannel analyser and recorded as a profile after several minutes. The duration of the profiles in figure 5.5 is shown at the bottom of the plot. Profiles 1–3, which have considerable Fraunhofer contributions, were obtained before the sun had set at 20 km.

In a single scan the FPS samples the background on either side of the emission line; thus the height of a scan on the chart record can be used as a measure of the intensity of the emission. Several ranges on the ratemeter were required to obtain a chart record through twilight and the ratemeter response varied for each range. Figure 5.7 shows the intensity of individual scans for the final range used. The numbered bars indicate the profile being acquired at that time. The intensity of the emission is approximately constant at the beginning of twilight then decreases as the sun sets at greater heights. The background intensity is indicated by open circles and heights are marked for various times of sunset. Once the emission intensity starts to decrease the proportional contribution of photochemical emission increases and the profile is broadened beyond its Doppler width. Figure 5.7 shows that profiles 7, 8, and 9 were obtained after the emission intensity started to decrease and thus have an enhanced photochemical contribution.

Decrease in intensity of the emission through twilight can be used to estimate the height and width of the layer (Chamberlain, 1961). Such calculations are not very precise as assumptions are made regarding the height at which the atmosphere screens out the component of the solar radiation producing the emission; the lower atmosphere produces a shadow with a diffuse edge. From figure 5.7 a screening height of about 45 km is suggested.

Sodium layer height and width measurements are more accurately measured using lidars. The height of the peak of the layer varies slightly over the year. Gibson and Sandford (1971), from lidar measurements, found the peak height to be at 87.5 km in summer and 91 km in

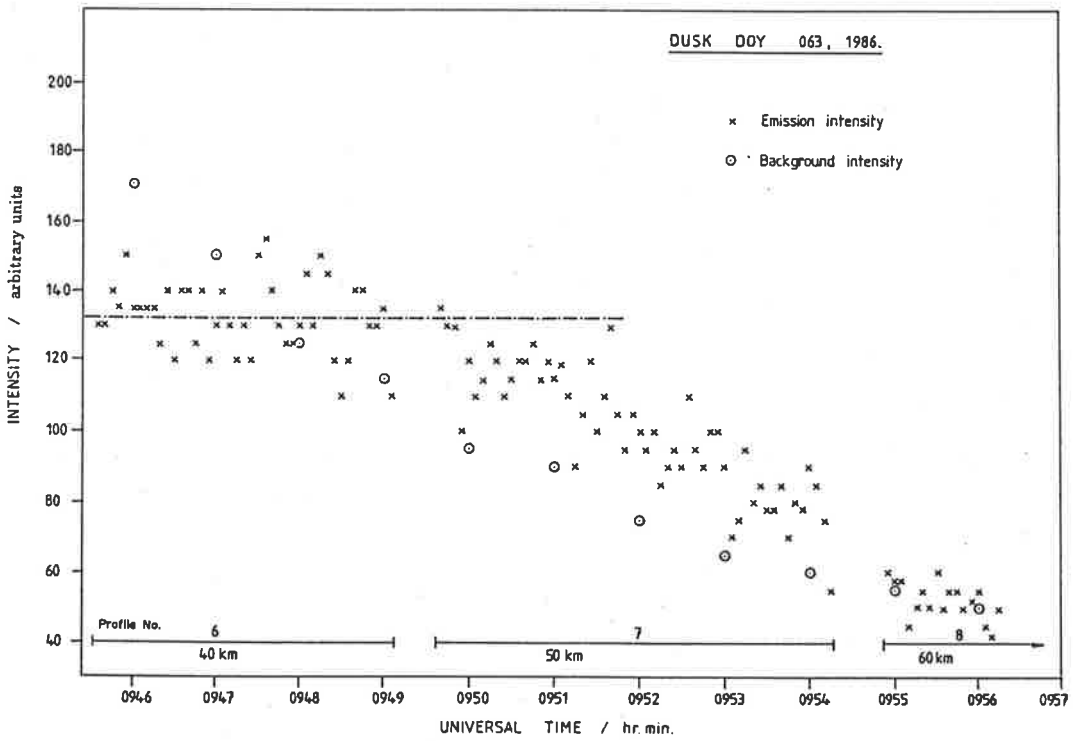

Figure 5.7: Crosses indicate the emission intensity at the peak of each profile as determined from individual FPS scans obtained from a chart recording of the photomultiplier output. The duration of profiles from figure 5.5 is indicated by a numbered bar at the bottom of the plot and the altitude of sunset at various times is also shown. Open circles indicate the background intensity. The dashed line is the average emission intensity determined from the scans in profile No. 6.

winter. Gardner et al., (1986b) found the mean centroid of the layer to be at 92 km with a 1.5 km decrease in December and November (winter). They suggested that the variation in the height of the centroid of the layer was due to a combined effect of the zonal winds and meridional circulation system. The FPS observations integrate the emissions from the whole of the layer, most weight being given to its densest part. In view of the variability in layer shape and the variation of 2–3 km in the height of its centroid, both spatially and temporally, a representative height of 90 km will be assumed in the following discussion.

Figure 5.8 shows the results of analysis of profile 6 on DOY 063, 1986. The best fit profile, as determined using the lamp analysis described above is shown on the same plot and residuals plotted below. A temperature of 178 ± 20 K was obtained.

Figure 5.9 shows the results of analysis of a D2 profile from DOY 062, 1986. For this profile a temperature of 172 ± 20 K was obtained.

The analysis also returns the peak position and intensity of the fitted Gaussian curve. Both the residuals and the χ^2 goodness of fit parameter can be used to assess results from the fitting routine (Wilksch 1975). Selection of profiles for analysis was critical and will be discussed at length in section 6.1. Profiles with significant Fraunhofer or photochemical contribution have to be discarded.

It has been shown here that the analysis described can be used for both the D1 and D2 lines. As few observations of the D2 line were made but results presented in the following chapters include only the D1 observations.

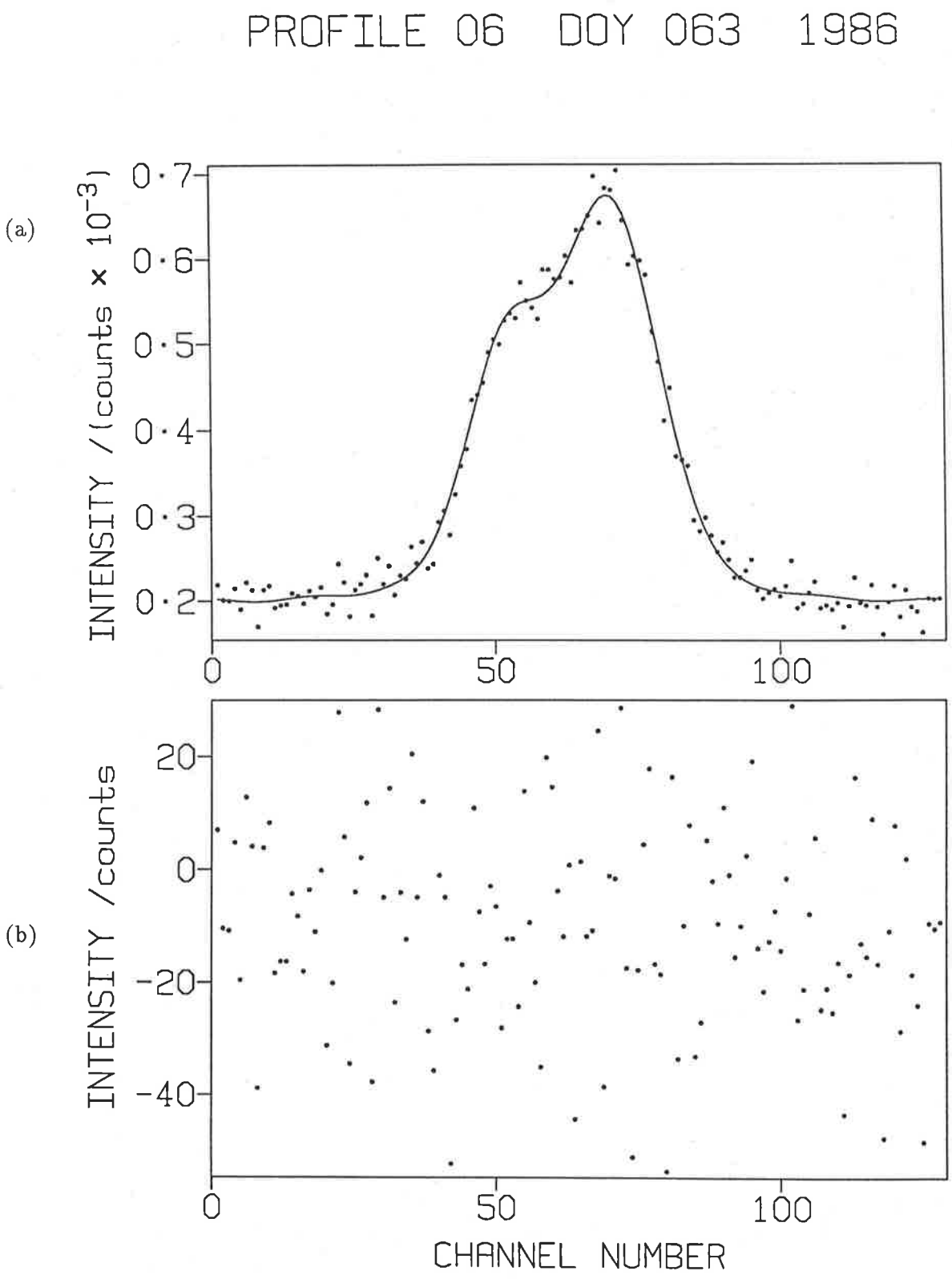

Figure 5.8: Analysis of a sodium D1 sky emission profile using the lamp analysis described in section 5.2. In plot (a) the dots show the number of counts in each channel of the profile. The smooth curve is the best fit profile from the lamp analysis. The dots in (b) indicate the difference between the number of counts in each channel and the best fit profile.

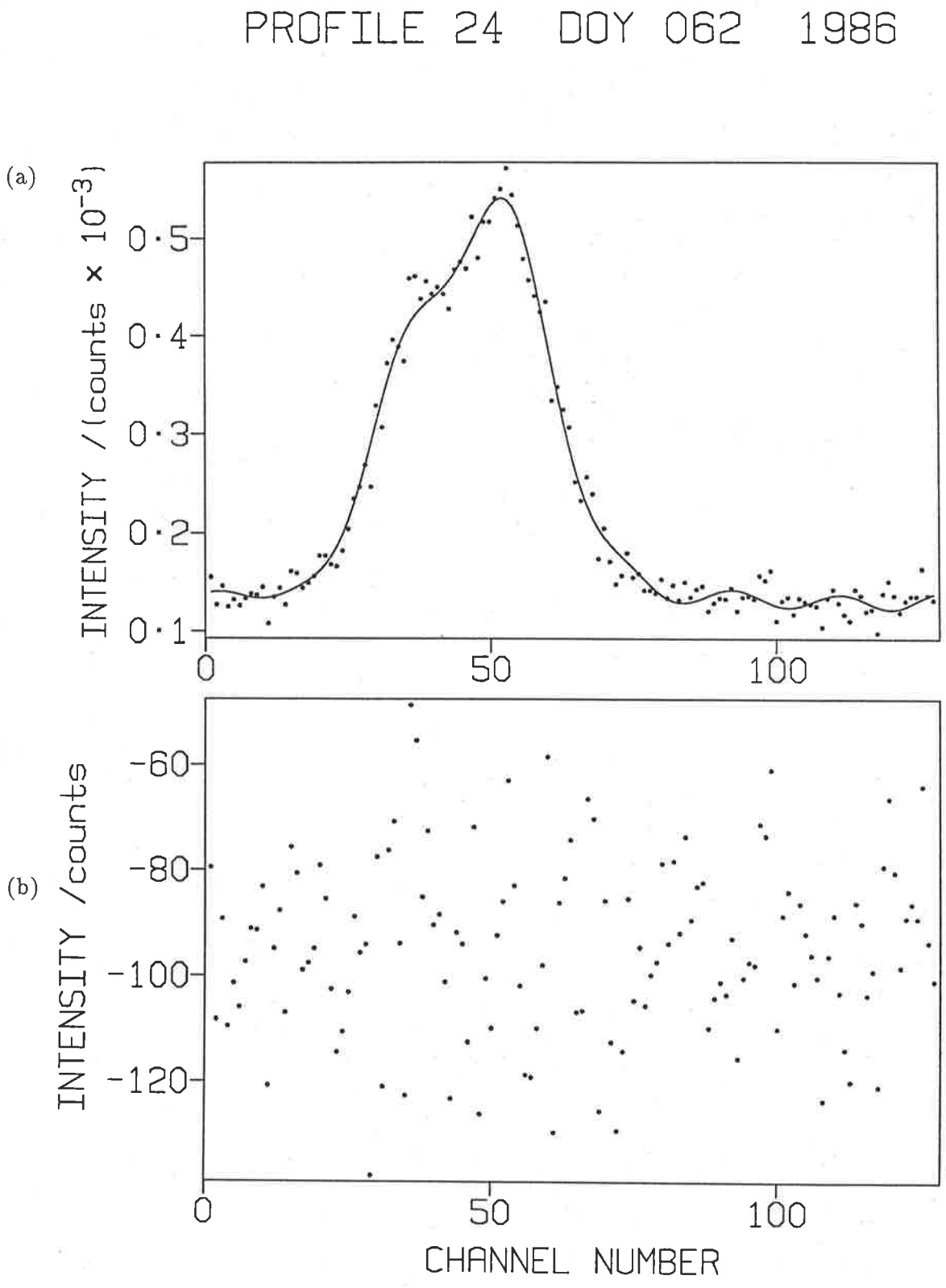

Figure 5.9: As for figure 5.8 except for a sodium D2 sky emission profile.

Chapter 6

TWILIGHT TEMPERATURE VARIATIONS

This chapter presents the results of temperature analysis of twilight sodium observations. These results have been accepted for publication and a copy of the manuscript is in appendix B.

6.1 Background and photochemical contamination

The D1 observations presented in section 5.1 have been analysed using the sodium lamp analysis discussed in section 5.2 and illustrated in figure 5.2. Temperatures obtained from analysis of the profiles from dusk on DOY 063, 1986 are shown in table 1. Also shown are the standard errors in individual temperature estimates obtained from the fitting routine, and the total background count rate per channel for each profile. These profiles were from zenith observations. Most profiles had similar acquisition times, thus the standard errors in the temperature estimates for 60° off zenith cardinal point observations were smaller than those given in table 6.1 as the emission intensity is proportionally higher. Some zenith profiles on individual days were combined to obtain a better signal to noise ratio.

A small contribution from the Fraunhofer absorption line masks the wings of the emission profile thus adding an apparent constant to the background. This effect was examined by

Table 6.1: Temperature estimates for the zenith profiles given in figure 5.5 using the analysis outlined in figure 5.2. The temperature errors are those returned from the fitting routine. In profile 2 an error of XX indicates an inadequate fit. Profiles 2, 3, and 4 show Fraunhofer contamination. Profile 8 has considerable photochemical broadening. Only profiles 5 and 6 would be accepted by the selection criteria given in the text.

profile	temperature (K)	background (counts/s)
2	640 ± XX	15980
3	68 ± 95	4681
4	177 ± 54	1244
5	187 ± 21	343
6	178 ± 20	115
7	231 ± 20	49
8	260 ± 64	31

subtracting a constant from each channel in a simulated profile. The simulated profile was then analysed as described above. An approximately linear relationship was obtained; a subtraction of 1 percent of the profile peak count rate resulted in underestimation of the temperature by 10 K.

An attempt was made to remove background contamination by fitting a polynomial to the wings of the profile; this was found to be inadequate. In principle, if a solar profile was obtained just prior to the sun setting, then the twilight profiles could be analysed in a manner similar to dayglow profiles (see chapter 4 for a description of dayglow analysis). Solar profiles have not been obtained to date. However, in view of the sensitivity of temperature estimations and the limited extra data which could be obtained by this method, it is unlikely to be a profitable exercise.

The photochemical emission, being exothermic, will broaden the profile beyond the Doppler

width. As twilight progresses and the ratio of photochemical to resonant emission intensities increases the profile width increases also. This effect was also simulated. By adding two simulated sodium profiles, one at 200 K for the resonant emission, and one at 700 K for the photochemical emission (Sipler and Biondi, 1978), and analysing as a single profile the effects of photochemical contamination can be seen. For small amounts of photochemical contamination a linear relationship is obtained. Photochemical emission at 1% of the intensity of the resonant emission will produce a change in width of the emission profile equivalent to a temperature increase of approximately 1 K. Although the exact emission intensity ratio is unknown the expected value is about 4%.

Care must be taken in interpreting the temperatures returned by the analysis described above. Obviously not all are representative of the atmospheric temperature. Useful information can be extracted from these results if stringent selection criteria are used to remove profiles with Fraunhofer background contamination or profile broadening due either to excess photochemical emission or scattered street light emission. The profile background is the count rate due to a combination of both photomultiplier dark count rate and sky background emission. The following selection criteria were used:

1. Fraunhofer background contamination can be allowed for by not selecting profiles with high background count rates. For zenith profiles a cut-off of 500 counts/s was used and for 60° off-zenith observations a cut-off of 2000 counts/s.

2. The problem of broadening by the photochemical reaction can be avoided by not selecting profiles with low background counts. For zenith profiles a background of 60 counts/s was considered the lowest acceptable background and for off zenith profiles a background of 120 counts/s was set.

3. No profiles from the west at dusk have been used in the temperature analysis as these profiles all show varying amounts of contamination by scattered street light.

4. The fitting procedure returns χ^2 values describing the goodness of fit. A limit on the

value of χ^2 was set to discard profiles for which a good fit was not obtained.

5. If a temperature estimate had a standard error of greater than 60 K it was not included in further analysis.

The background selection criteria under 1 and 2 above were determined by altering the limiting background values and calculating the monthly mean temperatures from the selected profiles; the monthly mean values reach a plateau. For example, when increasing the minimum acceptable background, the mean temperatures decrease until increasing the minimum value further does not significantly change the mean. The background limiting values were set to where the plateau commenced. Figure 6.1 illustrates this process. An average temperature from all profiles was calculated using the selection criteria above. In (a) the value of the background minimum cut-off was varied while assuming a background maximum cut-off of 500. It can be seen that as the background decreases the contribution from the exothermic photochemical emission increases and the temperature apparently increases. A background minimum count rate cut-off of 60 counts/s was chosen. All profiles would still have some contribution from the photochemical emission but the effect of this contribution and variations arising from different photochemical emission contributions through a single twilight should be minimized. In figure 6.1 (b) the mean temperature is shown as a function of background maximum count rate cut-off (with an assumed background minimum of 60 counts/s). It can be seen that some contribution from Rayleigh scattered sunlight occurs right through twilight. A maximum background count rate cut-off of 100 counts/s or less would be chosen if all profiles with any Fraunhofer contamination were to be eliminated. This would leave very few profiles in the data set. A background count rate of 500 count/s was chosen to give a reasonable sample and to exclude profiles for which excessive Fraunhofer contamination occurred.

These criteria also exclude some useful profiles. Profiles of a longer duration near the end of twilight start to become contaminated towards the end of the acquisition time. A shorter profile with the same background counts may not be contaminated. These rigid selection criteria were

(a)

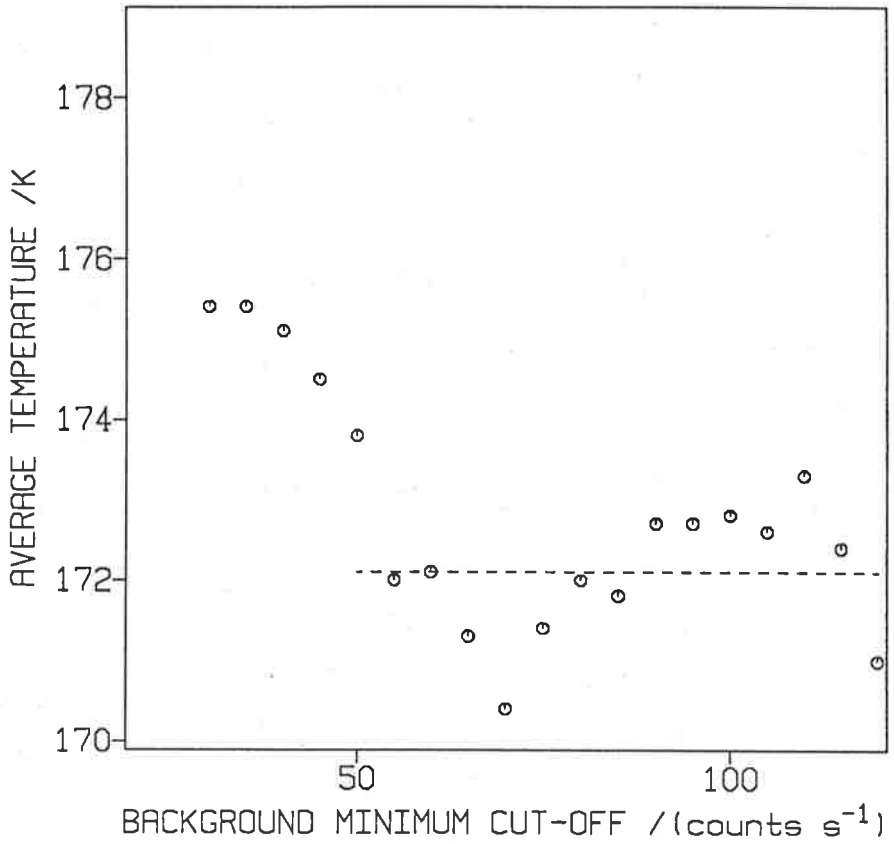

(b)

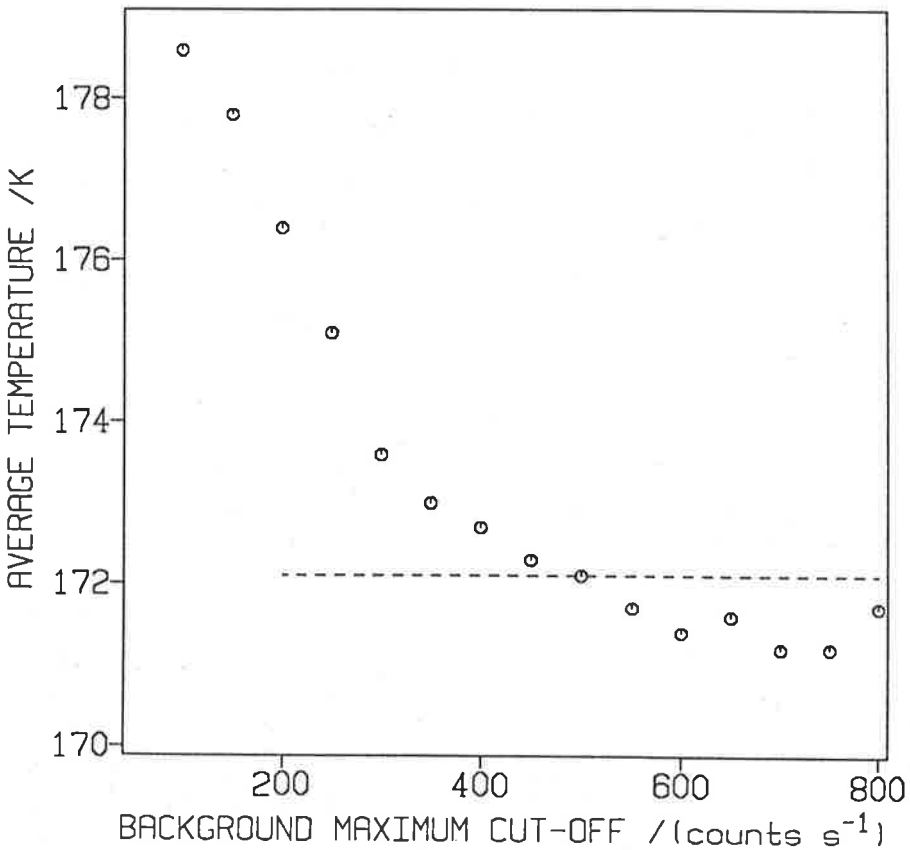

Figure 6.1: Figure (a) shows how the average inferred temperature from all profiles varied as the background minimum cut-off criteria was varied. The line indicates the mean obtained for the cut-off of 60 counts/s; the value used for profile selection. Figure (b) shows how the average inferred temperature varied as the background maximum cut-off criteria was varied. The line indicates the mean obtained for the cut-off of 500 counts/s; the value used for profile selection. The standard error was at least $\pm$ 3 K for all points in both figures.

used to avoid any subjective judgement in the selection of useful profiles.

When using the selection criteria described above a total of 166 profiles from 65 days data were obtained over the two years. A single lamp profile was used to obtain a sodium * instrument profile for the analysis of all data. The temperature of the lamp profile was determined by a five parameter fitting of two Gaussian curves using an instrument function derived from a profile obtained with a Hg 198 λ 546 nm emission lamp. The temperature obtained was 433.9 $\pm$ 1 K. This uncertainty includes both that from the fitting routine, $\pm$ 0.3 K, and an estimate of the error from the specification of the mercury lamp temperature.

6.2 Monthly mean temperatures and twilight variability

In this study profiles of 5–10 minutes duration were obtained over the short mid-latitude twilight. The temperatures calculated were highly variable both from day to day and on some individual days. Data are available for all months except August. In all months except May data from both dusk and dawn are available. The general trend was as expected; a warm winter mesosphere and a cold summer mesosphere. Taking June and July as the winter months (no August data are available) a winter mean temperature of 199 $\pm$ 5 K was obtained and for summer, December, January, and February, 150 $\pm$ 20 K.

Figure 6.2 shows the monthly mean dusk and dawn temperatures. A significant difference between dusk and dawn values can be clearly seen in the months January - April. As dusk and dawn are approximately 12 hours apart an obvious possible explanation of such a difference is the diurnal tide. Model values for 35° S from Groves (1988) are indicated by the dashed line in figure 6.2. This model was developed to match upper and lower atmosphere models and to fit available temperature data from satellites and rockets. The winter values are in reasonable agreement with those of the model but summer values are more variable and significantly lower.

To indicate the variability within estimates when more than two profiles have been used from any particular twilight, the range (maximum - minimum) of the estimates is used. From

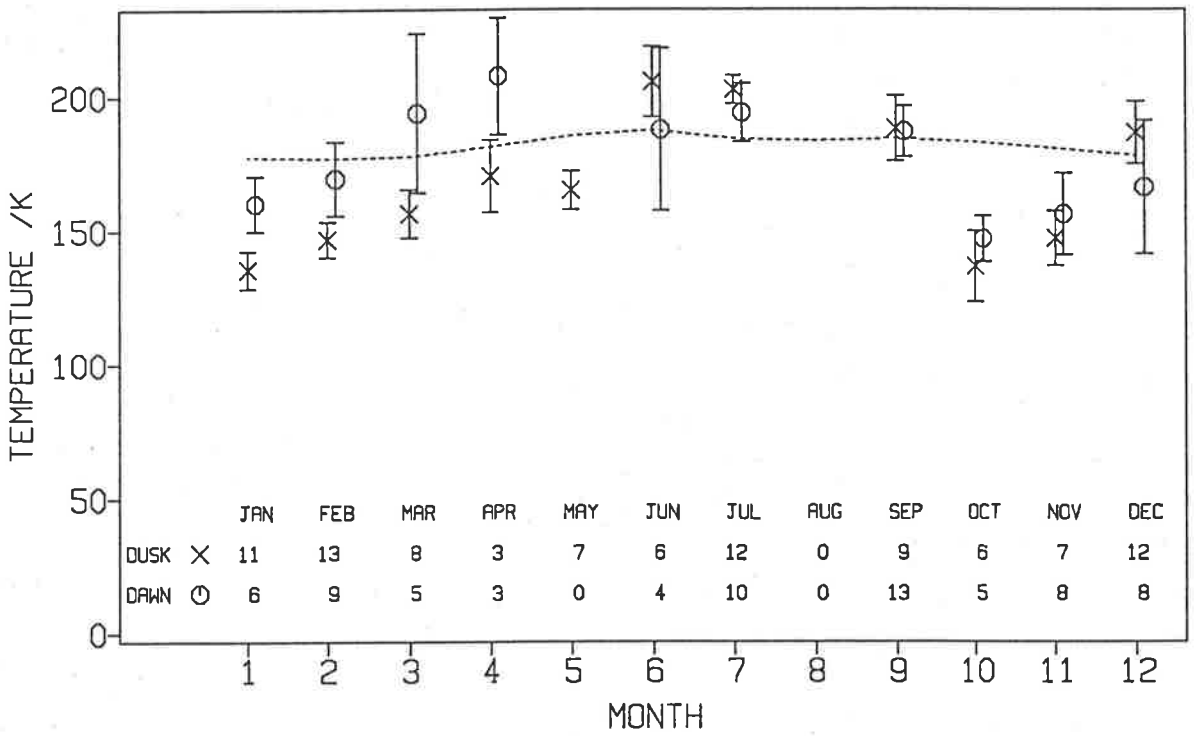

Figure 6.2: The monthly mean temperatures for dusk and dawn from the twilight observations are shown. Crosses indicate dusk values and circles, dawn. The error bars indicate the standard error in the mean computed on the basis of assigning equal weight to individual observations during any one month. The labels at the bottom of the plot show the month and number of profiles used to calculate the means. The dashed line represents model values from Groves (1988).

53 twilights the mean variability assessed in this way was 40 K; it does not change significantly through the year. This variability arises from several sources. The uncertainty in the fitting, as indicated by the standard error of the estimate, introduces some variability. The average value of this standard error from all data is ± 22 K; in Winter, (June and July), when twilights are longer and profiles have higher total counts, the average value of the standard error is ± 15 K. Another contribution to the variability arises from inadequacies in the selection criteria. As mentioned above the photochemical emission and the Fraunhofer background contamination can both affect the emission profile. The two effects act in opposite ways and would cancel each other to a certain extent. If the intensity of either was abnormal then this would produce an apparent change in temperature. If the background criteria are made more stringent the number of profiles satisfying them becomes too small to be useful.

A possible cause of actual variability of temperature during a single twilight is the presence of internal gravity waves. Hines (1965) predicted temperature variations of up to ± 30 K at 110 km. The tunable sodium lidar study of Neuber et al. (1988) found that temperature fluctuations of ± 25 K about the mean were not uncommon. Using the relationship (Hines, 1965)

$$\frac{\delta T}{T} \simeq \pm i(\gamma - 1)^{\frac{1}{2}} c^{-1} U_x$$

where γ is the ratio of specific heats, c the speed of sound, and U_x the wave induced horizontal wind speed, Vincent (1984a), from velocity measurements at Adelaide, estimated rms temperature variations of $\sim$ 10-12 K for gravity waves in the 85 km region. Zenith measurements over twilight span 15–20 minutes when more than one profile is obtained; thus a wave with a period less than an hour, not uncommon at mesospheric heights, could produce significant temperature fluctuations in the zenith observations.

Cardinal point observations span distances of 300 km and so waves with horizontal wavelengths of a few hundred kilometers, also not uncommon at mesospheric heights, could produce significant temperature fluctuations in any set of single twilight observations.

6.3 Tidal variations

To see if a connection with the diurnal tide could be substantiated a comparison was made with tidal measurements from the spaced-antenna partial-reflection radar at Buckland Park which is 50 km west-north-west of Mt. Torrens. The radar measures horizontal winds with a height resolution of a few kilometers. Wind data, including amplitude and phase of the diurnal tide for 1986–87, were supplied by Dr. R.A. Vincent (personal communication). To relate the amplitude of the wind variation with the amplitude of the temperature variation and to determine the phase difference between the wind and temperature variations a model is used viz. that presented by Forbes and Vincent, (1988). It incorporates the effects of mean winds and dissipation on the (1,1) mode of the diurnal tide. This model was used to calculate the phase shift between the zonal wind and the temperature variations at the March equinox. An amplitude of the variation in the wind of 30 ms^{-1} corresponds to an amplitude of the temperature variation of 8.5%; the time of maximum zonal wind lags the time of maximum temperature variation by 7 hours (Vincent, personal communication). Assuming that the ratio of the tidal temperature amplitude to the tidal zonal wind amplitude remains constant, and that the phase shift between the variations remains the same for all months, figure 6.3 compares the (dawn − dusk) temperature variation calculated from the model and radar data with that obtained from the FPS measurements. Reasonable agreement is obtained throughout the year except at the solstices. From January through April the FPS (dawn − dusk) temperature difference is slightly larger than the model/PRD values and in all other months it is slightly smaller. The diurnal tide maximizes in the autumn equinox (Vincent et al., 1988) and the phase is such that the maximum difference between dusk and dawn, 37 K or 20%, occurs then. The general agreement seen offers support for the predictions from the model of the temperature effects of the (1,1) mode of the diurnal tide.

An attempt to use an earlier model (Forbes and Gillette, 1982) gave diurnal temperature variations a factor of 2 less than those seen in the FPS data.

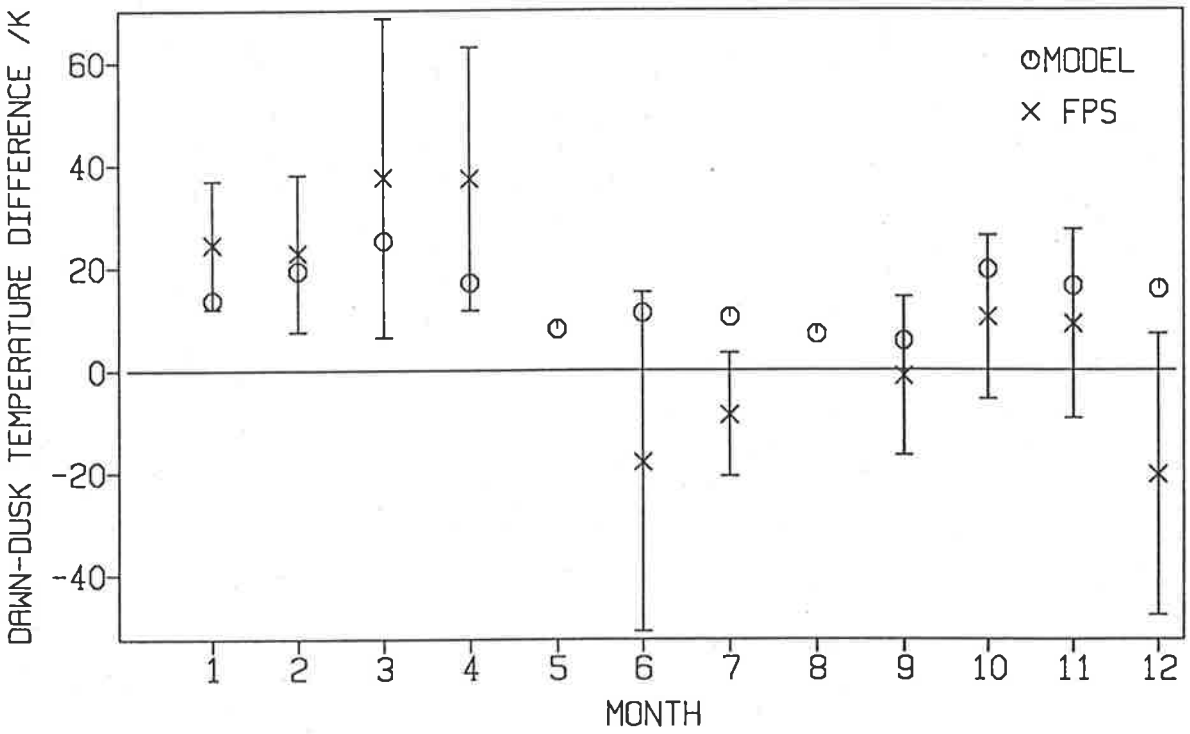

Figure 6.3: The dawn − dusk temperature difference is plotted for each month. Crosses represent the difference in the FPS average measurements, as plotted in figure 6.2. Open circles are the differences predicted by the model/radar measurements explained in the text.

Other factors could also produce systematic variations in the temperature of this region. The model used only accounts for the (1,1) mode of the diurnal tide; other modes of the diurnal tide may be important at times. No account has been taken of the semidiurnal tide which has been shown to have a significant effect on the density of the sodium layer (Batista et al., 1985; Kwon et al., 1987). Although the semidiurnal tidal data are available from the Buckland Park radar, the model amplitude and phase relationships are not. Phase information needs to be known fairly accurately to do a similar calculation of the dawn – dusk temperature difference produced by the semidiurnal tide. A 1 or 2 hour phase shift has quite a significant effect. Considering the times of dusk and dawn the largest effect would be expected at the solstices and least at the equinoxes. However, the phase is quite significant; the semidiurnal tide can cause the dawn temperatures to be lower than those at dusk and may explain the December and June/July negative temperature differences seen in FPS measurements.

Sipler and Biondi (1978) analysed 2 years of twilight and night-time measurements from Laurel Ridge, Pensylvania (40° N, 79° W). They found no systematic difference in the temperatures at evening and morning twilight. They were working with a fairly small data set; dawn temperatures were only available on about 10 days. The amplitude of the diurnal tide is large at Adelaide, 35° S (Vincent et al., 1988). It may be that at 40° N the temperature variation produced by the diurnal tide is not as significant as at Mt. Torrens and was therefore completely masked by other variations. The temperatures they obtained are in reasonable agreement with those reported here — their summer minimum of 150 K and winter maximum of 230 K compare with our means of 150 K in summer and 199 K in winter.

Neuber et al., (1988) used a tunable sodium lidar to obtain a winter mean temperature at 90 km of 205.2 K. These measurements were made at Andoya, Norway, 69° N.

6.4 Conclusions

Observations of the twilight sodium emission made with a high-resolution FPS can, with care, be used to infer temperatures at a height of about 90 km.

Observations from Mt. Torrens, a southern midlatitude station, have been used to determine monthly mean temperatures. A summer mean of 150 K and a winter mean of 199 K have been determined from two years of data.

The data show considerable short term variability some of which may be ascribed to the effects of gravity waves. The FPS measurements of the dawn −dusk temperature difference were in reasonable agreement with those calculated using a recent theoretical model together with measurements of the amplitude and phase of the diurnal tide from a nearby spaced-antenna partial-reflection radar. A systematic difference between dawn and dusk temperatures of up to 37 K in March and April is ascribed to the diurnal tide: at this time the amplitude of the tide is largest and the phase such as to maximize the effect.

Chapter 7

TWILIGHT WINDS

In this chapter the principles involved in determination of wind from FPS observations and data from twilight observations will be presented. In section 7.3 a comparison will be made with winds measured using the spaced antenna partial reflection radar at Buckland Park.

7.1 Wind analysis

The peak position of an FPS emission line profile can be used to determine the average line-of-sight component of velocity, v, of atoms in the line-of-sight of the spectrometer, if the rest wavelength, λ_0, is known. The equation for Doppler shift is given by

$$v = c\frac{(\lambda - \lambda_0)}{\lambda_0}. \tag{7.1}$$

For sodium observations the rest wavelength can be determined from hollow-cathode lamp profiles; advantages of this have been outlined in section 5.2.

From equation 7.1 and assuming typical values for the order (23150) of the etalon and channels per order (215) a line-of-sight wind velocity of 50 ms^{-1} would be indicated by a shift in the peak position of the profile of 0.85 channels. Changes in effective etalon spacing must be monitored to enable accurate measures of such small shifts. This is done by recording, at appropriate time intervals, a calibration profile; in this case a sodium lamp profile. Before the

sodium hollow-cathode lamp was obtained etalon drift was monitored by changing the filter wheel position and using a λ 546 nm ^{198}Hg lamp. In a transition period drift was monitored by using both sodium and mercury lamps. Figure 7.1 shows etalon drift determined from variations in peak position of both types of profiles on DOY 013, 1987. The peak positions of zenith sky sodium profiles are plotted as rectangles the height of which indicates the standard error returned by the fitting routine. Error in the peak position of each drift measurement is indicated by symbol size. It can be seen that the two drift curves are in general agreement. The initial drift is quite erratic but drift is uniform just before, and during, the time sky profiles were recorded (from about 0950 UT onwards).

When apparently erratic drift occurs during sky observations those data are discarded. If the drift is quite large, as in figure 7.1, but changes only monotonically, then the data are acceptable. The drift recorded was usually considerably less than that in figure 7.1.

A linear interpolation between drift points preceding and following an observation was used to allow for drift in etalon separation. When, for sodium observations, the drift was monitored using a sodium lamp the interpolation between drift points was used to define the rest wavelength. When drift was not monitored at the same wavelength, the peak position of the calibration profile, interpolated at the central time of the observation profile, was subtracted from the profile peak position. A further correction was then applied, using either a single rest wavelength lamp profile or assuming that the average vertical velocity was zero, to obtain a line-of-sight velocity estimate.

Line-of-sight winds, v, are converted to horizontal winds by assuming that the vertical velocity is zero. For an observing zenith angle, χ, the horizontal wind component is given by

$$v_{hor} = \frac{v}{\sin \chi}. \tag{7.2}$$

Zonal and meridional wind components are determined by observing in the cardinal directions at a zenith angle of 60°. This large zenith angle increases emission intensity according to the van Rhijn function V(z,χ). For an emission layer at height z, and for an Earth's radius 'a',

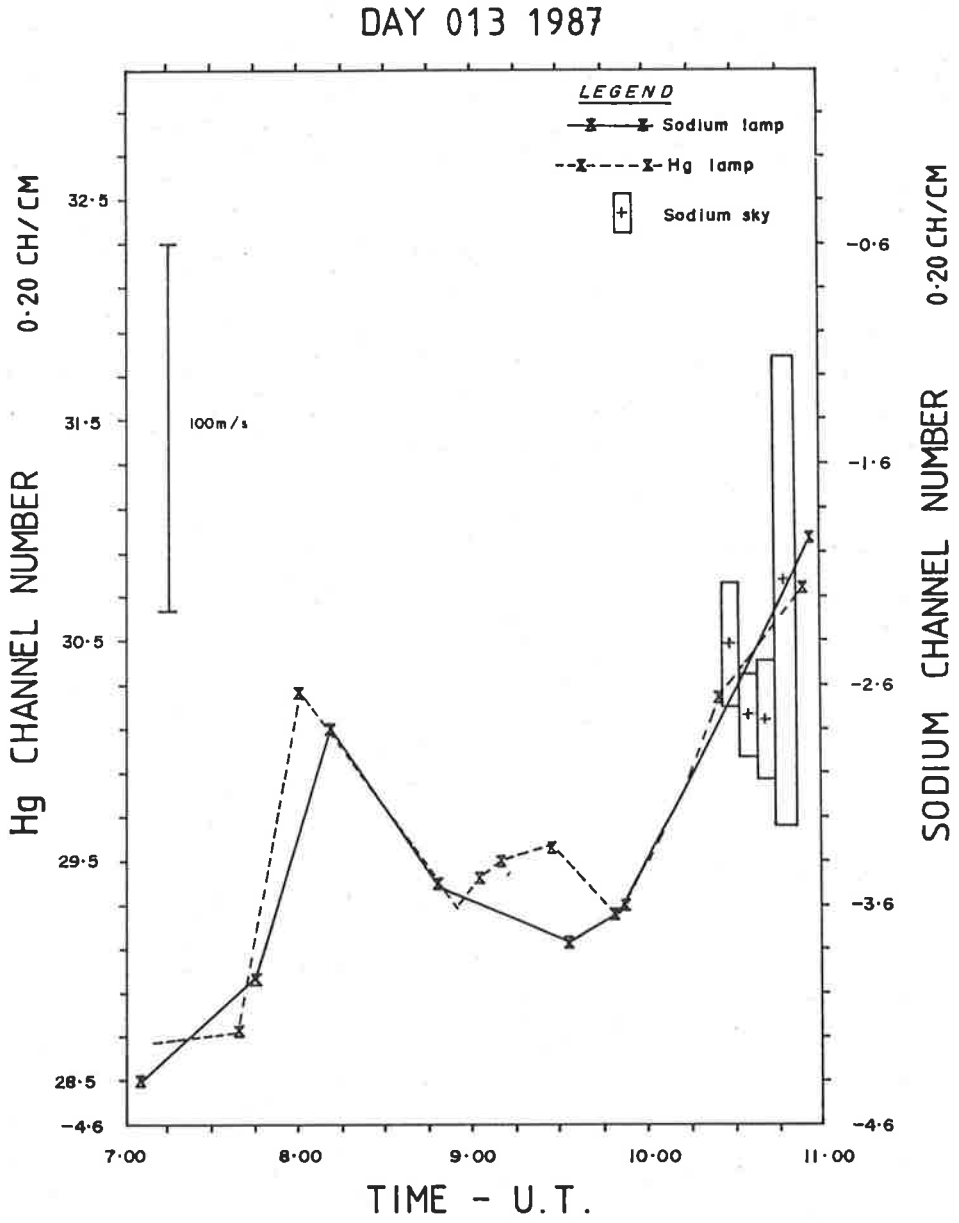

Figure 7.1: Etalon drift monitored using a mercury lamp and a sodium lamp. The rectangles indicate zenith observations of the sodium sky emission. The width of the rectangle indicates the duration of the profile and error in the peak position is represented by the height. The vertical bar on the left side indicates the Doppler shift for a 100 ms^{-1} wind.

intensity of observations at a zenith angle χ is related to intensity of the emission in the zenith by

$$\mathcal{I}(z,\chi) = \mathcal{I}(z,0)V(z,\chi) = \mathcal{I}(z,0)\frac{1}{\{1-[a/(a+z)]^2\sin^2\chi}^{\frac{1}{2}\}}. \tag{7.3}$$

The emission intensity at an observing angle of 60° is 1.92 times emission intensity in the zenith assuming the height of the emission to be approximately 90 km.

During twilight only a limited number of profiles can be obtained. Zenith profiles were not required for observations made when the hollow-cathode sodium lamp was available. This enabled a single profile in each of the cardinal points to be recorded during progression of twilight across the sky. Observations were usually made in the sequence east, south, north, then west, except in mid-summer when east, north, west, then south was more appropriate. More than four profiles were usually recorded, however background contamination was present and analysis not always possible. On several days suitably-attenuated sun observations were made just before sunset. By scaling and shifting these sun profiles to fit the Fraunhofer background in the profile wings an estimate of the background component can be removed.

Some profiles showed a linear variation in the residuals indicating a significant change in background intensity during individual scans. This could be corrected by scaling the profile before it was submitted to the fitting routine. The scaling factor was varied until no linear variation in the residuals was apparent.

Caution was essential when using background and ramp corrections. Ramp corrections were usually only required for profiles with background correction as well. These corrections could be misleading if the Fraunhofer contribution was significant or emission intensity low or both.

During 1986 the hollow-cathode lamp was not available and zenith observations were required to estimate the rest wavelength. A short twilight limits the value of wind estimates as tidal, mean wind, and wave components cannot be separated. Because of these two factors wind analysis has been restricted to data from 1987 onwards. The data fall into two groups, zenith observations and cardinal point observations, and these are presented in sections 7.2 and

7.3 respectively.

The FPS was originally designed for measurements of the O1 λ 558 and 630 nm thermospheric emissions. Mesospheric winds, typically of the order of 20–50 ms^{-1}, are considerably smaller in magnitude than thermospheric winds. The measurements presented here show that this FPS can be used for mesospheric measurements, but better drift monitoring is required for mesospheric winds if reasonable accuracy is to be obtained.

7.2 Zenith observations

Observations of mesospheric vertical winds using a high-resolution Fabry-Perot spectrometer pointed to the zenith challenge the instrument's limitations. Vertical winds of tens of metres per second have been reported from the thermosphere (Reiger 1974; Spencer *et al.* 1976; Peterherych *et al.* 1985; Wardill and Jacka 1986). Many of these observations have been associated with gravity waves produced by auroral disturbances. Ganguly (1980) has reported mesospheric vertical winds of up to 2 ms^{-1} from incoherent scatter radar observations. These winds were linked to the (1,1) mode of the diurnal tide. Widdel (1987) has reported velocities of up to 10 ms^{-1} from mesospheric foil cloud experiments which were associated with wave motions. Using the EISCAT UHF radar Hoppe and Hansen (1988) have measured mesospheric vertical velocities of up to 6 ms^{-1} in 4 hours of data.

Table 7.1 shows the days in 1987 on which zenith observations were made. Comments on instrument drift and vertical velocities (with errors from the fitting routine) are included. Instrument drift during these observations is generally poor. As can be seen, the drift is worse at dusk than at dawn as setting up the instrument for observations produces disturbances which take a while to settle. By dawn the instrument is usually more stable. Improving the capacitance balance, see section 3.2.2, can reduce drift; this was done several times in 1987.

For most of these observations both mercury and sodium lamp profiles were recorded. This allowed a comparison of several techniques for determining the rest wavelength. If no lamp

Table 7.1: Zenith observations, drifts, and vertical winds for 1987.
Modes of wavelength calibration are as indicated in figure 7.2.

DOY	time	Drift	Mode	Wind/error
013	dsk	large, monotonic	1	15/16, -13/11, -24/16, 0/64
015	dsk	large, erratic		discarded
	dwn	erratic		discarded
035	dsk	large, monotonic	1	-14/25, 0/14, -64/66
	dwn	large	2	-9/11, 4/11, 22/19
036	dsk	erratic		discarded
	dwn	large, monotonic	2	7/18, 0/15, 0/15, 19/78
037	dsk	large, monotonic		discarded
	dwn	large, monotonic	1	26/17, 15/13, -10/22
056	dsk	large, erratic		discarded
	dwn	small, monotonic	1	1/9, -10/12
069	dsk	large, erratic		discarded
	dwn	small, monotonic	1	12/22, 0/9, 18/12, -20/23
083	dsk	large, erratic		discarded
	dwn	large, erratic		discarded
114	dsk	small	1	-11/21, -4/13, -28/11, 8/17
	dwn	small, erratic	1	7/13, 14/12, 20/19

observations at the rest wavelength are available, the rest wavelength can be defined by setting the average of the vertical velocity measurements to zero (mode 3). The rest wavelength can be obtained from the sodium lamp drift curve (mode 1) or from a single lamp profile (mode 2). Note that for all modes drift corrections are made. A comparison of results obtained using these different methods for data from dusk of DOY 013 and for dawn of DOY 036 is given in figure 7.2.

Figure 7.2 also shows a plot of velocities for the asterisked mode in the table. If sufficient sodium lamp profiles were obtained to adequately monitor drift then mode 1 is used to determine winds. For some days, for example dawn on DOY 036, too few sodium lamp profiles were made to monitor drift so a single lamp profile was used to define the rest wavelength and drift corrections were made using mercury lamp profiles.

All modes of analysis produce similar trends in vertical winds; the wind decreases then increases on dusk of DOY 013, and similarly for dawn on DOY 036. Different modes tend to shift the winds vertically on the plots in figure 7.2. Except for the second mode 2 value, all modes on dusk of DOY 013 are in excellent agreement. The exceptional set of data was obtained using the final sodium lamp profile to specify rest wavelength. From figure 7.1 it can be seen that drift increased during this profile. The previous sodium lamp profile lies very close to the mercury drift curve. Results for dawn on DOY 036 show more variability. If observations were made over a sufficiently long period the average vertical velocity should be zero and, if drift is adequately monitored with either mercury or sodium lamps, all three methods would be the same.

Vertical velocities are included in table 7.1. Velocities are usually of the same order as errors from the fitting routine. In some instances, for example dawn on DOY 037 and dusk on DOY 114, significantly non-zero velocities are obtained. Unfortunately insufficient data were available to determine whether the vertical velocities are produced by wave motions.

From the results it can be seen that vertical wind measurements in the mesosphere are

Table A: Modes for wavelength calibration.

Mode	Type of wavelength calibration
1	linear interpolation of drift gives rest wavelength
2	single lamp profile defines rest wavelength
3	average zenith velocity defines zero

Table B: Vertical velocities using different modes.

DOY	time	mode	velocities / errors			
013	dusk	1*	15/16	-13/11	-24/16	12/64
		2	16/16	-9/11	-17/16	10/64
		2	0/16	-25/11	-33/16	-5/64
		3	14/16	-11/11	-18/16	9/64
036	dawn	1	-14/18	-24/15	-28/15	-6/78
		2	-11/18	-19/15	-20/15	0/78
		2*	7/18	0/15	0/15	19/78
		3	0/18	-6/15	-7/15	13/78

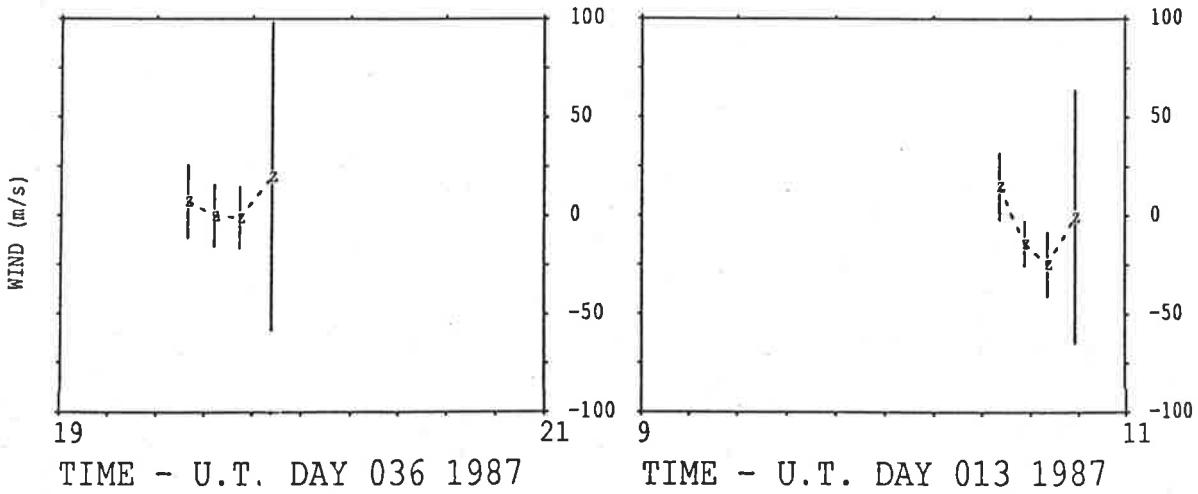

Figure 7.2: Table A indicates ways of determining rest wavelength. Table B gives wind velocities from two twilights determined using the different modes from table A. The vertical velocities for the asterisked values in table B are plotted.

possible using Fabry-Perot observations of the sodium emission, however optimum operating conditions (ie minimal drift) must be maintained.

7.3 Comparison with spaced antenna partial reflection radar

7.3.1 Horizontal winds

Other data obtained in 1987 were from observations to the north, south, east, and west at a zenith angle of 60°. From a set of such observations obtained over a single twilight the horizontal, neutral winds at the altitude of the sodium layer can be estimated.

Extensive horizontal wind measurements have been obtained using the spaced antenna partial reflection (SAPR) radar experiment (Vincent 1984b). One such radar is located at Buckland Park, 50 km from the Mt. Torrens field station. The need to compare FPS and radar determinations of the wind was highlighted at a workshop on Coupling, Energetics, and Dynamics of Atmospheric Regions (CEDAR) (Romick 1987). The SAPR radar obtains wind measurements at 2 km height intervals from 60 – 100 km. Reflections are not always obtained from all heights; data are most frequently obtained from the 80 – 90 km range. At dusk external interference can reduce the radar performance but at dawn operating conditions are usually good. Thus a comparison of SAPR radar wind measurements with winds from FPS observations of the twilight sodium emission is ideal as the height of the sodium layer (88 – 90 km) coincides with the region of densest radar data (Vincent 1984b).

Previous FPS sodium observations have not been used to obtain wind measurements (Hernandez 1975; Sipler and Biondi 1975, 1978). More extensive observations of the O1 λ 558 nm emission have been made but comparison of winds from these measurements with radar winds is more difficult as the height of the oxygen emission layer is about 97 km and width about 7 km which means the layer extends above the region of frequent radar data. Interpretation of the λ 558 nm emission is also complicated by thermospheric and auroral contributions. Hernandez and Roper (1979) made an indirect comparison between meteor radar wind measurements at

Atlanta, Georgia (34° N, 84° W) and winds from FPS observations of the O1 λ 558 nm emission at Fritz Peak, Colorado (40° N, 106° W). The distance which separates these two sites, over 2000 km, is such that significant differences in tidal and wave variations would be expected, and were seen in the data.

In the following section dusk on DOY 158, 1987 (7 June) will be used as an example to illustrate the method used to compare data. The bulk of the data will be presented in section 7.3.3.

7.3.2 Data reduction for wind comparison

Figure 7.3 shows the respective locations of Mt. Torrens and Buckland Park. Mt. Torrens is one of the highest peaks in the Mt. Lofty ranges which run approximately north-south. Mt. Torrens is on the eastern side of the range. Ground projections of FPS observing locations in the cardinal directions are shown; about 300 km separates them. The SAPR radar at Buckland Park observes in the zenith.

In a winter twilight the FPS obtains four or five usable profiles of about 7 min duration. Wind samples at 15 min intervals can be obtained by using the nearest meridional and zonal profiles.

Figure 7.4 shows 15 min averages of radar data from dusk on DOY 158. To compare these data with FPS values a height-weighted average of radar data for each 15 min average was calculated. A Gaussian function of a specified width and height was used to determine the weighting. Considering other sodium layer observations (see chapter 2) a layer full-width at half maximum of 7 km was chosen. Gaps in the data needed to be filled to weight the radar values. This was done by setting all values above the highest data point to the value of the highest data point and all values below the lowest data point to the value of the lowest data point. Where a gap between data points existed the wind was assumed to vary smoothly from the height below the gap to the height above the gap. If no data were obtained at any heights

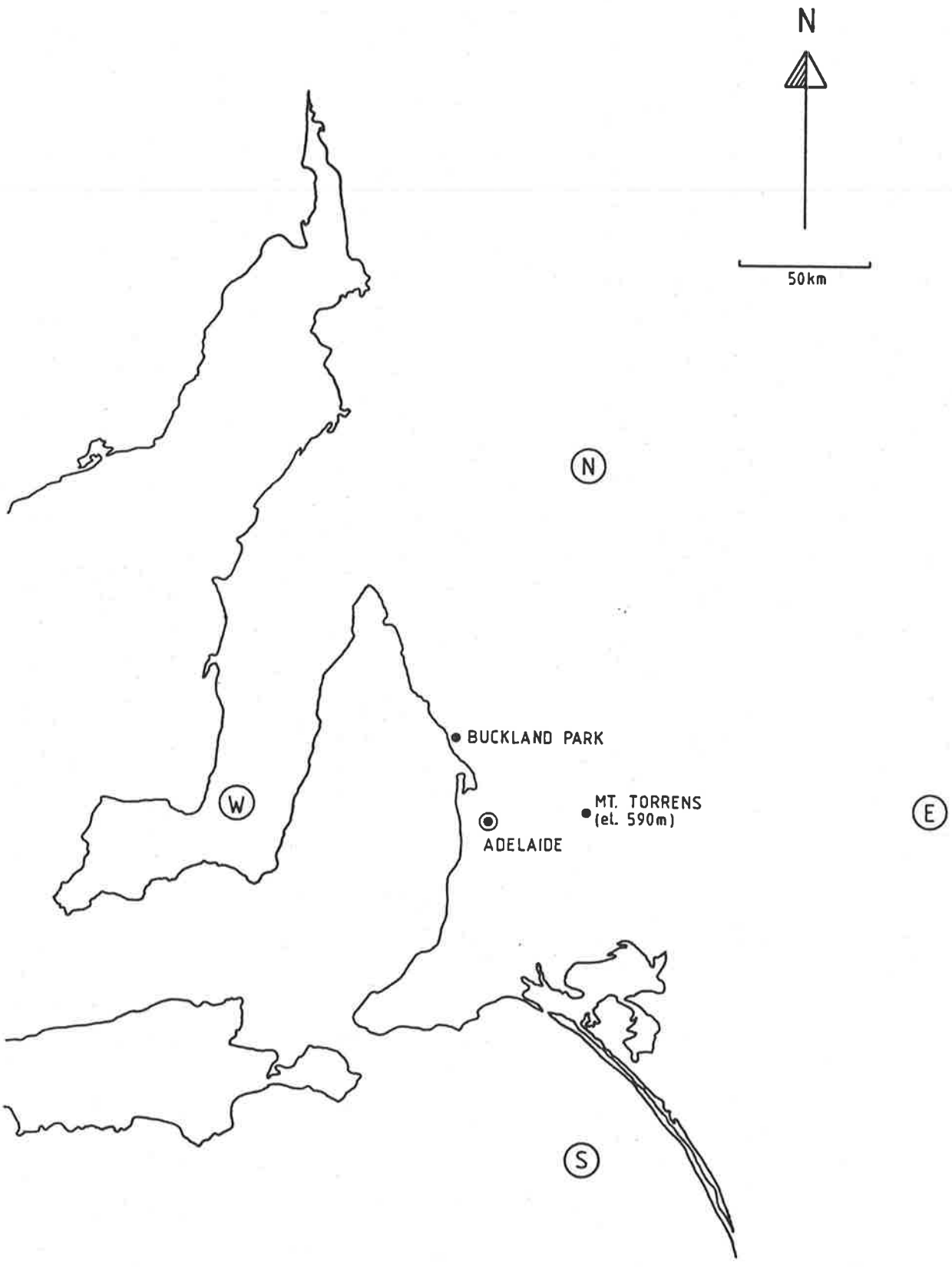

Figure 7.3: Locations of the Mt. Torrens (34° 52′ S, 138° 56′ E) and Buckland Park field stations are shown. The projection on the ground of the FPS cardinal point observing positions are also indicated by the symbols N , E etc.

a gap was left. Figure 7.5 shows the filled radar data set for dusk on DOY 158. Obviously this technique may be misleading if radar data are sparse. Data outside one half width of the Gaussian weighting function have little effect on the weighted results so gaps in the data above 94 and below 78 km are not important.

Figure 7.6 shows radar and FPS winds for dusk on DOY 158. The five sets of wind vectors are comparisons assuming the Gaussian function used to weight radar values is centred at five heights from 84 – 92 km. In this case, because the wind field was fairly uniform, there are few differences between weighted radar values at different heights. Reasonable agreement between the two data sets was obtained. Unfortunately a gap exists in the radar data at twilight due to the use of the SAPR radar for another experiment to measure turbulence. The first FPS vector is in excellent agreement with radar winds obtained before the data gap. Obviously a change in the wind occurs over twilight and although radar and FPS wind directions are not in agreement at the end of twilight the wind magnitudes are similar.

No uncertainties have been presented in this section. They will be discussed in detail in section 7.3.5.

7.3.3 Comparison of results

Table 7.2 summarizes the FPS/SAPR radar wind comparison. FPS wind measurements were rejected when the etalon drift was large and erratic as large drift typically yields unacceptably large and variable wind estimates. In some cases one or two of the FPS wind samples were reasonable and others unreasonable, however, all data from such times have been rejected. Unfortunately drift during these measurements was particularly bad. It was not until 1988, when a complete check of the separation transducer was made and an electronic fault isolated, that optimal operation was regained.

Complete confidence in both data sets is required for a comparison of two techniques. For this reason, the severe drift in the FPS data, and the shorter summer twilights, the wind analysis

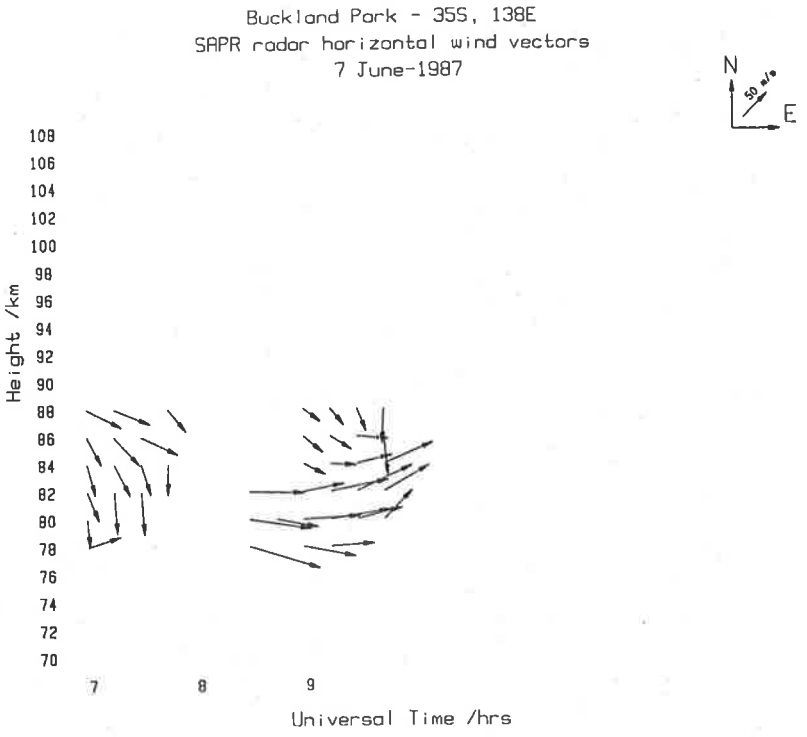

Figure 7.4: SAPR radar horizontal winds for DOY 158, 7 June 1987. The wind magnitude and direction are indicated on the right-hand side.

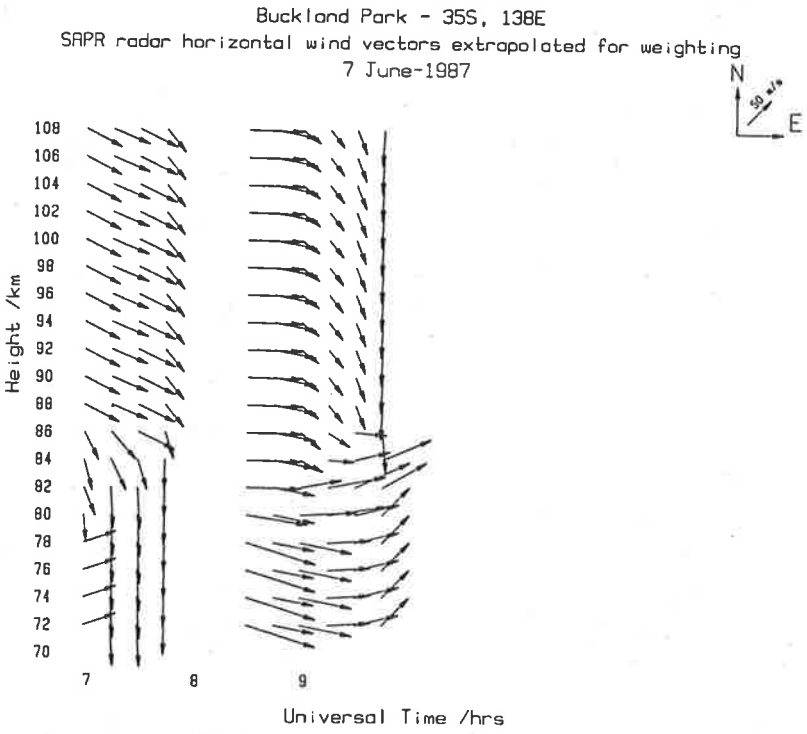

Figure 7.5: The same data as in figure 7.4 but with values interpolated and extrapolated to allow the weighting function to be applied at all heights.

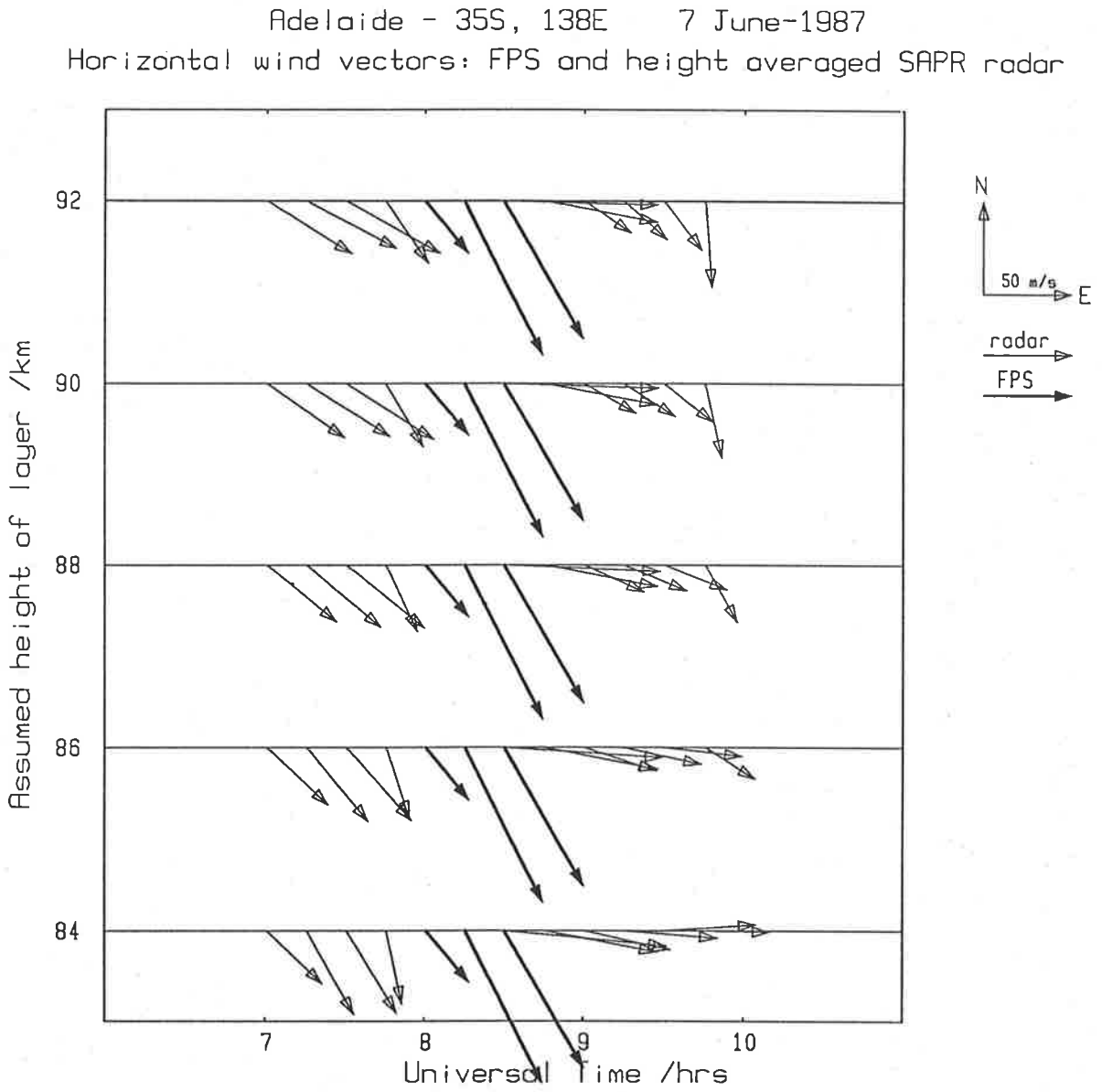

Figure 7.6: Comparison of the FPS and SAPR radar horizontal wind for dusk on 7 June, 1987. The five heights correspond to radar data weighted by a Gaussian 7.0 km FWHM centred on the heights marked. The vectors on the right side indicate the wind scale and direction.

Table 7.2: Summary of FPS/SAPR radar wind comparison.

DOY	Date	Time	FPS drift	SAPR coverage	Wind	Comparison				difference ms^{-1}		
						agreement	magnitude	meridional	zonal	N–S	E–W	tot
158	7 June	dusk	small	moderate 78–88	steady	fair	similar	FPS>>SAPR	SAPR>>FPS	-62	-23	-85
		dawn	small	dense 80–88	moderate, steady	fair	similar	same	opposite	20	49	69
182	1 July	dusk	small	sparse 78–98	light, variable	good	similar	similar	similar	19	-33	-14
184	3 July	dusk	vlge, monotonic									
		dawn	vlge, monotonic	no data								
186	5 July	dusk	lge, monotonic	moderate 76–98	light, variable	poor	FPS>SAPR	opposite	both varying	0	46	46
		dawn	lge, monotonic	no data								
187	6 July	dusk	small	78–98 dense 84–90	moderate, steady	poor	similar	opposite	FPS varying	0	-56	-56
		dawn	large, erratic	no data								
188	7 July	dusk	mod, monotonic	moderate 76–98	light, steady	good	similar	same	same	2	-6	-4
		dawn	mod, monotonic	no data								
189	8 July	dusk	moderate	moderate 80–94	variable, strong	poor	SAPR>FPS	SAPR varying	FPS varying	-4	-54	-58
245	2 Sept	dusk	large, erratic									
253	10 Sept	dusk	large	moderate 84–98	moderate, variable	poor	similar	both varying	different	-47	-71	-118
		dawn	moderate	sparse 84–98	moderate, variable	poor	similar	similar	opposite	18		
254	11 Sept	dusk	mod, erratic									
258	15 Sept	dusk	moderate	sparse 80–98	moderate	poor	FPS>SAPR	similar	opposite	23	-20	3
		dawn	moderate	sparse 90–98	light, variable	poor	similar	both varying	both varying	-44		
259	16 Sept	dusk	large, erratic									
		dawn	small, monotonic	moderate 82–98	moderate, variable	fair	similar	both varying	both varying	21	-10	11
260	17 Sept	dusk	large, erratic									
		dawn	large, monotonic	sparse 78–98	light, variable	poor	FPS>>SAPR	both varying	both varying	103	-70	33
264	21 Sept	dusk	large, erratic									
		dawn	large, monotonic	sparse 84–98	strong, variable	poor	similar	SAPR varying	both varying	-37	120	83
265	22 Sept	dawn	small, monotonic	sparse 82–98	light, variable	fair	similar	SAPR varying	SAPR varying	-4	-5	-9
274	1 Oct	dusk	large	no data								
275	2 Oct	dusk	moderate, erratic	no data								
		dawn	moderate, erratic	no data								
298	25 Oct	dusk	moderate, erratic	sparse 88–94	strong, variable	poor	similar	FPS varying	both varying	-112	-57	-169
		dawn	moderate	2 points, 88, 90	moderate, variable	fair	similar			21	-44	-23

of remaining 1987 data, from DOY 331–363, have not been presented.

Data rejected for wind analysis have been included in the temperature analysis presented in chapter 6. Since profiles are obtained from very short, 5–7 min runs, instrument drift during that period should be small. Extremely bad drift would distort a profile: for such profiles the fitting routine would return a high χ^2 value resulting in rejection by the selection criteria.

Table 7.2 also gives the radar data coverage during twilight. The height range of the data is given and the words sparse, moderate, and dense used to describe the number of points in that range or the range indicated. The wind is described as light if both radar and FPS winds were less than 50 ms^{-1} in the whole period; a moderate wind fluctuates around 50 ms^{-1}, and a strong wind is one in which most measurements were greater than 50 ms^{-1}. If the wind was consistent in both magnitude and direction then it was described as steady.

The next four columns in table 7.2 describe the FPS/SAPR radar comparison. The first column is a summary of the plots similar to figure 7.6. The second comment compares the wind magnitudes. In most cases the wind magnitudes are similar. The one case where FPS winds are much larger than radar winds the drift is large and this casts doubt on the reliability of the FPS winds. The last two columns describe the comparison of the zonal and meridional components. The meridional components are more often similar than the zonal components. In cases where both FPS and radar values are varying they may be in agreement for some of the time.

Of the 17 twilight data sets presented, agreement throughout the period in both zonal and meridional components was obtained in only two cases: dusk on 1 July and 7 July. In both cases the wind was light. On the 1 July the radar data coverage was sparse but on 7 July moderate coverage was obtained. The radar data and FPS/SAPR radar comparison for 7 July are shown in figure 7.7. The five sets of wind vectors are comparisons assuming the SAPR is weighted by a Gaussian function 7 km FWHM centred at five heights from 84 –92 km. From this figure it can be seen that the radar winds weighted by the Gaussian function centred at 88 km gives

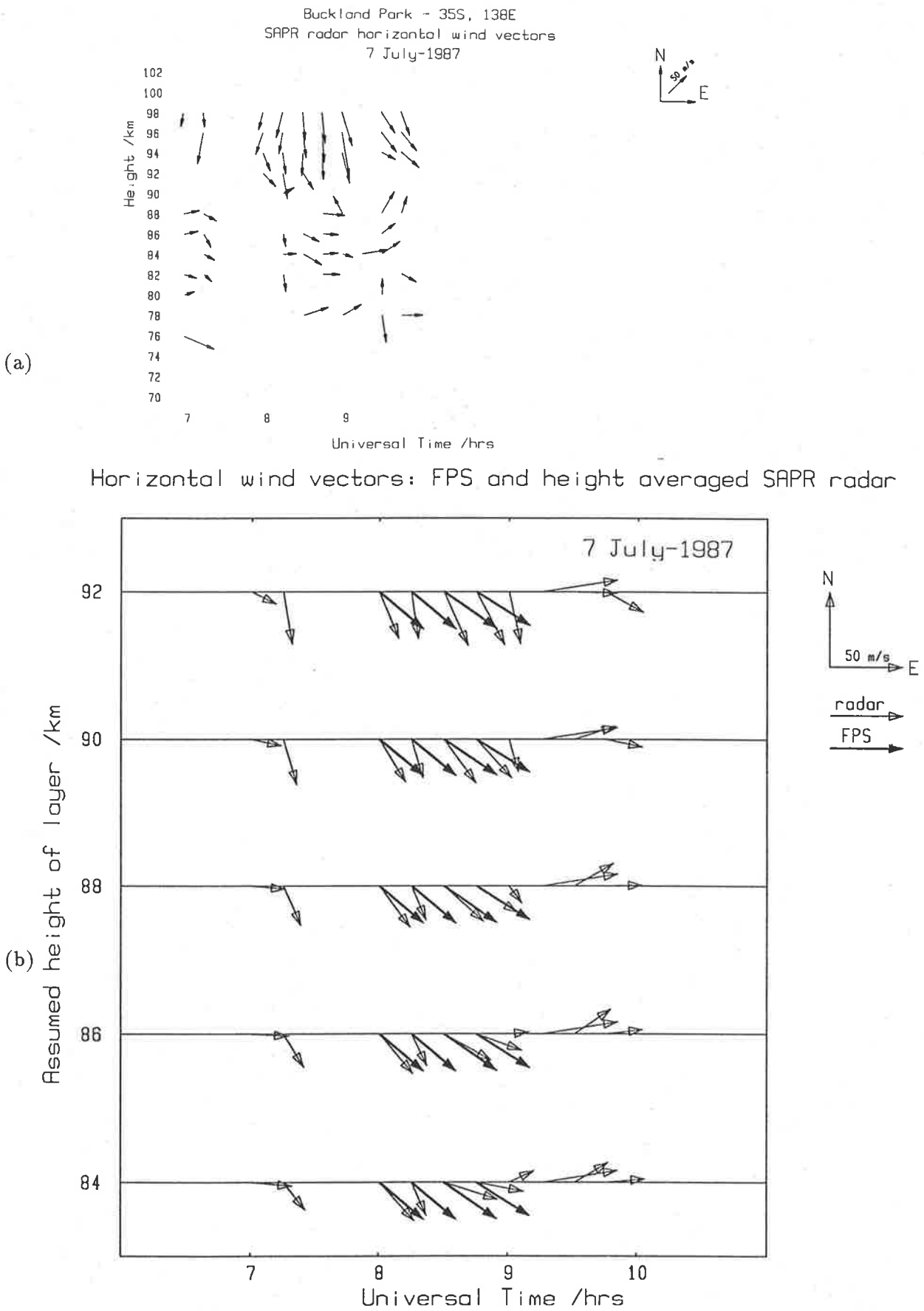

Figure 7.7: FPS/SAPR radar comparison for dusk on 7 July, 1987. The radar data are shown in (a) while (b) gives the comparison of radar horizontal winds, weighted at five different heights, and FPS horizontal winds. The best agreement was obtained for the radar data weighted by a Gaussian function centred at 88 km.

much better agreement than those from the weighting centred at 84 or 92 km. This supports the assumption that the sodium layer is centred near 90 km; it suggests a height slightly lower may be more appropriate.

On several twilights, for example dusk 7 June, dusk 10 Sept, and dawn 16 Sept, the radar winds were reasonably steady for the hour before twilight and then a change in wind direction occurred during twilight. Figure 7.8 shows the FPS/SAPR radar wind comparison for dawn on 16 September. In this figure the best agreement was obtained at 84 km. As the radar winds vary rapidly both with height and time, it is more likely that the wind at sodium layer heights is non-uniform over the spatial scales sampled by the FPS than that the layer has descended to 84 km. The centroid of the sodium layer is slightly lower in winter than in summer (Gibson and Sandford 1971; see also other references in section 2.1.1). However the separation of the observing points, as indicated in figure 7.3, is such that waves with a wavelength of less than 500 km could produce a significant difference in the winds measured by the two instruments.

A final example of the FPS/SAPR radar comparison is given in figure 7.9, dawn on 7 June. This example shows reasonable agreement in the meridional components, except that the FPS magnitudes are slightly larger than those from the radar, and although zonal magnitudes are similar the directions are opposite. This is representative of several cases. Velocities similar in magnitude but different in direction may result from a wave or waves propagating through the region. Beer (1977) has shown that the terminator may produce waves in the mesopause. Hall *et al.* (1987) have observed a wave in the mesosphere that was associated with the passage of the terminator. Such a wave, propagating zonally, could produce variations in the zonal wind and hence disagreement between FPS and radar measurements. The Mt. Lofty Ranges run approximately north-south and may also be a cause of some mesospheric wave activity. Such wave activity may also be seen in the FPS data as the north and south, and east and west observations are separated by approximately 300 km. Horizontal velocity divergence, calculated by subtracting velocites of south from north located observations, and east from west for the

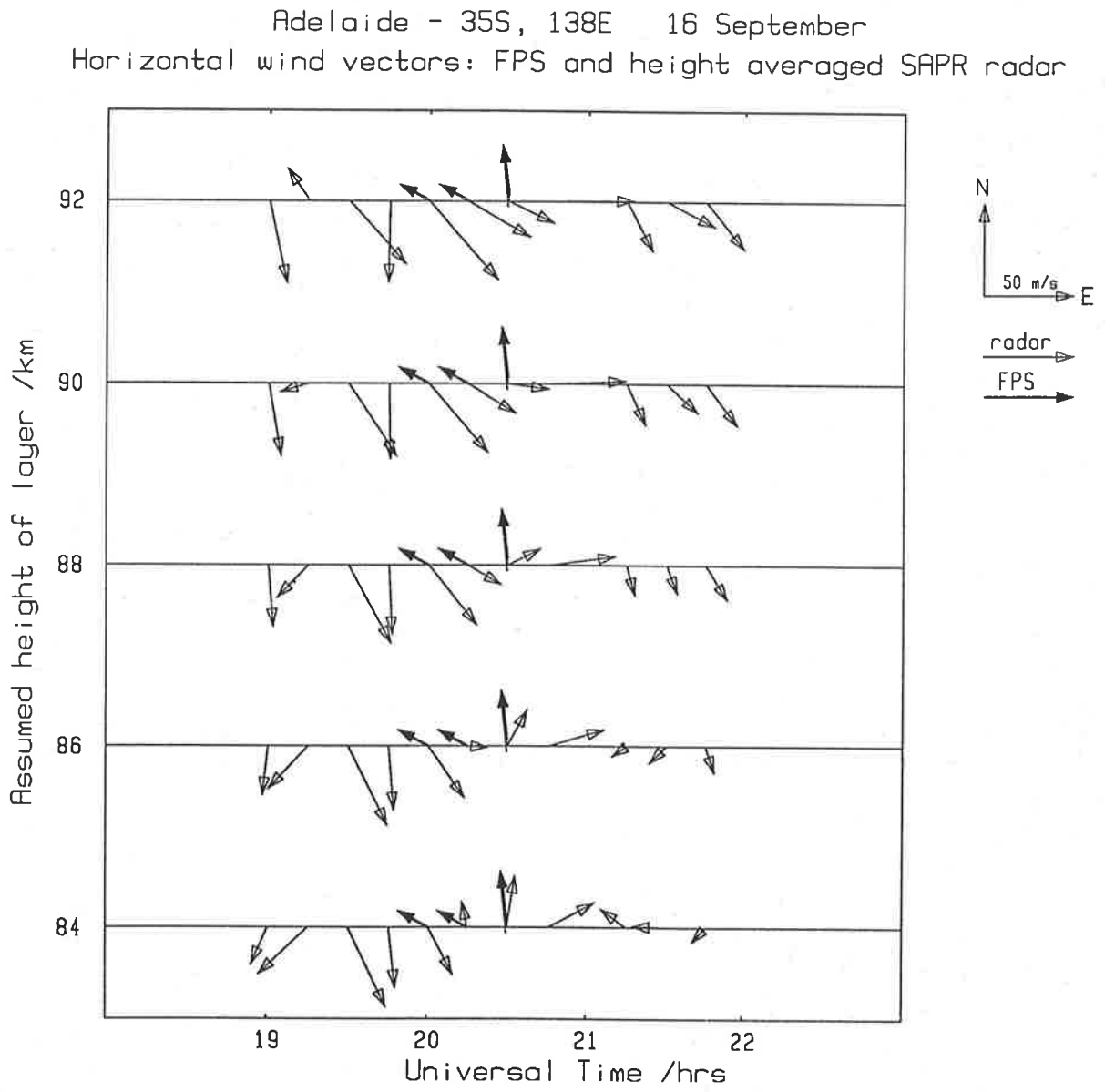

Figure 7.8: FPS/SAPR radar comparison for dusk on 16 Sept, 1987. Both sets of vectors were varying so differences between the two data sets probably reflect non-uniformities over the spatial scales sampled by the two systems.

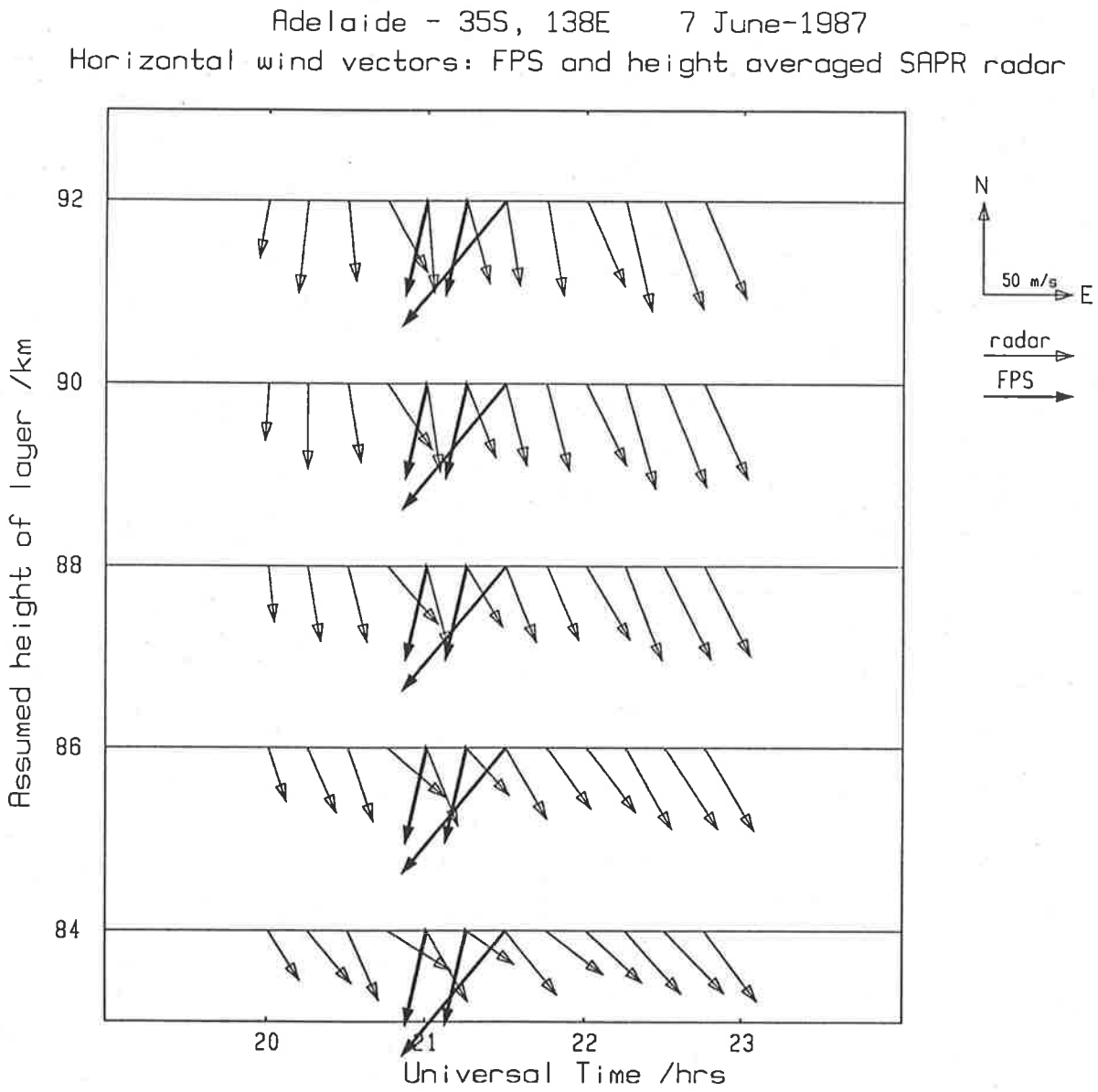

Figure 7.9: FPS/SAPR radar comparison for dawn on June 7, 1987. The meridional wind components are in reasonable agreement but zonal directions are different. This was possibly the result of wave motions propagating in the zonal direction.

FPS observations, has been included in table 7.2. The total horizontal velocity divergence is the sum of the meridional and zonal divergences. On all days when the divergence was less than 30 ms^{-1}, except one, the comparison between the FPS and radar is good. This indicates that significant variations in the wind are occurring over spatial scales of 100 km.

The sodium layer is near the mesopause. In this region gravity wave amplitudes are large and waves often saturate and dissipate producing quite large variations in wind velocities.

In conclusion, reasonable agreement has been found between the two techniques; the velocity amplitudes are usually similar and wind directions are usually in agreement when the divergence in the wind field is small. Variations in direction of the wind are possibly due to the presence of gravity waves and other in-homogeneities. To examine this point further some measurements were made where the FPS and SAPR radar were sampling the same region of the atmosphere. Preliminary results from these measurements are presented in the next section.

7.3.4 Line-of-sight winds over Buckland Park

FPS observations at a zenith angle of 29° and an azimuth angle of 302° have been made on several twilights in 1988. In these observations the FPS and SAPR radar are observing the same volume of the atmosphere. The FPS has a semi-angle field of view of 13 mR. The SAPR radar detects echoes from an approximately circular area of the ionosphere about 10 km in radius (Briggs, 1977). In figure 7.10 the relative positions of the two regions are shown. Note that the FPS samples a much smaller region than the radar. Therefore some spatially small fluctuations present in FPS winds may be averaged out in the radar measurements.

Only line-of-sight winds can be measured with the FPS pointed over Buckland Park; the horizontal component of this can be compared to the component of the wind in the same azimuth obtained from the radar measurements. The data have been analysed in a similar manner to the cardinal point observations. No temporal averaging has been performed and each FPS and radar wind value has been plotted. Radar data density is shown in figure 7.11 along with the

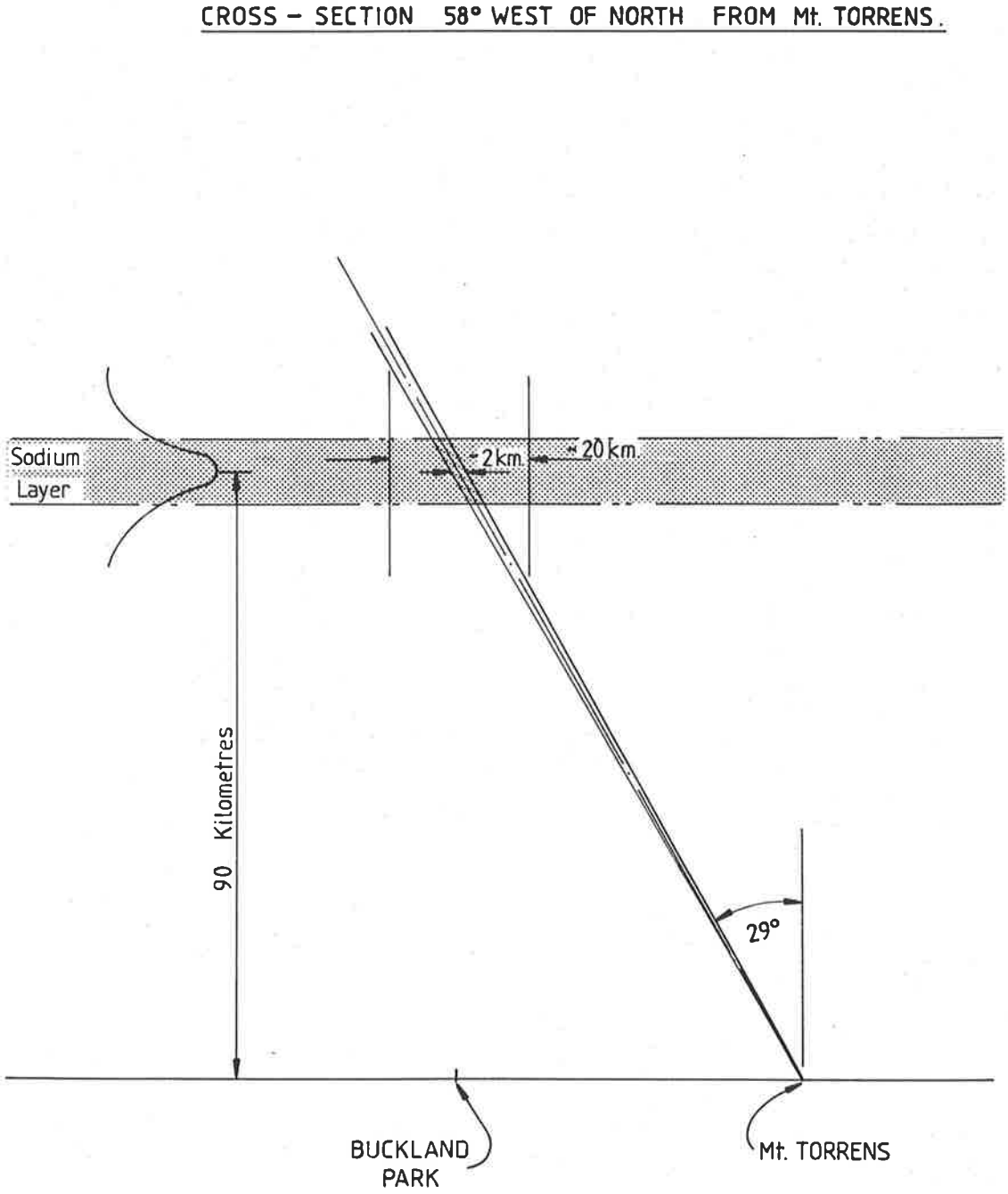

Figure 7.10: Cross-section through the Mt. Torrens, Buckland Park line-of-sight. The approximate regions sampled by the FPS and SAPR radar are shown.

FPS/SAPR radar comparison for dusk on 24 June, 1988. Radar data are weighted by a Gaussian function of 7 km FWHM centred on the five heights 84, 86, 88, 90, and 92 km. Especially good agreement between the two measurements is obtained for the weighting centred at 84 or 86 km. There was a light wind on this day. However changes in the wind amplitude were similar in both data sets. The error bars indicate the error for the FPS wind values derived from that obtained from the fitting routine.

One of the other line-of-sight observations was at dawn. This led to large background contributions as the eastern part of the sky is quite bright when the sun is rising in the north-west; this data has therefore been discarded. For the other two twilights the comparison is presented in figure 7.12. In both cases the SAPR radar data are sparse; on 17 June twilight fell when the radar was being used for another (turbulence) experiment. In both these cases the wind was larger and more variable than on 24 June. General agreement was obtained at lower heights, 84 –86 km.

To avoid the intermittent gaps produced by the turbulence experiment and to obtain a more detailed comparison, a joint FPS/SAPR radar comparison program was scheduled in which the radar was to be operated to sample the regions 70–90 km then 80–100 km at 2 km height intervals every 5 minutes. The first data from this program is presented in figure 7.13. SAPR radar data is dense in the interval. The FPS etalon drift was small and excellent agreement between the two data sets was obtained. As for other line-of-sight comparisons better agreement is obtained at lower heights, 84–86 km. These measurements have been made in winter when the sodium layer is expected to be slightly lower.

Further data will be obtained when the weather conditions allow the FPS to run. This will allow a more thorough comparison and more useful information to be obtained.

(a)

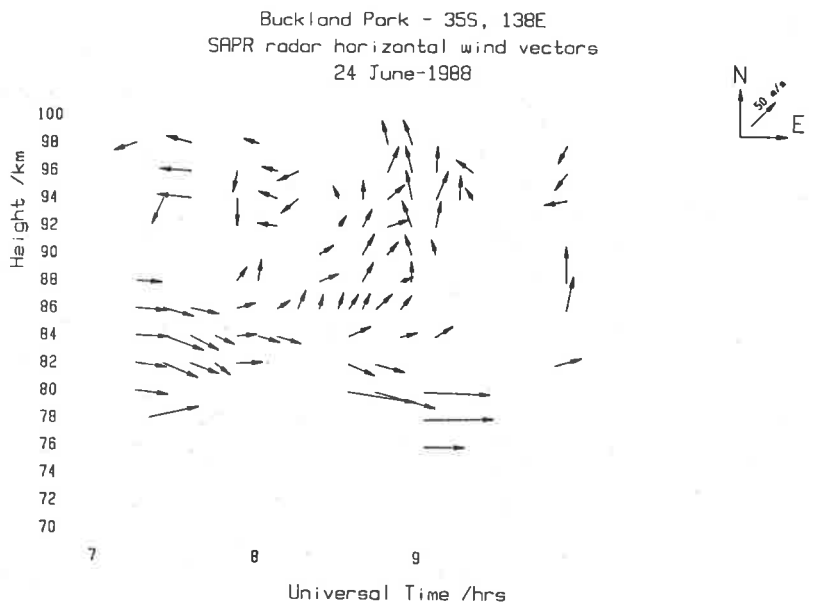

(b)

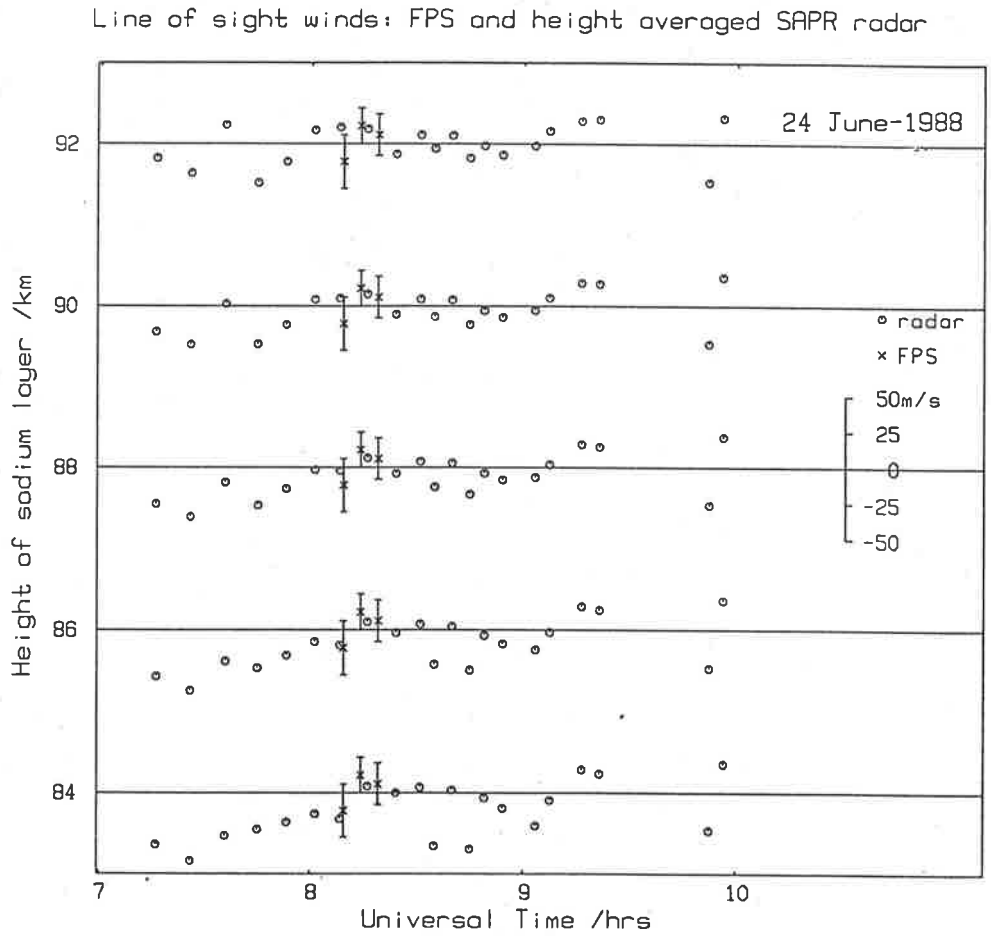

Figure 7.11: Comparison of line-of-sight velocities for 24 June, 1988. In (a) the SAPR radar vectors are given. In (b) the comparison between the radar values weighted by a Gaussian centred at five heights and FPS line-of-sight is given. The error bars on the FPS values are from the error from the fitting routine. The wind magnitude is indicated by the scale on the 88 km height.

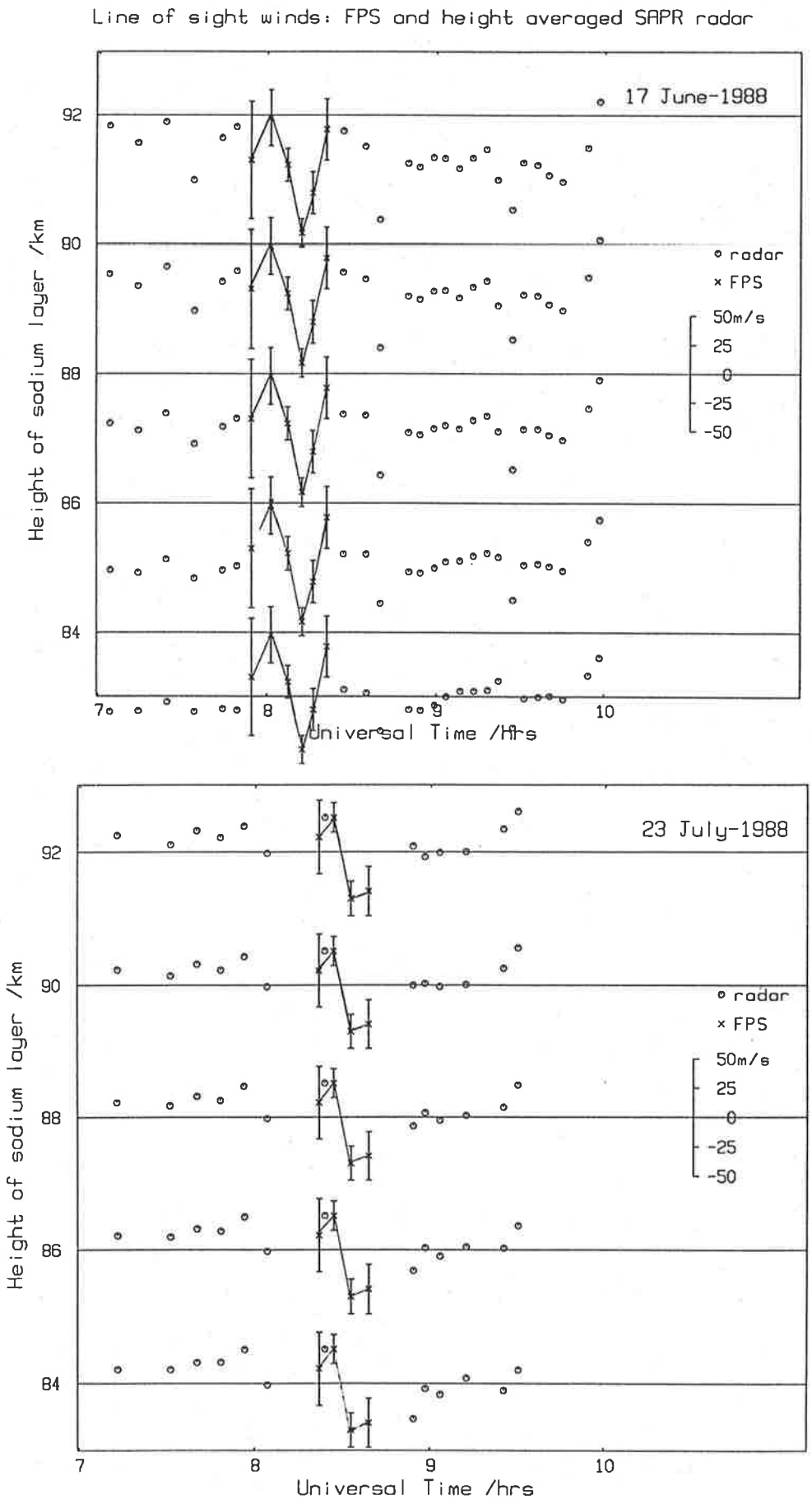

Figure 7.12: Line-of-sight wind comparisons for dusk on 17 June and 23 July, 1988. See figure 7.11 for further details.

(a)

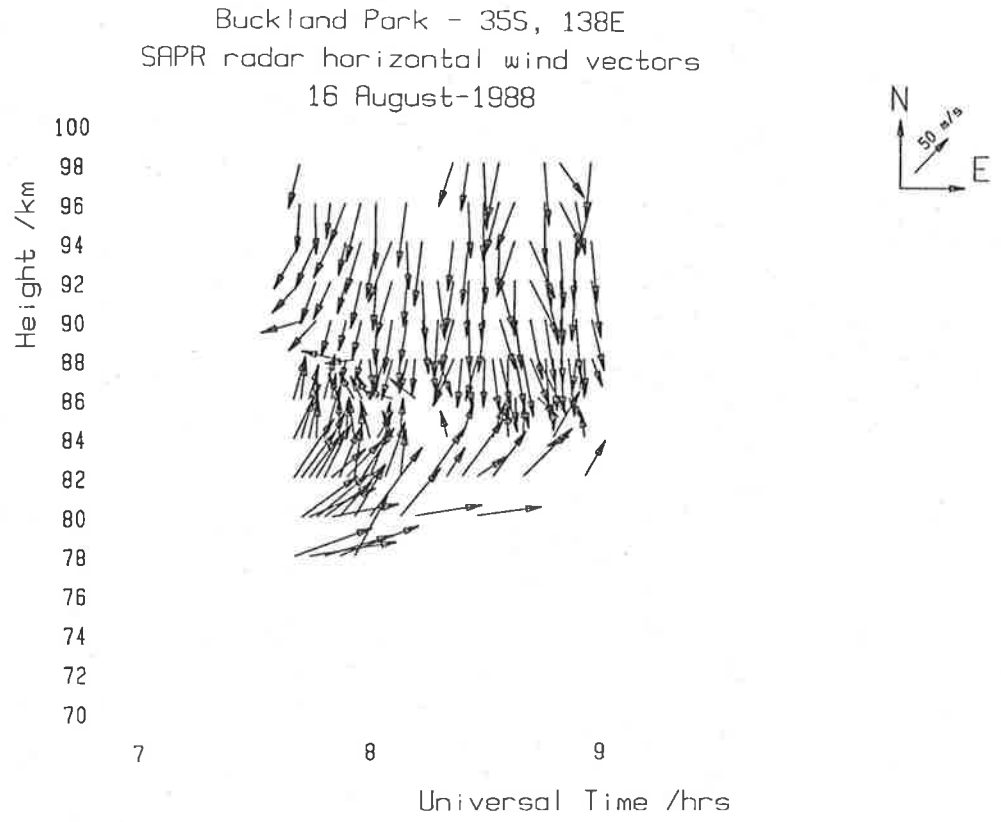

(b)

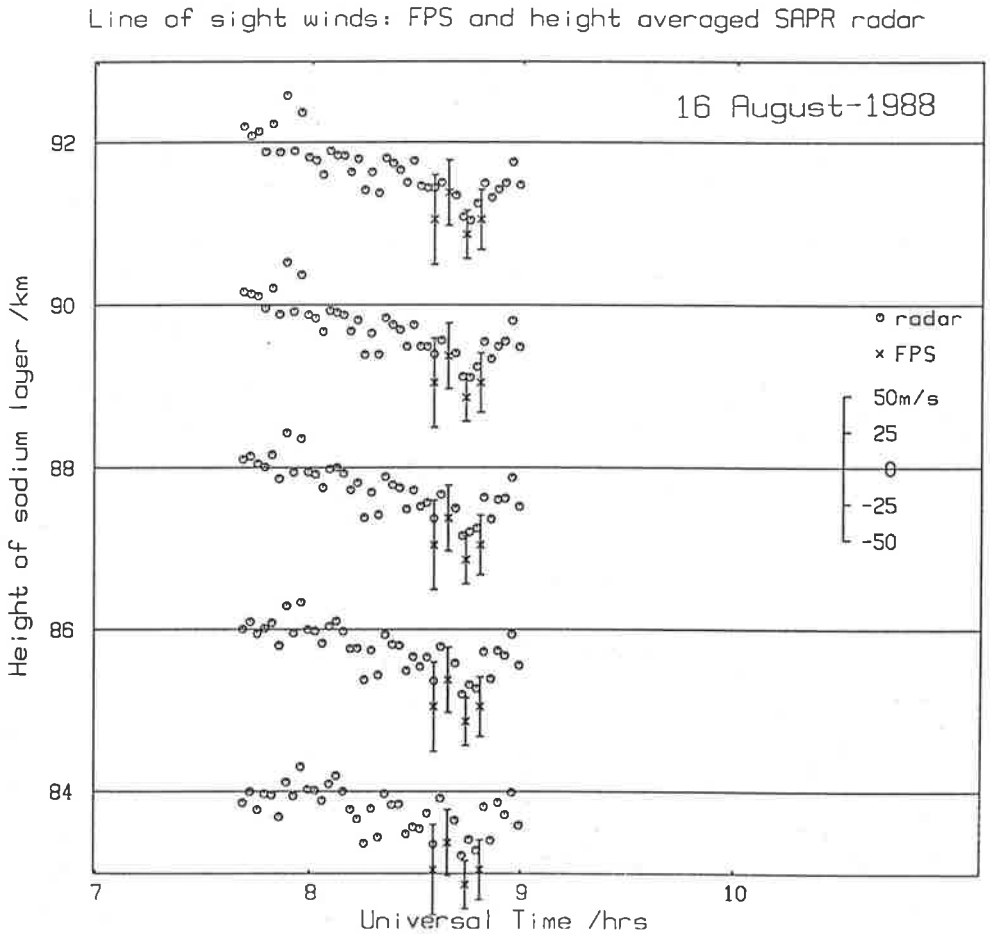

Figure 7.13: Comparison of line-of-sight velocities for 16 August, 1988. In (a) the SAPR radar vectors are given. The higher time resolution radar measurements give denser radar data. In (b) the comparison between the radar values weighted by a Gaussian function centred at five heights and FPS line-of-sight values are given. Excellent agreement between the two data sets is obtained at 84–86 km.

7.3.5 Uncertainties in the FPS and SAPR radar wind measurements

Uncertainties in the FPS measurements arise because of the fitting routine, the instrument drift, and contamination of the emission by Fraunhofer background and street light emission. Compensation for drift has been discussed at length in section 7.1. Bad drift and excessive contamination are obvious in the preliminary analysis and profiles affected were discarded. The uncertainties from the fitting routine, weighted appropriately for conversion from the line-of sight to horizontal wind, were plotted as error bars in the comparisons in the previous section. This uncertainty depends on the signal-to-noise ratio which is a function of emission intensity, background intensity, profile observing duration, and seeing conditions. The uncertainty in the wind estimates, similar to that for vertical winds (section 7.1), is typically 15–20 ms^{-1}. Profiles at the beginning and end of twilight often have larger uncertainties.

Conversion from line-of-sight to horizontal winds involves the assumption of zero vertical wind. Although, on average, the mesospheric, vertical wind will be zero it may at times have a significant effect. A vertical wind, v_z, contributes to the estimated horizontal wind by

$$v_z \frac{\cos 29^\circ}{\sin 29^\circ} = 1.80 v_z. \tag{7.4}$$

A 2 ms^{-1} vertical wind would contribute 3.6 ms^{-1} to the apparent horizontal wind. Vertical winds of up to 10 ms^{-1} have been measured in the mesosphere (Widdell, 1987). In most cases the contribution should be negligible but may, in some cases, explain some differences between FPS winds and radar winds.

No attempt has been made to quantify the uncertainty in the SAPR radar wind measurements. May (1988) discussed the theoretical and statistical errors in the SAPR technique. An rms difference between pairs of observations of 10–15 ms^{-1} was obtained from simultaneous independent wind measurements of spatially close regions. The distribution of the theoretical error estimates was strongly peaked at about 10–20 ms^{-1}. Thus an uncertainty of this magnitude exists for individual radar measurements. The values used in the comparisons are weighted with height. If good height coverage was obtained and the values are consistent

between heights, varying smoothly from one height to the next, then there would be less uncertainty in the weighted value used for comparison. For comparisons made when the radar data are sparse and interpolation or extrapolation over several height ranges occurred then the error associated with radar data is larger. This error will be minimized in the co-ordinated FPS/SAPR radar observations.

7.4 Conclusions and suggestions

FPS observations of the sodium emission at twilight can be used to measure winds in the mesosphere. The instrument is barely adequate for measurements of mesospheric vertical winds. The duration of twilight at Mt. Torrens is too short to resolve the tidal, wave, and mean wind components in the FPS wind measurements.

Comparisons of the FPS and SAPR radar horizontal winds are presented. There is excellent agreement in some cases and, in general, agreement between the two methods is good when the wind field is uniform spatially. A measurement of the uniformity was obtained from the divergence of the FPS measurements. Small divergence and reasonable agreement occurred on about one third of the twilights on which data are presented. At other times there is considerable variability, probably due to a non-homogeneous wind field.

The FPS/SAPR radar comparison was extended to wind magnitudes in the line-of-sight of the FPS over Buckland Park. These gave general agreement on all occasions. Although the two instruments are observing the same region the radar is averaging over a significantly larger volume, hence identical winds should not be expected all the time.

Although twilight wind measurements from Mt. Torrens are of limited value the technique would be more powerful for polar regions where dusk and dawn merge at mid-summer and mid-winter thus allowing considerably longer observing times. Longer data sets would allow identification of individual phenomena and more detailed study of the dynamics at the height of the sodium layer. This region is of considerable interest as it links the thermosphere and

mesosphere and is the region where waves generated in the lower atmosphere dissipate and saturate.

Chapter 8

CONCLUSIONS AND RECOMMENDED FURTHER STUDIES

The λ 589.0/589.6 nm sodium emission is produced by a thin layer of neutral sodium atoms centered at about 88 km in the atmosphere. The emission is produced by resonant excitation by sunlight and a small contribution is made by a photochemical excitation mechanism.

A brief review has been presented of earlier observations of the emission using Fabry-Perot spectrometers (Sipler and Biondi 1975, 1977; Hernandez 1975) to determined temperature at twilight, and to estimate the excess energy of the photochemical production reactions. Observations over a period of three years of twilight, and attempts at daytime observations using the Mt. Torrens dual-scanning Fabry-Perot spectrometer have been presented. Both wind and temperature have been determined from the twilight observations.

Upgrades to the instrument have been described with emphasis on testing new etalons. Application of hard antireflection coatings to the back surfaces of the etalons produced stress in the plates, significantly decreasing the etalon finesse. Removing the hard AR coatings and applying soft antireflection coatings gave a final etalon finesse of 15.9 $\pm$ 1.4 at λ 589.6 nm for

the high-resolution etalon. An instrument finesse of 12.0 ± 0.1, at an order of m = 23150 for λ 589 nm and using a 13 mR field of view at the etalon, was obtained with the instrument in its standard configuration for high-resolution twilight sodium observations.

Some improvement in the instrument would be obtained by replacing the photomultiplier with an imaging photocathode. This would also involve changes in the collecting and output optics to obtain an image of the sky on the photocathode. The etalon would still be scanned to give a profile at each unit of the photocathode. This would allow a considerable improvement in temporal and spatial resolution of the winds and temperatures. An imaging system may have some difficulty at twilight as conditions suitable for obtaining sodium twilight profiles occur in the east about 15 min prior to when they occur in the west. Meridional bands of data could be obtained with an imaging system at twilight. The instrument would then also be more useful for further studies of the oxygen thermospheric emissions.

A sodium hollow-cathode lamp emission line profile has been used for analysis of twilight data. This permits estimates of both the instrument function and the hyperfine structure in the sodium emission profile. The lamp is also very useful for specifying the rest wavelength for Doppler determinations of the wind.

Temperatures obtained from two years of twilight observations are presented in chapter 6. Care is required in interpretation and selection of data as contamination by Rayleigh-scattered sunlight and by photochemical emission affects the temperature derived from the analysis. A summer mean temperature of 150 K and a winter mean of 199 K have been obtained. Temperature measurements from both dusk and dawn have been obtained and a significant temperature difference has been noted for the months January - April. This difference can be ascribed to the diurnal tide. A comparison between the dawn − dusk temperature difference and that predicted by a recent theoretical model together with measurements of the amplitude and phase of the diurnal tide from the nearby Buckland Park spaced-antenna partial reflection (SAPR) radar gave reasonable agreement.

A comparison of the horizontal wind determined from the FPS sodium observations and the SAPR radar gave agreement when the wind field was uniform spatially. A estimate of the uniformity was obtained from the divergence of the FPS measured winds. Small divergence and reasonable agreement occurred on about one third of the twilights on which data were presented. Excellent agreement was obtained in some cases.

The FPS/SAPR radar comparison was extended to wind magnitudes in the line-of-sight of the FPS over Buckland Park. General agreement was obtained on all occasions. A significantly larger volume is being sampled by the radar hence indentical winds should not be expected at all times. This comparison is continuing with high time resolution radar observations to investigate possible seasonal effects.

The FPS winds alone are of limited value as the duration of twilight at Mt. Torrens is too short for tidal, mean wind, and wave components to be isolated. At polar latitudes twilights are much longer and near mid-Summer and mid-Winter dusk and dawn merge giving a period of several hours during which it may be possible to observe the twilight emission. Such observations are planned for Mawson, Antarctica, where a similar instrument is located. Variations in the winds and temperatures over longer twilights will permit studies in more detail than is possible at mid-latitudes.

A SAPR radar is also located at Mawson. Studies of the winds using the Mawson radar have found a correlation between both the mean wind and tides and geomagnetic activity — especially above 90 km in altitude (Phillips 1987; Price 1988). The SAPR radar observes reflections from charged ionization assumed to be travelling with the neutral wind. It is possible, especially at higher latitudes, that the thermospheric electric field may affect the motions of the ionization. The radar may be measuring motions produced by a combination of the neutral wind and electric field especially during periods of high geomagnetic activity and above 90 km height. Simultaneous SAPR radar/ FPS sodium observations at Mawson would permit comparisons of the wind field and, as the FPS measures the neutral wind, investigations into other possible

contributions to the drifts observed by the SAPR radar. This will be possible for the 85–90 km region where the sodium layer is located.

The two instruments at Mawson cannot be used to measure horizontal winds in a common volume as the two instruments are co-located and the radar field of view is in the zenith.

Improvements to the dual scanning FPS by using a three period filter at the D2 wavelength may enable isolation of the sodium dayglow feature. This would permit winds and temperatures of the 85–90 km region to be obtained over considerably longer periods, 24 hours at polar latitudes.

References

Ahmed, M., Silverman, S.M., and LLoyd, J.W.F. (1970). Rocket measurements of sodium dayglow. *Planetary and Space Science* **18**:1666–1668.

Akmaev, R.V. and Shved, G.M. (1980). Modelling of the composition of the lower atmosphere taking account of the dynamics with applications to tidal variations of the [OI] 5577a airglow. *Journal of atmospheric and terrestrial Physics* **42**:705–716.

Albano, J., Blamont, J.E., Chanin, M.L., Petitdidier, M. (1970). Observation of dayglow at the resonance wavelength of sodium and potassium, Seasonal and diurnal variations. *Annales de Geophysica* **26**:151–160.

Avery, S.K. and Tetenbaum, D. (1983). Simultaneous sodium and wind measurements in the upper mesosphere using the Urbana meteor radar and lidar systems. *Journal of atmospheric and terrestrial Physics* **45**:753–764.

Baker, D.J., Steed, A.J., Ware, G.A., Offermann, D., Lange, G., and Lauche, H. (1985). Ground-based atmospheric infra-red and visible emission measurements. *Journal of atmospheric and terrestrial Physics* **47**:133–145.

Bates, D.R. (1983). Forbidden atomic lines in auroral spectra. in *Atoms in Astrophysics.* edited by Burke, P.G., Eissner, W.B., Hummer, D.G., and Percival, I.C. Plenum Press, New York.

Barmore, F.E. (1975). The filling-in of Fraunhofer lines in the day sky. *Journal of atmospheric Science* **32**:1489–1493.

Barmore, F.E. (1977). High resolution observations of the 6300 A oxygen line in the day airglow. *Planetary and Space Science* **25**:185–191.

Barnett, J.J. and Corney, M. (1985). A middle atmosphere temperature reference model from satellite measurements. Advances in Space Science **5**:125–134.

Barnett, J.J., Corney, M., Murphy, A.K., Jones, R.L., Rodgers, C.D., Taylor, F.W., Williamson, E.J., and Vyas, N.M. (1985). Global and seasonal variability of the temperature and composition of the middle atmosphere *Nature* **313**:439–443.

Batista, P.P., Clemesha, B.R., Simonich, D.M., and Kirchhoff, V.W.J.H (1985). Tidal oscillations in the atmospheric sodium layer. *Journal of geophysical Research* **90**:3881–3888.

Battaner, E., and Sanchez-Saavedra, M.L. (1984). Temperature measurements of the high attmosphere by optical methods. *Annales Geophysicae* **2**:67–72.

Beatty, T.J., Bills, R.E., Kwon, K.H., and Gardner, C.S. (1988). CEDAR lidar observations of sporadic Na layers at Urbana Illinois. *Journal of geophysical Research* (in press).

Beer, T. (1977). On atmospheric wave generation by the terminator. *Planetary and Space Science* **26**:185–188.

Bens, A.R., Cogger, L.L. and Shepard, G.G. (1965). Upper atmosphere temperatures from doppler line widths III Observations of the [O1] dayglow emission at 6300A. *Planetary and Space Science* **13**:551–563.

Bernard, R. (1938). Das Vorhandensen von Natrium in der Atmosphäre auf Grund von interferometrischen Untersuchungen der D-line im Abend und Nachimmellicht. Zeitschrift fur Physic **110**:291–302.

Blamont, J.E., Chanin, M.L., and Megie, G. (1972). Vertical distribution and temperature profile of the nighttime atmospheric sodium layer obtained by laser backscatter. *Annales de Geophysica* **28**:833–838.

Blamont, J.E. and Donahue, T.M. (1961). The dayglow of the sodium D line. *Journal of geophysical Research* **66**:1407–1423.

Blamont, J.E. and Donahue, T.M. (1964). Sodium dayglow: Observation and interpretation of a large diurnal variation. *Journal of geophysical Research* **69**:4093–4127.

Blamont, J.E., Donahue, T.M., and Stull, V.R. (1958). The sodium twilight airglow 1955 – 1957 *Annales de Geophysica* **14**:253–281.

Blamont, J.E. and Luton, J.M. (1972). Geomagnetic effect on the neutral temperature of the F region during magnetic storm of September, 1969. *Journal of geophysical Research* **77**:3534–3556.

Born, M. and Wolf, E. (1970). *Principles of Optics.* Fourth Edition, Pergamon Press, Oxford.

Bracewell, R.N. (1978). *The Fourier transform and its applications.* McGraw-Hill International Book Company, Japan.

Briggs, B.H. (1977). Ionospheric drifts. *Journal of atmospheric and terrestrial Physics* **39**:1023–1033.

Briggs, B.H. (1984). The analysis of spaced sensor records by correlation techniques. *Handbook for MAP* **13**:166–186.

Bucholtz, A., Skinner, W.R., Abreu, V.J., and Hays, P.B. (1986). The dayglow of the O_2 atmospheric band system. *Planetary and Space Science* **34**:1031–1035.

Bullock, W.R. and Hunten, D.M. (1961). Vertical distribution of sodium in the upper atmosphere. *Canadian Journal of Physics* **39**:976–982.

Burnett, C.R. (1965). Anomalous abundance of upper atmospheric sodium. *Science* **147**:736–737.

Burnett, C.R. and Burnett, E.B. (1983). OH Pepsios *Applied Optics* bf 22:2887–2892.

Burnett, C.R., Lammer, W.E., Novak, W.T., and Sides, V.L. (1972). Absorption measurements of upper atmospheric sodium at Boca Raton, Florida, 1967–71. *Journal of geophysical Research* **77**:2934–2941.

Burnett, C.R., Lasher, R.W., Miskin, A.S., and Sides, V.L. (1975). Spectroscopic measurement of sodium dayglow: Absence of a large diurnal variation. *Journal of geophysical Research* **80**:1837–1844.

Chamberlain, J.W. (1961). *Physics of the Aurora and Airglow.* Academic Press, London.

Chanin, M.L. and Goutail, J.P. (1975). Diurnal variation of the sodium dayglow. *Journal of geophysical Research* **80**:2854–2858.

Chanin, M.L., Hauchecorne, A., and Smires, N. (1985). Contribution to the CIRA model from ground-based lidar. *Handbook for MAP* **16**:305–314.

Chanin, M.L., Smires, N., and Hauchecorne, A. (1987). Long-term variation of the temperature of the middle atmosphere at mid-latitude: Dynamic and radiative causes. *Journal of geophysical Research* **92**:10933–10941.

Chapman, S. and Lindzen, R.S. (1970). *Atmospheric Tides.* D.Reidel, Dordrecht, The Netherlands.

Chimonas, G. and Axford, W.I. (1968). Vertical movement of temperate zone sporadic E layers. *Journal of geophysical Research* **73**:111–117.

CIRA 1972 (1972). *COSPAR International Reference Atmosphere.* Akademie-Verlag, Berlin, G.D.R..

Clemesha, B.R., Kirchhoff, V.W.J.H., and Simonich, D.M. (1978). Simultaneous observations of the sodium 5893A nightglow and the distribution of sodium atoms in the mesosphere. *Journal of geophysical Research* **83**:2499–2503.

Clemesha, B.R., Kirchhoff, V.W.J.H., Simonich, D.M., Takahashi, H., and Batista, P.P. (1979). Simultaneous observations of sodium density and the NaD, OH(8–3), and OI 5577A nightglow emissions. *Journal of geophysical Research* **84**:6477–6482.

Clemesha, B.R., Kirchhoff, V.W.J.H., Simonich, D.M., Takahashi, H., and Batista, P.P. (1980). Spaced lidar and nightglow observations of an atmospheric sodium enhancement. *Journal of geophysical Research* **85**:3480–3484.

Clemesha, B.R., Simonich, D.M., Batista, P.P., and Kirchhoff, V.W.J.H. (1982). The diurnal variation of atmospheric sodium. *Journal of geophysical Research* **87**:181–186.

Cocks, T.D. (1977). *High spectral resolution studies of the atomic oxygen, λ630 nm, dayglow.* PhD Thesis, University of Adelaide.

Cocks, T.D. (1983). Dual Fabry-Perot spectrometer measurements of daytime thermospheric temperature and wind velocity : data analysis procedures. *Applied Optics* **22**:726–732.

Cocks, T.D., Creighton, D.F., and Jacka, F. (1980). Application of a dual Fabry-Perot spectrometer for daytime airglow studies. *Journal of atmospheric and terrestrial Physics* **42**:499–511.

Cocks, T.D. and Jacka, F. (1978). Daytime thermospheric temperatures, wind velocities and emission intensities derived from ground based observations of the OI λ630 nm airglow line profile. *Journal of atmospheric and terrestrial Physics* **41**:409–415.

Cogger, L.L., and Shepard,G.G. (1965). Interferometric observations of the day sky at 6300A. *Planetary and Space Science* **13**:1163–1164.

Coulson, K.L. (1971). On the solar radiation field in a polluted atmosphere. *Journal of quantitative Spectroscopy and radiative Transfer* **11**:739–755.

Coulson, K.L. (1975). *Solar and terrestrial radiation.* Academic Press, New York.

Coulson, K.L., Dave, J.V., and Sekera, Z. (1960). *Tables related to radiation emerging from a planetary atmosphere with Rayleigh scattering.* University of California Press, Berkeley.

Donahue, T.M. and Meier, R.R. (1967). Distribution of sodium in the daytime upper atmosphere as measured by a rocket experiment. *Journal of geophysical Research* **72**:2803–2829.

Donahue, T.M. Guenther, B., and Blamont, J.E. (1972). Noctilucent clouds in daytime: Circumpolar particulate layers near the summer mesopause. *Journal of atmospheric Science* **29**:1205–1209.

Delbouille, L., Roland, G., and Neven, L. (1973). *Photometric atlas of the solar spectrum from λ3000 to λ10,000 A.* Institute d'Astrophysique de l'Universite de Liege B-4200 Cointe-Ougree, Belgium.

Dunkerton, T.J. (1981). Wave transience in a compressible atmosphere. Part 1: Transient internal wave, mean flow interaction. *Journal of atmospheric Science* **38**:281–297.

Ennos, A.E. (1966). Stresses developed in optical film coatings. *Applied Optics* **5**:51–61.

Forbes, J.M. (1981). Tidal effects on D and E region ion chemistries. *Journal of geophysical Research* **86**:1551–1563.

Forbes, J.M. (1982a). Atmospheric tides **1.** Model description and results for the solar diurnal tide. *Journal of geophysical Research* **87**:5222–5240.

Forbes, J.M. (1982b). Atmospheric tides **2.** The solar and lunar semidiurnal components. *Journal of geophysical Research* **87**:5241–5252.

Forbes, J.M. (1982c). Temperature and solar zenith angle control of D-region positive ion chemistry. *Planetary and Space Science* **30**:1065–1072.

Forbes, J.M. (1984). Middle atmospheric tides. *Planetary and Space Science* **46**:1049–1067.

Forbes, J.M. (1985). Temperature structure of the 80 km to 120 km region. *Handbook for MAP* **16**:231–238.

Forbes, J.M. and Garret, H.B. (1978). Thermal excitation of atmospheric tides due to insolation absorption by O_3 and H_2O. *Geophysical research Letters* **5**:1013–1016.

Forbes, J.M. and Garret, H.B. (1979). Theoretical studies of atmospheric tides. *Reviews of Geophysics and Space Physics* **17**: 1951–1981.

Forbes, J.M. and Gillette, D.F. (1982). A compendium of theoretical tidal structures. Part 1: Model description and explicit structures due to realistic thermal and gravitational excitation. AFGL-TR-82-0173(1) Environmental Research Papers No. 780(1).

Forbes, J.M. and Hagan, M.E. (1982). Thermospheric extensions of the classical expansion functions for semidiurnal tides. *Journal of geophysical Research* **87**:5253–5259.

Forbes, J.M. and Vincent, R.A. (1988). Effects of mean winds and dissipation on the diurnal propagating tide: An analytic approach. *Planetary and Space Science* in press.

Forsyth, R.J. and Wraight, P.C. (1987). A survey of research on nightglow variability. *Planetary and Space Science* **35**:1449–1461.

Freund, J.T. and Jacka, F. (1979). Structure in the λ557.7 nm [O1] airglow. *Journal of atmospheric and terrestrial Physics* **41**:25–31.

Fricke, K.H. and von Zahn, U. (1985). Mesopause temperatures derived from probing the hyperfine structure of the D2 resonance line of sodium by lidar. *Journal of atmospheric and terrestrial Physics* **47**:499–512.

Fritts, D.C. (1984). Gravity wave saturation in the middle atmosphere: A review of theory and observations. *Reviews of Geophysics and Space Physics* **22**:275–308.

Fritts, D.C. and Rastogi, P.K. (1985). Convective and dynamical instabilities due to wave motions in the lower and middle atmosphere: Theory and observations. *Radio Science* **20**:1247–1277.

Fritts, D.C. and Vincent, R.A. (1987). Mesospheric momentum flux studies at Adelaide, Australia: Observations and a Gravity Wave-Tidal interaction model. *Journal of atmospheric Science* 44:605–619.

Fukuyama, K., Maekawa, Y., Fukao, S., and Kato, S. (1987). Ionospheric D-region temperatures, and electron and neutral densities observed by the incoherent scatter technique at Aricebo. *Annales Geophysicae* **5A**:289–296.

Ganguly, S. (1980). Incoherent scatter observations of mesospheric dynamics at Aricebo. *Geophysical research Letters* **7**:369–372.

Gadsden, M., Donahue, T.M., and Blamont, J.E. (1966). On the measurement of sodium dayglow emission by means of a Zeeman Photometer. *Journal of geophysical Research* **71**:5047–5057.

Gadsden, M. and Purdy, C.M. (1970). Observations of the sodium dayglow. *Annales de Geophysica* **26**:43–51.

Garcia, R.R., and Solomon, S. (1985). The effect of breaking gravity waves on the dynamics and chemical composition of the mesosphere and lower thermosphere. *Journal of geophysical Research* **90**:3850–3868.

Gardner, C.S., and Shelton, J.D. (1985). Density response of the neutral atmospheric layers to gravity wave perturbations. *Journal of geophysical Research* **90**:1745–1754.

Gardner, C.S., Senft, D.C., and Kwon, K.H. (1988). Lidar observations of a substantial sodium depletion in the summer-time Arctic mesophere. *Nature* **332**:142–144.

Gardner, C.S., and Voelz, D.G. (1985). Lidar measurements of gravity wave saturation effects in the sodium layer. *Geophysical research Letters* **12**:765–768.

Gardner, C.S., and Voelz, D.G. (1987). Lidar studies of the nighttime sodium layer over Urbana, Illinois. **2** Gravity Waves. *Journal of geophysical Research* **92**:4673–4694.

Gardner, C.S., Voelz, D.G., Philbrick, C.R., and Sipler D.P. (1986a). Simultaneous lidar measurements of the sodium layer at the Air Force Geophysics Laboratory and the Univesity of Illinois. *Journal of geophysical Research* **91**:12131–12136.

Gardner, C.S., Voelz, D.G., Sechrist Jr, C.F., and Segal A.C. (1986b). Lidar studies of the nighttime sodium layer over Urbana, Illinois. **1** Seasonal and nocturnal variations. *Journal of geophysical Research* **91**:13659–13673.

Geller, M.A. (1983). Dynamics of the middle atmosphere. *Space Science Reviews* **34**:359–375.

Gibson, A.J. and Sandford M.C.W. (1971). The seasonal variation of the nighttime sodium layer. *Journal of atmospheric and terrestrial Physics* **33**:1675–1684.

Gibson, A.J. and Sandford M.C.W. (1972). Daytime laser radar measurements of the atmospheric sodium layer. *Nature* **239**:509–511.

Gibson, A.J., Thomas, L., and Bhattacharyya S.K. (1979). Laser observations of the ground-state hyperfine structure of sodium and of temperatures in the upper atmosphere. *Nature* **281**:131–132.

Gossard, E.E., and Hooke, W.H. (1975). *Waves in the Atmosphere.* Elsevier Scientific Publishing Company, Amsterdam, The Netherlands.

Grainger, J.R. and Ring, J. (1962). Anomalous Fraunhofer line profiles. *Nature* **193**:762.

Granier, C., Jegou, J.P., Channin, M.L., and Megie, G. (1985). General theory of the alkalie metals present in the earth's upper atmosphere III Diurnal variations. *Annales Geophysicae* **3**:445–450.

Granier, C. and Megie, G. (1982). Daytime lidar measurements of the mesospheric sodium layer. *Planetary and Space Science* **30**:169–177.

Greer, R.G.H. and Best, G.T. (1967). A rocket-bourne investigation of the oxygen lines 5577A and 6300A, the sodium D lines and the continuum at 8300A in the night airglow. *Planetary and Space Science* **15**:1857–1881.

Greer, R.G.H., Murtagh, D.P., McDade, I.C., Dickinson, P.G.H., Thomas, L., Jenkins, D.B., Stegman, J., Llewellyn, E.J., Witt, G., Mackinnon, D.J., Williams, E.R. (1986). ETON 1: A database pertinent to the study of energy transfer in the oxygen nightglow. *Planetary and Space Science* bf 34:771–788.

Greet, P.A. (1986). Coating stress in Fabry-Perot etalons. *Applied Optics* **25**:3328–3330.

Groves, G.V. (1982a). Hough components of ozone heating. *Journal of atmospheric and terrestrial Physics* **44**:111–121.

Groves, G.V. (1982b). Hough components of water vapour heating. *Journal of atmospheric and terrestrial Physics* 44:281–290.

Groves, G.V. (1985). AFGL-TR-85-0129 AFGL Technical Report, Airforce Geophysics Laboratory, Hanscom, AFB, MA 01731.

Groves, G.V. (1988). AFGL Technical Report, Airforce Geophysics Laboratory.

Hake, R.D., Arnold, D.E., Jackson, D.W., Evans, W.E., Ficklin, B.P., and Long, R.A. (1972). Dye-laser observations of the nighttime atomic sodium layer. *Journal of geophysical Research* **77**:6839–6848.

Hall, C., Hoppe, U.-P., Williams, P.J.S., and Jones, G.O.L. (1987). Mesospheric measurements using the EISCAT VHF system: First results and their interpretation. *Geophysical research Letters* **14**:1187–1190.

Hauchecorne, A., Blix, T., Gerndt, R., Kokin, G.A., Meyer, W., and Shefov, N.N. (1987a). Large-scale coherence of the mesospheric and upper stratospheric temperature fluctuations. *Journal of atmospheric and terrestrial Physics* **49**:649–654.

Hauchecorne, A., Chanin, M.L., and Wilson, R. (1987b). Mesospheric temperature inversion and gravity wave breaking. *Geophysical research Letters* **14**:933–936.

Hays, P.B., Killeen, T.L., and Kennedy, B.C. (1981). The Fabry-Perot interferometer on Dynamics Explorer. *Space Science Instrumentation* **5**:395–416.

Hedin, A.E. (1983). A revised thermospheric model based on mass spectrometer and incoherent scatter data: MSIS-83 *Journal of geophysical Research* **88**:10170–10188.

Hedin, A.E. (1987). MSIS-86 Thermospheric model. *Journal of geophysical Research* **92**:4649–4662.

Henderson, G. and Slater, P.V. Interpretation of dayglow data obtained by Fabry-Perot Interferometry. *Planetary and Space Science* **14**:1035–1037.

Hernandez, G. (1975). Reaction broadening of the line profiles of atomic sodium in the night airglow. *Geophysical research Letters* **2**:103–105.

Hernandez, G. (1976). Lower-thermosphere temperatures determined from the line profiles of the O1 17924 K (5577A) emission in the night sky. **1** Long term behaviour. *Journal of geophysical Research* **81**:5165–5172.

Hernandez, G. (1986). *Fabry-Perot Interferometers.* in Cambridge Studies in Modern Optics Volume **3**. Cambridge University Press.

Hernandez, G., Mills, O.A., and Smith, J.L. (1981). TESS: A high resolution high luminosity twin etalon scanning spectrometer. *Applied Optics* **20**:3687–3686.

Hernandez, G. and Roper, R.G. (1979). A comparison between radio meteor and airglow winds. *Journal of Geomagnetism and Geoelectricity* **31**:419–426.

Hines, C.O. (1960). Internal atmospheric gravity waves at ionospheric heights. *Canadian Journal of Physics* **38**:1441–1481.

Hines, C.O. (1965). Dynamical heating of the upper atmosphere. *Journal of geophysical Research* **70**:177–183.

Hines, C.O. and Tarasick, D.W. (1987). On the determination and utilization of gravity waves in airglow studies. *Planetary and Space Science* **35**:851–866.

Hirschfield, T. (1968). Improvements in photomultipliers with total internal reflection sensitivity enhancement. *Applied Optics* **7**:443–449.

Holton, J.R. (1979). *An introduction to dynamic meteorology* 2nd ed. Academic Press, New York.

Holton, J.R. (1982). The role of gravity wave-induced drag and diffusion in the momentum budget of the mesosphere. *Journal of atmospheric Science* **39**:791–799.

Holton, J.R. (1983). The influence of gravity-wave breaking on the general circulation of the middle atmosphere. *Journal of atmospheric Science* **40**:2497–2507.

Hoppe, U.-P. and Hansen, T. (1988). Studies of vertical motions in the upper mesosphere using the EISCAT UHF radar. *Annales Geophysicae* **6**:181–186.

Houghton, J.T. (1986). *The physics of Atmospheres.* Cambridge University Press, Cambridge, U.K..

Hunten, D.M. (1955). Some photometric observations of auroral spectra. *Journal of atmospheric and terrestrial Physics* **7**:141–151.

Hunten, D.M. (1967). Spectroscopic studies of the twilight airglow. *Space Science Reviews* **6**:493–573.

Hunten, D.M. (1970). Surface albedo and filling-in of Fraunhofer lines in the day sky. *Astrophysical Journal* **159**:1107–1110.

Hunten, D.M. (1971). Airglow — Introduction and Review. in *The radiating Atmosphere.* McCormac, B.M. (ed.), D Reidel Publishing Company, Dordrecht Holland.

Hunten, D.M., Vallance-Jones, A., Ellyet, C.P., and McLauchlan, E.C. (1964). Sodium twilight at Christchurch New Zealand. *Journal of atmospheric and terrestrial Physics* **26**:67–76.

Hunten, D.M. and Wallace, L. (1967). Rocket measurements of the sodium airglow. *Journal of geophysical Research* **72**:69–79.

Jacka, F. (1984). Application of Fabry-Perot spectrometers for measurement of upper atmosphere temperature and winds. Ch 2 in *Middle Atmosphere Handbook for MAP* Vol. 13 ed. R. Vincent.

Jacka, F. and Argall, P.S. (1987). A lidar system for stratospheric studies — performance simulation. *ANARE Research Notes* **48**:226–235.

Jacka, F., Bower, A., and Wilksch, P.A. (1979). Thermospheric temperatures and winds derived from OI λ630 nm night airglow line profile. *Journal of atmospheric and terrestrial Physics* **41**:397–407.

Jacka, F., Bower, A., Creighton, D.F.,and Wilksch, P.A. (1980). A large-aperture high-resolution Fabry-Perot spectrometer for airglow studies. *Journal of Physics E: Scientific Instrumentation* **13**:562–568.

Jacob, P.G. and Jacka, F. (1985). Gravity wave vertical flux at 95 km. *Handbook for MAP* **18**:248–252.

Jarret, A.H., and Hoey, M.J. (1963). A ground level photographic observation of the day airglow emission of atomic oxygen at 6300A. *Planetary and Space Science* **11**:1251–1252.

Jarret, A.H., and Hoey, M.J. (1964). Temperature measurements of the day airglow of atomic oxygen at 6300A. *Planetary and Space Science* **12**:1139–1140.

Jegou, J.P., Granier, C., Channin, M.L., and Megie, G. (1985a). General theory of the alkalie metals present in the earth's upper atmosphere I Flux model: chemical and dynamical processes. *Annales Geophysicae* **3**:163–176.

Jegou, J.P., Granier, C., Channin, M.L., and Megie, G. (1985b). General theory of the alkalie metals present in the earth's upper atmosphere II Seasonal and meridional variations. *Annales Geophysicae* **3**:299–312.

Jenkins, F.A. and White, H.E. (1976). *Fundamentals of optics.* McGraw-Hill Kogakusha, Ltd., Toyko.

Kattawar, G.W., Young, A.T., and Humpreys, T.J. (1981). Inelastic scattering in planetary atmospheres I The Ring effect, without aerosols. *Astrophysical Journal* **243**:1049–1057.

Killeen, T.L. and Hays, P.B. (1983). $O(^1S)$ from dissociative recombination of O_2^+: Non-thermal line profile measurements from Dynamics Explorer. *Journal of geophysical Research* **88**:10163–10169.

Killeen, T.L, Kennedy, B.C., Hays, P.B., Symanow, D.A., and Ceckowski, D.H. (1983). Image plane detector fpr the Dynamics Explorer Fabry-Perot interferometer. *Applied Optics* **22**:3503–3513.

Kirchhoff, V.W.J.H. (1983). Atmospheric sodium chemistry and diurnal variations: An update. *Geophysical research Letters* **10**:721–724.

Kirchhoff, V.W.J.H. (1986). Thoery of the atmospheric sodium layer : A review. *Canadian Journal of Physics* **64**:1664–1672.

Kirchhoff, V.W.J.H. and Batista, P.P. (1983). Calculation of the vertical drift of the sodium ion. *Annales Geophysicae* **1**:509–514.

Kirchhoff, V.W.J.H., Batista, P.P., Clemesha, B.R., and Simonich, D.M. (1986). The twilight sodium layer. *Journal of geophysical Research* **91**:13303–13307.

Kirchhoff, V.W.J.H. and Clemesha, B.R. (1983a). The atmospheric neutral sodium layer: 2 Diurnal variations. *Journal of geophysical Research* **88**:442–450.

Kirchhoff, V.W.J.H. and Clemesha, B.R. (1983b). The dissipation of a sodium cloud. *Planetary and Space Science* **31**:369–372.

Kirchhoff, V.W.J.H., Clemesha, B.R., and Simonich, D.M. (1979). Sodium nightglow measurements and implications on the sodium photochemistry. *Journal of geophysical Research* **84**:1323–1327.

Kirchhoff, V.W.J.H., Clemesha, B.R., and Simonich, D.M. (1981a). The atmospheric neutral sodium layer **1** Recent modelling compared to measurements. *Journal of geophysical Research* **86**:6892–6898.

Kirchhoff, V.W.J.H., Clemesha, B.R., and Simonich, D.M. (1981b). Average nocturnal and seasonal variations of sodium nightglow at 23° S, 46° W. *Planetary and Space Science* **29**:765–766.

Kirchhoff, V.W.J.H., Clemesha, B.R., and Simonich, D.M. (1981c). Seasonal variation of ozone in the mesosphere. *Journal of geophysical Research* **86**:1463–1466.

Kirchhoff, V.W.J.H. and Takahashi, H. (1984). Sodium clouds in the lower thermosphere. *Planetary and Space Science* **32**:831–836.

Kondratyev K.YA. (1969). *Radiation in the atmosphere.* Academic Press, New York and London.

Kuiper, G.P. (1953). *The Sun.* University of Chicago Press, Chicago and London.

Kwon, K.H., Gardner, C.S., Senft, D.C., Roesler, F.L., and Harlander J. (1987). Daytime lidar measurements of tidal winds in the mesospheric sodium layer at Urbana, Illinois. *Journal of geophysical Research* **92**:8775–8780.

Kwon, K.H., Senft, D.C., and Gardner, C.S. (1988). Lidar observations of sporadic sodium layers at Mauna Kea observatory, Hawii. *Journal of geophysical Research* (in press).

Labitzke, K., Manson, A.H., Bartnett,J.J., and Corney,M. (1987). Comparison of geostrophic and observed winds in the upper atmosphere over Saskatoon, Canada. *Journal of atmospheric and terrestrial Physics* **49**:987–997.

Lathuillere, C., Wickwar, V.B., and Kofman, W. (1983). Incoherent scatter measurements of ion-neutral collision frequencies and temperatures in the lower thermosphere of the auroral region. *Journal of geophysical Research* **88**: 10137–10144.

Lindzen, R.S. (1981). Turbulence and stress owing to gravity wave and tidal breakdown. *Journal of geophysical Research* **86**:9707–9714.

Liu, S.C. and Reid G.C. (1979). Sodium and other constituents of meteoric origin in the atmosphere. *Geophysical research Letters* **6**:283–286.

Llewellyn, E.J. and Evans, W.F. (1971). The Dayglow. in *The radiating Atmosphere.* McCormac, B.M. (ed.), D Reidel Publishing Company, Dordrecht Holland.

McCartney, E.J. (1976). *Optics of the Atmosphere* John Wiley and Sons, New York.

McNutt, D.P. (1965). PEPSIOS purely interferometric high-resolution scanning spectrometer. **II** Theory of spacer ratios. *Journal of the Optical Society of America* **55**:288–292.

McNutt, D.P. and Mack, J.E. (1963). Telluric absorption, residual intensities and shifts in the Fraunhofer D lines. *Journal of geophysical Research* **68**:3419–3429.

May, P.T. (1988). Statistical errors in the determination of wind velocities by the spaced antenna technique. *Journal of atmospheric and terrestrial Physics* **50**:21–32.

Mack, J.E., McNutt, D.P., Roesler, F.L., and Chabbal, R. (1963). The PEPSIOS purely interferometric high-resolution scanning spectrometer. **I** The pilot model. *Applied Optics* **2**:873–885.

Maissel, L.J. and Glang, R. (1970). *Handbook of thin film technology.* Ch. 12, McGraw Hill, New York.

Meek, C.E. and Manson, A.H. (1983). Measurements of the structure and drift velocities of airglow (λ = 557.7 nm) irregularities: Saskatoon (52° N, 107° W), Canada. *Journal of atmospheric and terrestrial Physics* **45**:203–212.

Megie, G. and Blamont, J.E. (1977). Laser sounding of atmospheric sodium: Interpretation in terms of atmospheric parameters. *Planetary and Space Science* **25**:1093–1119.

Megie, G., Bos, F., Blamont, J.E., and Chanin, M.L. (1978a). Simultaneous night-time lidar measurements of atmospheric sodium and potassium. *Planetary and Space Science* **26**27–35.

Megie, G., Chanin, M.L., Tulinov, G.V., and Doudoladov, Y.P. (1978b). High latitude measurements of the atomic sodium concentration and neutral temperature at the mesopause level by the lidar technique. *Planetary and Space Science* **26**:509–511.

Miller, R.E. and Fastie, W.G. (1972). Skylight intensity, polarization, and airglow measurements during the total solar eclipse of 30th May, 1965. *Journal of atmospheric and terrestrial Physics* **34**:1541–1546.

Miyahara, S. (1985). Suppression of stationary planetary waves by internal gravity waves in the mesosphere. *Journal of atmospheric Science* **42**:100–107.

Moore, C.E. (1953). The identification of solar lines. in Kuiper, G.P. (ed) *The Sun.* University of Chicago Press, Chicago and London.

Myabro, H.K. (1984). Temperature variation at mesopause levels during winter solstice at 78° N. *Planetary and Space Science* **32**:249–255.

Myabro, H.K. (1986). Winter season mesopause and lower thermosphere temperatures in the northern polar region. *Planetary and Space Science* **34**:1023–1029.

Myabro, H.K., Deehr, C.S., and Viereck, R. (1987). Polar mesopause gravity wave activity in the sodium and hydroxyl night airglow. *Journal of geophysical Research* **92**:2527–2534.

Netterfield, R.D., Schaeffer, R.C., and Sainty, W.G. (1980). Coating Fabry-Perot interferometer plates with broadband multilayer dielectric mirrors. *Applied Optics* **19**:3010–3017.

Neuber, R., von der Gathen, P., and von Zahn, U. (1988). Altitude and temperature of the mesopause at 69° N latitude in Winter. *Journal of geophysical Research* (in press)

Newman, A.L. (1988). Night-time Na D emission observed from a polar orbiting DMSP satellite. *Journal of geophysical Research* **93**:4067–4075.

Nomura, A.,Kano, T., Iwasaki, Y., Fukunishi, H., Hirasawa, T., and Kawaguchi, S. (1987). Lidar observations of the mesospheric sodium layer at Swoya station, Antarctica. *Geophysical research Letters* **14**:700–703.

Noxon, J.F. (1968). Day airglow. *Space Science Reviews* **8**:92–134.

Noxon, J.F. and Goody, R.M. (1962). Observations of the day airglow emission. *Journal of atmospheric Science* **19**:342–343.

Noxon, J.F. and Goody, R.M. (1965). Noncoherent scattering of skylight. *IZN Atmospheric oceanic Physics* **1**:163–166.

Offermann, D., Gerndt, R., Kuchler, R., Baker, K., Pendleton, W.R., Meyer, W., von Zahn, U., Philbrick, C.R., Schmidlin, F.J. (1987). Mean state and long term variations of temperature in the Winter middle atmosphere above northern Scandinavia. *Journal of atmospheric and terrestrial Physics* **49**:655–674.

Olsson-Steel, D. and Elford, W.G. (1987). The height distribution of radio meteors: observations at 2 MHz. *Journal of atmospheric and terrestrial Physics* **49**:243–258.

Partowmah, M. and Roesler, F.L. (1977). Absorption studies of daytime sodium abundance. *Journal of geophysical Research* **82**:2607–2612.

Peteherych, S., Shepherd, G.G., and Walker, J.K. (1985). Observations of vertical E-region neutral winds in two intense auroral arcs. *Planetary and Space Science* **33**:869–873

Petitdidier, M. and Teitelbaum, H. (1977). Lower thermosphere emissions and tides. *Planetary and Space Science* **25**:711-721.

Petzoldt, K., Lenshow, R., Hauchecorne, A., Kokin, G.A., Meyer, W., O'Neill, A., Philbrick, C.R., Schmidlin, F., Thomas, R. (1987). Large scale structure of the stratosphere and the lower mesosphere(20-60 km) over the northern hemisphere during the MAP/WINE campaign. *Journal of atmospheric and terrestrial Physics* **49**:621–637.

Philbrick, C.R., Schmidlin, J.F., Grossman, K.V., Lange, G., Offermann, D., Baker, K.D., Krankowsky, D., and von Zahn., U. (1985). Density and temperature structure over northern Europe. *Journal of atmospheric and terrestrial Physics* **47**:159–172.

Phillips, A. and Jacka, F. (1987). Winds in the middle atmosphere at Mawson, Antarctica: III Geomagnetic and "meteorological" effects. ANARE Research Notes **48**:107–103.

Price, G.D. (1988). *Upper atmosphere dynamics in the auroral zone.* PhD Thesis, University of Adelaide.

Ramsay, J.V. (1962). A rapid-scanning Fabry-Perot interferometer with automatic parallelism control. *Applied Optics* **1**:411–413.

Rees, M.H., Romick, G.J., and Belan, A.E. (1975). Intensities of NaD lines in Auroral Zone *Annales de Geophysique* **31**:311–320.

Reid, I.M., and Vincent, R.A. (1987). Measurements of mesospheric gravity wave momentum fluxes and mean flow accelerations at Adelaide, Australia. *Journal of atmospheric and terrestrial Physics* **49**:443–460.

Reiger, E. (1974). Neutral air motions from barium releases experiments 1. Vertical winds. *Journal of atmospheric and terrestrial Physics* **36**:1377–1385.

Richter, E.S., Rowlett, J.R., Gardner, C.S., and Sechrist C.F. (1981). Lidar observations of mesospheric sodium layer over Urbana, Illinois. *Journal of atmospheric and terrestrial Physics* **43**:327–337.

Richter, E.S. and Sechrist C.F. (1979a). A cluster-ion chemistry for the mesospheric sodium layer. *Journal of atmospheric and terrestrial Physics* **41**:579–586.

Richter, E.S. and Sechrist C.F. (1979b). A meteor ablation cluster-ion atmospheric sodium theory. *Geophysical research Letters* **6**:183–186.

Rishbeth, H. and Garriot, O.K. (1969). *Introduction to Ionospheric physics.* Academic Press, New York.

Romick, F.J. (ed.) (1987). *The Cedar Post.* **5** No. 4.

Rundle, H.N. (1971). Dayglow and twilight excitation mechanisms for airglow. in *The radiating Atmosphere.* McCormac, B.M. (ed.), D Reidel Publishing Company, Dordrecht Holland.

Sandford M.C.W., and Gibson, A.J. (1970). Laser radar measurements of atmospheric sodium layer. *Journal of atmospheric and terrestrial Physics* **32**:1423–1430.

Schoeberl, M.R. (1985). The penetration of mountain waves in the middle atmosphere. *Journal of atmospheric Science* **42**:2856–2864.

Scrimger, J.A. and Hunten,D.M. (1957). Absorption of sunlight by atmospheric sodium. *Canadian Journal of Physics* **35**:918–927.

Shelton, J.D., Gardner, C.S., and Sechrist, C.F. (1980). Density response of the mesospheric sodium layer to gravity wave perturbations. *Geophysical research Letters* **7**:1069–1072.

Shibata, T., Kobuchi, M., and Maeda, M. (1986). Measurement of density and temperature profiles in the middle atmosphere with a Xe-F lidar. *Applied Optics* **25**:685–688.

Simonich, D.M., Clemesha, B.R., and Kirchhoff, V.W.J.H. (1979). The mesospheric sodium layer at 23° S: Nocturnal and seasonal variations. *Journal of geophysical Research* **84**:1543–1550.

Sipler, D.P. and Biondi, M.A. (1975). Evidence for chemiexcitation as the source of the sodium airglow. *Geophysical research Letters* **2**:106–108.

Sipler, D.P. and Biondi, M.A. (1978). Interferometeric studies of the twilight and nightglow sodium D-line profiles. *Planetary and Space Science* **26**:65–73.

Skinner, W.R., Hays, P.B., and Abreu, V.J. (1987). Optimization of a triple etalon interferometer. *Applied Optics* **26**:2817–2827.

Slipher, V.M. (1929). Emissions in the spectrum of the light of the night sky. Publications of the Astronomical Society of the Pacific **41**:262–263

Spencer, N.W., Theis, R.F., Wharton, L.E., and Carignan, G.R. (1976). Local vertical motions and kinetic temperature from AE-C as evidence for aurora-induced gravity waves. *Geophysical research Letters* **3**:313–316.

St. John, C.E., Moore, C.E., Ware, L.M., Adams, E.F., and Babcock, H.D. (1928). *Revision of Rowland's preliminary table of Solar Spectrum Wavelengths.* Carnegie Institution of Washington, U.S.A..

Swider, W. (1985). Enhanced seasonal variations for chemical rates with inverse temperature dependences: Application to seasonal abundance of mesospheric sodium. *Geophysical research Letters* **12**:589–591.

Swider, W. (1986a). Mesospheric sodium: Implications using a steady-state model. *Planetary and Space Science* **34**:603–608.

Swider, W. (1986b). Sodium nightglow: chemically independent of sodium content. *Journal of geophysical Research* **91**:6742–6746.

Sze, N.D., Ko, K.W., Swider, W., and Murad, E. (1982). Atmospheric sodium chemistry. 1. The altitude region 70–100 km. *Geophysical research Letters* **9**:1187–1190.

Takahasi, H., Batista, P.P., Sahai, Y., and Clemesha, B.R. (1985). Atmospheric wave propagation in the mesopause region observed by the OH(8,3) band, NaD, O_2 band, O1 5577 A nightglow emissions. *Planetary and Space Science* **33**:381–384.

Takahasi, H., Sahai, Y., and Batista, P.P. (1984). Tidal and solar cycle effects on the OI 5577 A, NaD, and OH (8,3) airglow emissions observed at 23° S. *Planetary and Space Science* **32**:897–902.

Takahasi, H., Sahai, Y., and Batista, P.P. (1986). Airglow $O-2(^1\Sigma)$ atmospheric band at 8645 A and the rotational ttemperature observed at 23° S. *Planetary and Space Science* **34**:301–306.

Tanaka, M. (1971a). Radiative transfer in a turbid atmosphere II Angular distribution of intensity of the solar radiation diffusely reflected and transmitted by turbid atmospheres. *Journal of the Meteorological Society of Japan* **49**:321–332.

Tanaka, M. (1971b). Radiative transfer in a turbid atmosphere III Degree of polarization of the solar radiation reflected and transmitted by turbid atmospheres. *Journal of the Meteorological Society of Japan* **49**:333–342.

Taylor, M.J., Hapgood, M.A., and Rothwell, P. (1987). Observations of gravity wave propagation in the O1(557.7 nm), Na(589.2 nm), and the near infra-red OH nightglow emissions. *Planetary and Space Science* **35**:413–427.

Tepley, C.A., Burnside, R.G., and Meriwether, J.W. Jr. (1981). Horizontal thermal structure of the mesosphere from observations of OH(8-3) band emissions. *Planetary and Space Science* **29**:1241–1249.

Thomas, L., Gibson, A.J., and Bhattacharyya, S.K. (1977). Lidar observations of a horizontal variation in the atmospheric sodium layer. *Journal of atmospheric and terrestrial Physics* **39**:1405–1409.

Thomas, L., Isherwood, M.L., and Bowman, M.R. (1983). A theoretical study of the height distribution of sodium in the mesosphere. *Journal of atmospheric and terrestrial Physics* **45**:587–594.

Thomas, R.J., and Donahue, T.M. (1972). Analysis of Ogo-6 observations of the O1 5577A tropical nightglow. *Journal of geophysical Research* **77**:3557-3565.

Tinsley B.A. and Vallance-Jones, A. (1962). The seasonal variation of the twilight sodium airglow in the southern hemisphere. *Journal of atmospheric and terrestrial Physics* **24**:345–351.

Vallance-Jones, A., Meier, R.R., and Shefov, N.N. (1985). Atmospheric quantal emissions: A review of recent results. *Journal of atmospheric and terrestrial Physics* **47**:623–642.

Vincent, R.A. (1984a). Gravity-wave motions in the mesosphere. *Journal of atmospheric and terrestrial Physics* **46**:119–128.

Vincent, R.A. (1984b). MF/HF radar measurements of the dynamics of the mesospause region — A review. *Journal of atmospheric and terrestrial Physics* **46**:961–974.

Vincent, R.A. and Ball, S.M. (1981). Mesospheric winds at low and mid-latitudes in the southern hemisphere. *Journal of geophysical Research* **86**:9159–9169.

Vincent, R.A. and Fritts, D.C. (1987). A climatology of gravity wave motions in the mesopause region at Adelaide, Australia. *Journal of atmospheric Science* **44**:748–760.

Vincent, R.A. and Reid, I.M. (1983). HF doppler measurements of mesospheric gravity wave momentum fluxes. *Journal of atmospheric Science* **40**:1321–1333.

Vincent, R.A., Tsuda, T., and Kato, S. (1988). A comparitive study of mesospheric solar tides observed at Adelaide and Kyoto. *Journal of geophysical Research* **93**:699–708.

von Zahn, U. (1987). The project MAP/WINE: an overview. *Journal of atmospheric and terrestrial Physics* **49**:607–620.

von Zahn, U. and Hansen, G. (1988). Sudden neutral sodium layers: a strong link to sporadic E. *Journal of atmospheric and terrestrial Physics* **50**:93–104.

von Zahn, U., Hansen, G., and Kurzawa, H. (1988). Observations of the sodium layer at high latitudes in summer. *Nature* **331**:594–596.

von Zahn, U., Fricke, K.H., Gerndt, R., and Blix, T. (1987a). Mesospheric temperature and the OH layer height as derived from ground-based Lidar and OH spectrometry. *Journal of atmospheric and terrestrial Physics* **49**:863–869.

von Zahn, U. and Neuber, R. (1987). Thermal structure of high latitude mesopause region in Winter. *Beiträge zur Physik der Atmosphäre* **20**:294–304.

von Zahn, U., von der Gathen, P., and Hansen, G. (1987b). Forced release of sodium from upper atmospheric dust particles. *Geophysical research Letters* **14**:76–79.

Wallace, L. and McElroy, M.B. (1966). The visual dayglow. *Planetary and Space Science* **14**:677-708.

Wardill, P. and Jacka, F. (1986). Vertical motions in the thermosphere over Mawson, Antarctica. *Journal of atmospheric and terrestrial Physics* **48**:289–292.

Wand, R.H. (1983a). Lower thermospheric structure from Millstone Hill incoherent scatter radar measurements. **1** Daily mean temperature. *Journal of geophysical Research* **88** 7201–7209.

Wand, R.H. (1983b). Lower thermospheric structure from Millstone Hill incoherent scatter radar measurements. **2** Semidiurnal temperature component. *Journal of geophysical Research* **88** 7211–7223.

Widdel, H.U. (1987). Vertical movements of the middle atmosphere derived from foil cloud experiments. *Journal of atmospheric and terrestrial Physics* **49**:723–741.

Wilksch, P.A. (1975). *Measurement of thermospheric temperatures and winds using a Fabry-Perot spectrometer.* PhD Thesis, University of Adelaide.

Wilksch, P.A. (1985). The instrument function of the Fabry-Perot spectrometer. *Applied Optics* **24**:1502–1411.

Witt, G. (1962). Height, structure, and displacements of noctilucent clouds. *Tellus* **14**:1–18.

Wolfe, W.L. and Zissis, G.J. (1953). *The infra-red Handbook.* Published by 'The Infra-Red Information and Analysis Centre' Environmental Research Institute of Michigan, USA.

Yee, J.H. and Abreu, V.J. (1987). Mesospheric 5577A green line and atmospheric explorer satellite observations. *Planetary and Space Science* **35**:1389–1395.

Yegingil, I., Ogelman, H., and Kiziloglna, N. (1980). Investigation of sodium in the upper atmosphere. *Journal of geophysical Research* **85**:5507–5510.

Zbinden, P.A., Hidalgo, M.A., Eberhardt, P., and Geiss,J. (1975). Mass spectrometer measurements of the positive ion composition in the D- and E- regions of the ionosphere. *Planetary and Space Science* **23**:1621–1642.

Zirin, H. (1966). *The solar Atmosphere.* Blaisdell Publishing Company, Waltham, Massachusetts. Toronto and London.

Appendix A

ETALON ANTIREFLECTION COATINGS

Low intensity of the airglow presents a major problem because long observation times are required to record a line profile. This justifies considerable effort to minimize all losses in the system.

Following Jacka (1984) the total light flux transmitted by a Fabry-Perot spectrometer is

$$\phi(\lambda) = t_c S L \Omega Y(\lambda) \tag{A.1}$$

where t_c is the effective transmission coefficient of all components other than the etalon, S is the etalon aperture area, Ω is the total solid angle of the field of view, L the radiance of the source, and Y the instrument function described in more detail in section 3.1.2. To minimize time required to acquire a line profile, $\phi(\lambda)$ must be as large as possible. Large etalon plates increase the throughput of photons but are more difficult to polish to the required flatness. The field of view must be kept suitably small to ensure that the instrument function width is small enough compared with the source bandwidth to enable that to be accurately estimated. In practice the output function $Y(\lambda)$ is usually limited by the defect finesse. Values of $N_D = 50$ are attainable with 150 mm diameter plates.

As L is the total radiance of the source and cannot be altered the only remaining variable in

equation A.1 is the effective transmission co-efficient t_c. Without any coatings a transmission loss of about 4% occurs at each optical surface. These losses can be minimized by using the appropriate coatings. The original optical components had single layer magnesium fluoride antireflection coatings. The new components, except for the etalons, have multilayer, dielectric, broadband, antireflection coatings (hard AR coatings) which reduce reflection losses to less than 0.5% for wavelengths from 450–750 nm. The moulded CR13 perspex lenses were coated with a new method using ion beam assistance to give adhesion to the perspex. All new coatings were applied by R. Schaeffer of A.G. Thompson and Co. (S.A.) Pty. Ltd., Adelaide.

An attempt was made to apply hard AR coatings to the back surfaces of the etalons. The following paper describes the resulting stress on the etalons and the final coatings applied.

Greet, P.A. (1986) Coating stress in Fabry-Perot etalons.
Applied Optics, v. 25 (19), pp. 3328-3330, October 1986

Appendix B

TWILIGHT TEMPERATURE VARIATIONS

The following manuscript has been accepted for publication in Journal of Atmospheric and Terrestrial Physics.

Observations of the sodium layer using a Fabry-Perot spectrometer: Twilight temperature variations.

P. GREET and F. JACKA

Mawson Institute for Antarctic Research

University of Adelaide

Adelaide, South Australia

1 Abstract

Observations of the twilight sodium emission from the 90 km level have been made at Mt. Torrens, a southern mid-latitude station using a high-resolution Fabry-Perot spectrometer. An outline of the analysis required to determine temperatures is presented. A winter-mean temperature of 199 K and a summer mean temperature of 150 K are determined from 2 years of data. The diurnal tide is shown to produce a distinct difference between the dawn and dusk temperatures during late summer and autumn.

2 Introduction

Few techniques for temperature measurements of the middle atmosphere have been available until recently (Forbes, 1985) and development of temperature models for this region has been based largely upon individual observations using rockets (Philbrick et al., 1985; Offerman et al., 1987) and satellites (Barnett

et al., 1985). Although satellite observations provide extensive spatial coverage the daily variation at a single position cannot be monitored.

Ground-based temperature measurements of the middle atmosphere can be obtained using incoherent scatter radar (Wand, 1983a, b; Lathuillere et al., 1983; Fukuyama et al., 1987) and several optical techniques. Emissions due to molecular OH and O_2 have been used to determine rotational temperatures of emission layers centred at 86 and 94 km respectively (Tepley et al., 1981; Myabro, 1984, 1986; Takahashi et al., 1986). Observations of the oxygen λ 558 nm emission with high-resolution Fabry-Perot spectrometers allow temperature measurements to be made in the lower thermosphere. At mid-latitudes this emission comes mainly from a layer near 97 km; a small contribution from the thermosphere near 250 km is also present (Hernandez, 1976; Killeen and Hays, 1983; Thomas and Donahue, 1972).

Neutral sodium atoms form a narrow layer centred at about 90 km with 12 km full-width at half-maximum. This layer was first studied using photometric observations of the twilight sodium D-line emission (see Hunten, 1967, for review) which is weakly excited photochemically, and strongly by resonant scattering of sunlight. Kirchhoff (1986) has reviewed models of the sodium layer photochemistry. The photochemical excitation is exothermic and typically about 40 R intensity. The resonant scattering is typically about 1 kR intensity.

Lidars have enabled detailed studies to be made of the sodium layer; recent examples include Gardner et al. (1986); von Zahn et al. (1988); and Nomura et

al. (1987). A tunable sodium lidar has been used to obtain temperature profiles of the mesopause region from 80-110 km (Fricke and von Zahn, 1985; von Zahn and Neuber, 1987; Neuber et al.,1988). These studies have shown the mesopause, defined as the region of smoothed minimum temperature above the mesosphere, to be situated at 100±2 km in the northern polar winter.

Temperature profiles of the stratosphere and mesosphere to 75 km have been obtained using Rayleigh lidars. These lidars yield density profiles from which the temperature profile can be determined by assuming a reference temperature, hydrostatic equilibrium, and the perfect gas law. Such temperature profiles have been reported from France (Chanin et al., 1987; Hauchecorne et al., 1987) and Japan, (Shibata et al., 1986).

The dominant features of all lidar studies of mesospheric temperature profiles are the temporal variability and the intermittent occurence of near-adiabatic temperature gradients. These features are manifestations of gravity waves which frequently have large amplitudes in the mesosphere and interact strongly with the mean flow (Fritts, 1984).

Tidal variations in temperature have been noted in measurements using incoherent scatter radars. Lathuillere et al. (1983) suggested that tidal processes may be the cause of variations seen in night-time temperatures from the 90–110 km region. They found variations of 14–20% in the averages of the first and second parts of the night at equinox. Wand (1983b) has studied the semidiurnal component of temperature variations in the lower thermosphere from 105–125 km;

tidal amplitudes of up to 28 K at 115 km were found. The amplitude of the tidal variations was found to be larger than that predicted by the current models.

Analysis of tidal variations in the density of the sodium layer have been made by Batista et al. (1985) and Kwon et al. (1987) using sodium backscatter lidars with the capacity to perform daytime measurements. In these studies the semidiurnal tide was found to have substantial influence on the column abundance and centroid height of the sodium layer.

This paper reports on observations of the sodium D-line emission at twilight obtained with a high-resolution Fabry-Perot spectrometer, (FPS). The FPS records the profile of the emission line. The temperature of the emission region can then be obtained from the width of this profile; allowance must be made for the finite width of the instrument profile. For the temperature to be interpreted as the atmospheric temperature it must be assumed that the emitting species are in thermal equilibrium with the dominant neutral species; for the twilight sodium emission, produced mainly by resonant excitation by sunlight, this assumption is certainly valid. The line of sight component of the wind velocity at the height of the emission can be determined from the Doppler shift of the line but no wind results will be presented here. Jacka (1984) has reviewed the application of Fabry-Perot spectrometers for airglow observations of this sort.

The height of the peak of the sodium layer varies slightly over the year. Gibson and Sandford (1971), from lidar measurements, found the peak height to be at 87.5 km in summer and 91 km in winter. Gardner et al., (1986) found the

mean centroid of the layer to be at 92 km with a 1.5 km decrease in December and November (winter). They suggested that the variation in the height of the centroid of the layer was due to a combined effect of the zonal winds and meridional circulation system. The FPS observations integrate the emissions from the whole of the layer, most weight being given to its densest part. In view of the variability in layer shape and the variation of 2–3 km in the height of its centroid, both spatially and temporally, a representative height of 90 km will be assumed in the following discussion.

Sipler and Biondi (1975) and Hernandez (1975) reported preliminary FPS observations of the twilight sodium emission obtaining temperature measurements of 210 ± 15 K and 215 ± 15 K respectively for single profiles. They also noted that the night-time emission was considerably broadened due to the photochemical excitation mechanism so that temperatures could not be obtained. Sipler and Biondi (1977) analysed 2 years of twilight and night-time measurements from Laurel Ridge, Pensylvania (40° N, 79° W). The temperatures they obtained from twilight observations ranged from 150 K in summer to 230 K in winter.

3 Instrumentation and Observations

Observations of the sodium D-line emission have been made at Mt. Torrens, (35° S, 139° E), for two years, 1986 and 1987. The instrument is a scanning FPS basically the same as that described by Jacka et al., (1980). The single etalon used for the twilight observations is part of a dual scanning instrument designed for

daytime observations. Some minor modifications were made; a Peltier cell cooler has replaced the original cooler, the photomultiplier now being maintained at approximately $-20°$ C; a new etalon, 150 mm in diameter, with an etalon finesse of 17 at λ 589 nm has replaced the previous etalon. Optimizing the instrument for operation at λ 589 nm by using an etalon plate separation of 6.828 mm and appropriate choice of field stop gives an instrument finesse of 12 at λ 589 nm.

A filter wheel houses six filters which can be used to select the spectral line of interest. Filters of 0.3 nm bandwidth at the sodium D2 (λ 589.0 nm) and D1 (λ 589.6 nm) lines were available for the observations. Although the D2 emission is approximately twice as intense as the D1 emission in the present work the D2 emission was not observed because the D2 filter bandpass was approximately 0.1 nm too low.

The precise order of the etalon used, ~23150, was chosen so that where the D1 order, n, was integral the D2 order was $n + m + \frac{1}{2}$, for m integral. This ensured that if some transmission of the unwanted D2 line occurred it would not contaminate the shape of the required line profile.

The etalon plate spacing is normally scanned in 128 steps each of 40 ms duration, the pulse output from the photomultiplier being accumulated in 128 separate channels of the recording system memory. The pulse count rate depends, of course, on the signal intensity and various instrument parameters.

The twilight observations fall into two groups; those made in the zenith and those made at a zenith angle of 60° in the four cardinal points. Figure 1 shows

a series of D1 zenith profiles obtained at dusk on day of year (DOY) 063, 1986. Each profile is the sum of about 50 scans in a 5 minute interval except profile 9 which was of 10 minutes duration. Within any one scan little variation in the background intensity occurs. To show the spectral structure in the profiles the background has been subtracted. The sodium Fraunhofer absorption line can be seen in profiles 1–3. This is due to a contribution from Rayleigh scattering of the solar spectrum from the lower atmosphere. As the sun sets at increasing altitude the resonant scattering from the sodium layer at 90 km becomes the dominant feature in the spectrum as in profiles 5–7. As the sun sets on the sodium layer the intensity of the emission rapidly decreases and the profile broadens as the exothermic photochemical reaction becomes the dominant source of photons. Profiles 8 and 9 in figure 1 show photochemical contamination. The night-time intensity of the photochemical emission is very low; this coupled with scattering of light from sodium street lamps in Adelaide and nearby towns makes night-time observations useless at Mt. Torrens.

4 Data analysis

The spectral line profile of the sodium emission is not a simple Gaussian shape. The D1 line has 2 × 2 and the D2 line 2 × 3 hyperfine components. In the D1 line the two groups of hyperfine components are separated about 2.1 pm and each group is 0.2 pm wide (very small compared to the Doppler width). If the instrument profile is deconvolved from the recorded profile the hyperfine

components appear as two Gaussian curves. The positions of the peaks of the two Gaussian curves contain the wind information and the width of each curve the temperature.

FPS profiles of emission from a hollow cathode sodium lamp were recorded during observation periods. The lamp operates at a temperature of about 400 K. Referring to figure 2, if a source Gaussian curve of the correct temperature is deconvolved from the recorded lamp profile the remaining profile is a convolution of the sodium profile at zero Kelvin and the instrument profile; in future denoted 'sodium $*$ instrument' profile. The sodium profile at zero Kelvin contains the necessary information about the hyperfine structure.

A Gaussian curve convolved with the sodium $*$ instrument profile is now fitted to the recorded sky profile. The fitting is done in the Fourier transform domain and only parts of the spectrum where the signal greatly exceeds the noise are used. The temperature and wind information are obtained from the fitted Gaussian curve.

Temperatures obtained from analysis of the profiles from dusk on DOY 063, 1986 are shown in the table 1. Also shown are the standard errors in individual temperature estimates obtained from the fitting routine, and the total background count rate per channel for each profile. These profiles were from zenith observations. Most profiles had similar acquisition times, thus the standard errors in the temperature estimates for cardinal point observations were smaller than those given in this table as the emission intensity is proportionally higher.

Some zenith profiles on individual days were combined to obtain a better signal to noise ratio.

A small contribution from the Fraunhofer absorption line masks the wings of the emission profile thus adding an apparent constant to the background. This effect was examined by subtracting a constant from each channel in a simulated profile. The simulated profile was then analysed as described above. An approximately linear relationship was obtained; a subtraction of 1 percent of the profile peak count rate resulted in underestimating the temperature by 10 K.

An attempt was made to remove background contamination by fitting a polynomial to the wings of the profile; this was found to be inadequate. In principle if a solar profile was obtained just prior to the sun setting then the twilight profiles could be analysed in a manner similar to dayglow profiles (see Cocks, 1983, for a description of dayglow analysis). Solar profiles have not been made in the observations obtained to date. However, in view of the sensitivity of temperature estimations and the limited extra data which could be obtained by this method, it is unlikely to be a profitable exercise.

The photochemical emission, being exothermic, will broaden the profile beyond the Doppler width. As twilight progresses and the ratio of photochemical to resonant emission intensities increases the profile width increases also. This effect was also simulated. By adding two simulated sodium profiles, one at 200 K for the resonant emission, and one at 700 K for the photochemical emission (Sipler and Biondi, 1977), and analysing as a single profile the effects of photochemical

contamination can be seen. For small amounts of photochemical contamination a linear relationship is obtained. Photochemical emission at 1% of the intensity of the resonant emission will produce a change in width of the emission profile equivalent to a temperature increase of approximately 1 K. Although the exact emission intensity ratio is unknown the expected value is about 4%.

Care must be taken in interpreting the temperatures returned by the analysis described above. Obviously not all are representative of the atmospheric temperature. Useful information can be extracted from these results if stringent selection criteria are used to remove profiles with any Fraunhofer background contamination or any profile broadening due either to excess photochemical emission or scattered street lights. The profile background is the background count rate due to a combination of both photomultiplier dark count rate and sky background emission. The following selection criteria were used:

1. Fraunhofer background contamination can be allowed for by not selecting profiles with high background count rates. For zenith profiles a cut-off of 500 counts/s was used and for off-zenith observations a cut-off of 2000 counts/s.

2. The problem of broadening by the photochemical reaction can be avoided by not selecting profiles with low background counts. For zenith profiles a background of 60 counts/s was considered the lowest acceptable background and for off zenith profiles a background of 120 counts/s was set.

3. No profiles from the west at dusk have been used in the temperature analysis as these profiles all show varying amounts of contamination by scattered

street lights.

4. The fitting procedure returns χ^2 values describing the goodness of fit. A limit on the value of χ^2 was set to discard profiles for which a good fit was not obtained.

5. If a temperature estimate had a standard error of greater than 60 K it was not included in further analysis.

The background selection criteria under 1 and 2 above were determined by altering the limiting background values and calculating the monthly mean temperatures from the selected profiles; the monthly mean values reach a plateau. For example when increasing the minimum acceptable background the mean temperatures decrease until increasing the minimum value further does not significantly change the mean. The background limiting values were set to where the plateau commenced. These criteria also exclude some useful profiles. Profiles of a longer duration near the end of twilight start becoming contaminated towards the end of the acquisition time. A shorter profile with the same background counts may not be contaminated. These rigid selection criteria were used to avoid any subjective judgement in the selection of useful profiles.

When using the selection criteria described above a total of 166 profiles from 65 days data were obtained over the two years. A single lamp profile was used to obtain a sodium * instrument profile for the analysis of all data. The temperature of the lamp profile was determined by a five parameter fitting of two Gaussian curves using an instrument function derived from a profile obtained with a Hg 198

λ 546 nm emission lamp. The temperature obtained was 433.9 $\pm$ 1 K. This uncertainty includes both that from the fitting routine, $\pm$ 0.3 K, and an estimate of the error from the specification of the mercury lamp temperature. Because of the mass ratio of mercury to sodium an uncertainty of 10 K in the mercury lamp temperature produces only a 1 K uncertainty in the sodium lamp temperature. Using a single instrument profile has the advantage that any uncertainty in the temperature determination arising from uncertainty in the lamp operating temperature will be the same for all profiles. Thus variations in temperature between different profiles will be real variations and not related to uncertainties in the lamp operating temperature. At times over the two years the Fabry-Perot etalon plate separation was changed for observations of other emissions but when reset for sodium observations the order was always within 200 of the value n = 23150 quoted above. Variations in the instrument function due to such small changes in instrument configuration should be negligible.

5 Results and discussion

In this study profiles of 5–10 minutes duration were obtained over the short mid-latitude twilight. The temperatures calculated were highly variable both from day to day and on some individual days. Data are available for all months except August and more data are available for the summer months since summer skies are more often clear than winter skies. In all months except May data from both dusk and dawn are available. The general trend is as expected; a warm winter

mesosphere and a cold summer mesosphere. Taking June and July as the winter months (no August data are available) a winter mean temperature of 199 ± 5 K is obtained and for summer, December, January, and February, 150 ± 20 K.

Figure 3 shows the monthly mean dusk and dawn temperatures. A significant difference between dusk and dawn values can clearly be seen in the months January - April. As dusk and dawn are approximately 12 hours apart an obvious possible explanation of such a difference is the diurnal tide. Model values for 35° S from Groves (1988) are indicated by the dashed line in figure 3. This model was developed to match upper and lower atmosphere models and to fit available temperature data from satellites and rockets. The winter values are in reasonable agreement with those of the model but summer values are more variable and significantly lower.

To indicate the variability within estimates when more than two profiles have been used from any particular twilight, the range (maximum - minimum) of the estimates is used. From 53 twilights the mean variability assessed in this way was 40 K; it does not change significantly through the year. This variability arises from several sources. The uncertainty in the fitting, as indicated by the standard error of the estimate, introduces some variability. The average value of this standard error from all data is ± 22 K; in Winter, (June and July), when twilights are longer and profiles have higher total counts, the average value of the standard error is ± 15 K. Another contribution to the variability arises from inadequacies in the selection criteria. As mentioned above the photochemical emission and the

Fraunhofer background contamination can both affect the emission profile. The two effects act in opposite ways and would cancel each other to a certain extent. If the intensity of either were abnormal then this would produce an apparent change in temperature. If the background criteria are made more stringent the number of profiles satisfying them becomes too small to be useful.

A possible cause of actual variability of temperature during a single twilight is the presence of internal gravity waves. Hines (1965) predicted temperature variations of up to ± 30 K at 110 km. The tunable sodium lidar study of Neuber et al. (1988) found that temperature fluctuations of ± 25 K about the mean were not uncommon. Using the relationship (Hines, 1965)

$$\frac{\delta T}{T} \simeq \pm i(\gamma - 1)^{\frac{1}{2}} c^{-1} U_x$$

where γ is the ratio of specific heats, c the speed of sound, and U_x the wave induced horizontal wind speed, Vincent (1984), from velocity measurements at Adelaide, estimated rms temperature variations of $\sim$ 10-12 K for gravity waves in the 85 km region. Zenith measurements over twilight span 15–20 minutes when more than one profile is obtained; thus a wave with a period less than an hour, not uncommon at mesospheric heights, could produce significant temperature fluctuations in the zenith observations.

Cardinal point observations span distances of 300 km and so waves with horizontal wavelengths of a few hundred kilometers, also not uncommon at mesospheric heights, could produce significant temperature fluctuations in any set of single twilight observations.

To see if a connection with the diurnal tide could be substantiated a comparison was made with tidal measurements from the spaced-antenna partial-reflection radar at Buckland Park which is 50 km west-north-west of Mt. Torrens. The radar measures horizontal winds with a height resolution of a few kilometers. Wind data, including amplitude and phase of the diurnal tide for 1986–87, were supplied by Dr. R.A. Vincent (personal communication). To relate the amplitude of the wind variation with the amplitude of the temperature variation and to determine the phase difference between the wind and temperature variations a model is used viz. that presented by Forbes and Vincent, (1988). It incorporates the effects of mean winds and dissipation on the (1,1) mode of the diurnal tide. Calculations from the model were carried out for the March equinox. An amplitude of the variation in the zonal tidal wind of 30 ms^{-1} corresponds to an amplitude of the temperature variation of 8.5%; the time of maximum zonal wind lags the time of maximum temperature by 7 hours (Vincent, personal communication). Assuming that the ratio of the tidal zonal wind amplitude to the tidal temperature amplitude remains constant, and that the phase difference between the variations remains the same for all months, figure 4 compares the (dawn − dusk) temperature difference variation calculated from the model and radar data with that obtained from the FPS measurements. Reasonable agreement is obtained throughout the year except at the solstices. From January through April the FPS (dawn − dusk) temperature difference is slightly larger than the model/PRD values and in all other months it is slightly smaller. The diurnal tide

maximizes in the autumn equinox (Vincent et al., 1988) and the phase is such that the maximum difference between dusk and dawn, 37 K or 20%, occurs then. The general agreement seen offers support for the predictions from the model of the temperature effects of the (1,1) mode of the diurnal tide.

An attempt to use an earlier model (Forbes and Gillette, 1982) gave diurnal temperature variations a factor of 2 less than those seen in the FPS data.

Other factors could also produce systematic variations in the temperature of this region. The model used only accounts for the (1,1) mode of the diurnal tide; other modes of the diurnal tide may be important at times. No account has been taken of the semidiurnal tide which has been shown to have a significant effect on the density of the sodium layer (Batista et al., 1985; Kwon et al., 1987). Although the semidiurnal tidal data are available from the Buckland Park radar, the model amplitude and phase relationships are not. To do a similar calculation of the (dawn − dusk) temperature difference produced by the semidiurnal tide the phase information needs to be known fairly accurately; a 1 or 2 hour phase shift has quite a significant effect. Considering the times of dusk and dawn the largest effect would be expected at the solstices and least at the equinoxes. The semidiurnal tide can cause the dawn temperatures to be lower than those at dusk and may explain the December and June/July negative temperature differences seen in FPS measurements.

Sipler and Biondi (1977) found no systematic difference in the temperatures at evening and morning twilight. They were working with a fairly small data

set; dawn temperatures were only available on about 10 days. The amplitude of the diurnal tide is large at Adelaide, 35° S (Vincent et al., 1988). It may be that at 40° N the temperature variation produced by the diurnal tide is not as significant as at Mt. Torrens and was therefore completely masked by other variations. The temperatures they obtained are in reasonable agreement with those reported here — their summer minimum of 150 K and winter maximum of 230 K compare with our means of 150 K in summer and 199 K in winter. Neuber et al., (1988) obtained a winter mean temperature at 90 km of 205.2 K.

6 Conclusions

Observations of the twilight sodium emission made with a high-resolution FPS can, with care, be used to infer temperatures at a height of about 90 km.

Observations from Mt. Torrens, a southern midlatitude station, have been used to determine monthly mean temperatures. A summer mean of 150 K and a winter mean of 199 K have been determined from two years of data.

The data show considerable short term variability some of which may be ascribed to the effects of gravity waves. The FPS measurements of the dawn-dusk temperature difference were in reasonable agreement with those calculated using a recent theoretical model togeather with measurements of the amplitude and phase of the diurnal tide from a nearby spaced-antenna partial-reflection radar. A systematic difference between dawn and dusk temperatures of up to 37 K in March and April is ascribed to the diurnal tide: at this time the amplitude

of the tide is largest and the phase such as to maximize the effect.

7 Acknowledgements

We would like to thank Dr. R.A. Vincent for the radar data and also for many helpful discussions. Thanks also to the technical staff of the Mawson Institute for assistance with instrument maintenance.

References

Barnett, J.J. et al.	1985	*Nature* **313**,439.
Batista, P.P., Clemesha,B.R., Simonich,D.M., and Kirchhoff, V.W.J.H.	1985	*J. Geoph. Res.* **90**,3881.
Chanin, M.L., Smires, N., and Hauchecorne, A.	1987	*J. Geoph. Res.* **92**,10933.
Cocks, T.D.	1983	*Appl. Opt.* **22**,726.
Forbes, J.M.	1985	*Handbook for MAP* **16**,231.
Forbes, J.M. and Vincent, R.A.	1988	*Planet. Spac. Sci.* in the press.
Fricke, K.H. and von Zahn, U.	1985	*J. Atm. Ter. P.* **47**,499.
Fritts, D.C.	1984	*Rev. Geophys.* **22**,275.
Fukuyama, K., Maekawa, Y., Fukao, S., and Kato, S.	1987	*Annales Geophysicae* **5A**,289.
Gardner, C.S., Voelz, D.G., Sechrist, C.F., and Segal, A.C.	1986	*J. Geoph. Res.* **91**,13659.
Gibson, A.J. and Sandford M.C.W.	1971	*J. Atm. Ter. P.* **33**,1675.
Hauchecorne, A., Chanin, M.L., and Wilson, R.	1987	*Geophys. R. L.* **14**,933.
Hernandez, G.	1975	*Geophys. R. L.* **2**,103.
Hernandez, G.	1976	*J. Geoph. Res.* **81**,5165.
Hines, C.O.	1965	*J. Geoph. Res.* **70**,177.
Hunten, D.M.	1967	*Space Sci. R.* **6**,493.
Jacka, F.	1984	*Handbook for MAP* **13**,19.
Jacka, F., Bower, A., Creighton, D.F., and Wilksch, P.A.	1980	*J. of Phys. E, Sci. Inst.* **13**,562.
Killeen, T.L. and Hays, P.B.	1983	*J. Geoph. Res.* **88**,10163.
Kirchhoff, V.W.J.H.	1986	*Canad. J. Phys.* **64**,1664.
Kwon, K.H. et al.	1987	*J. Geoph. Res.* **92**,8775.
Lathuillere, C., Wickwar, V.B., and Kofman, W.	1983	*J. Geoph. Res.* **88**, 10137.
Myabro, H.K.	1984	*Planet. Spac. Sci.* **32**,249.
Myabro, H.K.	1986	*Planet. Spac. Sci.* **34**,1023.
Neuber, R., von der Gathen, P., and von Zahn, U.	1988	*J. Geoph. Res.* (in press).
Nomura, A. et al.	1987	*Geophys. R. L.* **14**,700.
Offermann, D. et al.	1987	*J. Atm. Ter. P.* **49**,655.
Philbrick, C.R. et al.	1985	*J. Atm. Ter. P.* **47**,159.
Shibata, T., Kobuchi, M., and Maeda, M.	1986	*Appl. Opt.* **25**,685.
Sipler, D.P. and Biondi, M.A.	1975	*Geophys. R. L.* **2**,106.
Sipler, D.P. and Biondi, M.A.	1978	*Planet. Spac. Sci.* **26**,65.
Takahasi, H., Sahai, Y., and Batista, P.P.	1986	*Planet. Spac. Sci.* **34**,301.
Tepley, C.A., Burnside, R.G., and Meriwether, J.W. Jr.	1981	*Planet. Spac. Sci.* **29**,1241.
Thomas, R.J., and Donahue, T.M.	1972	*J. Geoph. Res.* **77**,3557-3565.
Vincent, R.A.	1984	*J. Atm. Ter. P.* **46**,119.
Vincent,R.A., Tsuda, T., and Kato, S.	1988	*J. Geoph. Res.* **93**,699.
von Zahn, U., Hansen, G., and Kurzawa, H.	1988	*Nature* **331**,594.
von Zahn, U. and Neuber, R.	1987	*Beiträge zur Physik der Atmosphäre* **20**,294.
Wand, R.H.	1983a	*J. Geoph. Res.* **88** 7201.
Wand, R.H.	1983b	*J. Geoph. Res.* **88** 7211.

Reference is also made in the text to the following unpublished material:

Forbes, J.M. and Gillette, D.F.	1982	AFGL-TR-82-0173(1) Environmental Research Papers No. 780(1).
Groves, G.V.	1988	AFGL Environmental Research Papers No. ??. (details to be supplied).

Table 1: Temperature estimates for the zenith profiles given in figure 1 using the analysis outlined in figure 2. The temperature errors are those returned from the fitting routine. In profile 2 an error of XX indicates an inadequate fit. Profiles 2, 3, and 4 show Fraunhofer contamination. Profile 8 has considerable photochemical broadening. Only profiles 5 and 6 would be accepted by the selection criteria given in the text.

profile	temperature (K)	background (counts/s)
2	640 ± XX	15980
3	68 ± 95	4681
4	177 ± 54	1244
5	187 ± 21	343
6	178 ± 20	115
7	231 ± 20	49
8	260 ± 64	31

Figure captions

Figure 1: Sodium D1 line profiles from dusk on DOY 063, 1986.The background has been subtracted to illustrate the spectral features. In profiles 1–4 features of the solar spectrum can be seen. In profiles 4–8 the emission line produced by resonant scattering of sunlight is the dominant feature. In profile 9 the line width is broader due to the photochemical excitation mechanism producing the emission after sunset.

Figure 2: Schematic representation of the analysis procedure. The asterisk denotes convolution. The recorded lamp profile is a convolution of the instrument profile and the lamp profile. The recorded sky profile is the convolution of the instrument profile and the sky sodium profile. In both cases they may be expressed as a convolution of the sodium $*$ instrument profile (at zero kelvin) and a source profile. The parameters of the Gaussian curves contain information on temperature and velocity of the source; they are adjusted for best fit with the recorded lamp and sky profiles.

Figure 3: The monthly mean temperatures for dusk and dawn from the twilight observations are shown. Crosses indicate dusk values and circles, dawn. The error bars indicate the standard error in the mean computed on the basis of assigning equal weight to individual observations during any one month. The labels at the bottom of the plot show the month and number of profiles used to calculate the means. The dashed line represents model values from Groves (1988).

Figure 4: The dawn-dusk temperature difference is plotted for each month. The crosses represent the difference in the FPS average measurements, as plotted in figure 3. The open circles are the differences predicted by the model/radar measurements explained in the text.

Figure 1

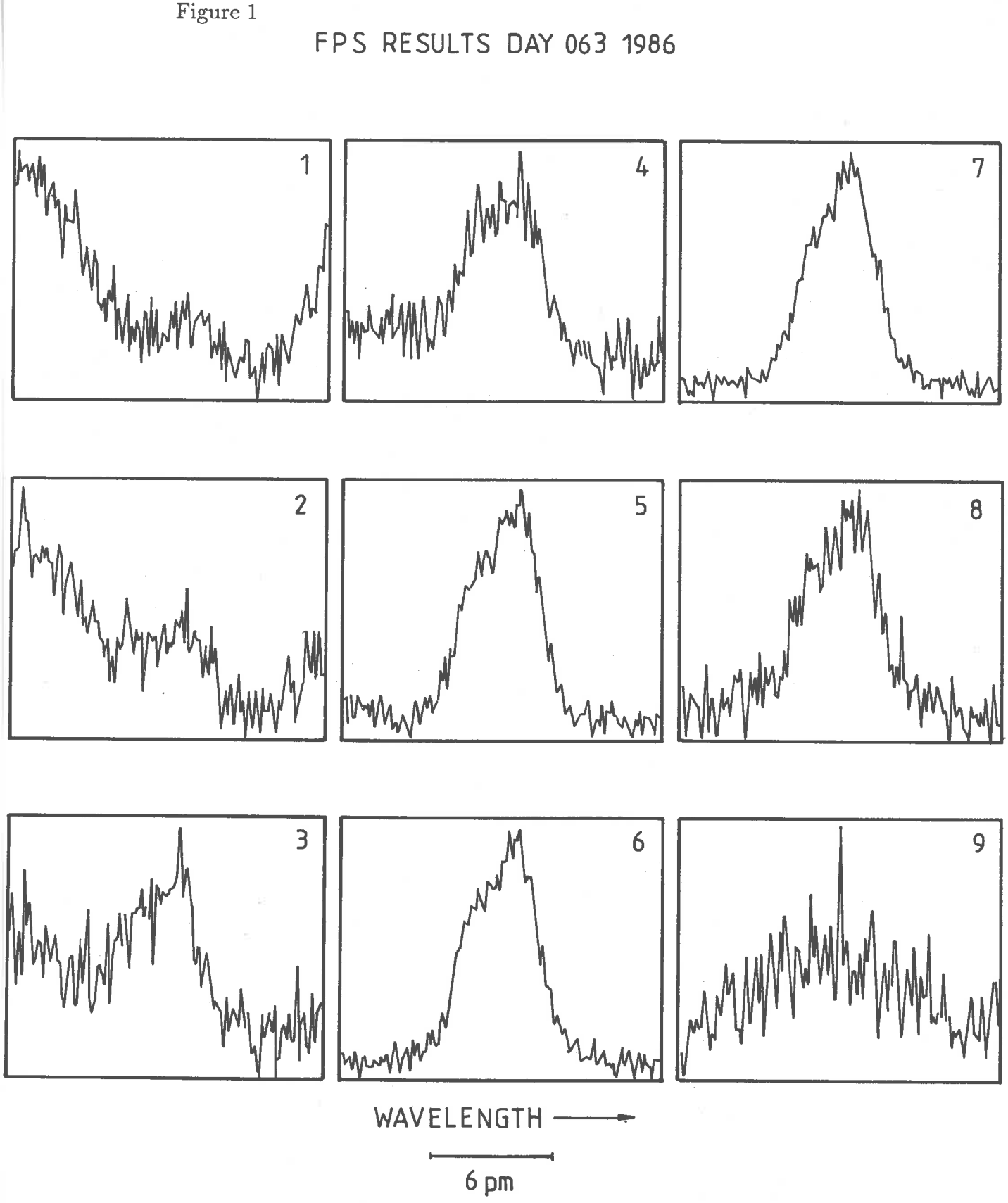

Figure 2

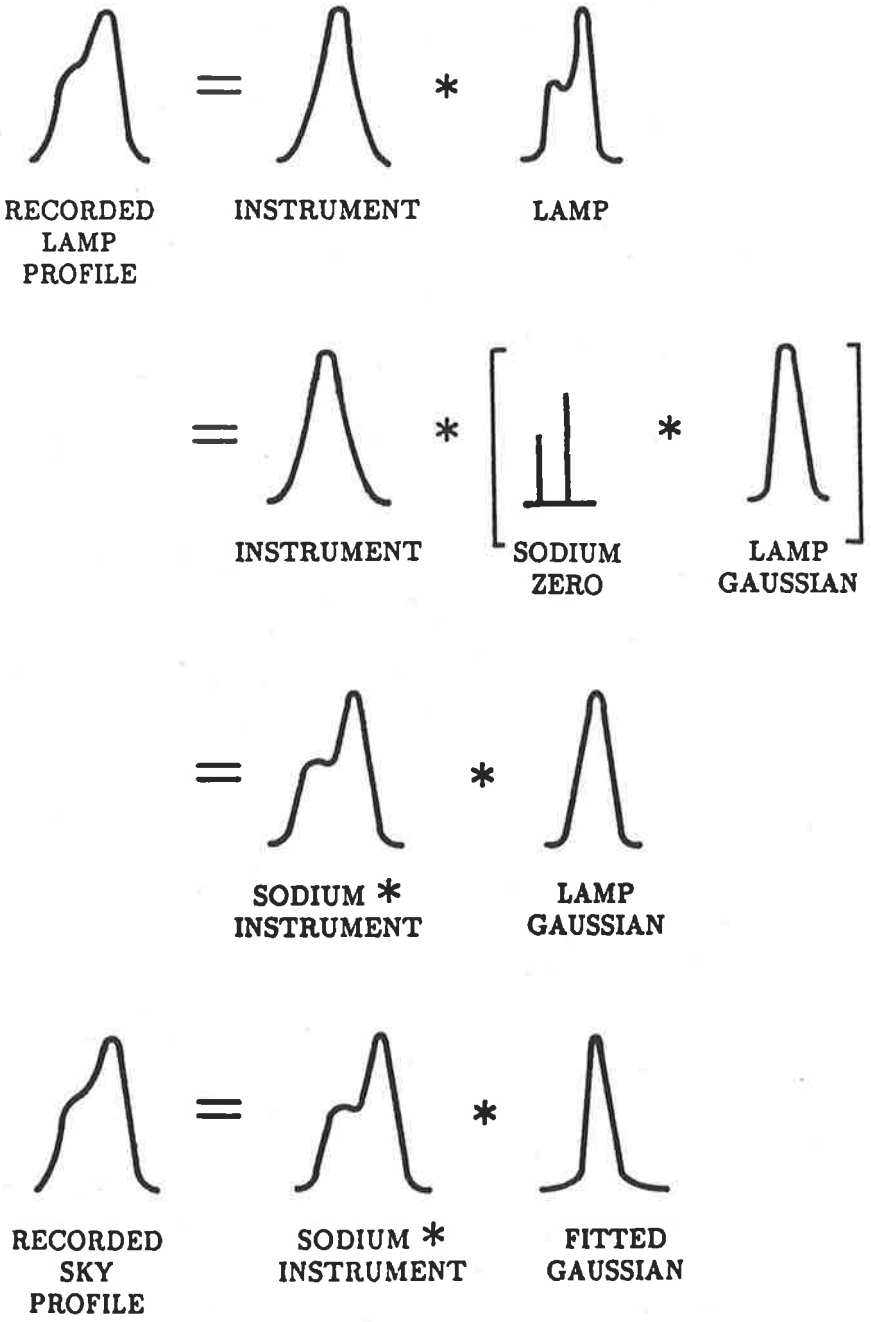
RECORDED LAMP PROFILE
INSTRUMENT
LAMP
INSTRUMENT
SODIUM ZERO
LAMP GAUSSIAN
SODIUM * INSTRUMENT
LAMP GAUSSIAN
RECORDED SKY PROFILE
SODIUM * INSTRUMENT
FITTED GAUSSIAN
* DENOTES CONVOLUTION

Figure 3

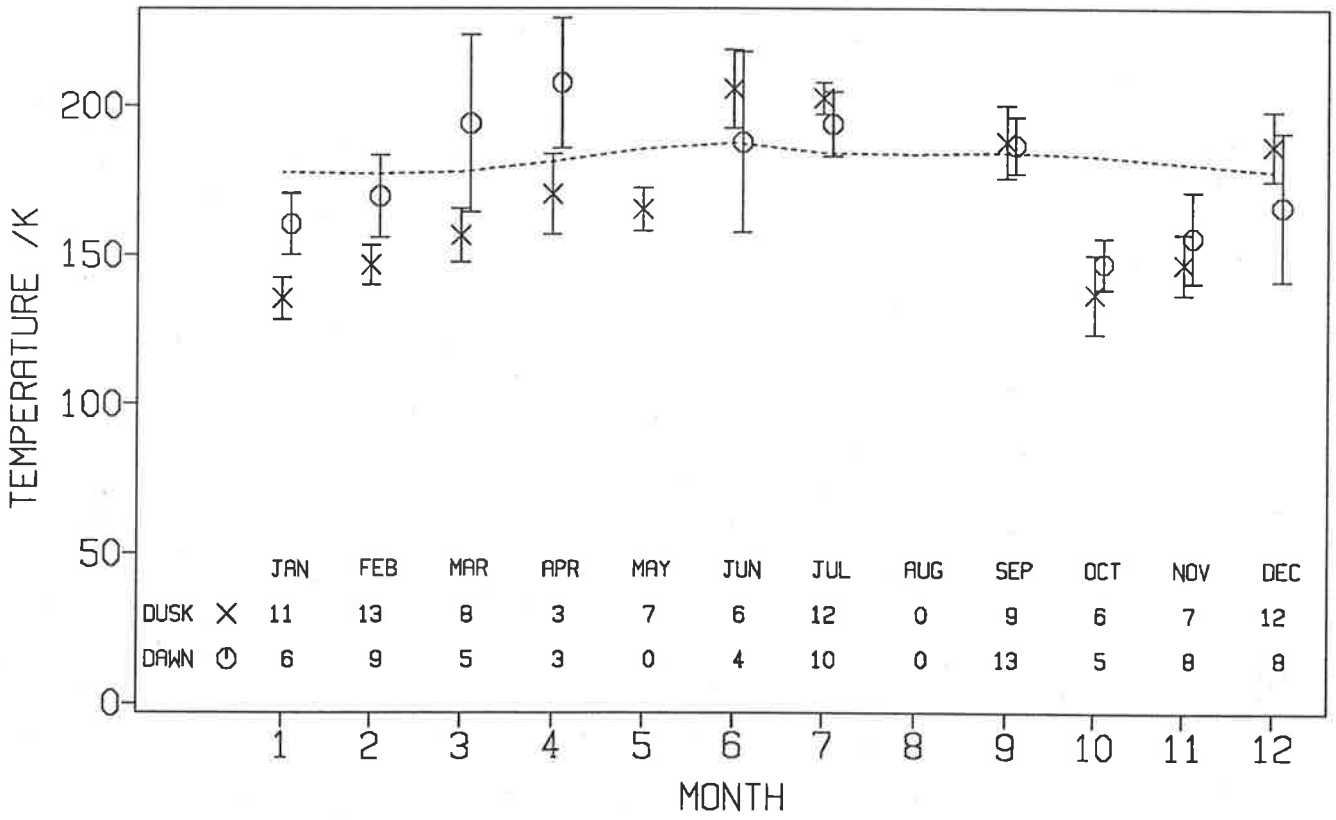
TEMPERATURE /K
200
150
100
50
0
1
2
3
4
5
6
7
8
9
10
11
12
MONTH
JAN FEB MAR APR MAY JUN JUL AUG SEP OCT NOV DEC
DUSK 11 13 8 3 7 6 12 0 9 6 7 12
DAWN 6 9 5 3 0 4 10 0 13 5 8 8

Figure 4

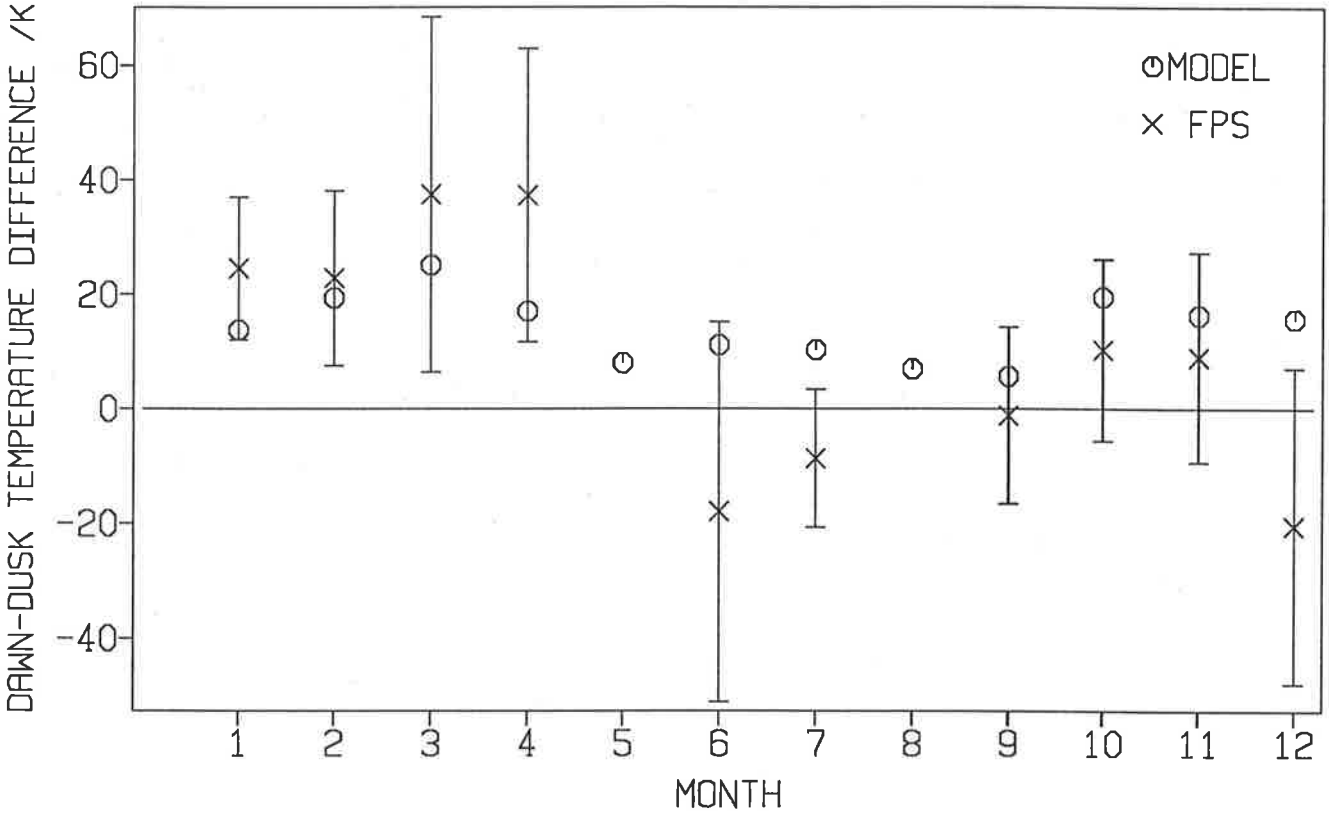
DAWN-DUSK TEMPERATURE DIFFERENCE /K
60
40
20
0
-20
-40
MODEL
FPS
1
2
3
4
5
6
7
8
9
10
11
12
MONTH

Appendix C

DAYGLOW: REVIEW OF THEORY AND OBSERVATIONS

Successful study of the dayglow requires a general understanding of both the solar spectrum and sky radiance. The following account is drawn mainly from textbooks on both subjects (Kuiper 1953; Kondratyev 1969; McCartney 1976; Coulson 1975).

C.1 Solar spectrum

The solar spectrum as seen from Earth originates in the outer region of the visible sun known as the photosphere. The shape of the spectrum reflects properties of the photosphere. Figure C.1 shows that the general shape of the spectrum is well described by the curve for blackbody radiation at 5900 K. This curve is modified by Fraunhofer absorption lines and also by absorption and scattering (attenuation) in the Earth's atmosphere which considerably modifies the spectrum, especially at wavelengths greater than 0.7 μm.

The Fraunhofer absorption lines are produced in the photosphere. The strongest lines are those of Ca^+, H, Fe, Mg, Na, Al, and Ca (St. John *et al.* 1928). Up to 96% of the local solar continuum is removed at these wavelengths. The oxygen λ 630 and λ 558 nm forbidden transitions produce Fraunhofer absorption lines where about 4% of the continuum is absorbed.

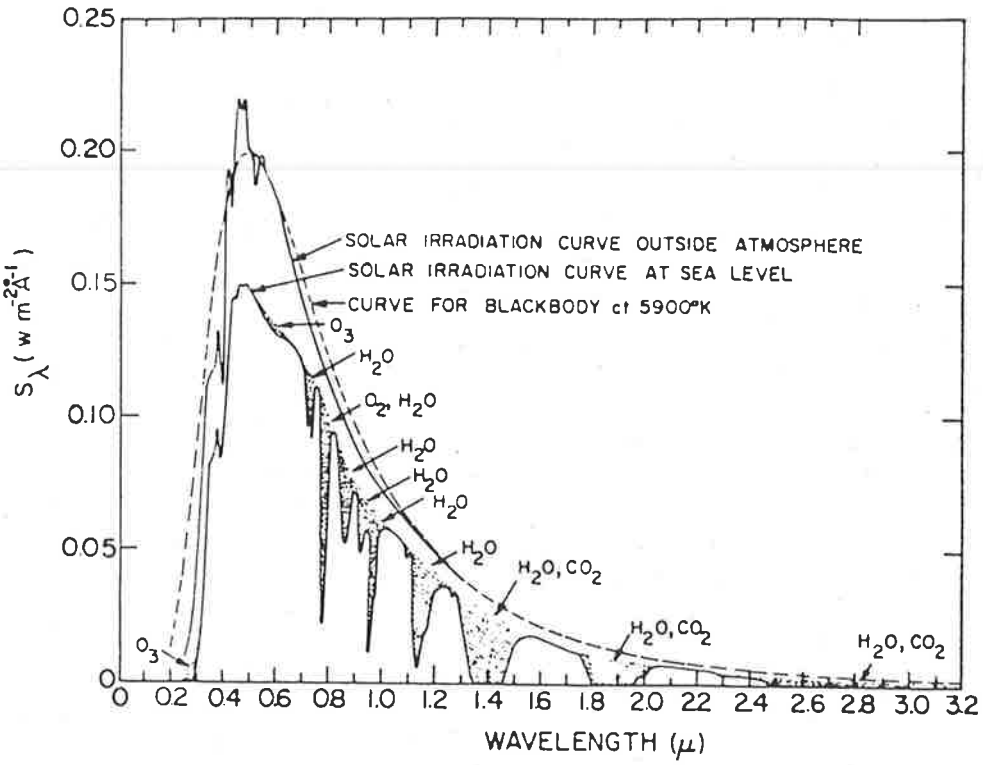

Figure C.1: Energy distribution in the solar spectrum. (after Kondratyev, 1969, p247)

Debouille *et al.* (1973) present a detailed map of the solar spectrum from 300 to 1000 nm made using a very high resolution spectrograph with an instrument width of about 1 pm.

Fraunhofer lines are structurally complex (Zirin 1966, p2950). The shape of the centre of a line is determined by the Doppler broadening produced by thermal motions of the atoms or ions in the photosphere. The width is characteristic of a temperature of 5900 K. This basic shape is modified by pressure broadening, especially in the wings of the lines. The deeper the Fraunhofer line the greater the deviation from the thermal Doppler profile. Broadening also results from absorption at lower levels of the photosphere where the temperature is higher. Variations in the Doppler shift from different parts of the solar disc, due to solar rotation and internal motion, cause profile broadening. For the sodium Fraunhofer lines, where 96% of the continuum is absorbed, the expected thermal Doppler width for a photosphere at 5900 K is about 8 pm but the measured width is about 20 pm. If the amount of pressure broadening is known, a Voigt profile can be used for an analytical description. For weak lines, such as the

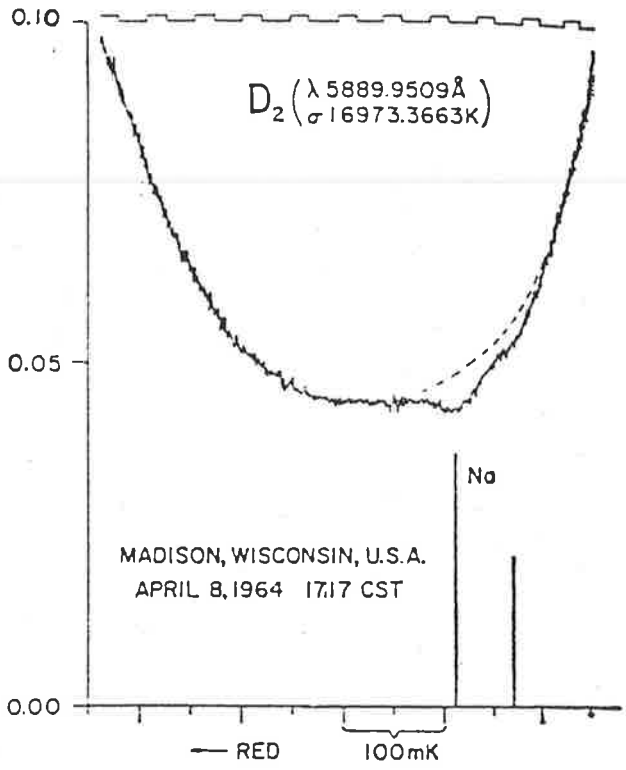

Figure C.2: Bottom of the Fraunhofer D_2 absorption line as measured by Burnett (1965). The centers of the two hyperfine components in the terrestrial absorption line are indicated.

oxygen lines at λ 630 and λ 558 nm, the Doppler profile is a reasonable approximation for some applications.

Earth's atmosphere considerably modifies the solar spectrum. Attenuation of the solar spectrum depends on the altitude and zenith angle of observations and the clarity of the sky. At infra-red wavelengths water vapour and other atmospheric molecules produce large absorption bands in the solar spectrum. Other less intense molecular and atomic absorption lines occur throughout the spectrum. These telluric absorption lines can be distinguished from Fraunhofer absorption lines because the Earth's atmospheric temperature (200-1500 K) is considerably less than the photospheric temperature. Figure C.2 shows the telluric sodium D2 absorption line superimposed on the bottom of the Fraunhofer absorption line at that wavelength.

Any relative motion of the sun with respect to the observer will produce a Doppler shift of the solar spectrum resulting in a change in the position of the airglow emission with respect to the Faunhofer feature. For dayglow observations the significant Doppler shifts are those

produced by the radial velocity component of the Earth's elliptical orbit and the apparent solar motion produced by the Earth's rotation (McNutt and Mack, 1963). These Doppler shifts vary in time; that due to the rotation of the Earth produces a measurable effect on a timescale of several minutes. The velocity of the sun's approach, v, for an observer at a latitude ϕ and the sun at hour angle h and declination δ is given by

$$v = -r\omega \cos\phi \sin h \cos\delta$$

where r and ω are the radius and angular velocity of the Earth. The shift varies from 0 pm at local noon to a maximum of about 0.7 pm at twilight. The other noticeable shift in the solar spectrum, as seen in Figure C.2, is the gravitational red shift. At λ 567.5 nm this amounts to 1.2 pm (C.E. Moore, 1953). Telluric emission or absorption features thus always appear on the short wavelength side of the Fraunhofer absorption features.

The solar constant is the amount of solar radiant energy from outside the atmosphere passing per unit time through unit surface area perpendicular to the suns rays and at a distance of mean radius of the terrestrial orbit, Kondratyev (op. cit., p252). The value of the solar constant is 1353 Wm^{-2} (Wolfe and Zeiss 1978). Tabulations of the solar irradiance at the Earth's surface as a function of wavelength can be found in most optical handbooks or texts on atmospheric radiation. Given these quantities, the solar energy absorbed in the atmosphere and incident on the Earth's surface can be calculated. Measurement of the solar constant from Earth is difficult because compensation for atmospheric effects must be made.

C.2 Skylight

C.2.1 Rayleigh scattering

Lord Rayleigh in 1899 applied electromagnetic theory to the scattering of light by atmospheric molecules in an attempt to explain the blue colour of the sky. The term Rayleigh scattering has since been used to describe scattering by particles much smaller than the wavelength of the

incident light. The radiant flux or irradiance produced by Rayleigh scattering can be derived by considering the interaction of the electric field of the incident light, E_0, with the dipole moment associated with a molecule (or atom). The applied field induces an oscillation in the scatterer which radiates energy derived from the incident wave. It is assumed that: (1) dimensions of the scatterers are small compared to the wavelength, λ, of the incident light; (2) the scatterers and surrounding medium are neither conductors nor contain free electric charges; (3) the refractive index, n, of a particle is not too high; (4) the particles scatter light independently of each other. The time averaged Poynting vector, $\overline{S}$, then gives the quantity of scattered energy passing per unit time per unit surface perpendicular to the direction of propagation of the scattered light,

$$\overline{S_1} = \frac{\pi c(1+\cos^2\theta)}{16R^2N\lambda^4}(n^2-1)(\overline{E}^0)^2.$$

θ is the angle of observation from the incident wave, N is the number of particles per unit volume, and R the distance from the scattering volume (Kondratyev 1969, p175).

The angular scattering coefficient $\beta_m(\theta)$ quantifies the scattered intensity from unit volume in an infinitesimal solid angle $d\omega$ observed at θ to the incident radiation of unit flux.

$$\beta_m(\theta) = \frac{I(\theta)}{\overline{S}_0} = \frac{\pi^2(n^2-1)^2}{2N\lambda^4}(1+\cos^2\theta)$$

$I(\theta) = R^2\overline{S_1}$ is the intensity of the scattered radiation and $\overline{S}_0 = \frac{c}{8\pi}(\overline{E}^o)^2$ is the Poynting vector of the incident radiation (Kondratyev 1969, p176). Values of this coefficient for different λ for standard atmospheric conditions are tabulated in reference books (e.g. McCartney 1976). The dependence of the scattering coefficient on λ^{-4} is characteristic of Rayleigh scattering and explains why the sky is blue. The shorter wavelengths are scattered more strongly than the longer ones. The term $(1+\cos^2\theta)$ gives the angular distribution of scattered radiation. Figure C.3 shows this distribution. It can be seen from the diagram that the maximum intensity occurs in the forward and backward directions. At 90 and 270° scattering is at a minimum. For dayglow observations at 90° to the incident sunlight, the Rayleigh scattering will be least and so the dayglow feature will be most prominent against the background.

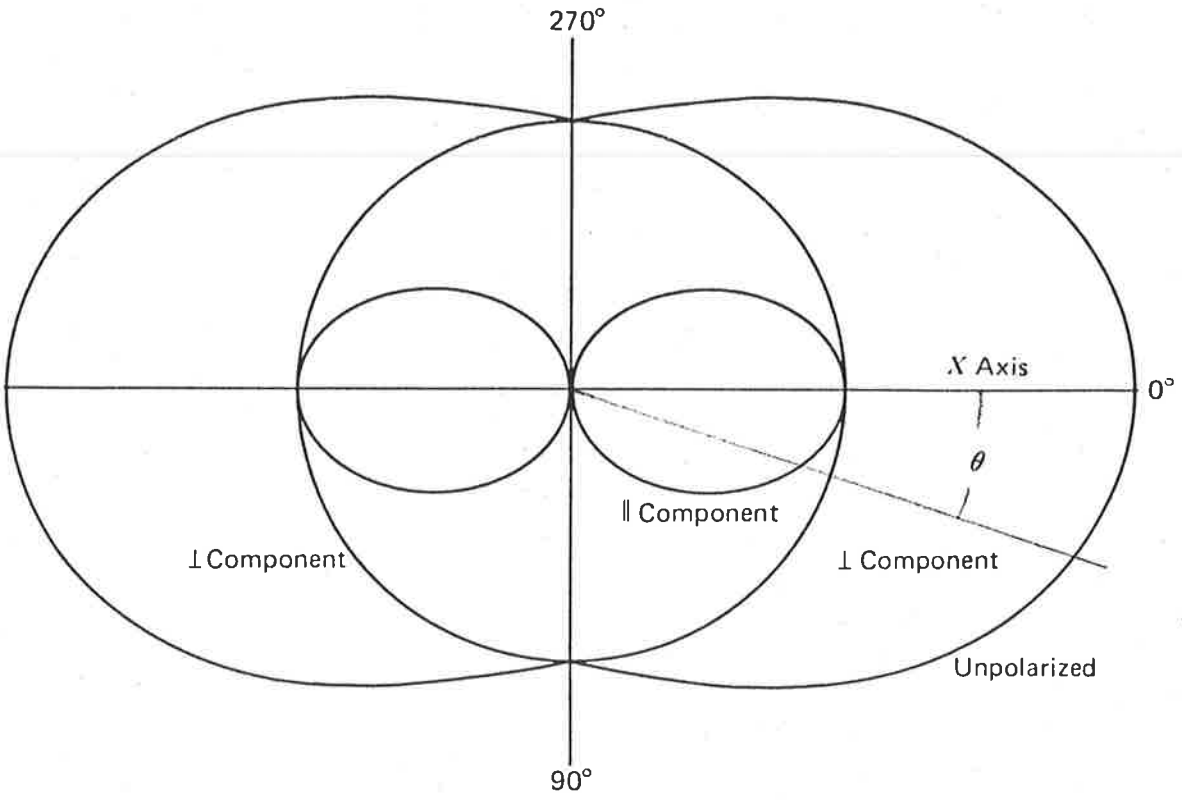

Figure C.3: Intensity distribution of Rayleigh scattering of unpolarized incident light. The polarization of the components is shown. (McCartney 1976)

Rayleigh scattering also polarizes the scattered light. Figure C.3 shows the distribution of the components with their electric vector perpendicular and parallel to that of the incident wave. This assumes that the incident light is unpolarized and that the scatterers are isotropic. In practice these two conditions do not strictly hold. Dayglow emission features are unpolarised and this fact can be used to discriminate against the background. At 90° to the incident solar flux Rayleigh scattered light is completely polarized. If dayglow observations are made in these directions with a polarizer set to minimize throughput of the background, the signal to background ratio is maximized. The background is still very much brighter than the emission feature.

Only single scattering has been considered and in reality some multiple scattering also occurs. Scattering from larger atmospheric particles, Mie scattering, also makes a significant contribution to sky light. The Earth reflects light back to the atmosphere and this is also

backscattered to Earth. An albedo of 1 implies complete reflection from the ground and 0 implies no reflection. For visible wavelengths snow covered ground has an albedo of about 0.8 – 0.9 and bare or vegetated ground an albedo of about 0.1 – 0.3. These values vary for different wavelengths and also vary, to a large extent, with the nature of the particular surface involved.

C.2.2 Mie scattering

The Rayleigh theory is usefully accurate for particles for which the radius, r, is less than about 0.03 wavelengths of the incident light. Although this applies to atomic and molecular atmospheric constituents other larger particles also contribute to scattering. Scattering by large particles is known as Mie scattering after G. Mie who first presented a theory to explain the phenomenon. Mie scattering treats scattering in terms of a dimensionless size parameter $\alpha = 2\pi r/\lambda$. It is a comprehensive theory which takes account of the varying relative size of the scatterers and different refractive indices. It can be used to treat scatterers of varying shape. In principle Mie scattering determines the scattered radiation by considering the scatterer, not as a dipole oscillator, but as a complex of multipoles. The resultant scattered radiation is the sum of all the partial waves produced by these poles when perturbed by the incident wave. In the limit for $\alpha < 0.2$ or $\lambda < 0.03r$ Mie scattering reduces to Rayleigh scattering. Figure C.4 (Mc Cartney, op. cit., p21) shows angular patterns of scattered intensity for three values of α. The theory will not be considered here, except for a few salient features, as it is most useful when accounting for scattering from clouds, fogs, smoke, and smog; conditions unsuitable for observation of dayglow.

Mie scattering is distinguished by: a complicated dependence of intensity on angle of observation, the complexity increasing with α; an increase in the ratio of forward scattering to backscattering with increasing α; and little dependence of scattering on wavelength when α is large, which explains the whiteness of clouds. Even in a very clear sky the presence of aerosols can be detected by observing the strong forward scattering, characteristic of Mie scattering, around the sun. This bright whitish region is known as the solar aureole. Coulson (1971)

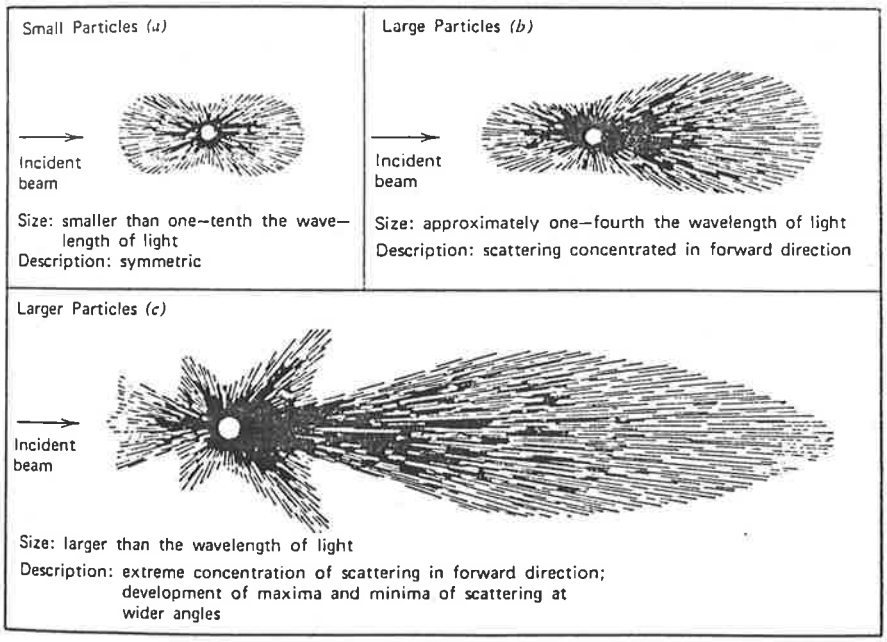

Figure C.4: Angular patterns of scattered intensity for particles of varying size. Small particles produce Rayleigh scattering. All distributions are explained by the theory of Mie scattering.

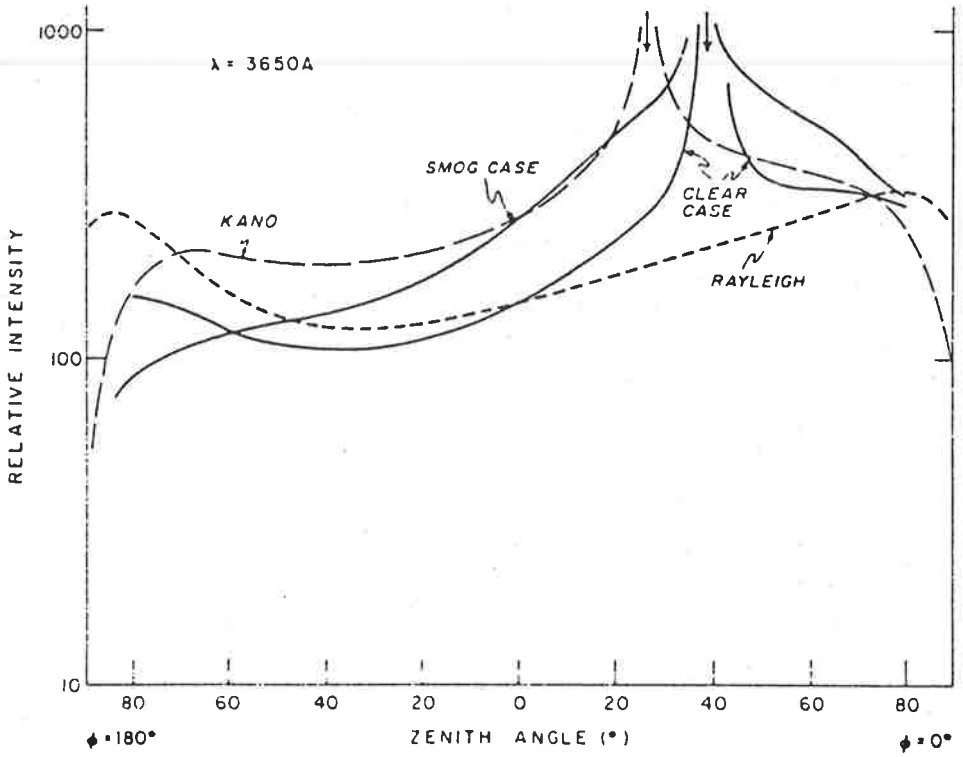

Figure C.5: Relative intensity of skylight as measured in clear and polluted atmospheres by Coulson (1971) are shown by solid lines. Model calculations of intensities for turbid (long dashes) and Rayleigh (short dashes) atmospheres are shown. Horizon brightening, obvious in the radiance measurements for the clear sky, indicates the dominance of Rayleigh scattering.

measured the sky brightness in clear and polluted atmospheres. Figure C.5 shows the results he obtained and a theoretical calculation for pure Rayleigh scattering and for a polluted atmosphere. The presence of the solar aureole marks the main deviation of a clear sky from a Rayleigh distribution. The marked forward scattering by aerosols enables even relatively small aerosol concentrations to be detected when illuminated by an intense source such as the sun. As the aerosol concentration increases the extent of the aureole increases. For a very polluted atmosphere or for a thin high cloud layer the whole sky is covered by the aureole. An increase in sky brightness near the horizon is indicative of the dominance of Rayleigh scattering in a clear sky. The minimum in scattering at 90° to the sun is masked when the aureole extends over the region.

C.2.3 Sky brightness

The previous two sections have outlined the principle mechanisms of atmospheric scattering. Precise theoretical calculation of sky brightness is difficult as the atmospheric composition must be accurately known. The composition varies daily, seasonally, and yearly. The sky brightness varies with atmospheric composition, solar zenith angle, wavelength, and changes in the Earth's albedo. Coulson *et al.* (1960) have tabulated Rayleigh scattered intensity and polarization for variations of these parameters. Models of sky brightness have been developed to try and explain the distributions obtained from measurements. The development of models is such that they can reproduce the general features obtained in measurements of sky brightness. As mentioned in the previous section, figure C.5 shows a comparison between model calculations and measurements made by Coulson (1971). Tanaka (1971a) used models to calculate sky brightness maps. Figure C.6 shows the transmitted radiation for 3 solar zenith angles assuming a small aerosol concentration and an albedo of 0.25. Such maps are useful for determining the optimum direction for measuring dayglow features. Maps of polarization were also presented (Tanaka, 1971b).

Measurement of airglow intensity is usually made in Rayleighs. One Rayleigh is is an apparent emission rate of 10^{10} photons m^{-2} (column) sec^{-1} (Chamberlain 1961). Sky brightness in Rayleighs can be estimated given the solar constant, solar irradiance per unit bandwidth, and intensity maps as in Figure C.6 . One Rayleigh is $(10^{10}\frac{hc}{\lambda})\ Wm^{-2}$ where h is Planks constant and c is the speed of light of wavelength λ. Table C.1 gives the relevant values for the continuum near the lines of present interest. If a value of solar flux, $\mathcal{F}$, is multiplied by the contour values given by the maps in Figure C.6 the brightness is obtained. This gives estimates of sky brightness varying from $\sim 1.5 \times 10^4$ kR nm^{-1} to $\sim 0.15 \times 10^4$ kR nm^{-1} for the conditions specified for the maps. These values are in reasonable agreement with the values of 1×10^5 kR nm^{-1} and 3×10^4 kR nm^{-1} as measured by Noxon and Goody (1962) and Miller and Fastie (1972).

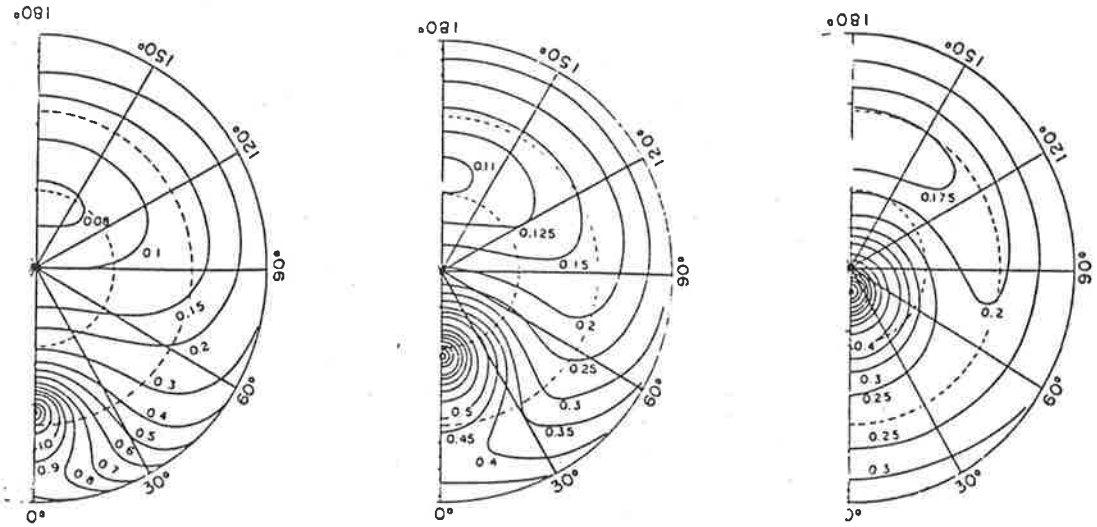

Figure C.6: Maps of the distribution of diffusely transmitted radiation at 450 nm for low turbidity, an albedo of 0.25, and varying solar zenith angles. Symmetry over 180° is assumed. The concentric rings mark the solar aureole and the contours of equal brightness are shown. (Tanaka 1971a)

Table C.1: Solar Flux

λ	Solar irradiance		$\mathcal{F}$
nm	W m^{-2} nm^{-1}	kR nm^{-1}	kR nm^{-1}
557.7	1.707	4.793×10^5	1.53×10^4
589.3	1.700	5.045×10^5	1.61×10^4
630.1	1.570	4.979×10^5	1.58×10^4

C.2.4 Other types of scattering

Although Rayleigh and Mie scattering can together give a reasonable estimate of sky brightness and explain most of the gross features of the sky spectrum, other forms of scattering can produce significant effects when isolation of a dayglow feature is required. The dayglow feature is usually isolated by subtraction of a suitably normalized solar spectrum from the sky spectrum. The immediate neighbourhood of the direct solar spectrum is very similar to that of Rayleigh scattered sunlight. After subtraction of the sun spectrum from the sky spectrum two features are apparent: one is the atomic or molecular emission profile and the other is a spectrally broad sky contribution. This contribution may be considered as filling-in of any Fraunhofer absorption line in the sky spectrum; absorption lines in the sky spectrum are proportionally less deep than the same lines in the direct solar spectrum. This was first noted by Grainger and Ring (1962) and has since been called the Ring effect. Noxon and Goody (1965), Barmore (1975), and others have reported measurements of the Ring effect. Notable characteristics are a lack of polarization and considerable variability in other features such as intensity and solar zenith angle.

Several mechanisms for production of the Ring effect have been proposed. Aerosol fluorescence was favoured by Barmore (loc. cit.). Hunten (1970) invoked reflection of sky and sunlight from the ground to try and explain the effect. Kattawar *et al.* (1981) discuss and discard these propositions and present a convincing hypothesis for a combination of rotational Raman scattering and Rayleigh-Brillouin scattering from air molecules. Both these mechanisms had been previously rejected as inadequate on their own to explain the intensities obtained. Brillouin scattering is caused by density fluctuations in the medium. Small Doppler shifts in frequency are produced by movements of the fluctuations. Rotational Raman scattering occurs when the electrons in the molecules which scatter incident light change their rotational energy level and light scattered by the molecule is shifted slightly in frequency.

Although the Ring effect only contributes a fraction of the overall sky brightness it is of the

same order of magnitude as the dayglow emission features.

C.2.5 Dayglow excitation mechanisms

Reviews of the dayglow were published in the late 1960s and early 1970s (Wallace and McElroy 1966; Noxon 1968; Hunten 1971; Llewellyn and Evans 1971; Rundle 1971). At that time most dayglow observations were made using ground-based techniques and rocket firings. Satellites have enabled dayglow observations to be made more simply than ground-based observations as the instrument can be pointed tangentially through the emission layer to avoid Rayleigh scattered sunlight. Vallance-Jones *et al.* (1985) and Bates (1983) review the chemistry and recent measurements of all atmospheric emissions including dayglow, aurorae, and nightglow. Most information relates to the brightest emissions viz. oxygen λ 630 nm and λ 558 nm and the sodium λ 589 nm doublet. Hunten (1971) gives a table of expected intensities, production mechanisms and heights for daytime, twilight, and night-time emissions. The table is still useful although some intensities, especially dayglow ones, have been considerably revised.

The major production mechanisms for dayglow are resonant scattering, fluorescence, photodissociation, chemiluminescent reactions, photoelectron excitation, and excitation transfer.

An atom can absorb a photon from the incident sunlight. If the photon is re-emitted at the same wavelength the process is called resonant scattering. The photon can be re-emitted at a different wavelength by the atom gaining or losing energy; the process is then called fluorescence. Resonant scattering is the principal mechanism in the production of the sodium D lines. It also contributes minimally to the O1 λ 630 nm and λ 558 nm emissions. Chamberlain (1961, ch11) gives an extensive discussion of resonant scattering, including intensity and polarization calculations and an application of the theory to the twilight sodium emission.

When an atom absorbs a photon an electron gains energy and makes a transition from one energy level, k, to another, j. Resonance radiation occurs when the electron in level j returns to level k emitting a photon similar to the one previously absorbed. The number of photons

scattered per atom per second, g, can be calculated given f_{ij}, the oscillator strength of the transition from level i to level j, A_{jk} and A_{jl} the Einstein coefficients for the j → k transition and the j → l transitions where l represents all states of energy less than j

$$g = \pi \mathcal{F} \frac{\pi e^2}{mc} f_{ij} \frac{A_{jk}}{A_{jl}}$$

(Chamberlain 1961). The number of resonantly scattered photons depends on the incident solar flux, $\mathcal{F}$, and, not included in the equation, on Earth's albedo. Tables of g values are given in most of the dayglow reviews mentioned above.

Sodium dayglow is produced both photochemically, i.e. by chemiluminescence, and by resonant scattering of sunlight. The emission has a daytime intensity of about 6 kR; chemiluminescent processes contribute about 40 R (Chamberlain 1961). In the case of atomic oxygen lines several processes contribute to the emission. Figure C.7 shows a proposed model of the relative contributions of the different mechanisms for the oxygen emissions. The model predictions of intensity compare well with experimental profiles. Considerable discussion about chemiluminescent processes and the contribution of particular reactions to the airglow continues due to a lack of laboratory measurements of the rate constants for the reactions; model calculations are a means of testing proposed excitation schemes with empirical measurements.

C.3 Dayglow observations

A review of previous attempts at observing features in the visible dayglow spectrum is useful to emphasize the difficulties of such measurements. Although dayglow emissions can be studied using satellite and balloon borne instruments most emphasis will be placed on ground-based techniques.

Although Scrimger and Hunten (1957) observed the sodium D Fraunhofer lines in the solar spectrum, measurements of sodium dayglow emissions were first reported by Blamont and Donahue (1961). A Zeeman photometer was used. This instrument uses specialized techniques only appropriate for alkali metal emissions (e.g. sodium, potassium, lithium) and will be dis-

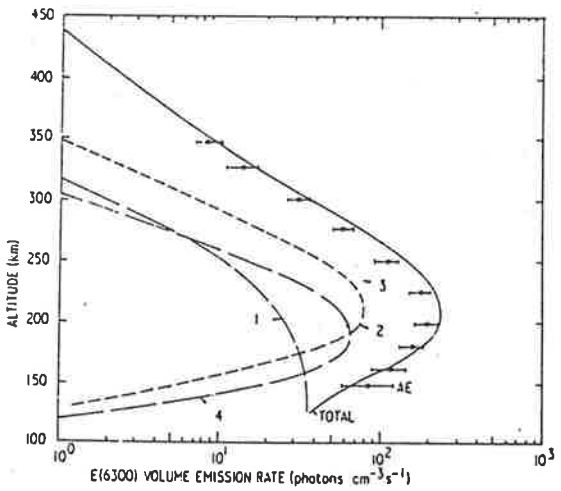

at λ 630 nm

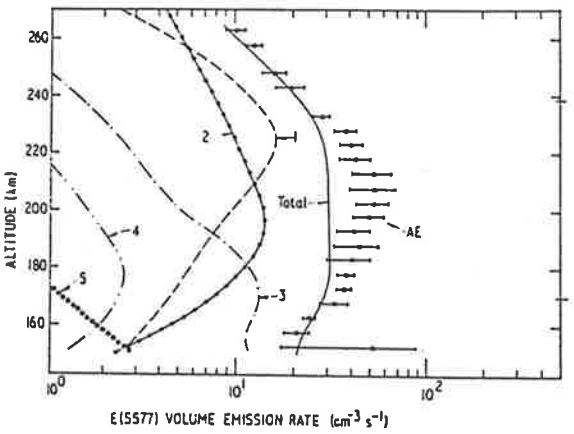

at λ 558 nm

Figure C.7: On the left dayglow O^1D sources are compared to Atmospheric Explorer measurements. The production curves are for: (1) photodissociation of O_2, (2) O_2^+ dissociative recombination, (3)photoelectron excitation, and (4) chemiluminescent processes. On the right O^1S sources and Atmospheric Explorer measurements. The sources in this case are: (1) O_2^+ dissociative recombination, (2) photoelectron excitation, (3)+(4) chemiluminescent processes. (Bates 1983)

cussed later. The results presented by Blamont and Donahue (1961) showed that the dayglow emissions could be detected, and provided impetus for others to obtain measurements of other emissions.

C.3.1 Oxygen λ 630 nm dayglow observations

The first reported dayglow measurements of the λ 630 nm emission were made using a technique which exploits the differences in polarization between the emission and the sky background. Dayglow emission features are almost completely unpolarized. Rayleigh scattered sunlight varies in polarization over the sky. At 90° to the sun maximum polarization of the scattered sunlight is obtained. The polarimeter observations of Noxon and Goody (1962) and Noxon (1968) were made by balancing the two components of polarization to equal intensity using polaroids and optical attenuators. Balance was obtained for observations at 90° to the sun at a wavelength away from the emission feature. When the wavelength was scanned through the emission feature (about 1.0 nm) using an Ebert spectrometer the emission was detectable as a modulation of the output intensity. The sky polarization does not change significantly over such wavelength ranges and polarization of the emission feature is zero. Measurements were reported of both the λ 630 nm oxygen emission and the λ 589 nm sodium emission .

Jarret and Hoey (1963, 1964) were the first to use Fabry-Perot etalons for observing dayglow. A Fabry-Perot etalon with a 1.5 nm filter was used to observe the sky. The fringe pattern obtained was photographed; it was claimed that this fringe pattern observed was due to the oxygen λ 630 nm emission (Jarret and Hoey 1963, 1964). Cogger and Shepherd (1965) tried to repeat these measurements. By using photoelectric instead of photographic recording techniques they found the background continuum to be significantly modulated. They proposed that the Fraunhofer structure in the solar continuum produced this modulation and, presumably, the fringes photographed by Jarret and Hoey.

Bens *et al.* (1965) presented a series of results from measurements using two Fabry-Perot

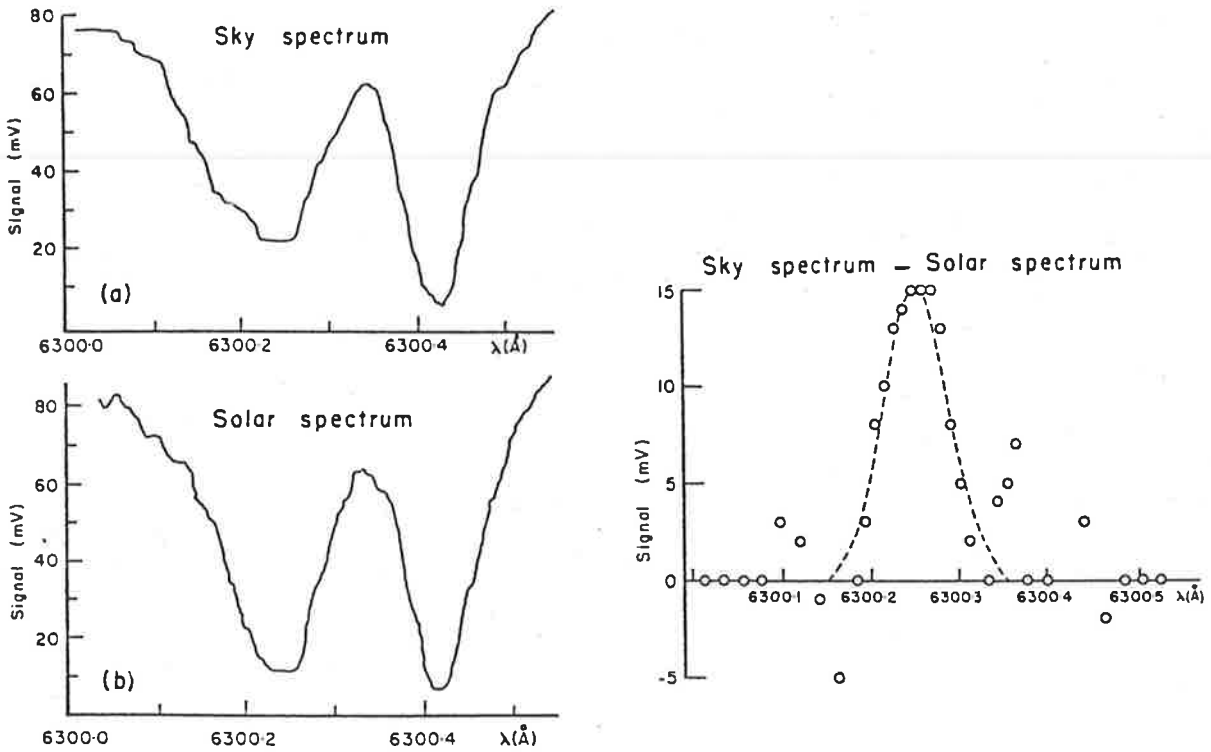

Figure C.8: λ 630 nm dayglow measurements as obtained by Bens et al. (loc. cit.) . Subtracting the solar spectrum from the sky spectrum results in the isolation of the emission feature.

etalons in series with an interference filter. The instrument parameters were varied to give successively more background discrimination. To allow for the background continuum alternate observations of the sun and sky were made in the final sequence of measurements. The results presented by Bens *et al.* are shown in Figure C.8. Although both spectra look very similar the emission feature is discernible in the sky spectrum. The emission feature is clearly visible when the sun spectrum is subtracted from the sky spectrum. This was the first result to isolate convincingly the λ 630 nm emission from the day sky light using a Fabry-Perot spectrometer. A Gaussian curve fitted directly to the subtraction feature was used to estimate temperature. The result obtained, $1700° \pm 500°$, is somewhat higher than to be expected for the source region in the thermosphere. Accurate temperature measurements require that the instrument finesse be known so that the increase in width of the profile, due to the finite width of the instrument passband, can be calculated (Henderson and Slater 1966). Bens *et al.* (1965) defined the basic

requirements for Fabry-Perot observations of dayglow emissions and highlighted the importance of detailed knowledge of the solar spectrum in the vicinity of the emission.

A direct solar spectrum was used as an approximation to the background of Rayleigh scattered sunlight. The sky profile consists of the sky emission feature plus the Rayleigh scattered sunlight and Ring component. Noxon and Goody (1965) realized the relevance of the Ring component for isolation of the dayglow feature. The magnitude of the Ring component depends on the depth of the Fraunhofer line in which the emission is sited. Unless this component is accounted for in analysis, spuriously high intensities and distorted profiles are obtained.

Noxon (1968) reported oxygen λ 630 nm intensities of 5–25kR. Later measurements reported much lower values, for example Barmore (1977) obtained 6–8 kR and Cocks and Jacka (1978), 2 kR.

The results reported by Barmore (1975) on the Ring effect and the oxygen λ 630 nm emission (Barmore 1977) were made with a PEPSIOS (Poly-Etalon, Pressure Swept, Interferometric Optical Spectrometer). This instrument will be discussed in more detail in chapter 3. It achieves very good background rejection by using a system of three Fabry-Perot etalons. Barmore (1975, 1977) recorded solar and sky spectra over 0.18 nm near λ 630 nm allowing studies of the Ring effect in three absorption features and the oxygen λ 630 nm emission feature. Intensity of the emission and estimates of temperature, with uncertainties of about 400 K, were presented.

Cocks *et al.* (1980) describe a dual Fabry-Perot spectrometer for daytime airglow studies. (This instrument was upgraded for the present project.) The instrument is similar to that of Bens *et al.* (1965), with two Fabry-Perot etalons and a 0.3 nm filter. Cocks and Jacka (1978) derived, from observations of the λ 630 nm oxygen emission, daytime thermospheric temperatures, wind velocities, and emission intensities. The signal to noise ratio was considerably better than that obtained by Barmore (1977) and enabled temperature determinations to within 100 K. This was the first reported measurement of wind velocities from measurements of daytime emission features.

Although Fabry-Perot spectrometers were used initially for studies of the λ 630 nm oxygen emission, considerable work was later done on the telluric absorption in the solar spectrum and on the sodium D2 emission. Before this work is discussed the observations of the sodium emission using Zeeman photometers will be reviewed.

C.3.2 Sodium Zeeman photometer observations

Scrimger and Hunten (1957) used a sodium absorption cell to observe the sodium D lines in the Fraunhofer structure. A lens was used to focus the solar image just behind a window in the absorption cell. Another lens, on an axis at 90° to the first, focussed the scattered light from the absorption cell onto the slit of a spectrometer which was scanned through 3 nm to cover both the D1 and D2 lines. The absorption cell was replaced by glass diffuser plates to observe direct scattering for every 5 alternate scans. This instrument was principally used to determine the intensity at the bottom of the Fraunhofer lines (residual intensity), 5.90 ± 0.46 for D1 and 5.06 ± 0.24 for D2, for a local continuum intensity of 100. The residual intensity was found to decrease slightly when the sun approached the horizon. Scrimger and Hunten (1957) proposed that this was due to increased absorption by telluric sodium over the longer path length of the sunlight in the sodium layer.

Zeeman photometers are also based on a sodium absorption cell. Blamont *et al.* (1958) used a Zeeman photometer to study the sodium twilight emissions and Blamont and Donahue (1961) reported the first measurements of the sodium dayglow. The Zeeman effect describes the wavelength splitting produced on applying a large magnetic field to an emitting gas. When a magnetic field is applied to an absorption cell, depending on the direction of the magnetic field, only one of the components is absorbed and so an effective wavelength shift is obtained. A photomultiplier is used to detect the signal from a sodium absorption cell at 90° to the incident sky spectrum. By switching the magnetic field off and on the intensity varies from that near the bottom of the Fraunhofer line (which includes the dayglow emission feature) to that about

0.08 nm (for a 4k Gauss field) from the bottom of the line. The dayglow contribution at this wavelength should be negligible. By comparing the ratio of these intensities with a similar ratio for observations of direct sunlight Blamont and Donahue (loc. cit.) inferred dayglow intensities. The dayglow intensities obtained implied a daytime sodium abundance four times that determined from twilight measurements.

Blamont and Donahue (1964) published further results obtained over 4 years. Photochemical and dynamical processes were proposed to explain the large diurnal variation. Revision of some chemical rates and rapid transport processes were required to account for the purported diurnal variation. It was also suggested that there could be other mechanisms which could explain the large intensities observed. If a telluric absorption line was in the vicinity of the sodium emission this could affect the background measurements or, if sufficiently close, the emission measurement. Blamont and Donahue (1964) did raise the possibility of some other contribution to the sky light not present in the solar spectrum as observed by Grainger and Ring (1962) in other Fraunhofer lines. However they did not consider it to be a serious possibility.

Gadsden *et al.* (1966) partially explained the high intensities observed by considering the different polarizations of sun and sky light. Polarization of sky light varies throughout the day and depends on the direction of observation and the solar zenith angle. Gadsden and Purdy (1970) used a Zeeman photometer incorporating a polarizer to observe the sodium emissions. The polarizer was set so that only the component perpendicular to the applied magnetic field was transmitted. After some measurements were made the instrument was rotated by 90° to ensure that the skylight was adequately removed. The measurements obtained in this way still implied a noon increase of 2 to 6 times the twilight abundance. The seasonal variation in the dayglow abundance was similar to that found in twilight. Albano et al. (1970), by theoretically allowing for the sky polarization, obtained similar results for the sodium abundance ratios.

Chanin and Goutail (1975) used a theoretical model to show that interpretions of large sodium daytime enhancements by previous Zeeman photometer studies could be explained,

without implying any diurnal variations in abundance, by the combination of an airglow emission feature and a continuum or Ring component. The Earth's albedo was found to have an effect on the intensity predicted by the model. Chanin and Goutail were thus finally able to obtain agreement between the Zeeman photometer measurements and mounting evidence from other types of measurements for the absence of any large diurnal variation in the sodium layer.

C.3.3 Fabry-Perot observations of the sodium dayglow

The presence of sodium in the Earth's upper atmosphere can be detected in two ways either by observation of the telluric absorption feature in the solar spectrum or by observation of the resonant emission in the sky spectrum.

Mc Nutt and Mack (1963) presented a comprehensive study of the sodium Fraunhofer D lines. They used a Fastie-Ebert grating spectrometer to isolate a single order of a Fabry-Perot interferometer. This gave a resolving power of 6×10^5 which implies an instrument width of about 1 pm. The instrument was pressure scanned over a wavelength range of 0.17 nm. Both the D1 and D2 lines were studied. The telluric sodium absorption feature is quite clear near the base of the Fraunhofer line as can be seen in Figure C.2. The same authors presented a table of all telluric absorption features they observed within 0.07 nm of the D lines. Atmospheric sodium abundances were inferred by interpolating the base of the solar profile and measuring the area of the telluric absorption feature. The equivalent width, obtained from the area, is directly related to abundance. An annual variation in abundance was found, the maximum abundance occurring in winter. The values obtained ($1 - 8 \times 10^9$ cm^{-2}) were considerably different to those reported by Blamont and Donahue (1964) who obtained abundances as high as 40×10^9 cm^{-2}. Mc Nutt and Mack's (1963) abundance estimates are in reasonable agreement with those from recent lidar measurements where abundances of about 7×10^9 cm^{-2} have been obtained (Kirchoff 1986). Mc Nutt and Mack (1963) also measured the residual intensities of the Fraunhofer D lines to be D1, 4.95 ± 0.10 and D2, 4.44 ± 0.10. Also the shifts of the solar

Fraunhofer line due to the gravitational red shift and the Doppler shifts for the Earth's motions were measured.

Similar measurements of the telluric absorption feature in the solar spectrum were made using a PEPSIOS spectrometer by Burnett (1965), and Burnett et al. (1972). Burnett *et al.* (1972) presented four years of absorption measurements made at Boca Raton, Florida (26° N, 80° W). The abundance measurements obtained showed considerable variation and any seasonal or diurnal trend was almost completely masked by the spread in abundances. This spread was interpreted as nonuniformities or patchiness in the abundance of the layer. Comparisions with the Zeeman photometer daytime measurements were made and discrepancies noted. Partowmah and Roesler (1977) presented several years of absorption measurements from Madison, Wisconsin and Yegingil et al. (1980) presented absorption measurements made with a PEPSIOS spectrometer at Ankara, Turkey (39° N, 32° E). Both observed a maximum abundance at the end of winter and a minimum near the end of summer. No significant diurnal variation was observed but, as with the Boca Raton measurements, considerable patchiness or sodium clouds were postulated to explain the large random fluctuations in the sodium abundance.

Burnett et al. (1975) presented PEPSIOS measurements of the sodium D2 dayglow emission feature. The measurements had been made both at Boca Raton and also at Fritz Peak (40° N, 105° W). The measurements were made at Fritz Peak to make a direct comparison with the Zeeman photometer measurements by Gadsden and Purdy (1970). This was to investigate the hypothesis that differences between abundances obtained from Zeeman photometer measurements and other measurements were due to latitudinal variations in the sodium distribution. An average daytime/twilight intensity ratio of 2 was obtained and explained by variation in solar flux with zenith angle and in the Earth's albedo. The sodium emission feature was extracted from the recorded spectrum by subtracting a normalized solar spectrum. The subtraction process also produced an estimate of the Ring effect. Any diurnal variation in the Ring component was masked by scatter in the values obtained. The abundance measurements were made by

calculating the area of the emission profile obtained from the subtraction process. No attempt was made to estimate winds or temperatures from the data.

Estimates of the sodium layer temperature have been obtained from Fabry-Perot observations of the sodium emission at twilight (Hernandez 1975; Sipler and Biondi 1975,1978). No studies have used the sodium emission to deduce winds.

C.3.4 Other sodium dayglow measurements

When Zeeman photometer measurements of the dayglow were shown to predict a large daytime/twilight abundance ratio verification of these results was required. The difficulty with dayglow observations is in isolating the emission feature from the background. Rayleigh scattering occurs mainly in the lower regions of the atmosphere where the air is densest. A rocket can be used to carry instruments above the Rayleigh scattering region and a simple photometer used to measure the dayglow emission intensity.

Hunten and Wallace (1967) reported rocket measurements of the sodium dayglow. They used a series of photometers to measure several different dayglow features and monitor background light levels. Two rocket firings were made in April and June. Twilight observations were made in conjunction with the rocket firings. The sodium photometer had a 1.6 nm filter so the results obtained are for the combined D1 and D2 emission lines. For the June flight, after allowing for the increased solar flux in the daytime, no increase in abundance was found between daytime and twilight results. In April a daytime twilight ratio of 1.45 was obtained. Twilight intensities at this time also varied considerably over the week of the flight. The enhancement measured was shown to be confined to a narrow layer around 90 km. The intensity of the daytime emission was 9.8 kR.

Donahue and Meier (1967) also reported rocket measurements of the sodium dayglow. They used a sodium resonance cell photometer, in a complicated flight pattern, to obtain measurements at various layer cross-sections at different angles and different heights. Use of a resonance

cell should not have been necessary; the data from the simple photometer measurements are more convincing than those obtained by this method. Ground-based Zeeman photometers were run in conjunction with this flight. The data obtained were interpreted, by constructing computer models, to imply a daytime/twilight abundance ratio consistent with those from Zeeman photometer measurements. The intensities obtained were not reduced to the zenith but were 19 kR for a 55° zenith angle and 60 kR for 83° zenith angle.

Ahmed *et al.* (1970) reported some early rocket measurements of the sodium dayglow in which a Fastie-Ebert spectrometer was used to measure the intensity. Intensities (presumably in the zenith) of 3-5 kR were obtained from below and within the layer.

Satellites can also be used to make observations of the dayglow. Observations of the limb of the Earth are made thus avoiding Rayleigh backscattering of sunlight. The angle of observation can be varied to allow vertical resolution of thermospheric emissions. Blamont and Luton (1972) describe the Fabry-Perot interferometer on OGO–6. This instrument was used for measurements of the λ 630 nm thermospheric oxygen emission. OGO–6 also carried a photometer for observations of the oxygen λ 558 nm and sodium λ 589 nm emissions (Thomas and Donahue 1972). The sodium observations have been used to infer the presence of noctilucent clouds (Donahue *et al.* 1972). Newman (1988) reported sodium photometer measurements from the Defense Meteorological Satellite Program satellite. The limb-scanning technique used allowed vertical profiles to be determined and the global distribution of sodium was studied. A wide variety of aeronomic instruments have been used on various satellites including the Atmospheric and Dynamics Explorers. The latter carries a Fabry-Perot interferometer with 8 filters in a wheel which can be used for observations of a range of emissions (Hays *et al.* 1981). Analysis of these satellite observations has been reported in a large number of papers, mainly on thermospheric emissions which go beyond the scope of this review. Further satellite observations of the dayglow are proposed (Bucholtz *et al.* 1986). Recent reviews, such as that of Vallance-Jones *et al.* (1985) give further references for satellite dayglow measurements.